PRINCIPLES AND APPLICATIONS OF QUANTUM DECOHERENCE IN BIOLOGICAL, CHEMICAL, AND CONDENSED MATTER SYSTEMS

By

Liam Terres Hall

SUBMITTED IN TOTAL FULFILLMENT OF THE
REQUIREMENTS FOR THE DEGREE OF
DOCTOR OF PHILOSOPHY
SCHOOL OF PHYSICS,
THE UNIVERSITY OF MELBOURNE
AUSTRALIA
SEPTEMBER 2013

PRODUCED ON ARCHIVAL QUALITY PAPER

"It's not the size of the dog in the fight,
it's the size of the fight in the dog."
Mark Twain

Abstract

This thesis focuses on the use of the Nitrogen-Vacancy (NV) defect centre in diamond as a single spin sensor of nanoscale magnetic fields. The NV system has attracted considerable interest in recent years due to its unique combination of sensitivity, nanoscale resolution, room temperature operation, and stable fluorescence, together with the inherent biocompatibility of diamond; making it ideal for measuring coherent quantum processes in biological, chemical and condensed matter systems.

Existing NV-based sensing techniques, however, are ultimately limited by sources of magnetic noise that act to destroy the very resource required for their operation: the quantum phase coherence between NV spin levels. We address this problem by showing that this noise is a rich source of information about the dynamics of the environment we wish to measure. We develop protocols by which to extract dynamical environmental parameters from decoherence measurements of the NV spin, and a detailed experimental verification is conducted using diamond nanocrystals immersed in a $MnCl_2$ electrolyte. We then detail how sensitivities can be improved by employing sophisticated dynamic decoupling techniques to remove the decoherence effects of the intrinsic noise, whilst preserving that of the target sample.

To characterise the effects of pulse errors, we describe the full coherent evolution of the NV spin under pulse-based microwave control, including microwave driven and free precession intervals. This analysis explains the origin of many experimental artifacts overlooked in the literature, and is applied to three experimentally relevant cases, demonstrating remarkable agreement between theoretical and experimental results.

We then analyse and discuss two important future applications of decoherence sensing to biological imaging. The first involves using a single NV centre in close proximity to an ion channel in a cell membrane to monitor its switch-on/switch-off activity. This technique is expected to have wide ranging implications for nanoscale biology and drug discovery. The second involves using an array of NV centres to image neuronal network dynamics. This technique is expected to yield significant insight into the way information is processed in the brain. In both cases, we find the temporal resolution to be of millisecond timescales, effectively allowing for real time imaging of these systems with micrometre spatial resolution.

We analyse cases in which environmental frequencies are sufficiently high to result in a mutual exchange of energy with the NV spin, and discuss how this may be used to reconstruct the corresponding frequency spectrum. This analysis is then applied to two ground-breaking experiments, showing remarkable agreement.

Protocols for *in-situ* monitoring of mobile nanodiamonds in biological systems are developed. In addition to obtaining information about the local magnetic environment, these protocols allow for the determination of both the position and orientation of the nanocrystal, yielding information about the mechanical forces to which it is subjected. These techniques are applied in analysing a set of experiments in which diamond nanocrystals are taken up endosomally by human cervical cancer cells.

Finally, we focus our attention on understanding the microscopic dynamics of the spin bath and its effect on the NV spin. Many existing analytic approaches are based on simplified phenomenological models in which it is difficult to capture the complex physics associated with this system. Conversely, numerical approaches reproduce this complex behaviour, but are limited in the amount of theoretical insight they can provide. Using a systematic approach based on the spatial statistics of the spin bath constituents, we develop a purely analytic theory for the NV central spin decoherence problem that reproduces the experimental and numerical results found in the literature, whilst correcting the limitations and inaccuracies associated with existing analytical approaches.

THE UNIVERSITY OF MELBOURNE
SCHOOL OF PHYSICS

This is to certify that

i. the thesis comprises only my original work,
ii. due acknowledgement has been made in the text to all other material used,
iii. the thesis is less than 100,000 words in length, exclusive of tables, maps, bibliographies, appendices and footnotes.

I authorize the Head of the School of Physics to make or have made a copy of this thesis to any person judged to have an acceptable reason for access to the information, i.e., for research, study or instruction.

Signature: _____

Date: _____

Acknowledgements

First and foremost, I would like acknowledge the unwavering support and guidance I have received from my supervisor, Professor Lloyd Hollenberg, over the course of my candidature. From the commencement of this project, I have been amazed at not only his vast knowledge of the physical sciences (not to mention the ability to focus on an unconstrained number of projects at any given time), but the broad-mindedness and genuine enthusiasm with which he approaches his work. Such qualities have provided me with a prime example of exactly how scientific research should be conducted. I am grateful for his trusting me with such an exciting, innovative and rewarding project and, should everything proceed according to plan, I look forward with a great deal of excitement to the continuation of this research in the future.

Thankyou to my good friend and colleague David Simpson, whose combination of work ethic, guidance, enthusiasm and technical brilliance has been a constant source of inspiration, not only to myself, but to every member of our group. I am grateful for the time he's given me during our lengthy discussions, and the invaluable insight that has come with it.

I am also greatly indebted to Charles Hill and Jared Cole for the vast amount of time and advice I have received from them over the past few years. It has seemed that no ask was too big, nor any question too silly, nor any time inconvenient; and for that I am truly grateful. Thankyou also to Rob Scholten and Andy Martin for their support, guidance and advice; and a special thankyou is also owed to Patricia Gigliuto for her friendly, tireless support with organisational matters (not to mention patience, as I certainly didn't make things easy!).

I would also like to acknowledge those colleagues with whom I have worked closely, and subsequently become great mates: Marcus Doherty, Florian Dolde, Brant Gibson, Kristijan Jovanoski, Stefan Kauffman, Liam McGuinness, Boris Naydenov, Viktor Perunicic, Alastair Stacey, Steffen Steinert and James Wood. Learning from, and

working with these guys has been an absolute privilege. To Stefan and Steffen, best of luck with your new families and new careers.

During my candidature, I had the privilege of visiting a number of other institutions, from which I received great support and warm hospitality. As such, I am greatly indebted to Jörg Wrachtrup and Claudia Unger from the University of Stuttgart, Fedor Jelezko and Maria Heuschmid from the University of Ulm, Vincent Jacques from École Normale Supérieure de Cachan, and Gerd Schön from the Karlsruhe Institute of Technology.

Finally, I would like to say a huge thankyou to my family (originals and in-laws) for their love, tolerance of my constant absent mindedness, genuine enthusiasm toward my work, and for giving me the opportunities necessary to chase my life-long dreams of becoming a scientist. To Mum and Dad, thanks for my sparking my love of mathematics long before I even knew what school was; and for teaching me to maintain an objective, inquisitive, and responsible approach to every endevour. A special mention goes to my brother Greg and his partner Sanae for their friendship and encouragement, and for Greg's diligent (but often brutal) scientific critiquing of my work. But most importantly of all, I would like to thank my beautiful wife Emily for her patience, tolerance of my bizarre sleeping patterns, and support over these past few years. No matter how much I love my work, nothing compares to coming home to you and our little Arthur at the end of the day.

List of Publications

During the course of this project, a number of derivative works were produced based on the material presented in this thesis. These include both peer-reviewed journal articles, and conference and invited talks, and are listed here for reference.

Refereed Publications

1. L.T. Hall, J.H. Cole, C.D. Hill and L.C.L. Hollenberg. Sensing of Fluctuating Nanoscale Magnetic Fields Using Nitrogen-Vacancy Centers in Diamond. *Physical Review Letters*, Vol. 103, no. 22, pg. 220802, 2009.

2. L.T. Hall, C.D. Hill, J.H. Cole and L.C.L. Hollenberg. Ultrasensitive diamond magnetometry using optimal dynamic decoupling. *Physical Review B*, Vol. 82, no. 4, pg. 045208, 2010.

3. L.T. Hall, C.D. Hill, J.H. Cole, B. Staedler, F. Caruso, P. Mulvaney, J. Wrachtrup and L.C.L. Hollenberg. Monitoring ion-channel function in real time through quantum decoherence. *Proceedings of the National Academy of Sciences of the United States of America*, Vol. 107, no. 44, pg. 045208, 2010.

4. B. Naydenov, F. Dolde, L.T. Hall, C. Shin, H. Fedder, L.C.L. Hollenberg, F. Jelezko and J. Wrachtrup. Dynamical decoupling of a single-electron spin at room temperature. *Physical Review B*, Vol. 83, no. 8, pg. 081201, 2011.

5. L.P. McGuinness, Y. Yan, A. Stacey, D.A. Simpson, L.T. Hall, D. Maclaurin, S. Prawer, P. Mulvaney, F. Caruso, R.E. Scholten and L.C.L. Hollenberg. Quantum measurement and orientation tracking of fluorescent nanodiamonds inside living cells. *Nature Nanotechnology*, Vol. 6, no. 6, pg. 358-363, 2011.

6. L.T. Hall, G.C.G. Beart, E.A. Thomas, D.A. Simpson, L.P. McGuinness, J.H. Cole, J.H. Manton, R.E. Scholten, F. Jelezko and J. Wrachtrup, S. Petrou and L.C.L. Hollenberg. Quantum measurement and orientation tracking of fluorescent nanodiamonds inside living cells. *Nature Scientific Reports*, Vol. 2, pg. 401, 2011.

7. F. Reinhard, F.Z. Shi, N. Zhao, F. Rempp, B. Naydenov, J. Meijer, L.T. Hall, L.C.L. Hollenberg, J.F. Du, R.B. Liu and J. Wrachtrup. Sensing of Fluctuating Tuning a Spin Bath through the Quantum-Classical Transition. *Physical Review Letters*, Vol. 108, no. 20, pg. 200402, 2012.

8. S. Steinert, F. Ziem, L.T. Hall, A. Zappe, M. Schweikert, A. Aird, G. Balasubramanian, L.C.L. Hollenberg and J.Wrachtrup. Nanoscale detection of stochastic spin fluctuations using quantum relaxation. *Nature Communications*, Vol. 4, pg. 1607, 2013.

9. L.T. Hall, D.A. Simpson, and L.C.L. Hollenberg. Nanoscale sensing and imaging in biology using the nitrogen-vacancy center in diamond. *MRS Bulletin*, Vol. 38, pg. 162, 2013.

10. S. Kaufmann, D.A. Simpson, L.T. Hall, V. Perunicic, P. Senn, S. Steinert, L.P. McGuinness, B.C. Johnson, T. Ohshima, F. Caruso, J. Wrachtrup, R.E. Scholten, P. Mulvaney, and L.C.L. Hollenberg. Monitoring ion-channel function in real time through quantum decoherence. *Proceedings of the National Academy of Sciences of the United States of America*, Vol. 110, no. 27, pg. 10894, 2013.

11. D. Maclaurin, L.T. Hall, A.M. Martin and L.C.L. Hollenberg. Nanoscale magnetometry through quantum control of nitrogen-vacancy centres in rotationally diffusing nanodiamonds. *New Journal of Physics*, Vol. 15, pg. 013041, 2013.

12. L.P. McGuinness*, L.T. Hall*, A. Stacey, D.A. Simpson, C.D. Hill, J.H. Cole, K. Ganesan, B.C. Gibson, S. Prawer, P. Mulvaney, F. Jelezko, J. Wrachtrup, R.E. Scholten and L.C.L. Hollenberg. Ambient nanoscale sensing with single spins using quantum decoherence. *New Journal of Physics*, Vol. 15, pg. 073042, 2013.

*These authors contributed equally to this work.

Conference Talks

- L.T. Hall, C.D. Hill, J.H. Cole and L.C.L. Hollenberg. Quantum Decoherence Imaging Using NV Centres in Diamond, delivered at
  - *Tenth International Meeting on Hole Burning, Single Molecule, and Related Spectroscopies: Science and Applications (HBSM 2009)*, Cairns, Australia, 2009.
  - *19th Congress of the Australian Institute of Physics (AIP)*, Melbourne, Australia, 2010.
  - *2010 International Conference On Nanoscience and Nanotechnology (ICONN)*, Sydney, Australia, 2010.
- L.T. Hall, L.P. McGuinness, D.A. Simpson, C.D. Hill, J.H. Cole, and L.C.L. Hollenberg. Quantum Decoherence Imaging of 'Life' at the Nanoscale. *3rd nano-MRI research conference*, Paris, France, 2010.
- L.T. Hall, J.H. Cole and L.C.L. Hollenberg. The central spin decoherence problem. *The Australian Centre of Excellence for Quantum Computation & Communication Technology annual workshop*, Sunshine Coast, Australia, 2013.

Invited Talks

- L.T. Hall, C.D. Hill, J.H. Cole and L.C.L. Hollenberg. Numerical solution of the central spin problem for NV centres in diamond. *3. Physikalisches Institut Theory seminar*, Universität Stuttgart, Germany, 2010.
- L.T. Hall, C.D. Hill, J.H. Cole and L.C.L. Hollenberg. Quantum Decoherence Imaging of 'Life' at the Nanoscale. *Institute für Theoretische Festkörperphysik and DFGCentre for Functional Nanostructures (CFN) theory seminar*, Karlsruhe Institute of Technology, 76128 Karlsruhe, Germany, 2010.
- L.T. Hall, J.H. Cole and L.C.L. Hollenberg. Analytic solution of the central spin problem for NV centres in diamond, delivered at
  - *Institute for Quantum Optics Theory seminar*, Ulm University, Germany, June, 2013.

– *Laboratoire de photonique quantique et moléculaire colloquium*, École normale supérieure de Cachan, France, 2013.

– *3. Physikalisches Institut Theory seminar*, Universitt Stuttgart, Germany, June, 2013.

Table of Contents

List of Figures

List of Tables

Chapter 1

Introduction

Whilst the physical realisation of a quantum computer remains a somewhat elusive goal, the quest has yielded a remarkable increase in our knowledge of physics at the sub-nanometre scale. Not only has our ability to control, characterise and manipulate quantum systems lead us to speak of manufacture and fabrication in terms of single atoms, so too have we deepened our understanding of the way in which open quantum systems interact with their external environment; perhaps to the point where we are on the verge of understanding just how the macroscopic world emerges from the microscopic world of quantum superpositions, correlations and uncertainties.

The basic operating element of any quantum-based technology is the qubit (quantum bit), which is, in principle, an isolated two-level system that can be accurately initialized, controlled and measured. We represent a qubit as a two-level quantum system with basis states $|0\rangle$ and $|1\rangle$. Whereas classical bits may take only the values 0 or 1, qubits have a distinct advantage in that they may be prepared in an arbitrary superposition of these basis states. The quantum phase relationship, or coherence, between these states is the resource that is used to process and store quantum information, and gives rise to not only the possibility of quantum computation, but a

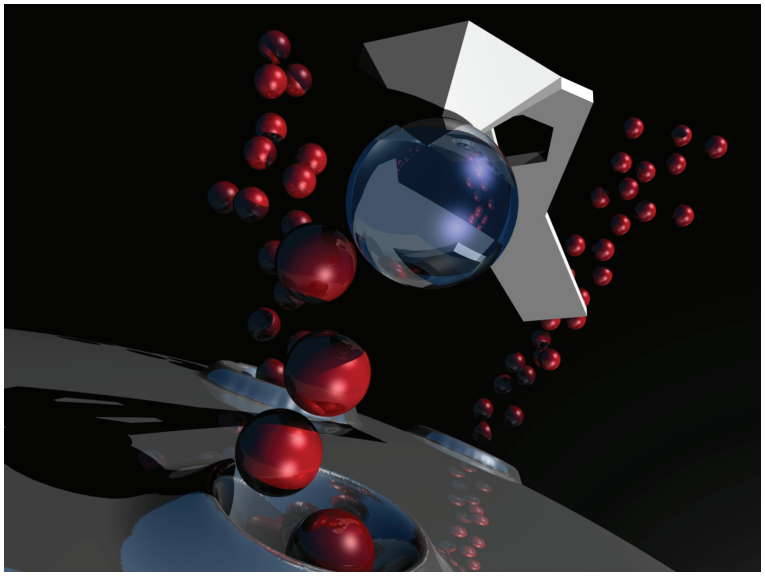

Figure 1.1: Quantum decoherence imaging of biological ion channel operation, as explored in chapter 8.

multitude of quantum based devices; their utility hinging on the lifetime of the phase coherence between these basis states, with the 'decoherence' arising from the unavoidable interaction between the system and its surrounding environment. In particular, we focus on the use of solid state spin qubits to measure nanoscale magnetic fields, as the phase interference between the basis states of a spin qubit is directly proportional to the strength of this field, by virtue of the Zeeman interaction. Such systems have remarkable advantages over traditional magnetometry techniques, as single spins offer a platform that is both highly sensitive and highly localised, permitting the detection of nanoscale magnetic fields with atomic spatial resolution. Furthermore, certain systems, such as the Nitrogen-Vacancy (NV) defect centre in diamond, are capable of room temperature operation.

Whilst theoretical and experimental investigations focussed on NV centre spin probes are showing great promise for the successful resolution of static nano-scale

magnetic structures within both condensed-matter and biological systems, decoherence presents a major obstacle in the improvement of the detection sensitivity. In each new proposal, the sensitivity of the imaging technique is ultimately limited by the coherence time of the associated quantum system. Thus decoherence is ubiquitously looked upon as a pathological phenomenon whose effects must be controlled and mitigated as far as possible. In this work we offer an inversion of this viewpoint: the focus of this thesis is to show that by exposing a 'Quantum Probe' to a sample environment in a controlled manner, the induced decoherence may be used to image dynamic characteristics not evident with the use of existing techniques. Such a device would employ current solid state qubit technology, thus ensuring comparable sensitivity to current techniques.

1.1 Layout and publication of material in this thesis

The material in this thesis is organised by topic, rather than chronologically, to improve the clarity of the presentation. In chapter 2 we provide a brief overview of the central themes of this thesis and review the relevant literature. In chapter 3, our focus shifts to consideration of Nitrogen Vacancy (NV) centres exclusively, and outlines the various protocols used to control the NV Quantum spin state, and how these may be employed to measure specific classes (DC and AC) of magnetic fields. In chapter 4, we discuss the limitations of these techniques and how they may be overcome by performing measurements on the decoherence properties of the NV centre. The material in this chapter is published in reference [HCHH09].

Chapter 5 provides a detailed theoretical analysis of an experimental investigation

into the techniques developed in chapter 4. The system chosen for this investigation is a diamond nanocrystal containing an NV centre which is exposed to an electrolyte containing manganese electronic spins. Experiments were performed by L.P. McGuinness and D.A. Simpson at the University of Melbourne, and show excellent agreement with our theoretical predictions. The material in this chapter is published in reference [MHS$^+$13].

Chapter 6 is focused on using more sophisticated dynamical decoupling and quantum control techniques to improve the magnetometer sensitivity of the NV spin, and investigates the optimality and efficiency of various control pulse sequences in the literature. The findings of this analysis were published in reference [HHCH10]. An experimental investigation of these techniques was performed by B. Naydenov and F. Dolde at the University of Stuttgart, and the corresponding analysis is described in section 4 of this chapter. These results were published in reference [NRB$^+$10].

Due to the high precision of microwave control required for the protocols in chapters 4-6, and some experimental artifacts uncovered in chapter 5, chapter 7 details an investigation into the fundamental limitations associated with the fidelity of pulsed microwave control. These results explain many of the noise features observed in previous experiments that cannot be explained by shot noise effects alone. The material in this chapter is being prepared for publication.

In chapters 8 and 9, we analyse and discuss two important applications of decoherence sensing techniques to biological imaging. The first involves using a single NV centre in close proximity to an ion channel in a biological cell membrane to monitor the switch-on/switch-off activity of the channel. This technique is expected to have wide ranging implications for nanoscale biology and drug discovery. The second

involves using a high density ensemble of NV centres to facilitate widefield imaging of the dynamics of a biological neuronal network grown on the diamond surface. This technique is expected to yield significant insight into the way information is processed in the brain. The material in chapters 8 and 9 has been published in references [HHC$^+$10] and [HBT$^+$12] respectively.

In chapter 10 we shift our focus from pure dephasing interactions to systems that exchange energy with the NV centre. A detailed analysis of the response of the NV spin state to an arbitrary spectral density is performed, and is used to develop a protocol by which the frequency spectrum of an arbitrary magnetic system can be measured. This material is currently under preparation for publication. This chapter also details and analyses two experimental investigations. In section 4, we analyse the results of an experiment performed by S. Steinert at the University of Stuttgart, in which the relaxation rate of an ensemble of NV centres was modified via coupling to an environment of Gadolinium electron spins of a controlled, variable density. These findings and the corresponding analysis of this chapter were published in reference [SZH$^+$]. In section 5, we analyse the results of an experiment performed by S. Kaufmann and D.A. Simpson at The University of Melbourne in which individually addressable nanodiamonds containing single NV centres are used to detect small clusters of gadolinium atoms in an artificial cell membrane. These findings and the corresponding analysis of this chapter have been published in reference [KSH$^+$13]. In both cases, these experiments are in excellent agreement with the theoretical analysis.

In chapter 11, we analyse two separate experiments performed by L.P. McGuinness and D.A. Simpson at The University of Melbourne, which demonstrate the use of these protocols inside living human cervical cancer cells. In the first experiment,

we perform an analysis of the first intracellular coherence measurement of a single quantum system, in which both Rabi and spin-echo signals are monitored, providing a foundation for further quantum nanobiomagnetometry studies. In the second experiment, we discuss how the the unique optical and spin properties of the NV centre allow for simultaneous nano-scale spatial and orientational tracking of nano-crystals in living biological systems. This material was published in reference [MYS+11].

In chapter 12, we return to the decades-old central spin problem outlined in chapter 2. We develop an analytic solution to this problem, and demonstrate excellent agreement with both numerical and experimental results. The material in this chapter is being prepared for publication.

Chapter 2

Background

2.1 Decoherence and open quantum systems

In the early years of our education in quantum physics, we are taught to think in terms of closed quantum systems, in which the degrees of freedom are sufficiently simple to permit a complete mathematical description of the system. However, in most cases of practical relevance, the *system*(S) of interest is coupled to a much larger quantum reservoir (referred to hereafter as a *bath* or the *environment*, E), whose presence has a non-trivial effect on its evolution (figure 2.1). Since we typically have no means by which to directly measure the properties of the bath, the system dynamics become non-unitary and irreversible when viewed in isolation. The central system is then referred to as an *open quantum system*, and we refer to the loss of quantum information from the system to the bath via their interaction (and resulting entanglement) as *decoherence*.

Typically we decompose the Hamiltonian of the complete system (S+E) into terms describing the explicit evolution of the system and the environment under their respective native processes, $\mathcal{H}_{\mathrm{S}}$ and $\mathcal{H}_{\mathrm{E}}$ respectively, and a term describing their interaction,

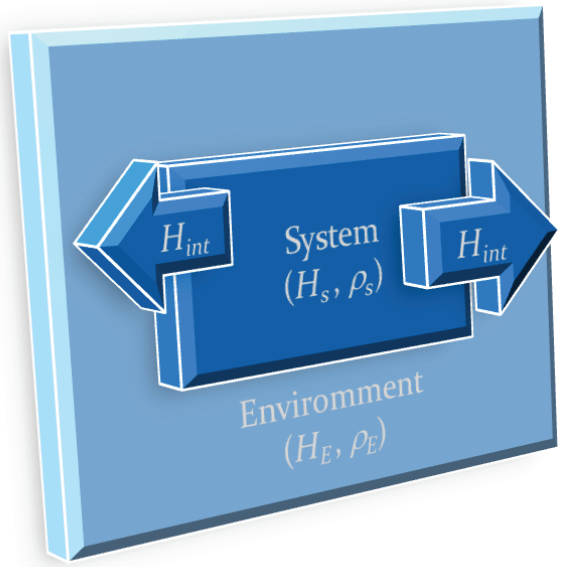

Figure 2.1: Schematic of an open quantum system (S) interacting with its external environment (E). The open quantum system can be viewed as a distinguished division of a larger closed quantum system. Because measurements can only be performed on the system, any information encoded in the environment via their interaction is then irreversibly lost.

$\mathcal{H}_{\text{int}}$. Thus we have that

$$\mathcal{H} \;=\; \mathcal{H}_{\text{S}} + \mathcal{H}_{\text{E}} + \mathcal{H}_{\text{int}}, \tag{2.1.1}$$

and the unitary evolution of the entire system is described by the Liouville equation

$$\frac{\mathrm{d}\rho}{\mathrm{d}t} \;=\; -\big[\mathcal{H}, \rho\big]. \tag{2.1.2}$$

Because we have individual control over the system, it may be initialised in a known state (meaning the complete system is in a product state between the system and the environment), however entanglements are generated between their respective quantum states, resulting in the information that was initially confined to the system

becoming partially encoded in the environment, and hence non-local. A complete wave function describing both the system and the bath still exists and evolves unitarily, however the loss of phase coherence between the basis states of the system means that certain elements of the system are no longer able to interfere with each other. This ultimately leads to probabilistically additive behaviour, an inherently classical property, and thus gives the appearance of 'wave function collapse'. Operationally, this means we must trace over the environmental degrees of freedom, to obtain the reduced density matrix of the central system

$$\rho_{\mathrm{S}}(t) = \mathrm{Tr}_{\mathrm{E}}\big\{\rho(t)\big\} = \rho_s(0) - \mathrm{Tr}_{\mathrm{E}}\left\{\int_0^t \big[\mathcal{H}, \rho(t')\big]\,\mathrm{d}t'\right\}. \tag{2.1.3}$$

Given the above discussion, the general solution of this equation is intractable because the evolution of the reduced system (which contains, by definition, all the information we can possibly know) depends on the past history of total the system, something we are not privy to. Ultimately, we seek a master equation separating the unitary evolution of the reduced system from the non-unitary evolution arising from the system-bath interaction,

$$\frac{\mathrm{d}}{\mathrm{d}t}\rho_{\mathrm{S}}(t) \;=\; -i\big[\mathcal{H}'_{\mathrm{S}}, \rho_{\mathrm{S}}(t)\big] + \mathcal{D}\big[\rho_{\mathrm{S}}(t)\big]. \tag{2.1.4}$$

We briefly point out here, for the sake of completeness, that $\mathcal{H}'_{\mathrm{S}} \neq \mathcal{H}_{\mathrm{S}}$. Rather, $\mathcal{H}'_{\mathrm{S}}$ contains a correction (referred to as the Lamb shift) to the unitary part of the reduced system's evolution due to the interaction with the bath (see, for example, [BP06]).

Many open quantum systems are described by the Born-Markov master equation, which is obtained by applying the Born-Markov approximation to the full density matrix in Eq. 2.1.2 under the assumption that

- The interaction is assumed to be sufficiently weak, and the environment sufficiently large, that changes in the density matrix of the environment due to the system are negligible (the 'Born' bit).

- The self interactions taking place within the bath are sufficiently fast to ensure that any correlations caused by the interaction are dissipated rapidly compared with the evolution of the system (the 'Markov' bit), essentially rendering the environment 'memoryless' with respect to the motion of the system.

Whilst both being extremely well understood theoretically and finding application in a large number of practical systems (see, for example, [BP06] for an extensive overview), these approximations are of little use in describing systems of interacting spins, where environmental couplings are typically weaker than, or of similar order to the interaction between the central system and the environment. This leads to the environmental evolution being heavily conditioned upon on the trajectories of the central system, thereby invalidating the Born-Markov approximation. As a detailed understanding of spin-spin environments is critical to the development of quantum devices based on solid-state spin architectures, the so-called central-spin problem is the primary focus of this work, and is discussed in greater detail below.

2.2 The Central Spin Problem

The central spin problem is a special class of open quantum system, and involves the study of the dynamics of a central spin interacting with a large number of strongly coupled spins in the environment, referred to as the spin bath. In most practical cases the central spin is electronic, and the surrounding bath is comprised of either

electron or nuclear spins, and in some cases, both. We are primarily concerned with the investigation of two effects:

1. Relaxation processes, in which the central system dissipates energy via its interaction with the environment. In the case of a central spin, these processes cause the projection (not necessarily coherent) of the spin state along its quantisation axis to decay with time.

2. Dephasing processes, in which quantum information is transported from the central spin via the generation of quantum entanglement between the system and the environment. This process is made irreversible due to interactions between environment constituents. in which the phase coherence between two quantum states comprising a superposition decays with time.

The timescales associated with these processes are referred to as T_1 and T_2 respectively. These designations arise by analogy with traditional NMR and ESR experiments investigating the decay of axial and lateral components of the magnetisation vector of a large spin ensemble.

This problem has received renewed attention over the last decade, due in no small part to localised electrons in solids being promising candidates for qubits in quantum computation, metrology and communication systems; a result of their long coherence times, ease of quantum control and already well established fabrication techniques. In the context of quantum information processing, the utility of these systems hinges upon the requirement for spin coherence times to be sufficiently long to ensure that the necessary number of quantum operations (typically of order 10^4 for fault tolerant quantum computation [Pre98]) can be performed within the associated coherence time. Examples of such systems that have been suggested as

building blocks for quantum computer architectures include spins qubits in quantum dots [LD98, LYS10], donor impurities [Kan98, dSDS04, HGAW06, ML11], and Nitrogen-Vacancy (NV) centers in diamond [WJ06]. In the context of metrology, with particular regard to parameter estimation, the NV centre has emerged as a unique physical platform for nanoscale magnetometry [Deg08, TCC$^+$08, BCK$^+$08, MSH$^+$08, HHCH10], nano-NMR [PHS$^+$13, SSP$^+$13, MKS$^+$13], bio-imaging [HHC$^+$10, MYS$^+$11, HBT$^+$12], electrometry [DFD$^+$11], thermometry [NJD$^+$13], and decoherence imaging [CH09, HCHH09, SZH$^+$, KSH$^+$13, MHS$^+$13]. In each case, the associated sensitivity is ultimately limited by the coherence properties of the NV spin that arise from the strong coupling to the surrounding bath of electron and/or nuclear spins. In all of these applications and platforms, a comprehensive understanding of the central spin problem is therefore necessary to make accurate predictions of the quantum properties and behaviour of the central spin arising from the material properties of the surrounding environment.

As noted in chapter above, the decoherence behaviour of many open quantum systems has been modeled using the Born-Markov master equations, which are predicated on the assumption of weak system-environment couplings and Markovian environment dynamics. Such approaches are not valid here, particularly in the case of a central electron coupled to a bath of nuclear spins, as the environmental dynamics are some three orders of magnitude slower than the central spin. Furthermore, because every spin present in the system is coupled to every other spin, non-commuting components of the Hamiltonian make finding even approximate solutions of the central spin's dynamics extremely challenging, particularly on timescales of similar order to those of the bath's dynamics.

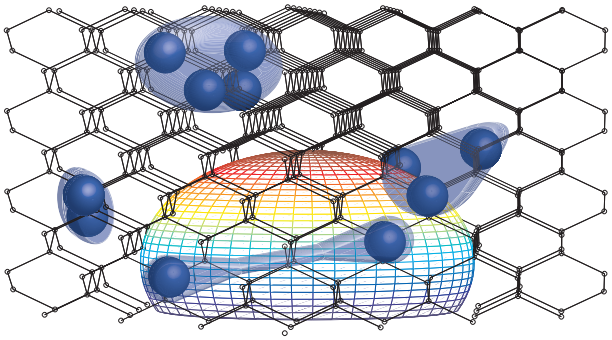

Figure 2.2: Schematic of the central spin problem. Groups of proximate spins (blue) form strongly interacting clusters, in which the constituents perform spin flip-flops as mediated by their magnetic dipole-dipole interaction. The central spin, being coupled to all environmental spins, thus constitutes an open quantum system, with the 'spin bath' playing the role of the environmental reservoir. Depending on their proximity to the central spin, the evolution of the environment is conditioned upon the state of the central spin, and hence cannot be treated as a semi-classical fluctuating field (See chapter 12).

2.3 Spin-based magnetometry

Given the already well established research effort devoted to the understanding of how single spins respond to their magnetic environments, Chernobrod and Berman [CB05] put forth the first theoretical proposal for a magnetometer based on optically detected interference of spin sub-levels of an atomic system. Monitoring of the spin state was to be based upon Optically Detected Magnetic Resonance (ODMR) of the spin system, in which the intensity of the resulting fluorescence gives some measure of the associated spin state populations; and scanning capabilities would be achieved by implanting the photo-luminescent nano-probe into the tip of an AFM or STM.

The tip would be scanned in close proximity to the target sample, facilitating angstrom scale resolution with the use of a single fluorescent molecule. A permanent magnet is used to split the magnetic sublevels of the spin system, and an RF coil

produces an oscillating field in resonance with the desired transition. The possibility of a resonant excitation is reduced by the presence of a magnetically active target, which acts to shift the transition frequency between the magnetic sublevels, and this reduction is monitored via a change in the photoluminescent intensity.

Fields from single electron spins located a few nanometres from the probe are typically of the order of 10 mT, which is significantly larger than the width of the narrowest intrinsic features of a typical ODMR spectrum in a spin-1 quantum dot at temperatures lower than 4K. As such, the presence of a target sample would be detected via the corresponding shift and splitting of the ODMR spectrum.

In a theoretical proposal in 2008, Degen applied this method to the ground-state spin-1 system of the Nitrogen Vacancy centre in diamond [Deg08]. This system exhibits rather sharp spectral features of roughly 1-10 MHz (5-50 nT) in width, and has the additional advantage of room temperature operation (See chapter 3 for a detailed technical overview of the NV centre). As such, Degen showed that an ODMR based NV magnetomoeter would be capable of resolving magnetic fields resulting in shifts larger than the natural linewidth of a chosen centre.

Typically this linewidth is the result of intrinsic quasi-static processes occurring within the NV system and is therefore inhomogeneously broadened, implying a substantial reduction may be achieved with the application of controlled microwave pulses. In particular, a 'spin-echo' (SE) sequence employing a bit-flip at the halfway point of the NV's free-evolution acts to re-focus the phase accumulation resulting from any quasi-static magnetic processes. As a result, spin lifetimes may be extended from $\sim 1\,\mu$s [PGD$^+$04] to 0.1-1 ms [JW06], equivalent to linewidths of 1-10 kHz, depending on the local magnetic environment of the diamond crystal (a more detailed study of

higher-order pulse sequences capable of refocusing more complicated dynamic effects is the focus of chapter 6). This would ultimately permit the resolution of fields as small as tens of nT, however it is necessary that the target fields oscillate on these timescales to ensure maximal phase accumulation. Fields with slower dynamics will be subject to refocussing, whilst the effects of faster fields will effectively average themselves out.

Given its sensitivity, this scheme was predicted to be capable of resolving single proton and electron spins at distances of 5 and 40 nm respectively. These predictions sat favourably with the size of the then smallest reported diamond nanocrystals containing stable NV centres, 15 nm, meaning the required probe-sample separation for single proton detection was less than an order of magnitude from being achieved in practice [Deg08]. Such a magnetic field sensor was therefore expected to out-perform MRFM, without the additional requirement of cryogenic operation, and would therefore have the potential to permit the imaging of nano-scale biological processes under physiological conditions.

At the same time, Taylor et-al[TCC$^+$08] investigated the use of pulse based protocols, namely FID, spin-echo and higher order CPMG sequences, to make theoretical predictions of the achievable sensitivity of an NV magnetometer. FID and spin-echo based sensitivities were predicted to be of order $\eta_{\text{fid}} \sim \mu\text{T}\,\text{Hz}^{-1/2}$ and $\eta_{\text{se}} \sim \text{nT}\,\text{Hz}^{-1/2}$ respectively, with higher order CPMG sequences achieving a $n^{-1/3}$ scaling in the sensitivity with the number of pulses, n.

In both works noted above, the application of a spin echo pulse sequence acts to refocus any static fields in the system, meaning that, despite an increased sensitivity, DC fields are no longer measurable. As such, detailed knowledge and control over the

target field is required for it to be measured, reducing the utility of these methods. Methods to measure and characterise more realistic randomly fluctuating fields are detailed in chapter 4.

The first experimental demonstrations of NV magnetometer capability came simultaneously from Balasubramanian et-al[BCK$^+$08] and Maze et-al[MSH$^+$08]. In the former, a magnetic tip was used to create a strong magnetic field gradient near a single NV centre, and showed its position could be located to within a few nanometres by monitoring the NV fluorescence as dependent on the NV-tip separation. This was an improvement of 2 orders of magnitude below the optical diffraction limit. In the latter, AC sensitivities were experimentally demonstrated at the $\eta_{\mathrm{se}} = 30\,\mathrm{nT\,Hz^{-1/2}}$ level in bulk diamond, and $0.5\,\mu\mathrm{T\,Hz^{-1/2}}$ in 30 nm diamond nanocrystals. Improvements to the sensitivity have also been experimentally demonstrated by employing isotopically pure diamond crystals to further increase the intrinsic coherence time of the NV spin to 1.8 ms, yielding an AC field sensitivity of $3\,\mathrm{nT\,Hz^{-1/2}}$ [BNT$^+$09].

These sensitivity figures were based on implementations of single NV spins, however it was pointed out in [TCC$^+$08] that an array of N_p independent NV spins would give a $\sqrt{N_p}$ improvement in the sensitivity due to a much greater rate of data acquisition, albeit at the cost of spatial resolution. The first experimental implementation of this idea was given in [SDN$^+$10], where both spatial mapping and full vectorial reconstruction of the magnetic field were demonstrated. Using an ODMR protocol, the sensitivity was determined to be at the $20\,\mathrm{nT}/\sqrt{\mathrm{Hz}}$, an improvement of 2-3 orders of magnitude over the single spin case.

2.4 Decoherence Microscopy

As mentioned above, much like the effectiveness of a qubit in quantum computation protocols, the sensitivity of a spin-qubit magnetometer depends primarily on the coherence time of the spin system employed. As such, one usually seeks to isolate the qubit from its environment so as to suppress the effects of decoherence as much as possible. In 2008, Cole and Hollenberg [CH09] proposed an inverted view where, by exposing a qubit to an environment in a controlled manner, one could use the resulting decoherence to obtain information about dynamic processes taking place in the environment itself. By scanning such a system over this environment, one can then produce a spatial map of both the strength and timescale of the environmental fluctuations. An example of this process (as taken from [CH09]) is shown in figure 2.3, where the qubit is scanned over a distribution of bistable fluctuators.

As many of the interesting processes taking place in both condensed matter and biological systems at the micro/nano scale produce fields that fluctuate about zero-mean, such a method holds a considerable advantage over existing techniques. In chapter 4, we show that the sensitivity with which fluctuating fields may be measured is effectively identical to existing magnetometry techniques based on spin qubits, and methods by which this may be improved are investigated in chapter. 6. By virtue of their high sensitivity and, in principle, universal applicability, decoherence microscopy techniques represent a revolutionary means by which to investigate, image and characterise nanoscale processes in the physical and life sciences. In this work, we extend these techniques to include processes such as self diffusing atoms in an electrolyte (chapter 5), ion flow through biological cell membranes (chapter 8), the propagation of neural information in microscale biological neural networks (chapter 9),

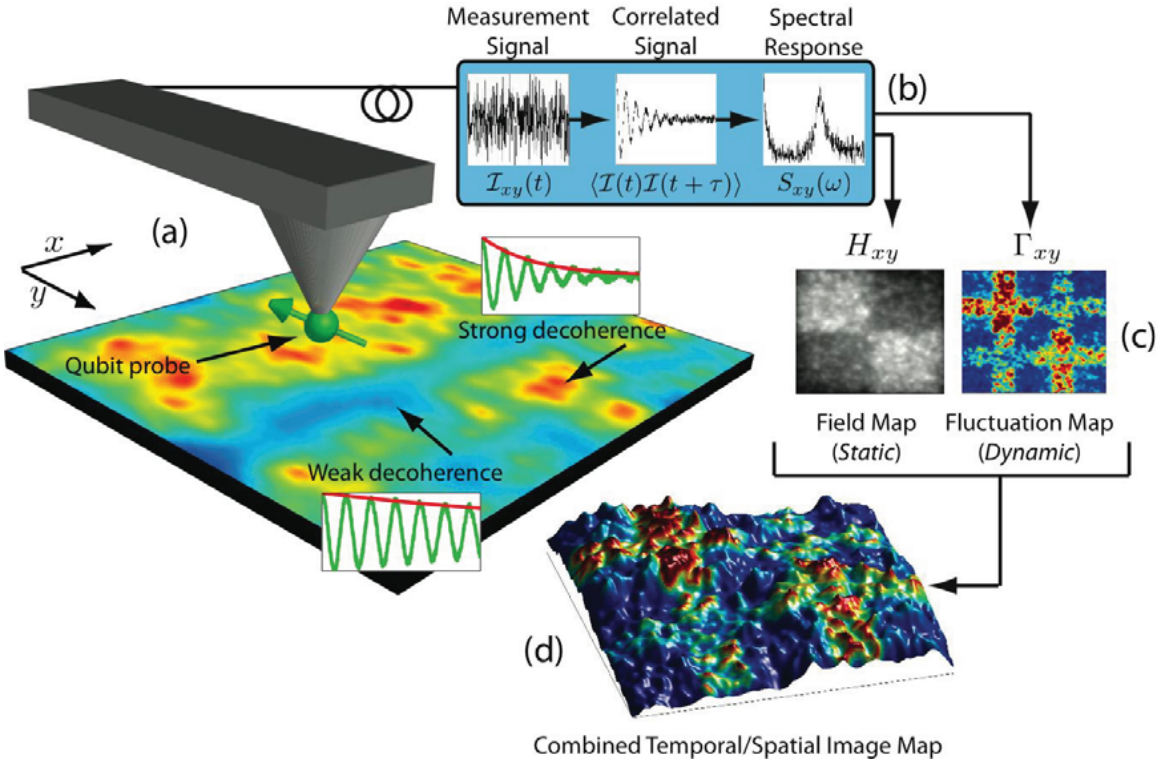

Figure 2.3: Schematic of a scanning decoherence microscopy set-up, as taken from [CH09]. (a) The probe qubit is scanned across the sample while its quantum state is (weakly) monitored. (b) At each point (x, y) a measurement record $I_{xy}(t)$ is obtained. Using the time-correlated signal, the spectral response $S_{xy}(\omega)$ of the qubit probe is determined. (c) From this data, a measurement of the effective qubit Hamiltonian H_{xy} (static magnetometer or electrometer) field map and decoherence rate Γ_{xy} map as a function of probe position is obtained. In this figure, the sample consists of fluctuators with a nonuniform distribution in both spatial density and fluctuation rate. The decoherence map reveals the fluctuator distribution not visible in the static field map. (d) Combining this information provides a direct window into the distribution and character of the sources of field fluctuations in both space and time. In this image, the vertical scale is given by the strength of the field, whereas the colouration is given by the effective decoherence rate.

microscale fluidic flows (chapter 10.4), atoms embedded in biological lipid membranes (chapter 10.5) and intra-cellular fluid dynamics in living cells (chapter 11).

Chapter 3

The Nitrogen Vacancy Centre-Technical overview and basic control protocols

In this chapter we discuss in detail the spin degrees of freedom of the Nitrogen Vacancy (NV) centre optical groundstate, and the various means by which we can control and manipulate this spin using optical and microwave fields. The development is intended to have a pedagogical focus, rather than a historical one. We begin with a brief discussion on the physical origin of the centre, and move into a detailed quantitative description of the basic control protocols that will be employed and extended in later chapters.

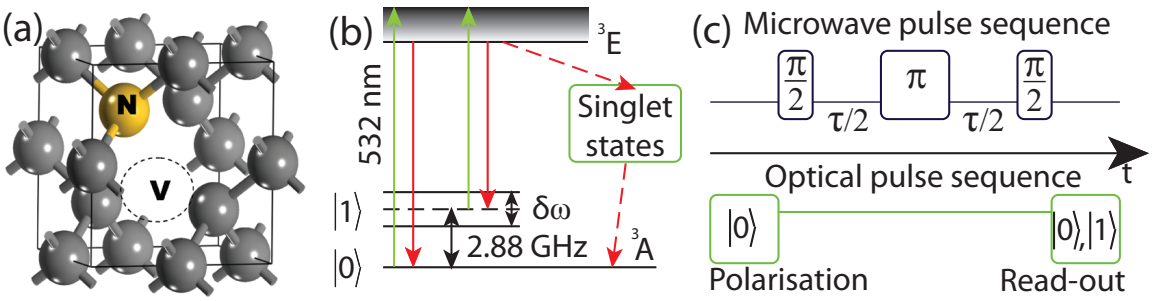

Figure 3.1: (a) NV-centre diamond lattice defect. (b) NV spin detection through optical excitation and emission cycle. Magnetic sublevels $|0\rangle$ and $|\pm 1\rangle$ are split by a D=2.88 GHz crystal field. The degeneracy between the $|\pm 1\rangle$ sublevels is lifted by a Zeeman shift, $\delta\omega$. Application of 532 nm green light induces a spin-dependent photoluminescence and pumping into the $|0\rangle$ ground state. (c) Microwave and optical pulse sequences for coherent control and readout.

3.1 Introduction

The Nitrogen Vacancy (NV) centre is a point defect in a diamond lattice comprised of a substitutional atomic nitrogen impurity and an adjacent crystallographic vacancy (figure 12.2 (a)). For cases where the nitrogen atom is greater than a few nanometres from the crystal boundary, it is thermodynamically favourable for the impurity and the vacancy to exist as a nearest-neighbour pair. Vacancies will therefore migrate through the lattice until either an impurity or crystal boundary is encountered.

The centre exhibits an axial, trigonal (C_{3V}) symmetry on account of the degenerate roles played by the three adjacent carbon atoms. Three of the five nitrogen valance electrons are covalently bonded to adjacent carbon atoms, leaving two free to form a lone-pair. Of the three unpaired electrons from the vacancy, two form an effective covalent bond, leaving a single unpaired electron. Owing to its neutral charge state, this configuration is referred to as the NV^0, and behaves as a spin-$\frac{1}{2}$ paramagnetic point defect. As the ground-state EPR signals are too broad, NV^0 must be optically

pumped into an electronic excited state to make EPR studies possible. The finite lifetime of excited states and the practical resources required make the NV^0 centre undesirable for magnetometry applications.

On the other hand, the NV^- configuration has a charge state of -1, resulting from the presence of an additional electron at the vacancy site, thus behaving as a spin-1 paramagnetic point defect in its ground state. In contrast to NV^0, the relatively narrow spectral properties of the NV^- ground state make it an ideal candidate for applications as a spin-based magnetometer, and is therefore the primary physical system with which we concern ourselves for this study. For this reason, we refer to the NV^- centre hereafter as simply the NV centre.

The energy level scheme of the C_{3v}-symmetric NV system (figure 12.2 (b)) consists of ground (^{3}A), excited (^{3}E) and meta-stable (^{1}A) electronic states. The ground state spin-1 manifold has 3 spin sub-levels $\left(\left|\,0\right\rangle, \left|\pm1\right\rangle\right)$, which in zero field are split by 2.88 GHz. An important property of the NV system is that under optical excitation the spin levels are distinguishable by a difference in fluorescence, hence spin-state readout is achieved by purely optical means [JPG$^+$02, JW06] as described below. The degeneracy between the $\left|\pm1\right\rangle$ states may be lifted with the application of a background field, with a corresponding separation of 17.6 MHz Gauss^{-1} permitting all three states to be accessible via microwave control, however the $\left|\pm1\right\rangle$ states are not directly distinguishable from one another via optical means. By isolating either the $\left|\,0\right\rangle \leftrightarrow \left|+1\right\rangle$ or $\left|\,0\right\rangle \leftrightarrow \left|-1\right\rangle$ transitions, we have a controllable, addressable spin qubit.

3.2 Optical and Microwave Control of the Quantum Spin State

The spin state of the NV centre may be determined by utilising optically active transitions from the ground state to the relevant electronic excited states. At low temperature, a resonant laser (637 nm) may be tuned to the spin conserving optical $|0\rangle$ transition, resulting in fluorescence only if the spin is in the $|0\rangle$ state [JPG+02]. This process may be performed of order $\sim 10^5$ times before relaxation of the spin state occurs, thereby facilitating what is effectively a single shot readout mechanism. The small probability of a spin-flip occurring during the read out process leads to a slight reduction in fidelity to 95%, as can be determined via the comparative heights of the peaks associates with the $|0\rangle$ and $|\pm 1\rangle$ states during photon counting experiments [WJ06].

This readout mechanism is not possible at room temperature, as thermal broadening of excited state energy levels makes resonant excitation impossible. Instead, a broadband laser (532 nm) is used to non resonantly excite optical transitions, involving both the $|0\rangle$ and $|\pm 1\rangle$ sublevels, to higher lying energy states. If initially in the $|0\rangle$ state, the system will transitions to the ^{3}E excited state and then returns to the ground state via the spontaneous emission of a photon. The same is true for the $|\pm 1\rangle$ states, however there is a chance that the system will instead undergo a non-radiative decay by emission of a phonon. We may thus infer the initial spin state by virtue of the fact that fluorescence rates are substantially lower for $|\pm 1\rangle$ states than for the $|0\rangle$, resulting in a contrast of fluorescence intensity; however, the non-radiative decay is also a non spin conserving processes and eventually leads to

polarisation into the $|0\rangle$ state. As a result, the means by which the spin state is read out also acts to initialise the system. Unlike the resonant excitation method above, poor collection efficiencies and a reduced contrast make it difficult to detect a photon before the system is polarised, significantly reducing the signal to noise ratio. As such, this technique does not constitute a 'single-shot'measurement process.

The full groundstate spin Hamiltonian of the NV centre ($\mathcal{S}$), the nuclear spin of the substitutional Nitrogen ($\mathcal{I}_N$) and the surrounding spin-bath environment is given by

$$\mathcal{H} \;=\; \vec{\mathcal{S}} \cdot \vec{\vec{D}} \cdot \vec{\mathcal{S}} + \vec{\mathcal{S}} \cdot \vec{\vec{A}}_N \cdot \vec{\mathcal{I}}_N + \vec{\mathcal{I}}_N \cdot \vec{\vec{Q}}_N \cdot \vec{\mathcal{I}}_N + \mathcal{H}_{\rm int} + \mathcal{H}_{\rm E}, \tag{3.2.1}$$

where $\vec{\mathcal{S}} \cdot \vec{\vec{A}}_N \cdot \vec{\mathcal{I}}_N$ describes the NV-N hyperfine interaction. The nitrogen quadrupole term, $\vec{\mathcal{I}}_N \cdot \vec{\vec{Q}}_N \cdot \vec{\mathcal{I}}_N$, is present for cases where the nitrogen nucleus exists in its 99.64% abundant spin-1 ^{14}N isotopic configuration, whereas the 0.36% abundant spin-$\frac{1}{2}$ ^{15}N isotope has no quadrupole term.

By choosing the z axis to coincide with the quantisation axis of the NV spin (as defined by the zero-field splitting tensor, $\vec{\vec{D}}$), we may make the secular approximation in which we ignore all couplings to the x and y components of $\mathcal{S}$. This is justified by the fact that all lateral couplings in the proximate mesoscopic environment are typically, at most, of order $\sim$1 MHz and are hence unable to flip $\mathcal{S}$ with respect to the direction of $\vec{\vec{D}}$. In cases where the dynamics of the environment give rise to processes occurring at GHz timescales, these lateral couplings may become important. This is the basis of all microwave control techniques for NV spin state, and is described in detail below. In the secular limit, the Hamiltonian becomes

$$\mathcal{H} \;\approx\; D\mathcal{S}_z^2 + A_{N,z}\mathcal{S}_z\mathcal{I}_{N,z} + Q\mathcal{I}_{N,z}^2 + \mathcal{H}_{\rm int} + \mathcal{H}_{\rm E}. \tag{3.2.2}$$

The axial component of the NV-N hyperfine coupling shows that the magnetic sublevels of the nitrogen nuclear spin present an effective magnetic field to the axial component of the NV spin of order $A_{N,z} \approx 2.2\,\mathrm{MHz}$. Furthermore, in the case where the nitrogen isotope present is $^{14}\mathrm{N}$, having nuclear spin $I_N = 1$, there exists a large quadrupole moment of $Q \approx 5\,\mathrm{MHz}$ [CK01], ensuring the NV spin cannot flip that of the nitrogen. The NV-N coupling therefore presents a static Zeeman shift to the NV, an idea that will become important in the discussion below.

The relationship between the NV control protocols discussed in this chapter is depicted in figure 3.2.

3.2.1 Optically Detected Magnetic Resonance (ODMR)

In an Optically Detected Magnetic Resonance (ODMR) experiment, both laser and microwave fields are continuously applied to the NV centre at constant power. The microwave field is swept across a broad range of frequencies, and will excite one of the $\left|0\right\rangle \leftrightarrow \left|\pm1\right\rangle$ transitions when on resonance. In the absence of the laser field (see below), this would cause the spin to periodically flip between the two states. The presence of the laser field acts to constantly re-polarise the system, hence a steady-state level of fluorescence is reached as a result of the competition between the microwave field trying to drive the system out of the $\left|0\right\rangle$ state, and the laser field trying to drive it back. As we will see, the ODMR protocol is somewhat unique in that both the measurement and evolution of the system are taking place simultaneously.

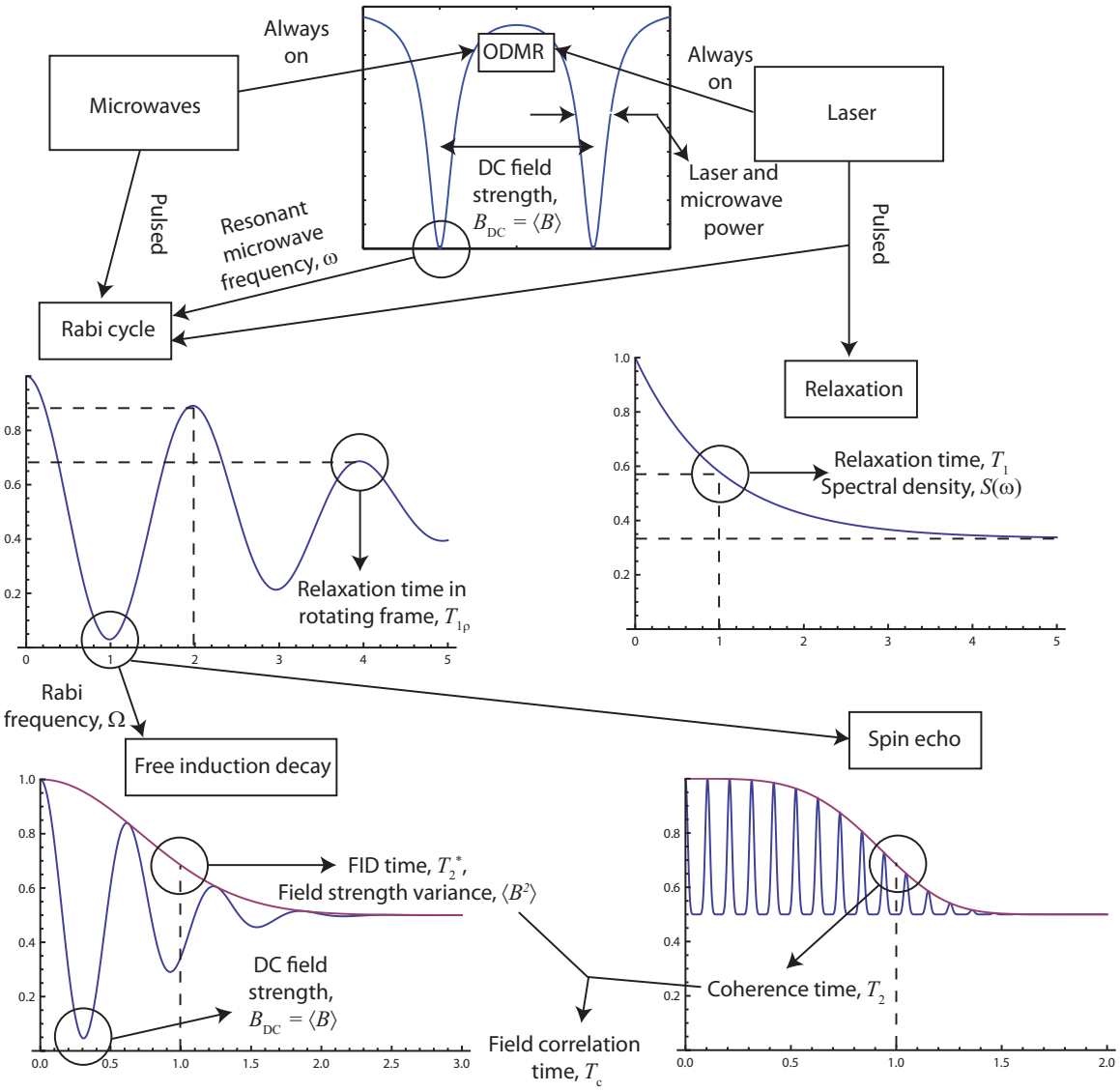

Figure 3.2: Flow map outlining the measurement of the dynamic parameters of a target environment using the NV centre. In an ODMR experiment, a broadband laser is used to excite the optical transition, whilst the microwave frequency is scanned to determine the resonant frequencies corresponding to transitions between magnetic sublevels. These frequencies are then used to resonantly drive these transitions during a Rabi cycle. By employing Rabi cycles of a particular duration, various control pulses may be constructed and used for pulsed-microwave spin resonant experiments such as FID and spin-echo. These represent the most natural measure of the local magnetic environment, and may be used to determine parameters such as effective axial magnetic field strengths, $\langle B \rangle$, $\langle B^2 \rangle$, and fluctuation rates, $f_e = 1/T_c$ (see chapter 4). Microwaves are not required to measure longitudinal relaxation rates, which may be used to sample high frequency regions of the environmental spectral density (see chapter 10).

Large magnetic fields and the qubit approximation

The static Hamiltonian, responsible for the axial splitting of the magnetic sublevels is given by

$$\mathcal{H}_0 \quad = \quad D\mathcal{S}_z^2 + (\omega_z + b)\,\mathcal{S}_z, \tag{3.2.3}$$

where we will work in units of frequency from here on to both simplify the analysis and facilitate a convenient means by which to compare various timescales. Note that we have included both the static background field, ω_z, and an effective axial field, b, to account for the random fluctuations in the Zeeman levels, which arise from interactions of the NV centre with its proximate environment. By virtue of these relatively weak couplings ($\sim$MHz), compared with the zero field splitting ($\sim$GHz), we may ignore the components of the bath that couple to the $\mathcal{S}_x$ and $\mathcal{S}_y$ components of the NV centre, since these are too weak to cause the NV spin to flip.

We also assume initially that the coupling to the laser field is not strong enough to induce any NV polarisation. This is, of course, an idealisation, since without polarisation we would have no fluorescence, and hence no means by which to monitor the spin state, but one we will proceed with for now. The case of a non-trivial coupling to the laser field is dealt with in section 3.2.1.

The Harmonic interaction with the microwave field is given by, $\mathcal{V} = \omega_x \cos(\omega t)\,\mathcal{S}_x$, where, owing to the axial symmetry, we choose the lateral component of the microwave field, ω_x, to lie along the x axis. To simplify the analysis, we transform to the interaction picture by transferring the time dependence due to the influence of the static Hamiltonian, $\mathcal{H}_0$, to the state vector, leaving the state to evolve exclusively under the influence of the harmonic interaction term (see appendix A). The Hamiltonian

in the interaction picture is then given by

$$\mathcal{V}_I = \omega_x \cos(\omega t)\, e^{i\mathcal{H}_0 t} \mathcal{S}_x e^{-i\mathcal{H}_0 t} \tag{3.2.4}$$

$$\approx \frac{\omega_x}{2\sqrt{2}} \begin{pmatrix} 0 & e^{-i\delta_+ t} & 0 \\ e^{i\delta_+ t} & 0 & e^{i\delta_- t} \\ 0 & e^{-i\delta_- t} & 0 \end{pmatrix}, \tag{3.2.5}$$

where $\delta_\pm = \omega - [D \pm (\omega_z + b)]$ is the detuning between the qubit transition frequency and the frequency of the applied oscillating field. Note that in this approximation we have we ignored all terms of the form $e^{\pm i(\omega + D \pm \omega_z)t}$, since these oscillate too rapidly to have any effect on the NV spin. Similarly, we assume the microwave field is significantly detuned from the $|0\rangle \rightarrow |-1\rangle$ transition, such that we may ignore any population of the $|-1\rangle$ state, thereby leaving us confined to an effective 2 state system (to order $\mathcal{O}(\omega_x^2/\omega_z^2)$). The breakdown of this assumption and the resulting implications for the various microwave control protocols are discussed in chapter 7. The equation of motion for the density matrix of the effective qubit in the interaction picture is then

$$\frac{\mathrm{d}\rho_I}{\mathrm{d}t} = -i\left[\mathcal{V}_I, \rho_I\right], \tag{3.2.6}$$

$$\text{where } \mathcal{V}_I = \frac{\omega_x}{2\sqrt{2}} \begin{pmatrix} 0 & e^{-i\delta t} \\ e^{i\delta t} & 0 \end{pmatrix},$$

$$\text{and } \rho_I = \begin{pmatrix} \rho_{11} & \rho_{10} \\ \rho_{01} & \rho_{00} \end{pmatrix},$$

where we have put $\delta \equiv \delta_+$ for notational clarity.

Rescaling t via $\tau = \omega_x t/2\sqrt{2}$ and $\delta t = \kappa\tau$, and rewriting the above system of four coupled first order linear differential equations as a single third order differential equation in ρ_{00} (using $\rho_{11} = 1 - \rho_{00}$), we have

$$\frac{\mathrm{d}^3}{\mathrm{d}\tau^3}\rho_{00} + \left(4 + \kappa^2\right)\frac{\mathrm{d}}{\mathrm{d}\tau}\rho_{00} = 0. \tag{3.2.7}$$

Solution and ensemble averaging

As the ODMR spectrum is a measure of the extent to which the system undergoes transitions between the various spin states ($|0\rangle \leftrightarrow |+1\rangle$ in the present context), the initial state of ρ is of no consequence since it is merely the amplitude of the oscillations we are seeking. As such, we just take $\rho_{00}(0) = 1$ (ie, the laser was switched on before the microwave field), which implies $\rho'_{00}(0) = 0$ and $\rho''_{00}(0) = -2$. The solution to this system is the well known Rabi solution,

$$\rho_{00} = 1 - \frac{4}{\kappa^2 + 4} \sin^2 \left(\frac{\tau}{2} \sqrt{\kappa^2 + 4} \right) \tag{3.2.8}$$

$$= 1 - \frac{1}{2} \frac{\omega_x^2}{\Omega^2} \sin^2 \left(\frac{\Omega t}{2} \right), \tag{3.2.9}$$

$$\text{where } \Omega = \sqrt{\frac{\omega_x^2}{2} + \delta^2}. \tag{3.2.10}$$

The ODMR signal is a long-time average over these oscillations, implying that we simply take the average of the oscillatory term as $t \to \infty$,

$$\frac{1}{t} \int_0^t \sin^2 \left(\frac{\Omega t'}{2} \right) \mathrm{d}t' \rightarrow \frac{1}{2}, \tag{3.2.11}$$

giving a signal contrast of

$$C_{\mathrm{ODMR}} = \frac{1}{4} \frac{\omega_x^2}{\Omega^2} = \frac{1}{2} \frac{\omega_x^2}{\omega_x^2 + 2\delta^2}, \tag{3.2.12}$$

which has a Lorentzian shape centred about $\delta = 0$, whose width is defined by the microwave field strength, ω_x (specifically, the FWHM $= \sqrt{2}\omega_x$). This shows that increasing the microwave field strength increases the probability that the $|0\rangle \rightarrow |+1\rangle$ transition may be excited at a given detuning.

At this point, it is important make the distinction between the intended detuning, given by $\delta_I = \omega - D - B_0$, and the actual detuning due to the presence of the spin

bath, $\delta = \omega - D - B_0 - b = \delta_I - b$. As the bath detuning is the result of the NV coupling to a large number of paramagnetic impurities in the environment (of spin E), we take b to follow a normal distribution, with variance given by

$$\begin{aligned}\left\langle b^2 \right\rangle &= \sum_{n,s} A_{z,n}^2 \\ &\approx \sum_{s} 2\pi n E(E+1) \int_{R_E}^{\infty} \left[\hbar \frac{\mu_0}{4\pi} \frac{\gamma_{\mathrm{NV}}\gamma_E}{r^3} \left(1 - 3\cos^2\theta\right)\right]^2 r^2 \,\mathrm{d}\cos\theta \,\mathrm{d}r \\ &= \sum_{s} E(E+1) \frac{4}{5} \left[\frac{4\hbar\pi n}{3} \frac{\mu_0}{4\pi} \gamma_{\mathrm{NV}}\gamma_E\right]^2, \end{aligned} \tag{3.2.13}$$

where $A_{z,n}$ is the axial component of the spin-spin coupling between the NV centre and the nth spin of species E; γ_{NV} is the gyromagnetic ratio of the NV centre; n, E and γ_E are the spatial density, spin and gyromagnetic ratio of species E; and we have replaced the sum by an integral due to the large numbers of spins present. The integral has been taken from $R_E = \left(\frac{3}{4\pi n}\right)^{1/3}$, which is the radius of the largest possible sphere in which we expect to find less than one spin impurity.

Typically, the species encountered will be the 1.1% abundant ^{13}C isotope, and in some cases, electron spins of naturally occurring N impurities at roughly ppm concentrations. In either case, both species give rise to an RMS zeeman shift of order $\sqrt{\langle b^2 \rangle} \sim 1 - 10\,\mathrm{MHz}$.

Furthermore, we assume that there is an additional zero-mean shift due to the strong hyperfine coupling between the NV electron spin and the nuclear spin of its nitrogen atom, which may be either spin-1 or spin-$\frac{1}{2}$, with isotopic abundances of 99.64% and 0.36% respectively. Despite its relatively low natural abundance, we mention ^{15}N here since it is specifically chosen for magnetic resonance applications due to its much narrower NMR linewidth and lack of a quadrupole moment as compared with the spin-1 ^{14}N. Note that we have essentially assumed that the bath adopts a

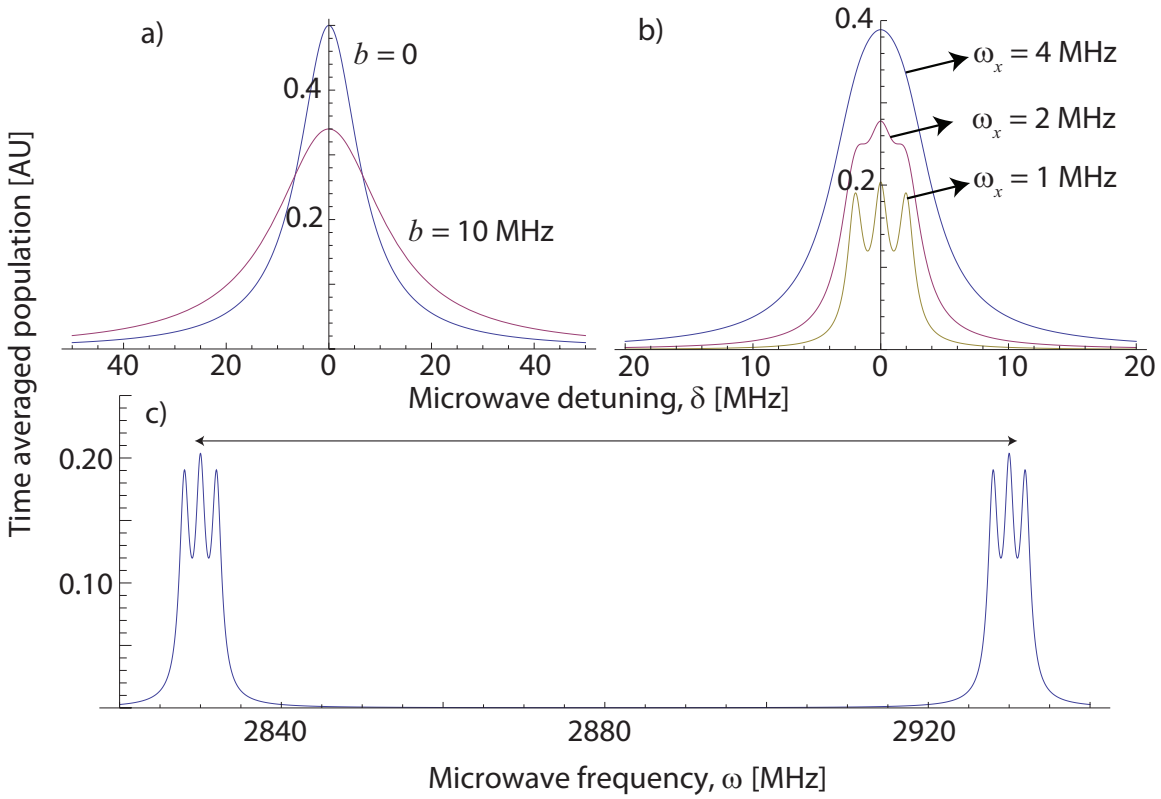

Figure 3.3: (a) ODMR spectrum showing the effect of broadening due to a zero-mean proximate electron spin bath of $\sqrt{\langle b^2 \rangle} = 10\,\text{MHz}$. (b) ODMR spectrum showing the peak splitting due to the spin-1 ^{14}N atom of the NV centre. As the microwave field is reduced from 4 to 2 to 1 MHZ, the individual peaks become increasingly apparent. (c) Full ODMR spectrum including both $\left|0\right\rangle \leftrightarrow \left|\pm 1\right\rangle$ transitions, as split by a static field of 50 MHz.

quasi-static behaviour, where each particular realisation of b is considered static, but we sample all possible realisations of b when computing the ensemble average. This approximation is valid since the timescales of both the Rabi oscillations and the NV polarisation are much faster than the fluctuation rate of the axial coupling to the bath (typically of order kHz or less).

The ensemble average of the contrast is then

$$\left\langle C_{\mathrm{ODMR}}\right\rangle \;=\; \frac{1}{2\sqrt{2\pi\left\langle b^2\right\rangle}}\int \frac{\omega_x^2}{\omega_x^2+2\left(\delta_T-b\right)^2}\exp\left[-\frac{\left(b-\left\langle b\right\rangle\right)^2}{2\left\langle b^2\right\rangle}\right]\mathrm{d}b.$$

Note that this integral has no closed-form solution, however we may investigate its asymptotic limits for the typical case where $b \ll \omega_x$ (in experimental situations, we typically have $b \sim 1-10\,\mathrm{MHz}$ and $\omega_x \sim 100\,\mathrm{MHz}$), from which we find

$$C_{\mathrm{ODMR}} \;\sim\; \frac{\omega_x^2}{2\left(\omega_x^2+2\delta_T^2\right)}+\frac{2b\delta_T\omega_x^2}{\left(\omega_x^2+2\delta_T^2\right)^2}+\frac{b^2\left(6\delta^2\omega_x^2-\omega_x^4\right)}{\left(\omega_x^2+2\delta^2\right)^3}+\mathcal{O}\left\{b^3\right\},$$

giving an ensemble average of

$$\left\langle C_{\mathrm{ODMR}}\right\rangle \;\sim\; \frac{\omega_x^2}{2\omega_x^2+4\delta_T^2}-\left\langle b^2\right\rangle\frac{\omega_x^2\left(\omega_x^2-6\delta_T^2\right)}{\left(\omega_x^2+2\delta_T^2\right)^3}, \tag{3.2.14}$$

and showing a fractional contrast change of

$$\frac{\Delta\langle C\rangle}{\langle C\rangle} \;\sim\; 2\left\langle b^2\right\rangle\frac{\left(\omega_x^2-6\delta^2\right)}{\left(\omega_x^2+2\delta^2\right)^2}, \tag{3.2.15}$$

corresponding to a fractional reduction in the peak height ($\delta_T = 0$) of $2\left\langle b^2\right\rangle/\omega_x^2$, and an increase in the heights of the distribution tails ($\delta_T \gg \omega_x$) of $3\left\langle b^2\right\rangle/\delta_T^2$. As such, we conclude that the presence of the spin bath has resulted in a broadening of the ODMR response to the frequency of an oscillatory microwave field. These effects are illustrated in figure 3.3(a).

Finally, we add the shifts due to the nuclear spin of the ^{14}N nuclear spin, as shown figure 3.3(b). To deduce the splittings, we refer back to the relevant terms of the full

NV Hamiltonian (equation 3.2.2), which implies that the NV spin will experience mean axial shifts of 0 and $\pm A_{N,z}$, resulting in a translation of the ODMR by the same amount. The full ODMR spectrum including both $\left|\,0\right\rangle \leftrightarrow \left|\pm 1\right\rangle$ transitions, as split by a static field of 50 MHz, is shown in figure 3.3(c).

Including optical polarisation

The above interaction of the NV centre with the microwave field alone constitutes an idealised case in which the presence of the readout laser field has no effect on the NV centre. In reality this is not possible, since the laser must cause the NV centre to polarise into the $\left|\,0\right\rangle$ state in order to produce the photons required for the measurement process. Rather than go into unnecessary detail about the true mechanism behind this process (see [MDH11] for and extensive overview), we will simply add a Linbladian relaxation term to the evolution of the density matrix to model the laser induced population transfer from the $|\,+1\rangle$ state to the $|\,0\rangle$ state,

$$\frac{\mathrm{d}\rho}{\mathrm{d}t} \;=\; -i\big[\mathcal{H},\rho\big] + \mathcal{D}, \tag{3.2.16}$$

where the Lindbladian operator describing the population transfer is given by [BP06],

$$\mathcal{D}_i \;=\; -\frac{\Gamma}{2}\begin{pmatrix} 2\rho_{11} & \rho_{10} \\ \rho_{01} & -2\rho_{11} \end{pmatrix}, \tag{3.2.17}$$

and Γ is the population transfer rate, or polarisation rate, from the $\left|\,+1\right\rangle$ state into the $\left|\,0\right\rangle$ state.

The equations of motion for the elements of the density matrix are then

$$\begin{aligned}
\frac{\mathrm{d}}{\mathrm{d}t}\rho_{11}(t) &= -\Gamma\rho_{11} + \frac{i}{2\sqrt{2}}\omega_x\rho_{10}e^{it\delta} - \frac{i}{2\sqrt{2}}\omega_x\rho_{01}e^{-it\delta}, && (3.2.18)\\
\frac{\mathrm{d}}{\mathrm{d}t}\rho_{10}(t) &= \frac{i}{2\sqrt{2}}\omega_x e^{-it\delta}\rho_{11} - \frac{1}{2}\Gamma\rho_{10} - \frac{i}{2\sqrt{2}}\omega_x e^{-it\delta}\rho_{00}, && (3.2.19)\\
\frac{\mathrm{d}}{\mathrm{d}t}\rho_{01}(t) &= -\frac{i}{2\sqrt{2}}\omega_x e^{it\delta}\rho_{11} - \frac{1}{2}\Gamma\rho_{01} + \frac{i}{2\sqrt{2}}\omega_x e^{it\delta}\rho_{00}, && (3.2.20)\\
\frac{\mathrm{d}}{\mathrm{d}t}\rho_{00}(t) &= \Gamma\rho_{11} - \frac{i}{2\sqrt{2}}\omega_x\rho_{10}e^{it\delta} + \frac{i}{2\sqrt{2}}\omega_x\rho_{01}e^{-it\delta}, && (3.2.21)
\end{aligned}$$

which may be reduced to

$$\begin{aligned}
&\frac{\mathrm{d}^3}{\mathrm{d}t^3}\rho_{00} + 2\Gamma\frac{\mathrm{d}^2}{\mathrm{d}t^2}\rho_{00} + \frac{1}{4}\left(5\Gamma^2 + 4\delta^2 + 2\omega_x^2\right)\frac{\mathrm{d}}{\mathrm{d}t}\rho_{00} + \frac{\Gamma}{4}\left(\Gamma^2 + 4\delta^2 + \omega_x^2\right)\rho_{00}\\
&\qquad = \frac{\Gamma}{8}\left(2\Gamma^2 + 8\delta^2 + \omega_x^2\right). \qquad (3.2.22)
\end{aligned}$$

By seeking solutions of the form $\rho_{00} = Ae^{\lambda t}$, we obtain

$$\begin{aligned}
\rho_{00} &= \frac{e^{t\lambda_2}\left(\omega_x^2 - 4\lambda_3\lambda_1\right)}{4\left(\lambda_1 - \lambda_2\right)\left(\lambda_2 - \lambda_3\right)} + \frac{e^{t\lambda_1}\left(\omega_x^2 - 4\lambda_2\lambda_3\right)}{4\left(\lambda_1 - \lambda_2\right)\left(\lambda_3 - \lambda_1\right)}\\
&\quad + \frac{e^{t\lambda_3}\left(\omega_x^2 - 4\lambda_1\lambda_2\right)}{4\left(\lambda_3 - \lambda_1\right)\left(\lambda_2 - \lambda_3\right)} + \frac{1}{2}\frac{2\Gamma^2 + 8\delta^2 + \omega_x^2}{\Gamma^2 + 4\delta^2 + \omega_x^2}. \qquad (3.2.23)
\end{aligned}$$

The full solution for arbitrary Γ and t is straightforward, but rather unsightly and not particularly enlightening, however we note that in all scenarios the steady state result is the same. In the case of low laser power, we expand the λ_i for small Γ, giving

$$\begin{aligned}
\lambda_1 &= -\Gamma\left(\frac{1}{2} + \frac{\delta^2}{2\delta^2 + \omega_x^2}\right), && (3.2.24)\\
\lambda_2 &= -\Gamma\left(\frac{\omega_x^2/4}{2\delta^2 + \omega_x^2} + \frac{1}{2}\right) + i\sqrt{\delta^2 + \frac{\omega_x^2}{2}}, && (3.2.25)\\
\lambda_3 &= -\Gamma\left(\frac{\omega_x^2/4}{2\delta^2 + \omega_x^2} + \frac{1}{2}\right) - i\sqrt{\delta^2 + \frac{\omega_x^2}{2}}, && (3.2.26)
\end{aligned}$$

and in the case of high laser power, where $\Gamma \gg \omega_x$, we have

$$\lambda_1 = -\frac{\Gamma}{2} - \frac{\omega^2}{2\Gamma} - i\delta, \tag{3.2.27}$$

$$\lambda_2 = -\Gamma + \frac{\omega^2}{\Gamma}, \tag{3.2.28}$$

$$\lambda_3 = -\frac{\Gamma}{2} - \frac{\omega^2}{2\Gamma} + i\delta. \tag{3.2.29}$$

As we can see, the presence of even a weak laser field causes the oscillating terms to decay on a timescale of $\sim 1/\Gamma$, leaving only the static term in equation 3.2.23. This is somewhat different to the case of having no laser field (as discussed above) where the average was calculated by integrating over the persistent oscillating terms. The steady state contrast in the presence of the laser field is then

$$\begin{aligned} C_{\mathrm{ODMR}} &= 1 - \frac{1}{2}\frac{2\Gamma^2 + 8\delta^2 + \omega_x^2}{\Gamma^2 + 4\delta^2 + \omega_x^2} \\ &= \frac{\omega_x^2/2}{\omega_x^2 + \Gamma^2 + 4\delta^2}, \end{aligned} \tag{3.2.30}$$

showing that the presence of the laser field acts to broaden the ODMR spectrum and reduce its contrast. Instead of the width being defined by the microwave power alone, ω_x^2, the spectrum is now also broadened as a result of the optical power, which is proportional to Γ^2. The FWHM of the ODMR spectrum is now $\frac{1}{2}\sqrt{\omega_x^2 + \Gamma^2}$.

3.2.2 Rabi cycling

A Rabi cycle employs the same experimental apparatus and physical conditions as the ODMR protocol outlined above, yet differs in the manner in which both the laser and microwave fields are applied. Instead of being applied to the NV continuously, the laser is pulsed only after specified fixed periods of microwave-driven evolution to read-out the subsequent quantum state of the NV spin, and the microwave field is employed

at a fixed, resonant frequency rather than being swept across a broad frequency range as in the ODMR case. The microwave frequency is chosen by examining the ODMR spectrum to find the frequency giving rise to the maximum possible contrast. As there is no laser field present during the microwave driven evolution, a Rabi cycle provides a much more natural measure of the environment surrounding the NV centre.

Specifically, a Rabi cycle involves an initial laser pulse to polarise the NV in the $|\,0\rangle$ state. The laser is then turned off and a microwave pulse is used to drive the spin state between one of the available spin transitions, say $|\,0\rangle \leftrightarrow |\,+1\rangle$, for a fixed time interval, t. A final laser pulse allows us to measure the population of the $|\,0\rangle$ state and acts to repolarise the spin state for the next measurement. By repeating this for different intervals of t, and then repeating many times for each value of t, we may build up a shot noise-limited ensemble of the time dependent population of the $|\,0\rangle$ state under the influence of the microwave field. As opposed to the continuous (CW) ODMR method, Rabi cycling represents the first of our Pulsed Wave (PW), or initialise-evolve-measure, spin resonance protocols.

From the ODMR analysis above, the time dependent population of the $|\,0\rangle$ state for a given detuning, δ, is described by

$$\rho_{00}(t) \;=\; 1 - \frac{\omega_x^2}{\omega_x^2 + 2\delta^2} \sin^2\left(\frac{t}{2}\sqrt{\frac{\omega_x^2}{2} + \delta^2}\right), \tag{3.2.31}$$

where, again, we have assumed that the $|\,0\rangle \leftrightarrow |-1\rangle$ transition is so far detuned that the $|-1\rangle$ state is never populated (again, this is the subject of chapter 7). To compute the ensemble average, we again make the quasi-static approximation, which is valid in this case because the time required for a typical Rabi signal to decay ($\approx 10\,\mu$s) is much less than the timescale on which the effective axial ^{13}C field fluctuates ($\approx 1 - 10\,$ms), thus, over the course of each individual quantum trajectory of its spin state, the NV

sees a static field, however the amplitude of this field changes over long timescales, thus ensuring the NV samples the entire ensemble over some $10^5 - 10^6$ repetitions for each time interval, t. Such an approximation would not be valid in the case of an electron spin bath, whose fluctuation rate is of the same order as the detuning ($\approx 1\,\mathrm{MHz}$). For a solution to this case, we refer the interested reader to the work in [DFHA09].

To compute the ensemble average of expression 3.2.31, we use the same probability density for the normally distributed detuning as was employed in the ODMR case,

$$\mathrm{P}(\delta) \;=\; \frac{1}{\sigma\sqrt{2\pi}}\frac{1}{2I_N+1}\sum_{i=1}^{2I_N+1}\exp\left(-\frac{(\delta-\mu_i)^2}{2\sigma^2}\right), \tag{3.2.32}$$

where the μ_i correspond to the equally probable hyperfine shifts induced by the coupling of the NV spin to the spin-I_N proximate nitrogen atom, and σ is the spread in these shifts due to the coupling to the surrounding bath. Depending on the isotope, these hyperfine shifts may take values of $\mu_i = \{0, \pm A_N\}$, or $\mu_i = \{\pm A_N\}$, where $A_N \approx 2\,\mathrm{MHz}$ [JW06]. The resulting integral of equation 3.2.31 over this distribution has no known solution for general δ; however, as typical microwave field strengths are $\omega_x \sim 100\,\mathrm{MHz}$ and $\delta \sim 1 - 10\,\mathrm{MHz}$, we may expand equation 3.2.31 to second order in δ/ω_x, giving

$$\rho_{00}(t) \;\approx\; 1 - \left(1 - 2\frac{\delta^2}{\omega_x^2}\right)\sin^2\left[\frac{\omega_x t}{2\sqrt{2}}\left(1 + 2\frac{\delta^2}{\omega_x^2}\right)\right], \tag{3.2.33}$$

which we integrate over the probability distribution above to give

$$\begin{aligned}\left\langle\rho_{00}\right\rangle_{\mathrm{Rabi}} \;=\; &\frac{1}{2} + \frac{1}{2I_N+1}\sum_{i=1}^{2I_N+1}\frac{1}{2}\left(\frac{2\sigma^4 t^2}{\omega_x^2}+1\right)^{-1/4}\exp\left(-\frac{t^2\mu_i^2\sigma^2}{2t^2\sigma^4+\omega_x^2}\right)\\ &\times\cos\left[\frac{t\omega_x}{\sqrt{2}}\left(\frac{\mu_i^2}{2t^2\sigma^4+\omega_x^2}+1\right)+\tan^{-1}\left(\frac{t\sigma^2}{\sqrt{2}\omega_x}\right)\right].\end{aligned} \tag{3.2.34}$$

This expression exhibits a number of interesting characteristics. Firstly, the population with a non-zero hyperfine shift, $\mu_i \neq 0$, experience an initially Gaussian decay to a final amplitude of $\exp\left(-\frac{\mu_i^2}{2\sigma^2}\right)$, which is then damped further by the (hyperfine state independent) power law decay. The component having $\mu_i = 0$ experiences only the power law decay, and therefore remains visible for much longer. This can be seen in figures 3.4 (a)&(b). This power law decay is only valid for as long as the N nuclear spin remains polarised, beyond which we would expect further Gaussian decay for the same reasons as the other two components, as discussed above.

Secondly, as the system evolves, a phase difference of

$$\Delta\phi = \frac{t\omega_x}{\sqrt{2}} \frac{\mu_i^2}{2t^2\sigma^4 + \omega_x^2} \tag{3.2.35}$$

develops, resulting in an interference between the oscillatory components associated with each of the μ_i. Depending on the relative magnitudes of the parameters describing the bath, this can lead to a dip in the overall population, from which it later recovers (figure 3.4 (d)). These dips have been observed experimentally in [HDF+08].

3.2.3 Free evolution- relaxation and dephasing

In the protocols discussed above, we have monitored the evolution of the NV spin under the influence of a laser field and/or a microwave field (in the case of ODMR and Rabi cycles respectively). Despite their utility, these methods arguably do not give the most accurate insight into the natural spin environment surrounding the NV centre, as the presence of the control fields obscure many of the physical processes taking place. In the following section, we consider protocols designed to measure the influence of the environment on the NV as apart from the external influence of these laser and microwave fields.

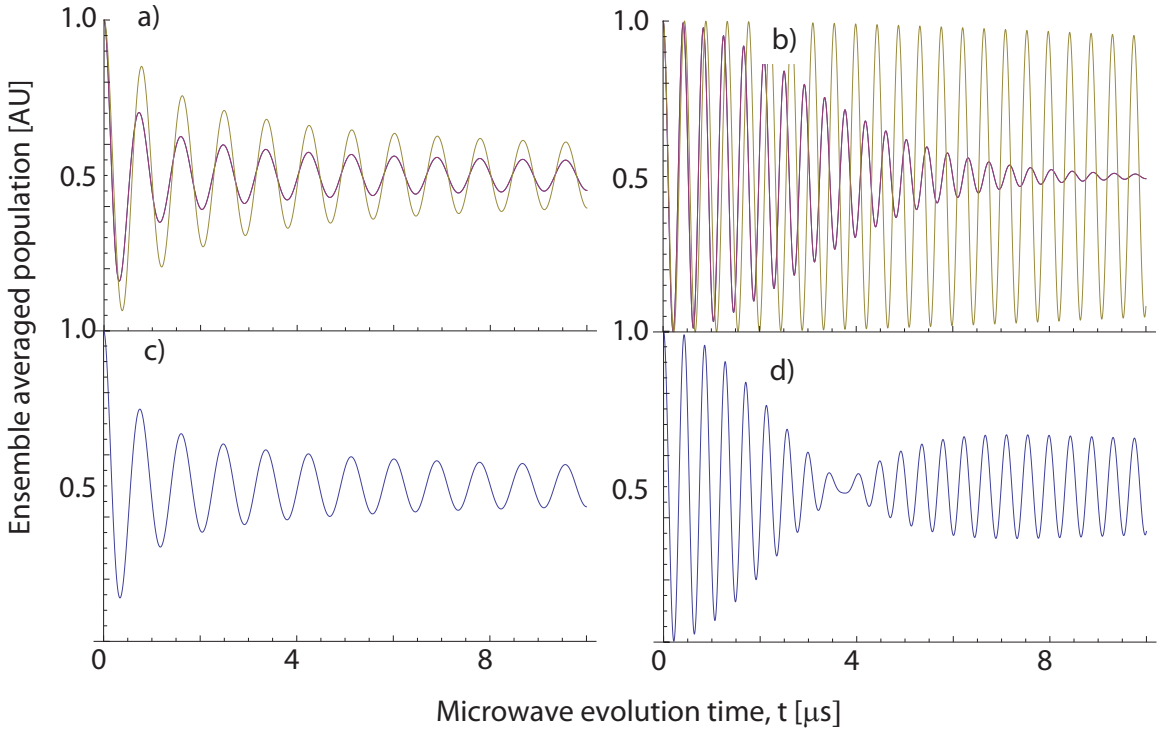

Figure 3.4: (a) Individual population components of a Rabi cycle corresponding to hyperfine shifts $\mu_i = 0$ (green) and $\mu_i = \pm A_N$ (blue) arising from the coupling between the NV spin and the spin of a proximate nitrogen nucleus. The non-zero components exhibit a much faster initial Gaussian decay. Parameter values are $\sigma = 4\,\text{MHz}$, $A_N = 2\,\text{MHz}$ and $\omega_x = 10\,\text{MHz}$. (b) As in (a), but with $\sigma = 1\,\text{MHz}$, $A_N = 2\,\text{MHz}$ and $\omega_x = 20\,\text{MHz}$. The power law decay is comparably slower, as the value of σ/ω_x is less than that of (a). The Gaussian decay is also slower because μ/ω_x is less than that of (a), however the final value is also much less because μ/σ is greater. (c) Average over all three nitrogen hyperfine states for the components shown in (a). (d) Average over all three nitrogen hyperfine states for the components shown in (b). A dip in the overall population arises due to interference between the individual population components associated with the three hyperfine states.

Measuring the relaxation time (T_1)

Relaxation protocols are designed to measure the time dependent projection of the spin along its quantisation axis, and thus investigate the manner in which the spin exchanges energy with its environment. The timescale on which this projection decays from its initial non-equilibrium state is referred to, by analogy with the NMR literature, as T_1. In the case of an NV centre, the initial state is prepared by optically polarising the spin into the $|0\rangle$ state and simply letting it evolve for given amount of time before measuring the $|0\rangle$ state population. In this way, a T_1 focused protocol measures the time required for the NV polarised in the $|0\rangle$ state to reach a state of equilibrium between all 3 spin sublevels. The population of each sublevel at equilibrium will depend on the relative rates of the transitions between each state.

Given the simplicity of the relaxometry protocol and the lack of an applied microwave field, it may seem odd that we have delayed its discussion until after the comparatively complex Rabi protocol. However, the T_1 process may be described using a very similar formalism to what was developed for the Rabi case.

The Rabi protocol measures the rate at which the longitudinal spin projection changes in response to a single applied frequency, ω (ie, the microwave frequency). A general fluctuating field however will possess a distribution of frequencies, each of which couples to the NV spin depending on its relative proportion and respective detuning. Specifically, to determine the response of the NV to an arbitrary field, we compute the average of equation 3.2.31 over the field's spectral density. Clearly the component of the field that has the largest effect on the evolution of the NV spin will be that for which $\delta = 0$, implying that the T_1 protocol essentially 'filters' the spectral component matching the energy separation of the spin states (the filter

function being the Lorenztian dependence on the detuning). We do not discuss this in detail here, however, as there are a number of other competing factors which determine the width of this filter function and hence the rate at which the NV spin will relax. To illustrate this briefly, consider a particular environment that has caused the originally polarised NV spin to evolve having a non-zero lateral projection of its spin vector. As per the discussion of the spin bath in chapter 2, the rates at which longitudinal and lateral spin projections decay will in general differ, hence even T_2 processes can have a significant impact on the longitudinal spin projection. Thus we must also understand the behaviour of the lateral spin projection in response to its environment, as discussed in the following. We return to the full discussion of relaxation processes in chapter 10.

Measuring the dephasing time (T_2)

By virtue of the large zero-field splitting of the NV groundstate spin, many of the processes we are interested in measuring are unable to affect the longitudinal spin component unless they exhibit dynamic properties at the GHz regime. Thus, following the initial polarisation into the $|\,0\rangle$ state, we need a means by which to rotate the spin to a state that will be sensitive to environmental processes coupling to $\mathcal{S}_z$. By employing a $\frac{1}{4}$ Rabi cycle, otherwise known as a $\frac{\pi}{2}$ pulse, we transform the NV spin into an equal superposition of $|\,0\rangle$ and $|+1\rangle$ states. As the sum of all axial couplings consititute an effective magnetic field, $b(t)$, to which only the $|+1\rangle$ state is sensitive, a phase difference will develops between the two states. This phase difference may then be transformed into a population difference using another $\frac{\pi}{2}$ pulse, allowing us to deduce the phase shift by optically measuring the population of the $|\,0\rangle$ state. This

phase shift is given by $\phi(t) = \int_0^t b(t')\,\mathrm{d}t'$, giving a resulting population difference of

$$\rho_{00}(t) \;=\; \frac{1}{2} + \frac{1}{2}\cos(\phi(t)), \tag{3.2.36}$$

where we have assumed, for the purposes of this discussion, that the microwave pulses are instantaneous and result in no excitation of the $\big|-1\big\rangle$ state. These effects are treated in chapter 7.

As was the case for the environment-induced detuning in the ODMR and Rabi protocols above, the value of $\phi(t)$ at a particular instant in time will be normally distributed with, by definition, mean $\langle\phi\rangle$ and variance $\langle\phi^2\rangle$. The ensemble averaged population is then

$$\begin{aligned}\big\langle\rho_{00}\big\rangle &= \frac{1}{2} + \frac{1}{2}\frac{1}{\sqrt{2\pi\langle\phi^2\rangle}}\int_{-\infty}^{\infty}\exp\left[-\frac{\big(\phi-\langle\phi\rangle\big)^2}{2\langle\phi^2\rangle}\right]\cos(\phi)\,\mathrm{d}\phi \\ &= \frac{1}{2} + \frac{1}{2}e^{-\langle\phi^2\rangle/2}\cos\langle\phi\rangle. \end{aligned}\tag{3.2.37}$$

Thus we may relate the statistics associated with the phase shifts directly to the dynamic statistics of the magnetic field, by noting that

$$\begin{aligned}\langle\phi\rangle &= \left\langle\int_0^t b(t')\,\mathrm{d}t'\right\rangle \\ &= \int_0^t\big\langle b(t')\big\rangle\,\mathrm{d}t', \\ \big\langle\phi^2\big\rangle &= \left\langle\int_0^t b(t')\,\mathrm{d}t'\int_0^t b(t'')\,\mathrm{d}t''\right\rangle \\ &= \int_0^t\int_0^t\big\langle b(t')b(t'')\big\rangle\,\mathrm{d}t'\,\mathrm{d}t'', \end{aligned}$$

where we recognise $\big\langle b(t')\big\rangle$ to be the average static Zeeman shift of the NV spin, and $\big\langle b(t')b(t'')\big\rangle$ to be the dynamic autocorrelation function of the effective axial field between times t' and t''. Because this protocol essentially measures the decay of the

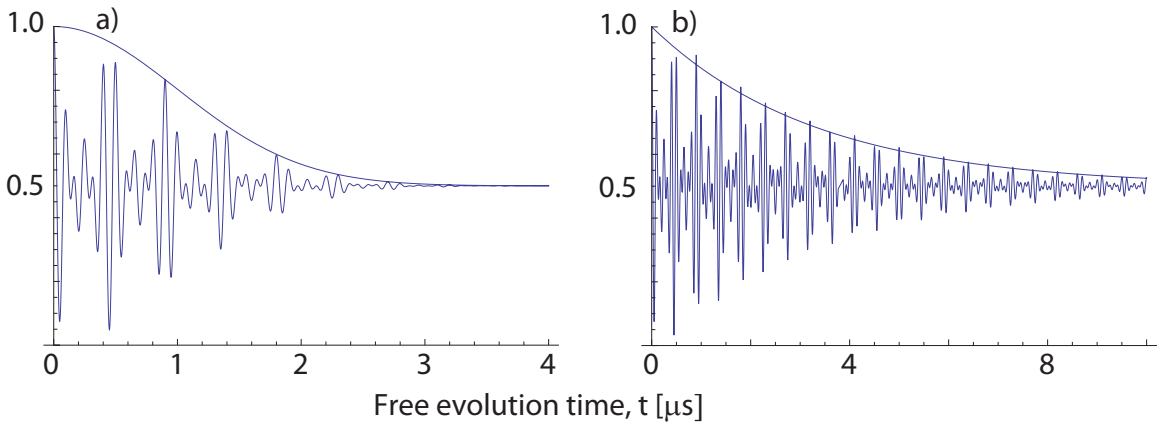

Figure 3.5: (a) Free Induction decay (FID) signal of the NV spin due to a proximate nuclear spin bath. Oscillations are due to the interaction with the nuclear spin of the adjacent nitrogen atom, and the overall Gaussian decay is due to a quasi-static (sub-kHz internal dynamics) ^{13}C nuclear spin bath of 1 MHz RMS amplitude. (b) FID signal with the same amplitude as in (a), but for an electron spin bath. The much faster internal dynamics of an electron spin bath (occurring on a MHz scale) result in the transition to an exponential decay within the overall FID time.

lateral components of the NV spin, with no influence from the microwave or laser fields during its free evolution, it is referred to as a Free-Induction Decay (FID), or sometimes Ramsey interferometry.

Typically in the literature (see the discussion in chapter 2), the autocorrelation function, $\langle b(t')b(t'')\rangle$ is approximated by a simple decaying exponential,

$$\langle b(t')b(t'')\rangle \;=\; \langle b^2\rangle \exp\left(-\frac{|t'-t''|}{T_c}\right), \tag{3.2.38}$$

where T_c is referred to as the correlation time of the environment. This approximation is, in fact, not valid in many cases, however a detailed analytic discussion regarding this issue is deferred until chapter 12. For the purposes of this illustration we will assume that equation 3.2.38 holds.

If we consider again the case of the ^{13}C nculear spin bath, we have that $T_c \sim 10$ ms,

whereas $\sqrt{\langle b^2 \rangle} \sim 1\,\mathrm{MHz}$. As such, the FID is effectively the result of a normally distributed ensemble of quasi-static realisations of b (see equation 3.2.32), giving

$$\langle \rho_{00} \rangle_{\mathrm{FID}} \approx \frac{1}{2} + \frac{1}{4I_N + 2} \sum_{i}^{2I_N+1} \exp\left[-\frac{1}{2}\langle b^2 \rangle t^2\right] \cos\left(\mu_i t\right), \tag{3.2.39}$$

The decay rate, $\Gamma_{\mathrm{FID}} \equiv \sqrt{\langle b^2 \rangle / 2}$ is referred to as the inhomogeneous linewidth, and the decay time is denoted $T_2^* = 1/\Gamma_{\mathrm{FID}}$, by analogy with the FID time of the lateral spin projection from the NMR literature.

In the case of an electron spin bath, we again have $\sqrt{\langle b^2 \rangle} \sim 1\,\mathrm{MHz}$, however now we also have that $T_c \sim 1\,\mu\mathrm{s}$, hence the bath becomes 'motionally narrowed' as a result of the comparatively rapid bath dynamics (owing to the much stronger electron-electron couplings in the environment), and the FID is now enveloped by a simple exponential, as given by

$$\langle \rho_{00} \rangle_{\mathrm{FID}} \approx \frac{1}{2} + \frac{1}{4I_N + 2} \sum_{i}^{2I_N+1} \exp\left[-\langle b^2 \rangle T_c t\right] \cos\left(\mu_i t\right). \tag{3.2.40}$$

Despite providing an accurate measure of both the static hyperfine shifts due to the nitrogen nuclear spin and the RMS strength of the quasi-static ^{13}C nuclear spin field, the FID protocol does not grant us an insight of the dynamic structure of the environment because it decays on timescales much shorter than the timescales associated with these dynamics (note that there is no mention of the quantity T_c in equation 3.2.39). To investigate the dynamic properties of the ^{13}C environment, we must employ more complicated pulse sequences to remove the effects of the static components of the bath (See figure 3.5(b)).

Multi-pulse sequences- dynamic decoupling

The simplest multi-pulse sequence we can imagine to refocus static noise is the Spin-Echo (SE), or Hahn-echo, pulse sequence. Such a sequence involves the two $\frac{\pi}{2}$ pulses from the Ramsey sequence, but employs an additional bit flip at the halfway point of the evolution (essentially, this is a concatenation of two FID pulse sequences). This bit-flip is achieved using a microwave pulse of twice the duration of the $\frac{\pi}{2}$ pulses, and is thus referred to as a π pulse.

Because the effect of the π pulse is to invert the amplitudes of the $|\,0\rangle$ and $|+1\rangle$ states, its application essentially changes the sign of the effective axial magnetic field seen by the NV centre. As such, the relative phase accumulation becomes

$$\phi_{\mathrm{SE}} \;=\; \int_0^{t/2} b(t')\,\mathrm{d}t' - \int_{t/2}^{t} b(t')\,\mathrm{d}t', \tag{3.2.41}$$

the most immediate consequence of which is that the oscillations due to persistent static shifts are removed due to $\langle\phi_{\mathrm{SE}}\rangle = 0$. Of more importance however, is the effect on the dynamic components,

$$\begin{aligned}
\left\langle \phi_{\mathrm{SE}}^2 \right\rangle &= \left[\int_0^{t/2} \mathrm{d}t' - \int_{t/2}^{t} \mathrm{d}t'\right]\left[\int_0^{t/2} \mathrm{d}t'' - \int_{t/2}^{t} \mathrm{d}t''\right]\left\langle b(t')b(t'')\right\rangle \\
&= -2\left\langle b^2\right\rangle T_c^2\left[3 - \frac{t}{T_c} + \exp\left(-\frac{t}{T_c}\right) - 4\exp\left(-\frac{t}{2T_c}\right)\right] \\
&\approx \frac{\left\langle b^2\right\rangle t^3}{4T_c},
\end{aligned} \tag{3.2.42}$$

giving a spin-echo population of

$$\left\langle \rho_{00}\right\rangle_{\mathrm{SE}} \;\approx\; \exp\left[-\frac{\left\langle b^2\right\rangle}{8T_c}t^3\right]. \tag{3.2.43}$$

This implies that the SE signal decays on a timescale of $T_2 = 2\left(T_c/\left\langle b^2\right\rangle\right)^{1/3} \approx 43\,\mu\mathrm{s}$ (using $\sqrt{\langle b^2\rangle} = 1\,\mathrm{MHz}$ and $T_c = 10\,\mathrm{ms}$), representing a factor of 19 improvement over the coherence time of an FID sequence.

Though it serves as a useful exercise in the relevant physics, the expression is not an accurate depiction of the true story. Despite the accuracy of a pure exponential autocorrelation function in predicting T_2^*, from experiment, we know that the application of a π pulse typically yields (conservatively, we remark) T_2 times of around 200-400 μs. These problems are addressed in detail in Chapters 4, 6 and 12, however we merely remark here that if we replace the simple exponential form of the autocorrelation with a Gaussian form,

$$\left\langle b(t')b(t'')\right\rangle \;=\; \left\langle b^2\right\rangle \exp\left[-\left(\frac{t'-t''}{T_c}\right)^2\right], \tag{3.2.44}$$

and apply the same method, we find the phase variance to be

$$\begin{aligned}\left\langle \phi_{\mathrm{SE}}^2\right\rangle \;=\; & \left\langle b^2\right\rangle T_c\Bigg(\sqrt{\pi}t\left[1-2\mathrm{erf}\left(\tfrac{t}{2T_c}\right)+\mathrm{erf}\left(\tfrac{t}{T_c}\right)\right]\\ & +T_c\left[4\exp\left(-\tfrac{t^2}{4T_c^2}\right)-\exp\left(-\tfrac{t^2}{T_c^2}\right)-3\right]\Bigg),\end{aligned}$$

which yields the same expression for T_2^* as in the simple exponential case, however for spin-echo we obtain $T_2 = 2\left[T_c^2/\left\langle b^2\right\rangle\right]^{1/4} = 200\,\mu$s, showing instead an improvement of a factor of $\sim$280, as consistent with the experimental case. Even if we were to retain the pure exponential and simply argue for a redefinition of T_c, we would still require $T_c \sim 8$ s to provide results that are consistent with experimental observations, which is nonsense. Furthermore, Nuclear Magnetic Resonance (NMR) experiments conducted on pure 1.1% ^{13}C diamond crystals show linewidths in the 1-10 kHz range [LBP$^+$94], as consistent with $T_c \sim 1$ ms (the slight discrepancy was attributed to electronic paramagnetic centres, although the species was not identified). The choice of autocorrelation function has been the source of some debate for decades, however, as we will discuss in chapter 12, the concept of an autocorrelation function has little

merit in the presence of a central spin strongly coupled to its surrounding environment.

These techniques may be extended to include multiple π pulses, with the free evolution intervals between each pulse defining the sequence in question. Typical examples include

- *Carr-Purcell-Meiboom-Gill (CPMG)*

  During a total evolution time of t, the j^{th} π pulse in a total of n pulses is applied at

$$t_{n,j} = \frac{t}{n}\left(j - \frac{1}{2}\right). \tag{3.2.45}$$

- *Uhrig Dynamic Decoupling (UDD)* [Uhr07]

  During a total evolution time of t, the j^{th} π pulse in a total of n pulses is applied at

$$t_{n,j} = t\sin^2\left(\frac{j\pi}{2n+2}\right). \tag{3.2.46}$$

- *Concatenated spin-echo*

  The sequence is constructed by using a concatenated series of $\tau - \pi - \tau - \pi$ sequences, where each successive level is reached by sandwiching this sequence inside the free-precession intervals of the previous level. Note that the uninterrupted application of an even number of π pulses results in a full rotation, and is thus disregarded. By the same reasoning, an odd number of π pulses is just treated a single π pulse.

CPMG and UDD protocols will be the primary focus of chapter 6.

Chapter 4

Sensing of Fluctuating Nanoscale Magnetic Fields via Dephasing of Electron Spins in solids

New magnetometry techniques based on Nitrogen-Vacancy (NV) defects in diamond allow for the detection of static (DC) and oscillatory (AC) nanoscopic magnetic fields, yet are limited in their ability to detect fields arising from randomly fluctuating (FC) environments. We show here that FC fields restrict DC and AC sensitivities, and that probing the NV dephasing rate in an FC environment permits the characterisation of FC fields inaccessible to DC and AC techniques. FC sensitivities are shown to be comparable to those of AC magnetometry, and require no additional experimental overheads or sample control. The material of this chapter has since been published in [HCHH09].

4.1 Introduction

The exploitation of controlled quantum systems as ultra-sensitive nanoscale detectors has tremendous potential to advance our understanding of complex processes occurring in biological and condensed-matter systems at molecular and atomic scales (see section 2.3 for a brief overview of spin based magnetometry). However, many important biological and condensed matter systems exhibit non-sinusoidal fluctuating magnetic fields with extremely low or zero mean values (figure 4.1). An important question is therefore to what extent these quantum based magnetometry techniques are applicable to such situations. In this chapter we address this by quantifying the detection sensitivities for these modes for samples with fluctuations characterized by the RMS field and dominant spectral frequency. The results indicate that by probing the dephasing rate of a spin qubit placed in such environments one can characterize the underlying fluctuation rates and RMS field strengths that would be otherwise inaccessible with the use of DC and AC magnetometry techniques, thereby opening the way for non-invasive nanoscale imaging of a range of biological and condensed matter systems using NV centres in diamond.

The theory behind the detection of magnetic fields using quantum systems is heavily reliant on the phase estimation program of quantum metrology, particularly the determination of coupling parameters that are constant in time. In the context of DC magnetometry, this corresponds to measurement of the first moment (the mean) of the magnetic field strength. For zero mean fields, complex microwave control pulse sequences are necessary. For fields exhibiting oscillatory (AC) time dependence with

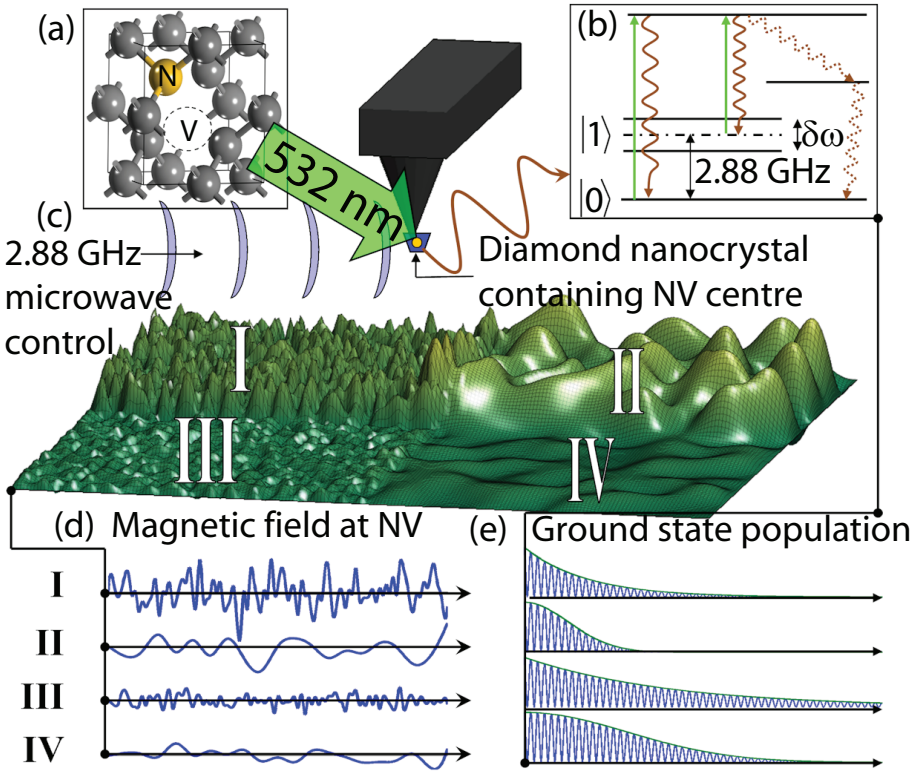

Figure 4.1: Schematic of a scanning NV qubit magnetometer/decoherence probe for the detection of nanoscale field fluctuations. (a) NV-centre diamond lattice defect. (b) NV spin detection through optical excitation and emission cycle. (c) Microwave control of the NV spin state and 532 nm optical pulse for read-out. (d) Simulated magnetic field signals at the NV probe corresponding to regions I-IV of an inhomogeneous test sample with different fluctuation amplitudes and frequency spectra. (e) The corresponding NV ground state populations show that the regions can be distinguished by the dephasing information: I: Strong, rapid fluctuations $\rightarrow$ fast exponential dephasing. II: Strong, slow fluctuations $\rightarrow$ fast Gaussian dephasing. III: Weak, rapid fluctuations $\rightarrow$ slow exponential dephasing. IV: Weak, slow fluctuations $\rightarrow$ slow Gaussian dephasing.

which either a spin-echo or CPMG [MG58] sequence may be synchronised, sensitivities are predicted to be as low as 3 nTHz$^{-1/2}$ [TCC$^+$08], based on the standard quantum limit. Excellent agreement between theory and experiment has been demonstrated in [MSH$^+$08]. Such techniques require accurate knowledge of the field dynamics which may not be available, or more commonly, the field may exhibit a stochastic time dependence. Examples include nuclear dipole fields of ion channels [Hil05] (figure 4.2(a)) and lipid bi-layers in biological cell membranes [PKH$^+$03], Overhauser fields in Ga-As quantum dots [RTL$^+$08], and even self-diffusing water molecules [TV02, RS71] (figure 4.2(b)). In what follows, we investigate the effects of a more general fluctuating (FC) field on the dephasing of a spin qubit as the primary detection mechanism, and the implications for the characterisation of the magnetic field from the surrounding environment. In this sense, we are estimating the second moment of the field strength, and the corresponding temporal dynamics.

4.2 Modeling the response of a spin qubit to a randomly fluctuating magnetic field

A spin qubit placed in a randomly fluctuating magnetic environment will experience a complex sequence of phase kicks, leading to an eventual dephasing of the population spectrum. For an NV centre, this will be in addition to the intrinsic sources of dephasing, which are due to paramagnetic impurities in the diamond lattice [CDT$^+$06]. The dephasing rate can be quantified via repeated projective measurements of the qubit state, and the corresponding dephasing envelope, $L(\tau)$, can be determined via a suitably chosen quantum state reconstruction technique. We use the technique

of Hamiltonian characterisation [CSG$^+$05] rather than quantum tomography techniques, as it requires only a single measurement basis yet is robust in the presence of dephasing [CGO$^+$06].

The motivation for the environment model used here comes from consideration of magnetic dipoles in motion. Other models in which a two level system is coupled to a bath of bistable fluctuators have been previously considered [SSMM05, SMS06, PFFF02, GABS06]. These models, however, do not capture the dephasing effects due to gradual transitions between environmental states in slowly fluctuating fields. Later we will show this to be of particular importance in the case of spin-echo based experiments. Additionally, these models require a large number of fluctuators to model a continuous signal. In contrast, we wish to consider the dephasing effects of small numbers of spins in motion.

Consider a qubit with gyromagnetic ratio γ_p undergoing a $\frac{\pi}{2} - \tau - \frac{\pi}{2}$ Ramsey sequence in the presence of a classical FC magnetic field, $B(t)$. An example of such a field due to a uni-directional spin current is shown in figure 4.2(a), and that of a bath of self-diffusing spins in figure 4.2(b). The field has mean $\langle B \rangle \equiv B_0$, standard deviation $\sqrt{\langle B^2 \rangle - \langle B \rangle^2} \equiv B'$, and typical fluctuation rate $f_e \equiv 1/\tau_e$, where τ_e is the self correlation time of the field (figure 4.2(c)). This gives rise to two natural frequency scales, given by $\omega_0 = \gamma_p B_0$ and $\omega' = \gamma_p B'$. The average precession frequency of the qubit is set by ω_0, and is decoupled from all dephasing effects for cases where $\omega', f_e \ll \omega_0$. Additional relaxation processes may dominate the qubit evolution when this condition is violated, however such cases are not considered here since we are interested in the characterisation of weak magnetic fields. The nature of the dephasing will depend on the fluctuation rate of the environment, f_e, or more specifically the

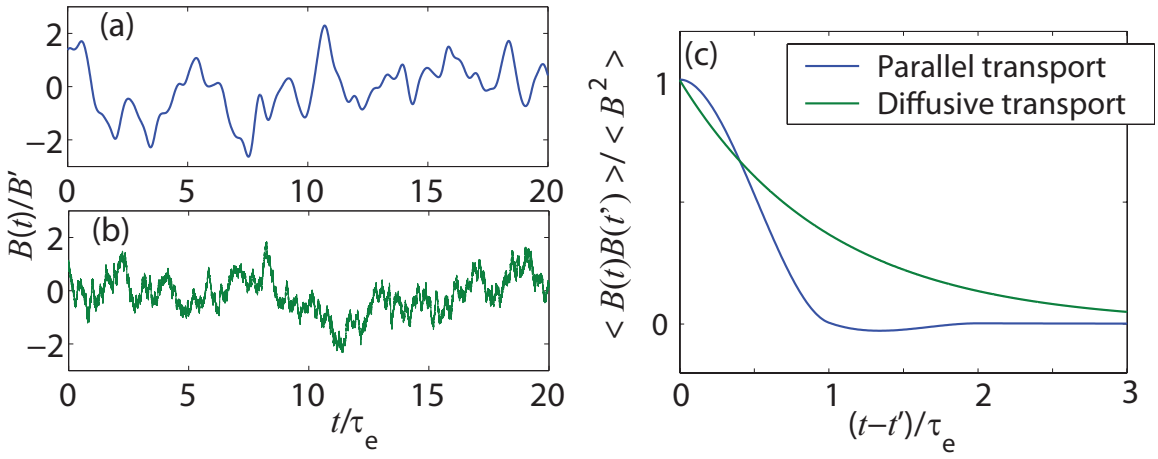

Figure 4.2: Simulated magnetic field traces, $B(t)/B'$, for (a) a channel of dipoles in unidirectional motion, and (b) a self diffusing dipole bath. (c) Temporal correlation function $\langle B(t)B(t')\rangle/\langle B^2\rangle$. Time axes are rescaled by τ_e.

magnitude of the quantity defined by $\Theta \equiv f_e/\omega'$.

4.2.1 Rapidly fluctuating fields

In the case of $\Theta \gg 1$, or fast-fluctuation limit (FFL), the qubit will experience many environmental fluctuations during its natural timescale. Whilst B' need not necessarily be normally distributed, the accumulated phase error of the qubit at some time $t \gg 1/f_e$ will be, by way of the Central Limit Theorem. As such, the variance of the phase error at time $t \gg 1/\omega'$ will be $\langle \Delta\phi^2 \rangle \sim t\gamma_p^2 B'^2/f_e$, giving rise to an FFL dephasing rate of

$$\Gamma_{\text{fast}}\left(B', f_e\right) \;=\; \frac{\gamma_p^2 B'^2}{2f_e}. \tag{4.2.1}$$

This is akin to the motional narrowing result from NMR and reproduces the ubiquitous exponential dephasing envelope given by $L_{\text{fast}}(t) = \exp\left(-\Gamma_{\text{fast}}t\right)$.

4.2.2 Slowly fluctuating fields

In the slow-fluctuation limit (SFL), where $\Theta \ll 1$, we note that the magnetic field may be locally approximated by a Taylor expansion in t about some initial time t_0: $B(t) = \sum_{k=0}^{N} \frac{1}{k!} \frac{d^k B}{dt^k}\Big|_{t_0} (t-t_0)^k \equiv \sum_{k=0}^{N} a_k (t-t_0)^k$, where each of the a_k has a specific statistical distribution containing information about the kth order derivative of $B(t)$, and thus gives rise to a different dephasing channel.

For the special case where the a_k are normally distributed with mean μ_k and variance σ_k^2 (as consistent with random dipole motion), the resulting density matrix following the free evolution time τ, but prior to the second $\pi/2$ pulse is defined by $\rho_{11} = \rho_{22} = 1/2$, and $\rho_{12} = \rho_{21}^* = \prod_{k=0}^{\infty} L_{\text{slow}}^{(k)}(\tau)\Omega_{\text{slow}}^{(k)}(\tau)$; where

$$L_{\text{slow}}^{(k)}(t) = \exp\left[-\left(\Gamma_{\text{slow}}^{(k)} t\right)^{2k+2}\right], \tag{4.2.2}$$

and

$$\Omega_{\text{slow}}^{(k)}(t) = \exp\left[-i\left(\omega_{\text{slow}}^{(k)} t\right)^{k+1}\right]. \tag{4.2.3}$$

Thus we see the emergence of a hierarchy of dephasing and beating channels, with the dephasing rates and beat frequencies of the k^{th} channel given by

$$\Gamma_{\text{slow}}^{(k)} = \left(\frac{1}{\sqrt{2}} \frac{\sigma_k \gamma_p}{k+1}\right)^{1/(k+1)}, \tag{4.2.4}$$

and

$$\omega_{\text{slow}}^{(k)} = \left(\frac{\mu_k \gamma_p}{k+1}\right)^{1/(k+1)}, \tag{4.2.5}$$

respectively. In the case of the zeroth order channel this corresponds to the rigid lattice result from NMR, and we have $\sigma_0^2 = \langle B^2 \rangle - \langle B \rangle^2$. This effect will be suppressed

by a spin echo pulse sequence. For the first order channel, we may approximate $\sigma_1^2 \sim (\langle B^2 \rangle - \langle B \rangle^2) f_e^2$.

The relative contributions of each channel to the overall dephasing rate of the qubit depend explicitly on the dynamics of the field, however, dominance of the zeroth order channel (ie $\Gamma_{\text{slow}}^{(0)} > \Gamma_{\text{slow}}^{(j)},\ \forall\ j \geq 1$) is a necessary and sufficient condition for the system to exist in the slow fluctuation regime, $\Theta \ll 1$. This justifies the use of the Taylor expansion, since the resulting polynomial may be well approximated by a low-order truncation.

4.2.3 Intermediate regime

The intermediate regime of $\Theta \sim 1$ is more complicated. Figure 4.3(a) shows dephasing envelopes for various values of Θ. For times much longer that τ_e, pure exponential dephasing behaviour is observed in all cases (with dephasing rate Γ_{fast}), however fast fluctuating environments still exhibit slow (Gaussian) dephasing behaviour on timescales τ where $\omega'\tau < \sqrt{2}/\Theta$. If Θ is large, contributions to L from the $\Gamma_{\text{slow}}^{(k)}$ will decay rapidly. The abrupt transition from $L_{\text{slow}} \rightarrow L_{\text{fast}}$ is shown more clearly in the corresponding insert.

4.3 Sensitivity

Before proceeding to the specific NV implementation, we summarize the different field detection protocols. While DC detection involves letting the qubit evolve under the influence of a constant, or near static, background field, AC detection requires driving the sample at a particular frequency ν while timing the spin-echo pulse synchronously.

In both cases the qubit phase shift, proportional to the time integral of the magnetic field, is detected. For FC fields, the accumulated phase is instead random, and detection is achieved via a change in the qubit decoherence rate[CH09], which can be obtained from a spin-echo measurement in a similar manner to the AC case, albeit with no synchronization required.

For the purpose of comparison with existing spin-based magnetometer proposals, we take the NV centre as our example qubit. The Hamiltonian used to describe the time evolution of an NV-centre is given by $\mathcal{H} = \vec{\mathcal{S}} \cdot \mathbf{D} \cdot \vec{\mathcal{S}} + \hbar\gamma_p \mathbf{B} \cdot \vec{\mathcal{S}} + \mathcal{H}_{\text{other}}$, where $\mathcal{H}_{\text{other}}$ describes higher order effects such as hyper-fine splittings, etc. which can be ignored in the present context. We consider weak external fields such that $|\gamma_p B'| \ll D$, thereby ensuring the crystal-field splitting tensor, $\mathbf{D}$, sets the quantisation axis of the NV centre, and that $\omega' \ll \omega_0$.

The shot-noise-limited DC sensitivity for an NV-based magnetometer subject to a Ramsey-style pulse sequence is given by [TCC+08] $\eta_{\text{dc}} \equiv B_{\min}\sqrt{T} \approx (\gamma_p C\sqrt{\tau})^{-1}$,where $\sqrt{T}$ and C represent the combined effects of spin projection and photon shot noise for N_s measurements ($C \to 1$ for the ideal case), τ is the free evolution time of the qubit, and $T = N_s\tau$ is the total averaging time. Dephasing times due to nearby paramagnetic lattice impurities will in general be different for different centres and will thus require individual characterisation. For comparison with [TCC+08], we take $\tau = T_2^* \sim 1\,\mu$s. We emphasise that the expression for η_{dc} applies solely to the detection of DC magnetic fields where the dephasing of the qubit is exclusively due to intrinsic crystal effects. If the sample produces a fluctuating field of sufficient amplitude, the dephasing time ($1/\Gamma$) may be shorter than T_2^*, resulting in poorer static field sensitivity. In this context, η_{dc} refers to the sensitivity with which the mean

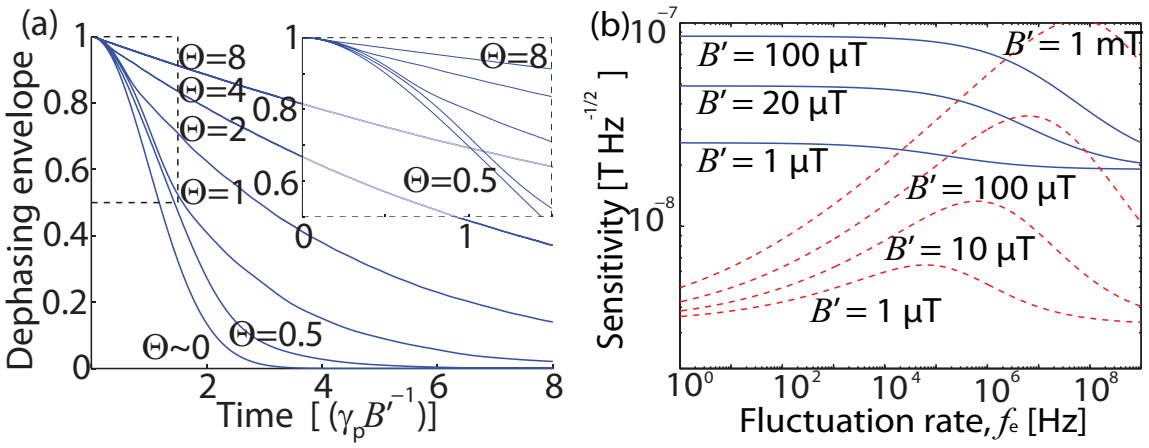

Figure 4.3: (a) Plot of simulated dephasing envelopes for $N_s = 10^4$ runs, showing agreement with Eqs. (4.2.1) & (4.2.2). Time is in units of $(\gamma_p B')^{-1}$. (insert) Zoomed plot showing that fast fluctuating environments still exhibit non-exponential dephasing for short timescales $\tau : \omega'\tau < \sqrt{2}/\Theta$. (b) Magnetic field sensitivities of DC (blue) and AC (red-dashed) protocols as a function of f_e for different contours of B'. The largest effect on $\eta_{\rm ac}$ comes from FC regimes in which $\Theta \sim 1$, away from which $\eta_{\rm ac} \to \frac{\pi \exp(\tau/T_2)^3}{2\gamma_p C\sqrt{\tau}} = 3\,\mathrm{nT\,Hz^{-1/2}}$. Assumed parameter values are $T_2^* = 1\,\mu$s, $T_2 = 300\,\mu$s, and $C = 0.3$.

field, $\langle B \rangle$, may be measured as the field fluctuates over the course of the experiment.

To gain insight into the effect of FC fields on the DC field sensitivity, we consider again a $\frac{\pi}{2} - \tau - \frac{\pi}{2}$ sequence. The DC sensitivity as a function of B' and f_e is shown in figure 4.3 (b). From this, we see that fluctuating environments can have a dramatic effect on the DC field sensitivity of an NV based magnetometer, depending on both field strength and fluctuation frequency.

As detailed in chapter 3, we may extend the dephasing time of the NV-centre to $T_2 \sim 300\,\mu$s, as dictated by the 1.1% carbon-13 content in the lattice, using coherent control techniques. The case of perfectly oscillatory magnetic fields, in which the π pulse coincides with the first zero-crossing of the magnetic field, has been considered

in detail in [TCC$^+$08], giving AC sensitivities as low as $\eta_{\rm ac} \approx \frac{\pi \exp(\tau/T_2)^3}{2\gamma_p C\sqrt{\tau}} \approx 3$ nT Hz$^{-1/2}$ (figure 4.4(b)). As with DC magnetometry, the AC sensitivity will be strongly dependent on the FC characteristics of the environment, as shown in figure. 4.3 (b) as a function of B' and f_e.

We now study the magnetometer's sensitivity to a more general class of fluctuating fields via consideration of the induced dephasing rate. For a $\frac{\pi}{2} - \frac{\tau}{2} - \pi - \frac{\tau}{2} - \frac{\pi}{2}$ pulse sequence, the probe will show decreased sensitivity to environments for which $f_e < 1/\tau$. For $\Theta \gg 1$, the effect will be negligible. For $\Theta \ll 1$, this may appear problematic, however complete insensitivity only comes with $f_e \to 0$. A spin echo sequence will modify the $L^{(k)}_{\rm slow}$ via $\Gamma^{(k)}_{\rm slow} \longmapsto \left(1 - 2^{-k}\right)^{\frac{1}{k+1}} \Gamma^{(k)}_{\rm slow}$, thus only the effects of the zeroth order dephasing channel will vanish. Perturbations on the dephasing rate may be measured from $(1 - L)_{\rm min} = \frac{\exp\left[(\tau/T_2)^3\right]}{C\sqrt{N_s}}$[TCC$^+$08, CDT$^+$06]. This implies an optimal free-evolution time of $\tau \sim T_2/\sqrt[3]{6}$. Thus we find that perturbations on the $1/T_2$ dephasing rate as slow as 200 Hz for exponential dephasing and 800 Hz for Gaussian dephasing may be detected by this method after 1 s of averaging time. By performing measurements of the total dephasing rate, Γ, both the field variance and average fluctuation rate may be inferred from Eqs. (4.2.1) & (4.2.4). Of course, the question remains of which fluctuation regime a given sample system resides in. In the absence of any prior knowledge of the environment being measured, this question may be answered via determination of the shape of the dephasing envelope, a task to which the Hamiltonian characterisation method is well suited [CH09].

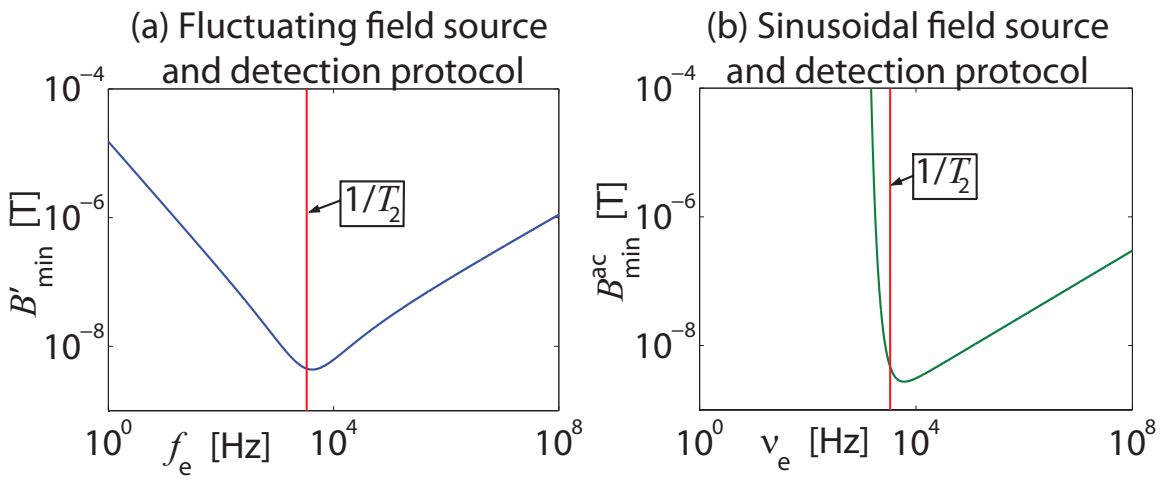

Figure 4.4: (a) Minimum resolvable FC field strength using FC detection protocol, $B_{\min}$, vs environmental fluctuation rate, f_e, for $T = 1\,\mathrm{s}$ averaging time. In contrast to the AC case, an FC detection requires no prior knowledge of fluctuation timescales. (b) Minimum resolvable AC field amplitude using AC detection protocol, $B^{\mathrm{ac}}_{\min}$, vs field oscillation frequency, ν_e, for $T = 1$ s averaging time in the absence of environmental noise ($B' = 0$). Here we have assumed that the AC field is initialised in phase with the probe qubit, and that the π pulse of a spin-echo sequence coincides with the first zero-crossing of the field.

4.4 Discussion and conclusions

The optimal FC sensitivity will occur when $\Theta \sim 1$, since this ensures maximal dephasing for a given field variance. Considering the special case of pure exponential decay, we therefore expect an optimal sensitivity of $\eta_{\mathrm{FC}} = \frac{e^{1/6}}{C\gamma_p\sqrt{T_2}} = 1.7\,\mathrm{nT\,Hz^{-1/2}}$. However, such sensitivity may be difficult to realise due to memory effects in the fluctuating environment. For systems that satisfy $\Theta \gg 1$, thus exhibiting long-time exponential dephasing behaviour, Gaussian dephasing is still exhibited for $\tau < 1/f_e$ (figure 4.3(a)). For spin-echo experiments, the effect is worsened as the dominant contribution to L_{slow} comes from $k = 1$. Taking this into consideration, the minimum resolvable field obtained after $T = 1$ s averaging time is plotted in figure 6.4(a) against f_e. We see that FC field strengths as low as 4.5 nT may be achievable after $T = 1$ s averaging time ($N_s \sim 3000$), and that the qubit will be sensitive to FC fields fluctuating on timescales much slower than $1/T_2$. This is in direct contrast with the AC case, which shows poor sensitivity to fields oscillating with periods less than T_2 (figure 4.4(b)).

We have theoretically investigated the effects of a fluctuating magnetic field on an NV centre spin qubit. This analysis was used to place new limits on the sensitivity with which the mean field strength may be measured. Furthermore, we have built upon the idea of decoherence microscopy [CH09] to theoretically demonstrate the ability of an NV centre to measure field strengths and fluctuation rates of randomly fluctuating magnetic fields. This analysis shows that the methods presented here require no experimental resources beyond those of existing techniques, no prior control or knowledge of the external field, and thus may be implemented with current technology.

Chapter 5

Experimental Investigation: Ambient Nanoscale Sensing with Single Spins Using Quantum Decoherence

In this chapter we discuss an application of the analytic techniques developed in the previous chapter: the characterisation of physical and chemical properties of spin rich aqueous solutions. We begin by developing the theory of the different processes to which the NV will be exposed, and make predictions about its resulting behaviour. These predictions are validated via an experimental demonstration[1] where 45 nm diamond nanocrystals containing NV centres are exposed to an aqueous solution of spin-$\frac{5}{2}$ Mn^{2+} ions. The influence of the Mn spins on the NV, resulting from both freely diffusing and accreted Mn atoms, yielded changes in the NV decoherence rate of up to 60%. Furthermore, drastic changes in the shape of the decoherence envelope indicate remarkable changes in the dynamical behaviour of the local environment. We apply the analytic techniques developed in this chapter to characterise the dynamic

[1] All NV-based experiments described in this chapter were performed by L.P. McGuinness and D.A. Simpson at the University of Melbourne. Atomic Force Microscopy (AFM) of the diamond nanocrystals was performed by B.C. Gibson at the University of Melbourne.

parameters describing the Mn environment, and use these findings to make conclusions about the physical processes giving rise to these dynamic processes, specifically ruling out the possibility of magnetic dipole-dipole mediated relaxation of spins on the nanocrystal surface. The material of this chapter has since been published in [MHS$^+$13].

5.1 Introduction

In this study, we report on the changes in decoherence of NV centre spins arising from the controlled introduction of electron spin-rich magnetic nanoscale environments, each of which exhibit remarkably different dynamic behaviour. We begin by characterizing the native environment of the NV spin, including the coupling to electron spins both within the crystal itself, resulting from nitrogen donor impurities, and delocalised electrons within the graphitic layer on the crystal surface. This characterisation processes is then repeated in water and finally in an aqueous $MnCl_2$ solution. The crystals are removed from the solution, with subsequent decoherence measurements showing the accretion of atomic Mn onto the nanocrystal surface. Finally, treating the crystals with hydrochloric restores the original decoherence properties, showing NV spins in diamond nanocrystals to be not only highly sensitive, but an extremely robust magnetic detection system.

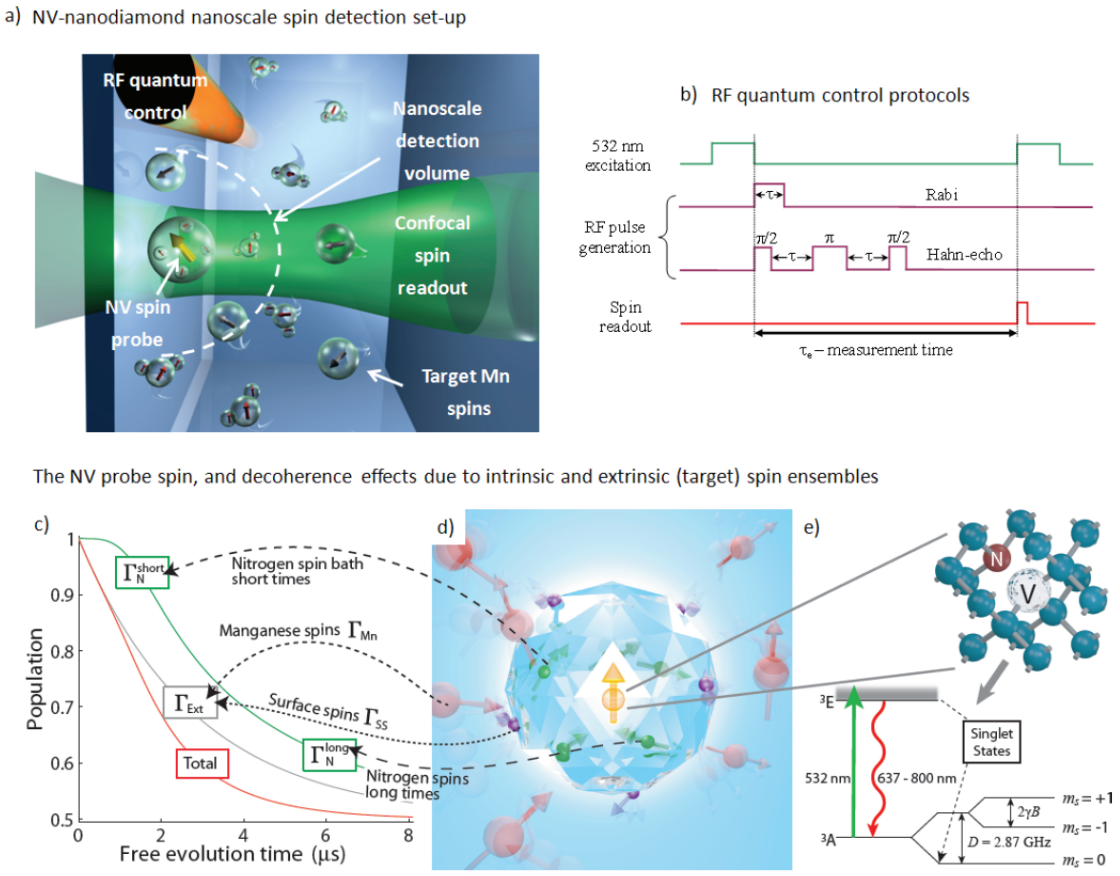

Figure 5.1: Overview of nanoscale decoherence sensing with NV spins, as taken from ref. [MHS+13]. (a) Experimental set-up: NV nanodiamonds are immersed into a spin-rich $MnCl_2$ solution (spin target). The NV spin is controlled by an RF microwave line and read-out optically using a confocal system. (b) Quantum control protocols to measure the decoherence of the NV spin in response to the local magnetic field fluctuations. (c) The decoherence contribution from internal spins (green), external spins (grey), and total effect (red) on NV coherence (T_2) time measured in spin-echo. Environmental spin baths can be detected by their effect on the NV coherence. (d) Magnetic sources local to the NV centre include diffusing Mn^{2+} spins (red), surface spins (blue) and internal nitrogen spins (green). (e) Physical and electronic energy structure of the NV centre in diamond.

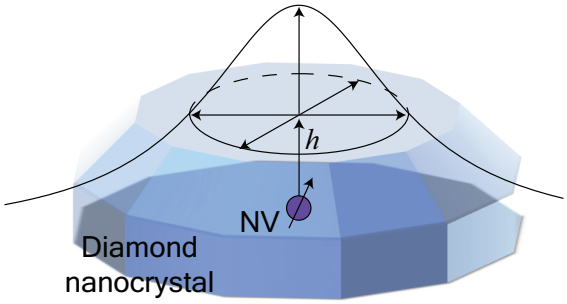

Figure 5.2: Schematic showing the attenuation of the effective NV-environment coupling strength as a function of lateral distance from the NV position with the NV a distance h below the diamond surface. .

5.2 Background

As in the previous chapter, we define the fluctuation regime of the various nanoscale magnetic environments to which the NV spin is exposed via the dimensionless parameter $\Theta = f_e/B$, where f_e is the characteristic fluctuation rate (defined by the inverse of the correlation time, $f_e = 1/T_c$), and $B = \sqrt{\langle \mathcal{B}^2 \rangle}$ is the RMS field strength of the effective magnetic field operator, $\mathcal{B}$. Rapid and slowly fluctuating fields are characterised by the conditions $\Theta \gg 1$ and $\Theta \ll 1$ respectively.

5.2.1 Determination of dynamic environmental parameters

In this section, we theoretically derive the natural timescales associated with the various physical processes taking place in this system and their effect on the dephasing rate of the NV spin. These theoretical predictions will be validated below via comparison with experimental results.

NV-Environment Interaction

We relate the effective environmental RMS magnetic field strength (in Hz, not Tesla) due to the presence of Mn spins in solution to the components of the corresponding axial magnetic field operator via,

$$B \equiv \sqrt{\langle \mathcal{B}_z^2 \rangle}, \tag{5.2.1}$$

where $\mathcal{B}_x$, $\mathcal{B}_y$ and $\mathcal{B}_z$ are defined by the total dipolar coupling of the effective environmental fields to the x, y and z components of the NV spin respectively. The magnetic field operators from an arbitrary Mn spin, $\vec{\mathcal{S}}_i$, are then

$$\mathcal{B}_x^i = \frac{\mu_0}{4\pi}\frac{\gamma_{\rm nv} g_E \mu_B}{R_i^3}\left[\mathcal{S}_{i,x} - \frac{3}{R_i}\sin(\Theta_i)\cos(\Phi_i)\left(\mathbf{R}_i \cdot \vec{\mathcal{S}}_i\right)\right], \tag{5.2.2}$$

$$\mathcal{B}_y^i = \frac{\mu_0}{4\pi}\frac{\gamma_{\rm nv} g_E \mu_B}{R_i^3}\left[\mathcal{S}_{i,y} - \frac{3}{R_i}\sin(\Theta_i)\sin(\Phi_i)\left(\mathbf{R}_i \cdot \vec{\mathcal{S}}_i\right)\right], \tag{5.2.3}$$

$$\mathcal{B}_z^i = \frac{\mu_0}{4\pi}\frac{\gamma_{\rm nv} g_E \mu_B}{R_i^3}\left[\mathcal{S}_{i,z} - \frac{3}{R_i}\cos(\Theta_i)\left(\mathbf{R}_i \cdot \vec{\mathcal{S}}_i\right)\right], \tag{5.2.4}$$

where $\mathbf{R}_i = R_i\big(\sin(\Theta_i)\cos(\Phi_i), \sin(\Theta_i)\sin(\Phi_i), \cos(\Theta_i)\big)$ denotes the separation vector between the NV and a given Mn spin. Squaring these operators and taking the trace over the spin degrees of freedom, the variance of the axial field is given by

$$\left\langle \mathcal{B}_{i,z}^2 \right\rangle = \frac{1}{3}S(S+1)A^2\frac{1+3\cos^2(\Theta_i)}{R_i^6}, \tag{5.2.5}$$

where $A = \frac{\mu_0}{4\pi}\gamma_{\rm nv} g_E \mu_B = \frac{\mu_0}{4\pi}\hbar\gamma^2$. Finally, the total variance is found by summing over all spins in the system for an NV located a distance h below the diamond surface. Because of the relatively small separation of environmental spins compared with R, we may treat the environmental spins as a continuum. Furthermore, given the relatively large size of the nanocrystals as compared with R, we regard the surface of the nanocrystal as being locally flat. This allows us to replace this sum with an

integral over x and y from $-\infty$ to ∞, and z from h to ∞, giving

$$\begin{aligned} \left\langle \mathcal{B}_z^2 \right\rangle &= \int n \left\langle \mathcal{B}_{i,z}^2 \right\rangle \mathrm{d}^3\mathbf{R} \\ &= S(S+1)A^2 \frac{n\pi}{6h^3}, \end{aligned} \tag{5.2.6}$$

which then implies an RMS field strength due to all Mn spins of

$$\begin{aligned} B_{\mathrm{Mn}} &= \frac{\mu_0}{4\pi}\hbar\gamma^2 \sqrt{S(S+1)\frac{n\pi}{3h^3}} \\ &= 317\,\mathrm{MHz\,nm^3} \times \left(\frac{n}{h^3}\right)^{1/2} \sqrt{S(S+1)} \\ &= 246\,\mathrm{MHz\,nm^{3/2}\,M^{-1/2}} \times \frac{c^{1/2}}{h^{3/2}} \sqrt{S(S+1)}, \end{aligned} \tag{5.2.7}$$

where c is the concentration in M, or mol/L, of a particular chemical species in the electrolyte.

We may use this result to determine both the effective number of aqueous spins, and the effective electrolytic volume to which the NV is sensitive. If we consider a single spin placed at directly above the NV at height h, its variance is

$$\left\langle \mathcal{B}_{0,z}^2 \right\rangle = \frac{4}{3} S(S+1) \frac{A^2}{h^6}. \tag{5.2.8}$$

The effective number of such spins due to the entire environment is then

$$\begin{aligned} N_{\mathrm{eff}} &= \left\langle \mathcal{B}_z^2 \right\rangle / \left\langle \mathcal{B}_{0,z}^2 \right\rangle \\ &= \frac{n\pi h^3}{8}, \end{aligned} \tag{5.2.9}$$

with corresponding effective volume

$$V_{\mathrm{eff}} = \frac{\pi h^3}{8}. \tag{5.2.10}$$

This quantity is a measure of the effective sensing volume of environmental spins to which the NV is exposed, which implies the effective spatial resolution of this sensing

protocol is $\Delta L \sim h$, which is ultimately limited by how closely an NV centre may reside to the diamond surface.

Environmental Dipole-Dipole Relaxation

The coupling between a pair of environmental spins is described by the following Hamiltonian

$$\mathcal{H}_{ij} = \frac{\mu_0}{4\pi\hbar}\frac{g^2\mu_B}{r^3}\left[\vec{\mathcal{S}}_i\cdot\vec{\mathcal{S}}_j - 3\frac{\left(\mathbf{r}\cdot\vec{\mathcal{S}}_i\right)\left(\mathbf{r}\cdot\vec{\mathcal{S}}_j\right)}{r^2}\right]. \tag{5.2.11}$$

The time evolution operator is given by

$$\mathcal{U}_{ij} = \exp\left(-i\mathcal{H}_{ij}t\right).$$

Using this, we find the autocorrelation function for the axial magnetisation using the corresponding Heisenberg picture operator to be,

$$\begin{aligned}\left\langle M_z(t)M_z(0)\right\rangle &= \frac{1}{\left\langle\mathcal{S}_j^2\right\rangle}\left\langle\mathcal{U}_{ij}(t)^\dagger\mathcal{S}_j\mathcal{U}_{ij}\mathcal{S}_j\right\rangle \\ &= \frac{1}{2}\left(\cos(2\theta)\sin^2\left(2\frac{S(S+1)bt}{r^3}\right)+\cos^2\left(2\frac{S(S+1)bt}{r^3}\right)\right),\end{aligned}$$

and averaging over θ, we obtain

$$\left\langle M_z(t)M_z(0)\right\rangle = \frac{1}{3}\left[2\cos\left(4S(S+1)\frac{bt}{r^3}\right)+1\right], \tag{5.2.12}$$

where $b = \frac{\mu_0}{4\pi\hbar}g^2\mu_B$. The probability distribution for the separation distance between a given spin and its nearest neighbour, r, is given by[2]

$$P(r) = 4\pi n r^2\exp\left(-\frac{4\pi n r^3}{3}\right). \tag{5.2.13}$$

[2]See chapter 12 for the derivation of this distribution.

Integrating the autocorrelation function over this distribution yields

$$\begin{aligned}
&\int_0^\infty 4\pi n r^2 \exp\left(-\frac{4\pi n r^3}{3}\right)\frac{1}{3}\left[2\cos\left(4S(S+1)\frac{bt}{r^3}\right)+1\right]\,\mathrm{d}r \\
&= \frac{1}{6}+\frac{1}{3}\int_0^\infty \exp(-v)\cos\left(\frac{\tau}{v}\right)\,\mathrm{d}v \\
&= \frac{1}{3}+\frac{2}{3}\mathfrak{G}^{3,0}_{0,4}\left(\frac{\tau^2}{16}\middle|\ 0,\tfrac{1}{2},1,\tfrac{1}{2}\ \right), \qquad (5.2.14)
\end{aligned}$$

where $v=\frac{4\pi n r^3}{3}$ and

$$4S(S+1)\frac{bt}{r^3}\frac{4\pi n r^3}{3} \equiv \frac{\tau}{v}, \qquad (5.2.15)$$

implying that

$$\tau = 4S(S+1)bt\frac{4\pi n}{3}; \qquad (5.2.16)$$

and $\mathfrak{G}$ is the Meijer-G function. Hence, for $\tau \ll 1$

$$\begin{aligned}
\left\langle M_z(t)M_z(0)\right\rangle &\approx \frac{1}{3}+\frac{2}{3}\left[1-\frac{\pi}{2}\tau+\mathcal{O}\left(\tau^2\right)\right] \\
&\approx \frac{1}{3}+\frac{2}{3}\left[1-2S(S+1)bt\frac{4\pi^2 n}{3}+\mathcal{O}\left((bnt)^2\right)\right]. \qquad (5.2.17)
\end{aligned}$$

Therefore the relaxation rate of the axial component of the magnetisation vector for a 2-spin pair due to their mutual dipolar coupling is given by

$$\begin{aligned}
f_{\mathrm{dip}} &= 2S(S+1)\frac{\mu_0}{4\pi}\hbar\gamma^2\frac{4\pi^2 n}{3} \\
&= 8.1\,\mathrm{GHz\,nm^3}\times n\times S(S+1) \\
&= 4.9\,\mathrm{GHz\,M^{-1}}\times c\times S(S+1), \qquad (5.2.18)
\end{aligned}$$

which we take for the dipole-dipole contribution to the total fluctuation rate, f_e.

We mention briefly that this analysis is only valid for the case where the dipolar interaction sets the quantisation axis for the environmental spins. As will be discussed in chapter 12, if their quantisation axis is set by their Zeeman interaction with

the background field, their axial magnetisation must be a constant of motion (ie, conserved). When this is true, the overall decay will not be exponential. Discussion of this behaviour is postponed until chapter 12, as it does not apply to the systems considered here.

Spatial Diffusion of Environmental Spins

At low concentrations the interactions between adjacent MN spins become less important, and fluctuation rates of the effective field as seen by the NV are instead determined the self diffusion of aqueous Mn spins. Consider a single Mn spin residing at an arbitrary position $\mathbf{x} = (x, y, z)$ at time t, where $x, y \in (-\infty, \infty)$ and $z > h$. At some time later, $t + \Delta t$, much greater than the collision time of fluid constituents, the Mn ion will have moved an RMS distance $r = \sqrt{D\Delta t}$, where D is the associated self diffusion coefficient. The magnetic field at time t is given by

$$\begin{aligned}
\mathcal{B}_x^i(t) &= \frac{\mu_0}{4\pi}\frac{\gamma_{\mathrm{nv}} g_G \mu_B}{\left(z^2 + x_0^2 + y_0^2\right)^{3/2}}\left[\mathcal{S}_x - 3\frac{x_0^2\mathcal{S}_x + x_0 y_0 \mathcal{S}_y + x_0 z \mathcal{S}_z}{z^2 + x_0^2 + y_0^2}\right], \\
&\equiv b_{xx}(t)\mathcal{S}_x + b_{xy}(t)\mathcal{S}_y + b_{xz}(t)\mathcal{S}_z, \qquad (5.2.19) \\
\mathcal{B}_y^i(t) &= \frac{\mu_0}{4\pi}\frac{\gamma_{\mathrm{nv}} g_G \mu_B}{\left(z^2 + x_0^2 + y_0^2\right)^{3/2}}\left[\mathcal{S}_y - 3\frac{x_0 y_0 \mathcal{S}_x + y_0^2\mathcal{S}_y + y_0 z \mathcal{S}_z}{z^2 + x_0^2 + y_0^2}\right], \\
&\equiv b_{yx}(t)\mathcal{S}_x + b_{yy}(t)\mathcal{S}_y + b_{yz}(t)\mathcal{S}_z, \qquad (5.2.20) \\
\mathcal{B}_z^i(t) &= \frac{\mu_0}{4\pi}\frac{\gamma_{\mathrm{nv}} g_G \mu_B}{\left(z^2 + x_0^2 + y_0^2\right)^{3/2}}\left[\mathcal{S}_y - 3\frac{x_0 z \mathcal{S}_x + y_0 z \mathcal{S}_y + z^2 \mathcal{S}_z}{z^2 + x_0^2 + y_0^2}\right], \\
&\equiv b_{zx}(t)\mathcal{S}_x + b_{zy}(t)\mathcal{S}_y + b_{zz}(t)\mathcal{S}_z. \qquad (5.2.21)
\end{aligned}$$

During the time interval Δt, the system evolves to $(x, y, z, t) \mapsto (x + \Delta x, y + \Delta y, z + \Delta z, t + \Delta t)$, where Δx, Δy and Δx are distributed according to a Brownian diffusion

process. At time $t + \Delta t$ the magnetic field operators become

$$\mathcal{B}_x^i(t+\Delta t) \equiv b_{xx}(t+\Delta t)\mathcal{S}_x + b_{xy}(t+\Delta t)\mathcal{S}_y + b_{xz}(t+\Delta t)\mathcal{S}_z, \quad (5.2.22)$$

$$\mathcal{B}_y^i(t+\Delta t) \equiv b_{yx}(t+\Delta t)\mathcal{S}_x + b_{yy}(t+\Delta t)\mathcal{S}_y + b_{yz}(t+\Delta t)\mathcal{S}_z, \quad (5.2.23)$$

$$\mathcal{B}_z^i(t+\Delta t) \equiv b_{zx}(t+\Delta t)\mathcal{S}_x + b_{zy}(t+\Delta t)\mathcal{S}_y + b_{zz}(t+\Delta t)\mathcal{S}_z. \quad (5.2.24)$$

Hence, the autocorrelation function of the axial field produced by a single diffusing Mn spin is given by

$$\left\langle \mathcal{B}_z^i(t)\mathcal{B}_z^i(t+\Delta t)\right\rangle = \frac{21}{4}\left[b_{zx}(t)b_{zx}(t+\Delta t) + b_{zy}(t)b_{zy}(t+\Delta t) + b_{zz}(t)b_{zz}(t+\Delta t)\right],$$

where we have used the fact that $\mathrm{Tr}\,(\mathcal{S}_i\mathcal{S}_j) = 0$ for $i \neq j$.

Expanding for Δx, Δy, $\Delta z \ll h$, we find, to second order in Δx, Δy and Δz

$$\begin{aligned}\langle \mathcal{B}_z(t)\mathcal{B}_z(t+\Delta t)\rangle &= \frac{21n\pi A^2}{16h^3} - \frac{189n\pi A^2}{256}\frac{\langle\Delta x^2\rangle + \langle\Delta y^2\rangle + \langle\Delta z^2\rangle}{h^5} \\ &= \frac{21n\pi A^2}{16h^3} - \frac{189n\pi A^2}{256}\frac{D\Delta t}{h_p^5} \\ &= \frac{21n\pi A^2}{16h^3}\left[1 - \frac{9}{16}\frac{D\Delta t}{h^2}\right]. \end{aligned} \quad (5.2.25)$$

To obtain the autocorrelation for long times, $T = N\Delta t$, we apply this geometric scaling N times,

$$\mathcal{B}_z(t)\mathcal{B}_z(t+N\Delta t) = \mathcal{B}_z(t)\mathcal{B}_z(t+T) = \frac{21n\pi A^2}{16h^3}\left[1 - \frac{9}{16}\frac{DT}{h^2}\frac{1}{N}\right]^N, \quad (5.2.26)$$

which for large N becomes

$$\langle \mathcal{B}_z(t)\mathcal{B}_z(t')\rangle = \frac{21n\pi}{16h^3}\left(\frac{\mu_0}{4\pi}\gamma_{\mathrm{nv}}g_G\mu_B\right)^2 \exp\left[-\frac{9}{16}\frac{D(t-t')}{h^2}\right]. \quad (5.2.27)$$

The fluctuation rate of the effective field due to translational diffusion is then

$$f_{\mathrm{diff}} = D\left(\frac{3}{4h}\right)^2. \quad (5.2.28)$$

Taking the diffusion coefficient to be bounded above by that of water at 298 K ($D_{\mathrm{H_2O}} = 3 \times 10^{-9}\,\mathrm{m^2 s^{-1}}$), and $h = 5\,\mathrm{nm}$, we find $f_{\mathrm{diff}} = 68\,\mathrm{MHz}$.

Rotational Diffusion of Environmental Spins

The relaxation rate due to molecular rotation is equal to the rotational diffusion rate as given by Stokes' law,

$$f_{\mathrm{rot}} = \frac{k_B T}{8\pi d^3 \eta} \sim 10\,\mathrm{kHz}, \tag{5.2.29}$$

for *freely* diffusing nanodiamonds of d=45 nm diameter in water at 300 K. The actual relaxation rate is expected to be lower, as such massive crystals would be most likely confined to regions near the sample boundary, rather than freely diffusing. We thus neglect the effects of rotational diffusion in what follows.

Motional Narrowing of the Dipole-Dipole fluctuation rate

Because of the diffusive motion of spins in the electrolyte, the effective fluctuation rate due to dipolar flip-flops may, in some cases, be reduced significantly. This is because any two spins may not interact long enough for a magnetisation exchange to occur with an appreciable probability. We may use a semi-classical argument to estimate this revised relaxation timescale.

Whilst two spins are in contact (ie, they exist temporarily as a nearest-neighbour pair before the diffusion process redistributes them), we assume they are sufficiently close that no terms from the full dipolar interaction may be ignored. If the spins are in contact for a time δt, the rate of rotation of the polar angle of one of the spin vectors may be taken straight from equation 5.2.17, and the total polar angle rotation during this time will be

$$\delta\theta \;=\; 4S(S+1)\frac{b}{\langle r\rangle^3}\delta t, \tag{5.2.30}$$

where $\langle r \rangle$ is the average separation of spins in the electrolyte, and is found from equation 5.2.13 to be $\langle r \rangle \approx \frac{1}{2} n^{-1/3}$. Over a long period of time, $t \gg \delta t$, these angular shifts will accumulate in a fashion reminiscent of a random walk. Hence, by the central limit theorem, the total accumulated angular shift will be normally distributed with variance of $N = t/\delta t$ times the variance of a single shift, that is

$$\begin{aligned} \Delta\theta^2 &= \frac{t}{\delta t} (\delta\theta)^2 \\ &= t\,\delta t \left[4S(S+1) \frac{b}{\langle r \rangle^3} \right]^2 . \end{aligned} \tag{5.2.31}$$

Using the above analysis of diffusive motion, the effective dwell time over which the interaction takes place is

$$\delta t = \frac{1}{D_{\mathrm{Mn}}} \left(\frac{4 \langle r \rangle}{3} \right)^2 . \tag{5.2.32}$$

Hence, the motionally narrowed relaxation rate is then

$$\begin{aligned} f_{\mathrm{narr}} &= \frac{1}{2} \frac{\delta\theta^2}{\delta t} \\ &= \frac{1}{5} \frac{\Gamma_{\mathrm{dip}}^2}{n^{2/3} D} . \end{aligned} \tag{5.2.33}$$

This analysis, of course, hinges on the assumption that the 'hopping rate', $R_{\mathrm{hop}} = 1/\delta t$, is much faster than the dipolar flipping rate, Γ_{dip}, otherwise the fluctuation can be attributed to dipolar flip-flops alone. The crossover point at which motional narrowing becomes important occurs when $1/\delta t \sim \Gamma_{\mathrm{dip}}$, or when

$$\begin{aligned} D \left(\frac{3}{4 \langle r \rangle} \right)^2 &= 2S(S+1) \frac{\mu_0}{4\pi} \hbar \gamma^2 \frac{4\pi^2 n}{3} \\ \Rightarrow \quad n &= \left[\frac{D}{S(S+1)} \frac{3}{32} \left(\frac{\mu_0}{4\pi} \hbar \gamma^2 \right)^{-1} \right]^3 . \end{aligned} \tag{5.2.34}$$

For the specific case of $MnCl_2$, we have $S = 5/2$. To estimate the diffusion coefficient of manganese, we note that atomic manganese has a mass 55/18 times that of water.

Given that the number density of water molecules is roughly 3 orders of magnitude greater than that of Mn, most collisions involving an Mn atom will be with a water molecule, thus each molecular collision will result in a Mn atom changing its velocity by a factor 18/55 less than that of the corresponding water molecule. Thus if the expected translational variance of a water molecule during time interval t is $\left\langle r^2_{\mathrm{H_2O}}\right\rangle = D_{\mathrm{H_2O}}t$, that of the Mn atom will be $\langle r^2_{\mathrm{Mn}}\rangle = (18/55)^2\left\langle r^2_{\mathrm{H_2O}}\right\rangle = (18/55)^2 D_{\mathrm{H_2O}}t$. Thus the effective diffusion constant for Mn is $D_{\mathrm{Mn}} = (18/55)^2 D_{\mathrm{H_2O}} \approx 0.3\,\mathrm{nm^2\,ns^{-1}}$ at 300 K. Thus, the density at which motional narrowing becomes important is

$$n_c \approx 1\,\mu\mathrm{M}, \tag{5.2.35}$$

which is well below the regimes considered in this work. This result is essentially due to the fact that both dipolar relaxation and effective hopping rates increase with the aqueous spin concentration (see figure 5.3), albeit with a differing power-law dependence. Motionally narrowed behaviour is regularly observed in the realm of NMR, as can be appreciated from examination of equation 5.2.34. Noting that the nuclear magneton is a factor of 2000 less than that of an electron, motionally narrowed behaviour will occur for all practically realisable nuclear spin densities in aqueous solutions.

Combined dynamics

The total autocorrelation function is the product of the functions associated with spin-spin, self diffusion and, by extension, rotational dynamics,

$$\langle \mathcal{B}(t)\mathcal{B}(t')\rangle = \left\langle \mathcal{B}^2\right\rangle \exp\left(-f_{\mathrm{Mn}}\,|t-t'|\right)\cos\left(\omega_0 t\right), \tag{5.2.36}$$

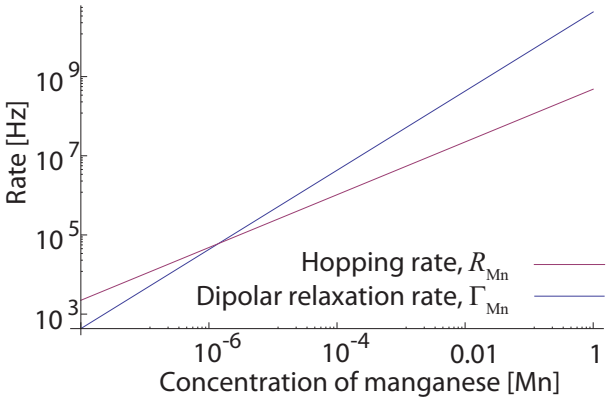

Figure 5.3: Graph showing the dependence of the diffusional hopping rate, R_{Mn}, and the dipolar relaxation rate, R_{Mn}, on the concentration of manganese spins in an electrolytic solution. At sub-μM concentrations the hopping rate dominates, resulting in the dipolar relaxation rate being reduced via motional narrowing. At higher concentrations, spins are in contact long enough for dipole mediated flip-flops to occur and thus exhibit behaviour essentially identical to that of a frozen lattice of spins.

with a total decay rate given by the sum of the respective decay rates, $f_{\mathrm{Mn}} = f_{\mathrm{dip}} + f_{\mathrm{diff}} + f_{\mathrm{rot}}$. The corresponding normalised spectral density is then given by

$$S(\omega) = \sqrt{\frac{2}{\pi}} \frac{f_{\mathrm{dip}} + f_{\mathrm{diff}} + f_{\mathrm{rot}}}{(\omega - \omega_0)^2 + (f_{\mathrm{dip}} + f_{\mathrm{diff}} + f_{\mathrm{rot}})^2}, \tag{5.2.37}$$

and is centred about the Larmor frequency of the Gd spins, ω_0.

5.2.2 Decoherence of NV spins due to both intrinsic sources and external Mn spins.

The decoherence of the NV spin is due to its interaction with the numerous spin baths present. In what follows, we discuss the separate contributions from the graphitic surface layer, electron spins from nitrogen donor impurities, and the external spins from the aqueous spin bath.

The field produced by spins on the nanocrystal surface fluctuate rapidly due to

their extremely fast relaxation rate, and therefore present an environment in the rapid fluctuation regime in which $\Theta \gg 1$, or $f_s \gg B_s$. As such, their decoherence rate is given by $\Gamma_s = \frac{1}{2}B_s^2/f_s$ (See chapter 4), which provides an exponential damping to the overall decoherence envelope of

$$L_s(t) \;=\; \exp\left(-\frac{B_s^2}{2f_s}\right). \tag{5.2.38}$$

The Nitrogen donor spins are somewhat more difficult to describe, owing to their existence in a $\Theta \sim 1$ regime, however we do know from equation 4.2.2 that at short times, their decoherence behaviour follows an $L(t)_N \sim \exp\left[-\left(\Gamma_N^{\text{short}}t\right)^4\right]$ dependence, whereas at long times, we have $L(t)_N \sim \exp\left(-\Gamma_N^{\text{long}}t\right)$. As such, we employ a hybrid function that provides an asymptotic match to these two regimes,

$$L_N(t) \;\equiv\; \exp\left[-\frac{1}{\left(\Gamma_N^{\text{short}}t\right)^{-4} + \left(\Gamma_N^{\text{long}}t\right)^{-1}}\right], \tag{5.2.39}$$

where $\Gamma_N^{\text{short}} = f_N/\sqrt{2\sqrt{2}\Theta_N}$, and $\Gamma_N^{\text{long}} = B_N^2/2f_N$, as defined in the previous chapter. The complete decoherence envelope is then a product of expressions 5.2.38 and 5.2.39. Theoretically calculated spin-echo profiles are shown in figure 5.4(c) for different NV depths below the crystal surface. When the NV is close to the diamond surface, it is heavily exposed to the rapidly fluctuating field from the surface spins, meaning the spin-echo profile will exhibit a predominantly exponential decay. On the other hand, when the NV resides deep below the crystal surface, the surface spins will have less of an effect and will modulate the N-dominated curve only slightly.

Introduction of the $MnCl_2$ solution provides an additional channel by which the NV spin may decohere. By virtue of the fast internal dynamics of the Mn bath and the large NV-Mn standoff as compared with the average Mn-Mn separation distance,

this process also exists in the $\Theta \gg 1$ regime, and like the surface spins, will introduce an additional damping of the decoherence envelope, as given by

$$L_{\mathrm{Mn}}(t) \;=\; \exp\left(-\frac{B_{\mathrm{Mn}}^2}{2f_{\mathrm{Mn}}}\right). \tag{5.2.40}$$

There is some evidence to suggest that this is in fact a relaxation effect, rather than the result of dephasing processes we have considered so far, however the resulting expression (equation 5.2.40) is independent of this distinction, as relaxation processes must also necessarily result in simultaneous dephasing (one way to decrease the lateral projection of the Bloch vector is to rotate out of the lateral plane). We defer discussion of relaxation process and their effects until chapter 10.

Combining these results, we have that the full envelope in the presence of the Mn target spins is given by

$$L(t) \;\equiv\; \exp\left[-\Gamma_{\mathrm{ext}} - \frac{1}{\left(\Gamma_N^{\mathrm{short}}t\right)^{-4} + \left(\Gamma_N^{\mathrm{long}}t\right)^{-1}}\right], \tag{5.2.41}$$

where $\Gamma_{\mathrm{ext}} = \Gamma_{\mathrm{s}} + \Gamma_{\mathrm{Mn}}$.

5.3 Results and discussion

The Rabi and spin-echo traces for NV centres 1-4 are shown in figure 5.5, with immersion in air, water and $MnCl_2$ being depicted by blue, green and red curves respectively. Very little change occurs upon immersion in water, due to the size of the nano diamond size, and that hydrogen nuclear spins have a magnetic moment roughly 2000 times smaller than that of the Mn electron spins. Despite this, a small change in the decoherence envelope is both expected and observed, but is not statistically significant within the bounds of experimental errors. The associated decoherence rates are

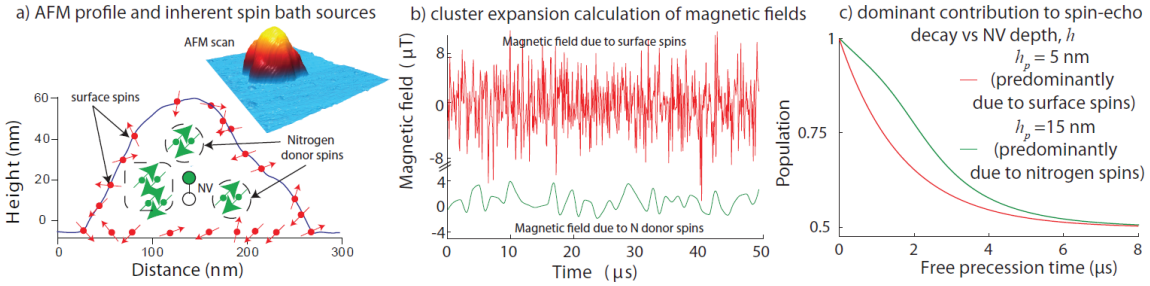

Figure 5.4: Topology of nanodiamond sensors, inherent spin baths, and their effect on the NV spin coherence. (a) Atomic Force Microscope (AFM) profile (blue curve and insert) of an agglomeration resulting from spin-coating nanodiamond (45 nm median diameter) onto a glass substrate. Overlaid with the AFM data is a schematic depicting the intrinsic crystal spin-baths comprising strongly interacting clusters of internal nitrogen (green) and surface spins (red). (b) Simulation of the resulting typical magnetic fields felt by an NV centre (depth $h = 5$ nm in this case) due to the various intrinsic spin-bath sources. Surface spins are distributed with a much greater density than the internal spins, and the fluctuation frequency of the surface spins is much faster than the nitrogen spin bath. In these simulations we have assumed a mean fluctuation rate of 100 MHz and a spin density of 1 nm^{-2} for the surface spins. (c) NV spin-echo envelopes corresponding to NV depths of 5 nm and 15 nm below the nanocrystal surface. NV centres closer to the surface have a shorter coherence time, due to proximity to surface spin bath.

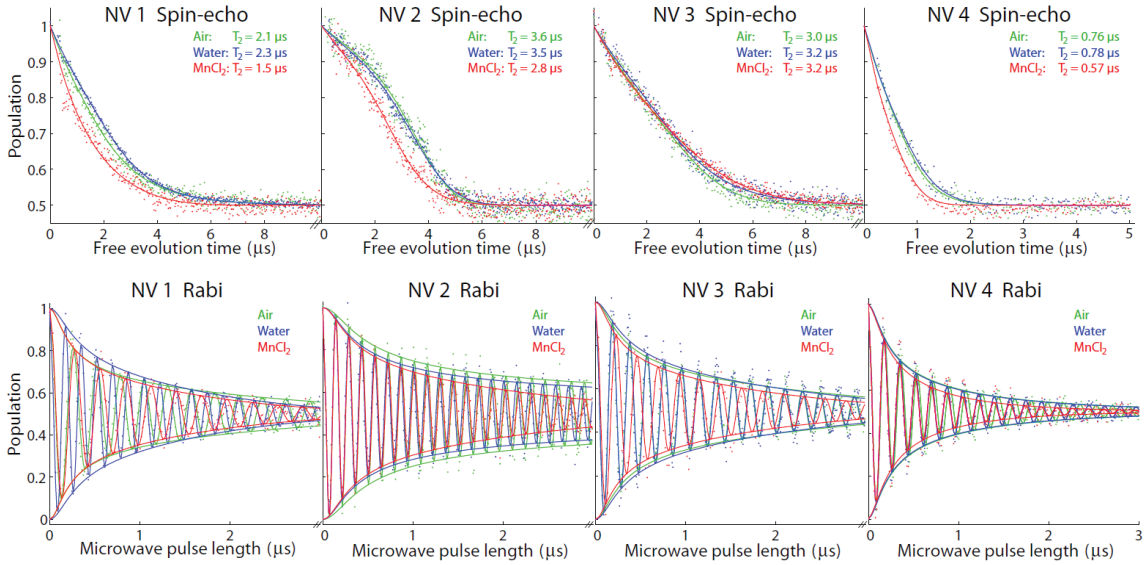

Figure 5.5: Decoherence properties of NV centres under various immersion conditions and exposure to Mn2+ spins in solution. Top row: Measured spin-echo decoherence profiles for four NV centres, performed on nanocrystals in air (green), deionised water (blue), and 1MMnCl2 (red). Fits to the data-points (shown as the solid lines) allow the decoherence rates under the various immersion conditions to be determined. Bottom row: Rabi measurements corresponding to the spin-echo data for each NV.

given in table 5.1.

5.3.1 Analysis of the initial surface spin bath

Using the results above, me may characterise the physical processes occurring on the nanodiamond surface giving rise to the decoherence of the NV spin, and use this to draw conclusions regarding their physical origin. By integrating over the surface spin density, we find the RMS field strength to be

$$B_s \quad = \quad 48.8\,\mathrm{MHz\,nm^3} \times \frac{\sigma^{1/2}}{h^2}, \tag{5.3.1}$$

	Γ_{Ext}[Air]	Γ_{Ext}[H_2O]	Γ_{Ext}[$MnCl_2$]	Γ_{Ext}[HCl]	Evaporated
NV1	410 (60)	350 (15)	660 (20)	470 (20)	-
NV2	120 (20)	140 (10)	200 (40)	90 (30)	-
NV3	270 (20)	240 (30)	280 (10)	-	-
NV4	1,140 (100)	1,130 (70)	1,600 (70)	-	-
NV5	136 (100)	-	160	-	260

Table 5.1: Decoherence rates, Γ_{ext} (kHz), due to environmental sources both on and outside the nanodiamond surface. Values are extracted from fits to the data in figures 5.5 and 5.6. Fitting uncertainties in parentheses at the 95% confidence level.

where σ is the effective surface spin density and h is the depth of the NV below the surface. We may combine this with equation 5.2.38 to compare the relative depths of each NV below the surface via $\Gamma_s^{(i)}/\Gamma_s^{(j)} = (h_j/h_i)^4$. As the NV depths are large compared with the average separation of spins on the surface, we may assume that each of the nanocrystal surface fields exhibit equivalent surface densities and fluctuation rates.

Despite not knowing the exact mechanism responsible for the relaxation of the surface spins, we may use these measurements to provide insight into its physical origin, thereby ruling out certain processes. If we consider a magnetic dipole-dipole mediated relaxation mechanism, we find the surface relaxation rate to have a dependence on the surface spin density of $f_s = 5.56\,\text{GHz}\,\text{nm}^3 \times \sigma^{3/2}$. Combining this expression with equation 5.2.38 together with the $\Theta \gg 1 \Rightarrow f_s \gg B_s$ condition, we find the following *upper limit* for the NV depth as a function of the surface contribution to the decoherence rate,

$$h \ll \left(\frac{2.28\,\text{MHz}}{\Gamma_s}\right)^{1/3}. \tag{5.3.2}$$

From this expression, we see that under the assumption of dipole-dipole mediated surface spin relaxation, even a decoherence rate as small as 100 kHz would imply

an NV depth much less than 2 nm. As these NV depths are well below those at which either the NV vacancy or electron will leave the centre and migrate to the surface [BGN+10], we have ruled out the possibility of surface spin relaxation being caused by this mechanism. Rather, we suggest that the more likely cause of surface spin relaxation is the spin-orbit coupling of dangling electron spins of sp^2 hybridised carbon layers at the nanocrystal surface, which causes surface spins to relax at rates of 0.1 to 10 GHz at 300 K [PS11], and is independent of the surface spin density.

5.3.2 Analysis of $MnCl_2$ spin bath

As a means by which to probe the response of the NV spin to a controllable external spin bath, nanodiamonds were immersed in a 1 M $MnCl_2$ aqueous solution dissolved in 1 M HCl to prevent oxidation of the Mn^{2+} ions. A noticeable increase in the decoherence rate, together with a transition to a more exponentially shaped decoherence envelope was exhibited by NVs 1,2 and 4. This change in shape is indicative of a rapidly fluctuating environmental regime, as expected from the analysis in the previous section.

Very different behaviour is exhibited by NV3. The predominantly exponential shape of NV3's envelope in both air and water suggests that its environment is dominated by a rapidly fluctuating field, implying NV3 resides very close to the nanodiamond surface, as compared with, say, NV2. Very little change is apparent with the addition of the $MnCl_2$ solution however, which suggests that the proximate surface is not exposed to the solution. As such, we conclude that NV3 must reside close to a surface (see figure 5.4(a)) that has adhered to the glass substrate, rather than a surface exposed to the solution.

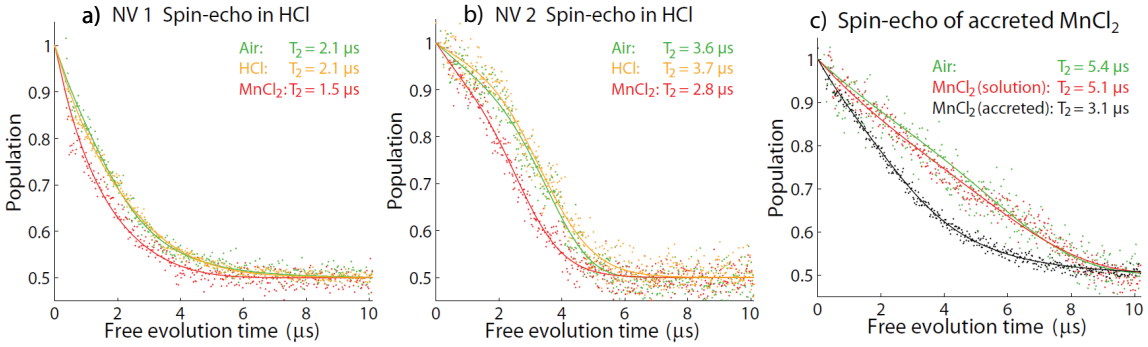

Figure 5.6: (a) & (b) Restoration of NV quantum coherence after washing in spin-free acid. Measured spin-echo decoherence profiles for NV1 and 2, performed in air (green), 1M $MnCl_2$ (red), 1M HCl (orange). Fits to the data-points using Eq. (2) are shown as the solid lines. The same spin-echo profiles in air and HCl confirm Mn spins are responsible for the observed changes in decoherence. (c) Measurements on NV5 showing detection of Mn^{2+} spin accretion on the nanodiamond surface. Rabi and spin-echo measurements in air (green), 1 M $MnCl_2$ solution (red), accreted $MnCl_2$ (black).

Following the immersion, NV1 and NV2 were subsequently immersed in an equivalent 1 M HCl solution to remove any residual Mn spins. As shown in Figures 5.6 (a)&(b), this results in the restoration of the original decoherence properties observed prior to immersion. This constitutes a control experiment, and confirms that changes in decoherence observed upon immersion are solely attributable to the presence of the Mn bath, rather than to changes in pH levels or surface charge transfer in the presence of an acid.

As discussed in the theoretical anlysis above, both free-diffusion and dipole-dipole mediated relaxation amongst Mn spins are possible mechanisms for the fluctuating Mn field experience by the NV. Which mechanism dominates depends on the depth of the NV below the nanodiamond surface, a quantity that was not able to be measured

during this experiment. Shallow centres essentially experience a more rapidly fluctuating field, as each Mn atom takes less time to traverse the smaller area of sensitivity (recall $f_{\text{diff}} = D\,(3/4h)^2$ from the analysis of spatial diffusion above). Dipolar relaxation on the other hand is independent of height. To find the NV depth at which an NV would experience the crossover between these two regimes, consider $f_{\text{diff}} = f_{\text{dip}}$, which occurs at

$$h \;=\; \frac{3}{4}\sqrt{\frac{D_{\text{Mn}}}{43\,\text{GHz}}}, \tag{5.3.3}$$

for a 1 M solution of $MnCl_2$. Again taking the diffusion coefficient of Mn^{2+} to be $D_{\text{Mn}} \approx 0.3\,\text{nm}^2\,\text{ns}^{-1}$ at 300 K, and substituting this result into equation 5.3.3, we find the crossover height to be at $h \sim 0.1\,\text{nm}$. Thus we conclude that, for all sensible standoff heights, the dominant physical mechanism responsible for the Mn field fluctuations is dipolar-dipole induced relaxation.

We may use this result to interrogate the effective standoff height between the NV centre and the surface exposed to the electrolyte. By combining expressions 5.2.7, 5.2.18 & 5.2.40, we find the contribution to the decoherence rate from the Mn bath to be

$$\begin{aligned}\Gamma_{\text{Mn}} &= \frac{1}{h^3}\left(246\,\text{MHz}\,\text{nm}^{3/2}\right)^2 \Big/ \, 2\times 4.9\,\text{GHz} \\ &= 3.95\,\text{MHz}\,\text{nm}^3 \times \frac{1}{h^3}.\end{aligned} \tag{5.3.4}$$

To experimentally determine the contribution from the Mn bath to the decoherence, we subtract the external decoherence rate measured in HCl from the external decoherence rate measured in the $MnCl_2$ solution. For NV1, we have

$$\Gamma^{(1)}_{\text{Mn}} = \Gamma_{\text{Ext}}[MnCl_2] - \Gamma_{\text{Ext}}[HCl] = 190\,\text{kHz}, \tag{5.3.5}$$

implying an NV depth of $h^{(1)} = 2.8\,\text{nm}$, with a 95% confidence interval of (2.6 nm - 3.0 nm). Similarly, for NV2, we have

$$\Gamma_{\text{Mn}}^{(2)} = 110\,\text{kHz}, \tag{5.3.6}$$

implying an NV depth of $h^{(2)} = 3.3\,\text{nm}$, with a 95% confidence interval of (2.8 nm - 4.6 nm). These depths are consistent with previous decoherence measurements made on nanocrystals of 10 nm [TBN^+] and 5 nm [BGN^+10] in diameter. Upon determining the depths of NV1 and NV2, together with equation 5.2.9, we find the effective number of detected spins to be approximately 5 and 8 respectively.

To determine the sensitivity of this technique, recall that to measure an arbitrary signal change, ΔS, we require that the signal change is greater than the shot-noise resulting from some N_s measurements, that is

$$\Delta S \;>\; \frac{1}{C\sqrt{N_s}}, \tag{5.3.7}$$

where C is the effective contrast as defined in the previous chapter, and N_s is the number of repeated measurements performed at a given timepoint in the signal, t_s, which may be related to the total measurement time, T, via $T = N_s t_s$. The signal change is the result of the additional decoherence induced by the presence of the Mn bath, thus $\Delta S = \Gamma_{\text{Mn}} t_s$. The sensitivity with which an external decoherence rate may be measured is then

$$\eta \;\equiv\; \Gamma_{\text{Mn}}\sqrt{T} = \frac{1}{C\sqrt{t_s}}, \tag{5.3.8}$$

which appears to suggest that the sensitivity may be improved indefinitely by unboundedly increasing the free-precession interval before the point of measurement, however this is ultimately limited by the intrinsic coherence time of the system, and

going beyond this will drastically reduce the contrast associated with the shot noise. We therefore take $t_s = T_2$, where in this case T_2 represents the intrinsic coherence time of the NV centre as unperturbed by the presence of an external decoherence source.

The temporal resolution of the sensor, or minimum total time required to detect a decoherence source via its induced decoherence rate, Γ, is then readily obtained from

$$\Delta T = \frac{1}{T_2 \left(C\Gamma\right)^2}. \tag{5.3.9}$$

Using a conservative value of $C = 0.05$ [TCC+08], the time taken to detect the 5 spins of NV1 is 4 ms. Similarly, the 8 spins detected by NV2 required 9 ms for detection, due to its deeper position below the surface.

As a final experiment, the $MnCl_2$ solution surrounding a fifth NV centre (NV5) was left to evaporate, leaving behind an adsorbed layer of Mn spins on the nanodiamond surface. Spin echo measurements were then repeated, and the decoherence rate due to external sources was observed to have increased from 135 kHz in air to 160 kHz in $MnCl_2$, to a final rate of 260 kHz upon evaporation (see table 5.1 and figure 5.6 (c)). These observations show that decoherence sensing techniques could be used monitor the changes in surface spin densities of during various chemicals reactions, and help gain an understanding of the way nano-surfaces are functionalised and controlled.

5.4 Summary and Conclusion

This combined experimental and theoretical study has demonstrated the effectiveness of decoherence based sensing in studying the effects of external nanoscale magnetic environments on a central quantum system. These techniques have allowed

us to probe the physical origins of the dynamic magnetic processes taking place in nanoscale quantum environments at ambient conditions, revealing both quantitative and qualitative information that would not be accessible with traditional magnetometry techniques, even at cryogenic temperatures. Furthermore, the sub-10 nm spatial resolution reported here represents an improvement of more than 4 orders of magnitude over what is currently available with state of the art magnetic resonance based detection.

Using these techniques, we have characterised the decoherence resulting from a number of magnetic systems proximate to individual NV centres, and used this information to answer a number of critical questions, including the physical origins of fluctuating magnetic phenomena on the nanodiamond surface, and the depths at which a given NV centre resides below the surface. Given the high sensitivity, spatial resolution, robustness and broad applicability of these techniques, decoherence based sensing represent an exciting new methodology for investigating magnetic based phenomena in physical, chemical and biological environments.

Chapter 6

Ultra-sensitive diamond magnetometry using optimal dynamic decoupling

The sensitivity of a single NV magnetometer is primarily determined by the transverse spin relaxation time, T_2. Current approaches to improving the sensitivity employ crystals with a high NV density at the cost of spatial resolution, or extend T_2 via the manufacture of isotopically pure diamond crystals. In this chapter, we adopt a complementary approach, in which optimal dynamic decoupling techniques are used to extend NV coherence times, allowing for a greater phase acquisition. The effectiveness of this approach is verified via an experimental demonstration[1]. Our analysis suggests single spin, room temperature magnetometer sensitivities as low as $5\,\mathrm{pT\,Hz^{-1/2}}$ may be possible with current technology. The theoretical developments of this chapter have since been published in [HHCH10], and the experimental demonstration and corresponding analysis were published in [NDH$^+$11].

[1]All experiments described in this chapter were performed by B. Naydenov and F. Dolde at the University of Stuttgart.

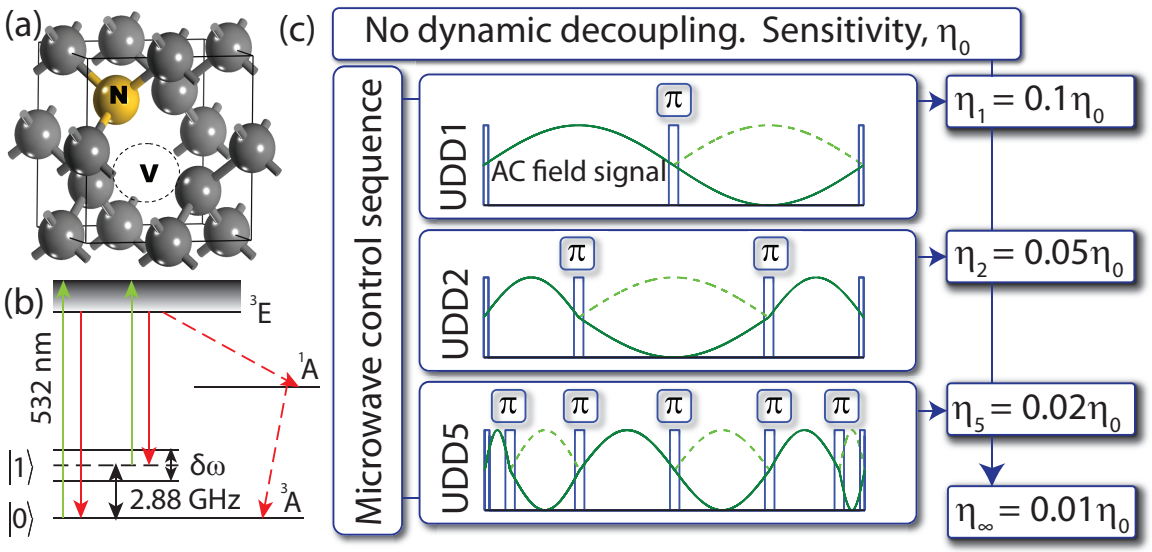

Figure 6.1: (a) NV-centre diamond lattice defect. (b) NV spin detection through optical excitation and emission cycle. Magnetic sublevels $|0\rangle$ and $|\pm 1\rangle$ are split by a D=2.88 GHz crystal field. Degeneracy between the $|\pm 1\rangle$ sublevels is lifted by a Zeeman shift, $\delta\omega$. Application of 532 nm green light induces a spin-dependent photoluminescence and pumping into the $|0\rangle$ ground state. (c) Examples of controlled-AC fields (solid) as seen by the NV centre (dashed) in the presence of the 1st, 2nd and 5th UDD sequence. Negative regions of the AC trace are mapped to positive, ensuring maximal phase accumulation of the NV spin. Slow FC fields, such as the surrounding nuclear spin bath, will be suppressed, permitting the detection of AC and fast FC fields with greater sensitivity.

6.1 Introduction

It is well known that coherence times may be improved with the use of Carr-Purcell-Meiboom-Gill (CPMG), concatenated (CDD)[KL07a], random and periodic dynamic decoupling schemes [WD07, KL07b]. The more recent Uhrig (UDD) scheme was shown to be optimal for decoupling a spin qubit from a bosonic bath [Uhr07], and has since been shown to be optimal for all systems in which dephasing is the dominant decoherence channel [UL10]. This optimality stems from the required UDD resources

scaling linearly with the order to which the environmental effects are suppressed. However, UDD is unable to suppress longitudinal relaxation, whereas CDD can. The use of UDD is ideally suited to the NV centre owing to long relaxation times ($T_1 > 1\,\mathrm{s}$ [BNT$^+$09]), even at room temperature. The large Debye temperature allows for negligible decoherence via phonon excitation of the crystal lattice, and a large zero field splitting (2.88 GHz) of the ground state magnetic sublevels prevents longitudinal spin-spin relaxation. Hence longitudinal relaxation may be neglected, ensuring UDD is the optimal decoupling method.

Both AC and FC magnetometry schemes are based upon a spin-echo microwave control sequence, in which a π pulse is used to flip the qubit at the half way point of its evolution (figure. 6.1(c)), suppressing any quasi-static effects of the spin bath. The AC scheme is concerned with detection of fields of the form $b_{\mathrm{ac}}\sin(\nu t)$, where the π pulse coincides with $t = \pi/\nu$, ensuring a non-zero integral of the field trace, and hence maximal phase shift of the NV spin. In this chapter, we incorporate UDD into AC and FC magnetometry schemes and show that the sensitivity of a single NV centre magnetometer may be as low as 5 $\mathrm{pT\,Hz^{-1/2}}$ with the use of existing technology. Furthermore, we show that UDD yields superior results to CPMG, a theoretical analysis of which is given in [TCC$^+$08].

In chapter 4 it was shown that a particularly intuitive analysis of a spin qubit placed in a slowly fluctuating classical magnetic field could be performed by expanding the effective time dependent field as a Taylor series [HCHH09]. Whilst this may seem like a special case, this technique applies to a more general class of pure-dephasing quantum problems in which longitudinal relaxation may be ignored. We investigate the effect of UDD on a spin qubit placed in such a field, and show that it is the n^{th}

UDD sequence that suppresses the effect of all terms up to and including order n in the Taylor expansion of the field. These results are applied to the NV centre and used to obtain improved sensitivities for NV based magnetometry.

An NV centre interacting with an external magnetic field is described by the Hamiltonian $\mathcal{H} = \mathcal{H}_{\text{zfs}} + \mathcal{H}_{\text{ext}} + \mathcal{H}_{\text{int}}$. The first term describes the zero field splitting of the ground state Zeeman levels, $\mathcal{H}_{\text{zfs}} = \hbar D \mathcal{S}_z^2$, where $D = 2.88\,\text{GHz}$. The interaction with an external magnetic field $\mathbf{B}_{\text{ext}}(t)$ is described by $\mathcal{H}_{\text{ext}}$. The fields we consider here are small relative to D and are hence unable to induce a spin-flip, permitting us to ignore all $\mathcal{S}_{x,y}$ terms, giving $\mathcal{H}_{\text{ext}} \approx \gamma B_{\text{ext}}^{(z)} \mathcal{S}_z$, where γ is the NV gyromagnetic ratio. For simplicity, we put $B_{\text{ext}}^{(z)} \equiv B_{\text{ext}}$. The final term describes the interaction with the paramagnetic environment of the diamond crystal. As we will see, for resolving the non-unitary dynamics of the reduced density matrix of the NV centre, these interactions may be subsumed into a single 'internal magnetic field,' $B_{\text{int}}(t)$. We define the fluctuation regime of the external/internal environment via the dimensionless numbers, $\Theta_{\text{ext}} = (\gamma \sigma_0^{\text{ext}} \tau_{\text{ext}})^{-1}$ and $\Theta_{\text{int}} = (\gamma \sigma_0^{\text{int}} \tau_{\text{int}})^{-1}$, where $\sigma_0^{\text{ext}}/\sigma_0^{\text{int}}$ are the RMS field strengths, and $\tau_{\text{ext}}/\tau_{\text{int}}$ are the correlation times of the internal and external environments respectively. Rapidly and slowly fluctuating fields satisfy $\Theta \gg 1$ and $\Theta \ll 1$ respectively.

6.2 Dephasing in the presence of dynamic decoupling

In this section, we make a quantitative comparison of two commonly used dynamic decoupling sequences, namely Uhrig Dynamic Decoupling (UDD) and the CPMG

pulse sequence.

6.2.1 Uhrig Dynamic Decoupling (UDD)

An arbitrary time-dependent magnetic field may be decomposed as a Taylor series in t: $B(t) = \sum_{k=0}^{\infty} a_k t^k$ (See chapter 4). The validity of this expansion rests upon the condition that $a_{k+1}t^{k+1} < a_k t^k$ for all k. This is satisfied for $t < \tau_{\rm int}/\sqrt{2}$. For times $t \gg \tau_{\rm int}$ the qubit will exhibit motional-narrowing behaviour. In many cases of practical interest, $B_{\rm int}$ is the sum of fields from a large number of dipoles. This implies, by the central limit theorem, that the $\{a_j\}$ are normally distributed, with zero mean at room temperature and variance $\sigma_j^2 = \langle a_j^2 \rangle$. This leads to the following dephasing envelope,

$$L(t) \;=\; \prod_{j=0}^{\infty} \exp\left[-\left(\Gamma_j t\right)^{2j+2} \right],$$

where

$$\Gamma_j \;=\; \left(\frac{1}{\sqrt{2}} \frac{\gamma \sigma_j}{j+1} \right)^{1/(j+1)}. \tag{6.2.1}$$

Since $\Gamma_0 \gg \Gamma_k \,\forall\, k \geq 1$, Γ_0 serves to define the free induction decay time, $T_2^* = 1/\Gamma_0$. For a 1.1% ^{13}C bath, the variance of the magnetic field is given by $\sigma_0^2 = \sum_i \langle B_i^2 \rangle$. For a ^{13}C density n_c and gyromagnetic ratio γ_c, $\sigma_0 \approx \sqrt{\frac{2\pi}{3}} \frac{\mu_0}{4\pi} n_{\rm c} \hbar \gamma_{\rm c} \approx 2\,\mu$T, and $T_2^* \approx 4\,\mu$s, in good agreement with [TCC$^+$08, MNR$^+$09]. Similarly, using an 0.3% ^{13}C bath yields $T_2^* \approx 15\,\mu$s, in agreement with [BNT$^+$09].

The Hahn-echo sequence removes the effect of a static field on the system as each π pulse effectively sends $B \to -B$. For a field described by $\sum_k a_k t^k$, this will remove the effect of the a_0 term, and modify all other terms as $a_j \mapsto (1 - 2^{-j})\, a_j$ [HCHH09].

For an NV centre, the correlation time of the environment is dictated by interactions between ^{13}C nuclei. A straight-forward calculation shows

$$\tau_{\rm int} \sim \sqrt{\frac{6}{\pi}}\frac{4\pi}{\mu_0}/(n_{\rm c}\hbar\gamma_{\rm c}^2) = 15\,{\rm ms}. \tag{6.2.2}$$

Using this in equation (6.2.1) for $j = 1$ gives $\Gamma_1 = 2.1$ kHz. We identify $T_2 = 1/\Gamma_1 = 400$ μs, in agreement with [TCC$^+$08, MNR$^+$09]. For an 0.3% ^{13}C bath we achieve $T_2 = 1.5\,$ms as seen in [BNT$^+$09]. We do not define $\tau_{\rm int}$ via interaction between ^{13}C nuclei and any background fields, B_0, since this manifests as decays and revivals on timescales of $\tau_{\rm r} \sim 1/\gamma_{\rm c}B_0$ and does not represent a true loss of information. Such effects may be mitigated by aligning B_0 along the NV axis.

The phase shift of the NV spin, $\Delta\phi$, is proportional to the time integral of the applied field. If pulses m are applied at the instants t_1, t_2, $\ldots t_m$, the effect of the pulse sequence on the phase shift will be

$$\Delta\phi = \gamma\left(\int_0^{t_1} - \int_{t_1}^{t_2} + \ldots + (-1)^m \int_{t_m}^{\tau}\right) B(t)\,{\rm d}t. \tag{6.2.3}$$

The effect of an arbitrary sequence of pulses on the $j^{\rm th}$ term in the Taylor expansion is then

$$\begin{aligned} a_k &\mapsto a_k \frac{\left(\int_0^{t_1} - \int_{t_1}^{t_2} \ldots + (-1)^m \int_{t_m}^{\tau}\right) t^k\,{\rm d}t}{\int_0^{\tau} t^k\,{\rm d}t} \\ &= a_k\left[2\sum_{j=1}^{m}(-1)^{j+1}\left(\frac{t_j}{\tau}\right)^{k+1} + (-1)^m\right]. \end{aligned} \tag{6.2.4}$$

For a pulse sequence to suppress the effect of a field to order n, the instants at which the pulses are applied must be chosen to ensure

$$\left(\int_0^{t_1} - \int_{t_1}^{t_2} + \ldots + (-1)^m \int_{t_m}^{\tau}\right) t^j\,{\rm d}t = 0, \tag{6.2.5}$$

not only for $j = n$, but for all $j < n$.

For example, we may wish to modify our $\frac{\tau}{2} - \pi - \frac{\tau}{2}$ pulse sequence in order to remove the effect of the $a_1 t$ term. If we apply pulses at $t = \frac{\tau}{4}$ and $t = \frac{3\tau}{4}$, we find that the effects of both a_0 and a_1 terms are suppressed. In general, suppression of all terms up to and including order n will require at least $n+1$ π-pulses. We define $\tau_{n,k}$ as the time at which the k^{th} pulse is applied in the sequence that suppresses all field components up to, and including, order n. Evaluation of equation (6.2.4) implies that determination of the $n+1$ elements of the set $\mathcal{P}_n = \left\{\tau_{n,0}, \ldots, \tau_{n,n+1}\right\}$ will require the solution of the following set of $n+1$ algebraic equations for $\tau_{n,k}$:

$$\begin{aligned}
a_0 &: \quad 2\sum_{k=1}^{n+1} (-1)^{k-1} \tau_{n,k} + (-1)^{n+1} \tau = 0, \\
a_1 &: \quad 2\sum_{k=1}^{n+1} (-1)^{k-1} \tau_{n,k}^2 + (-1)^{n+1} \tau^2 = 0, \\
&\vdots \\
a_m &: \quad 2\sum_{k=1}^{n+1} (-1)^{k-1} \tau_{n,k}^{m+1} + (-1)^{n+1} \tau^{m+1} = 0.
\end{aligned} \tag{6.2.6}$$

To this point, there is some freedom in our choice of pulse sequence, as equations (6.2.6) are satisfied to $n = 1$ by both CDD and UDD. However, if we solve equations (6.2.6) to $n = 2$, we find $\mathcal{P}_2 = \left\{\frac{\tau}{4}\left(2 - \sqrt{2}\right), \frac{\tau}{2}, \frac{\tau}{4}\left(2 + \sqrt{2}\right)\right\}$, which is the third UDD sequence. It is reasonable to conjecture that the n^{th} component of the field, $a_n t^n$, will be suppressed by the $(n+1)^{\text{th}}$ UDD sequence, which we prove below.

For an interrogation time of τ, the time of application of the jth pulse in the nth UDD sequence is given by

$$\tau_{n,j} \quad = \quad \tau \sin^2\left(\frac{\pi j}{2n+2}\right), \tag{6.2.7}$$

where $1 \leq k \leq n$ [Uhr07]. Substituting these times into the expression in 6.2.4, we

find

$$\begin{aligned}
\text{UDD}_1 \;\; a_k &\mapsto a_k \left[2^{-k} - 1\right] \\
\text{UDD}_2 \;\; a_k &\mapsto a_k \left[2\,(1/4)^{k+1} - 2\,(3/4)^{k+1} + 1\right] \\
\text{UDD}_3 \;\; a_k &\mapsto a_k \left[2\left[\sin^2\left(\frac{\pi}{8}\right)\right]^{k+1} - 2\left[\sin^2\left(\frac{\pi}{4}\right)\right]^{k+1} + 2\left[\sin^2\left(\frac{3\pi}{8}\right)\right]^{k+1} - 1\right] \\
&\vdots \\
\text{UDD}_n \;\; a_k &\mapsto a_k \left[2\sum_{j=1}^{m}(-1)^{j+1}\left[\sin^2\left(\frac{\pi j}{2n+2}\right)\right]^{k+1} + (-1)^m\right]. \qquad (6.2.8)
\end{aligned}$$

We wish to show that the $(n+1)^{\text{th}}$ UDD sequence suppresses the effect of all terms up to and including the nth term in the Taylor expansion of a time dependent magnetic field; and that the effect of all terms beyond n will be reduced.

The phase accumulation of a spin qubit is proportional to the time integral of the magnetic field to which it is exposed. Each π pulse exchanges the basis states of the qubit Hilbert space, which has the same effect on their relative phase as mapping $B \mapsto -B$. Recall from equation (6.2.6) that the action of the $(n+1)^{\text{th}}$ Uhrig pulse sequence will be to modify each of the a_j via $a_j \mapsto \left[2\sum_{k=1}^{n+1}(-1)^{k-1}\sin^{2j+2}\left(\frac{\pi k}{2n+4}\right) + (-1)^{n+1}\right] a_j$. To prove our claim, we must firstly show that,

$$2\sum_{k=1}^{n+1}(-1)^{k-1}\sin^{2m}\left(\frac{\pi k}{2n+4}\right) \;=\; (-1)^n. \qquad (6.2.9)$$

Using $N \equiv n+2$, $\sin(x) = \frac{1}{2i}\left(e^{ix} - e^{-ix}\right)$ and expanding as a binomial series in j, we arrive at

$$\text{LHS} \;=\; 2^{1-2m}\sum_{j=0}^{2m}(-1)^{j+m}\begin{pmatrix} 2m \\ j \end{pmatrix}\sum_{k=0}^{n-1} e^{i\pi a_{jmN}k}, \qquad (6.2.10)$$

where $a_{jmN} = \frac{m-j-N}{N}$. Note that we have added the $k=0$ term, since

$$\sum_{j=0}^{2m}\tbinom{2m}{j}(-1)^j \;=\; 0. \qquad (6.2.11)$$

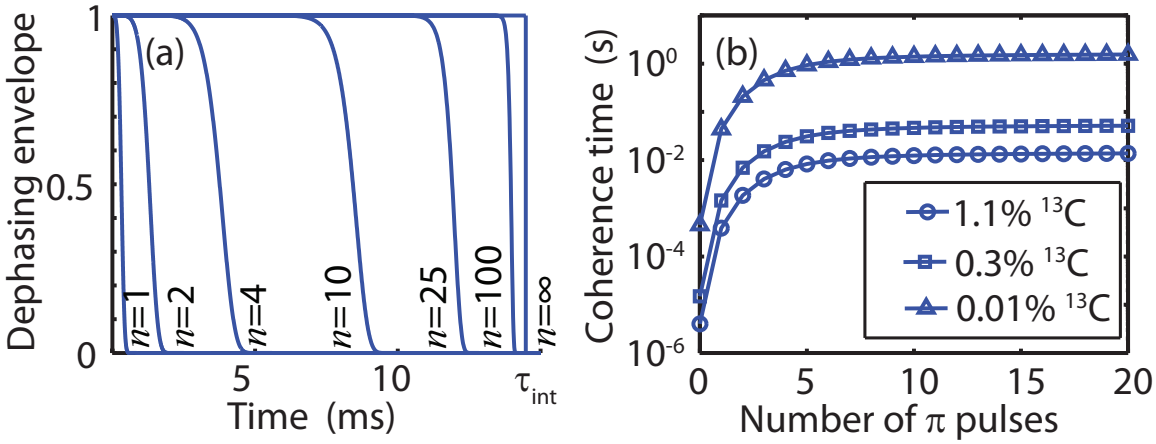

Figure 6.2: (a) Dephasing envelopes, $L^{(n)}$, for an NV centre in a 1.1% ^{13}C bath for n π pulses. As $n \to \infty$, $L^{(n)}$ approaches the Heaviside step function, $H(\tau_{\text{ext}} - t)$. (b) Effect of the number of π pulses on NV coherence times for different ^{13}C concentrations. In each case, the coherence time is limited by τ_{int}.

Since we have restricted ourselves to $m \leq N-1$, we have that $e^{i\pi a_{jmN}} \neq 1$, so we are free to sum over k as a geometric series in equation (6.2.10), which is not possible for $m \geq N$. This gives LHS $= 2^{-2m}(-1)^{2m+N} \sum_{j=0}^{2m} \binom{2m}{j}$, which is just the sum of terms in the $(2m+1^{\text{th}})$ row of Pascal's triangle, and evaluates to 2^{2m}, proving equation (6.2.9).

Replacing N with $n+2$, we can see that $a_j \mapsto 0\,, \forall\, j \leq n$. Hence all terms in the Taylor expansion of $B(t)$ up to and including order n are zero. Furthermore, since $0 \leq \sin^2(x) \leq 1$, the term in the square brackets is always less than 1, hence the effect of the remaining a_j is reduced. Two immediate consequences are that the $(n+1)^{\text{th}}$ UDD sequence will suppress dephasing to n^{th} order; and that dephasing effects beyond n^{th} order will be reduced. If $a_0, \ldots, a_n = 0$, then $\langle a_0^2 \rangle, \ldots, \langle a_n^2 \rangle = 0$. By equation (6.2.1) all rates, $\Gamma_0, \ldots, \Gamma_n$, are zero.

From the above analysis, we see that the application of a UDD sequence of any

order will decrease the intrinsic NV dephasing rate. This allows us to extend the interrogation time, thus improving the sensitivity to an external magnetic field, $B_{\text{ext}}(t)$. Clearly the dynamics of B_{ext} will be an important factor in ensuring that the effect of the external field is not also suppressed by the pulse sequence. Simple examples include telegraph signals switching in sync with the UDD sequence, or an AC field of controllable frequency whose nodes coincide with each π pulse, which could be realised by a single spin or ensemble of spins being driven by a controllable microwave field. FC sensitivities to rapidly fluctuating fields will also be improved, since fields with correlation times shorter than the interrogation time will not be refocussed by the UDD sequence.

6.2.2 CPMG Dynamic Decoupling

As for the UDD case above, we expand the effective magnetic field as a Taylor series in t,

$$B(t) \;=\; \sum_{k=0}^{\infty} a_k t^k. \tag{6.2.12}$$

For a CPMG sequence, the time of application of the jth pulse in an n pulse sequence is

$$t_j \;=\; \frac{2j-1}{2n}\tau, \tag{6.2.13}$$

where $j \in \{1, 2, \ldots, n\}$, and τ is the full free-precession time. For 1 pulse (spin-echo), the effect on the kth Taylor term is

$$a_k \;\mapsto\; (1 - 2^{-k})a_k, \tag{6.2.14}$$

and in general, we have

$$\begin{aligned}
\text{CPMG}_2 \;\; a_k &\mapsto a_k \frac{1}{4^{k+1}} \left[2 - 2\,(3)^{k+1} + 4^{k+1}\right] \\
\text{CPMG}_3 \;\; a_k &\mapsto a_k \frac{1}{6^{k+1}} \left[2 - 2\,(3)^{k+1} + 2\,(5)^{k+1} - 6^{k+1}\right] \\
&\vdots \\
\text{CPMG}_n \;\; a_k &\mapsto a_k \frac{1}{(2n)^{k+1}} \left[2 - 2\,(3)^{k+1} + \ldots + 2(-1)^{n-1}(2n-1)^{k+1} + (-1)^n (2n)^{k+1}\right] \\
&= a_k \frac{1}{(2n)^{k+1}} \left[2 + (-1)^n (2n)^{k+1} + 2\sum_{j=1}^{n-1} (-1)^j (2j+1)^{k+1}\right].
\end{aligned} \tag{6.2.15}$$

From this expansion we can see that, unlike the UDD case above, the CPMG pulse sequence does not entirely suppress the leading order terms of the expansion (with the exception of UDD2 and CPMG2, which are equivalent). This is explored in greater detail below.

6.2.3 Comparison of UDD and CPMG pulse sequences

To compare the performance of both UDD and CPMG techniques, we plot the effect of both sequences in the suppression of the first 20 terms in the Taylor expansion of an arbitrary magnetic field (figure. **??**). From this we can see that an n pulse UDD sequence will fully suppress the first n terms in the expansion, a_0 to a_{n-1}, and more importantly, UDD is shown to greatly outperform CPMG by this measure. We remind the reader that this result hinges on the assumption that the magnetic environment exists in the slow-fluctuation regime, or equivalently, that the spectral distribution has a hard cutoff at high-frequency, as is the case for a nuclear spin bath. Where this is not true, it is no longer valid to expand the field as Taylor series about $t = 0$, as the

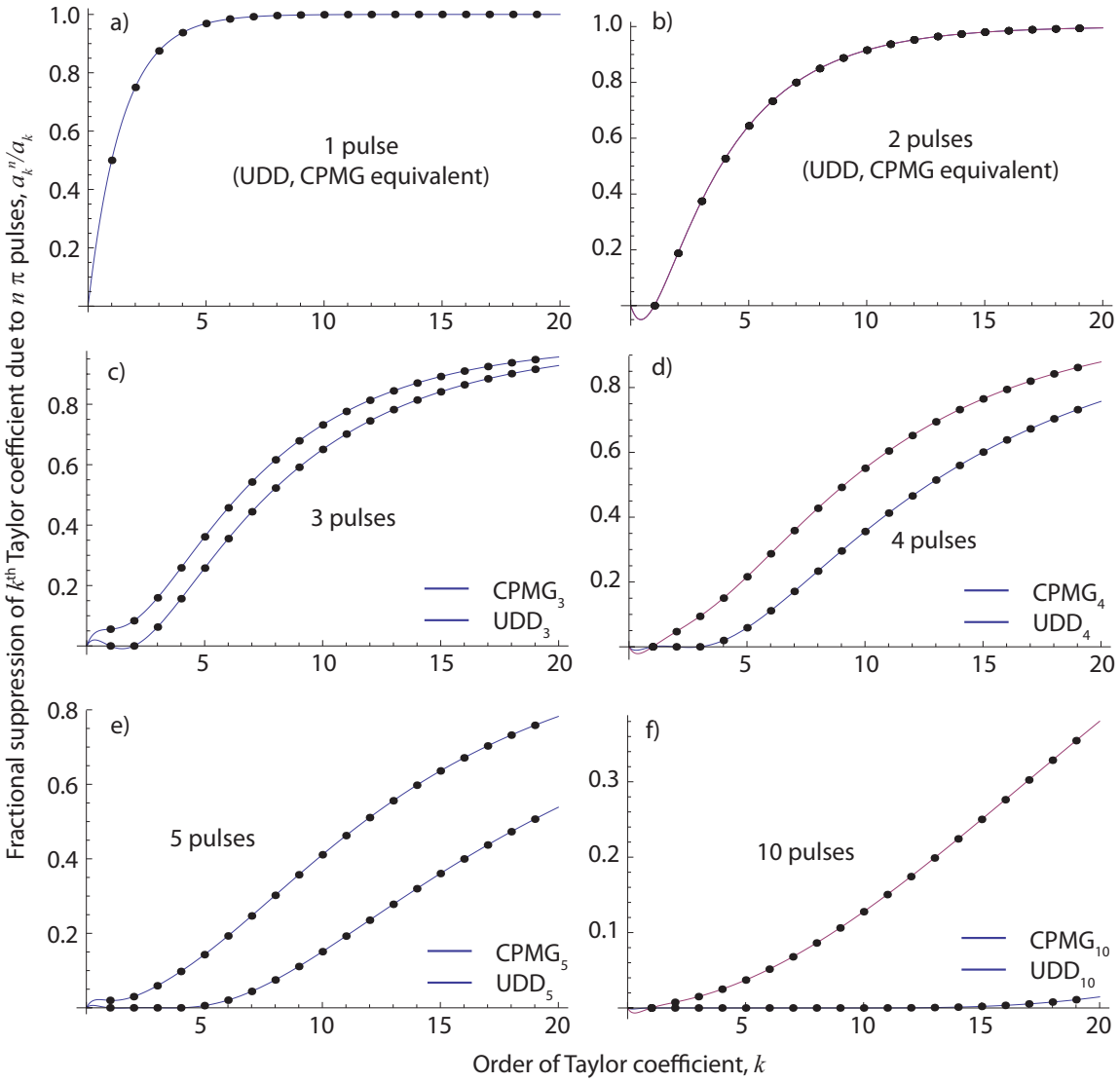

Figure 6.3: Plots showing the relative scaling of the first 21 terms in the Taylor expansion of an arbitrary field in the presence of UDD and CPMG pulse sequences. Where this expansion is valid, UDD is shown to greatly outperform CPMG for an equivalent number of pulses, with greater improvement shown as the number of pulses increases. By 'relative scaling', we refer to the ratio of the Taylor coefficient in the presence of a given sequence to that in the presence of no pulse sequence. A relative scaling of one therefore implies no effect, whereas a scaling of 0 implies full suppression of that particular channel. Note the change of scale in (f).

truncated series will not converge, as even short times will exceed the autocorrelation time of the field (as in the case of an electron spin bath). This is consistent with recent findings which show that the UDD sequence is optimal in suppressing decoherence in the presence of a noise source with a hard cutoff at high frequencies [CLNS08]. Despite these findings, the regular spacing of CPMG sequences not only makes its practical implementation more straightforward, but also makes it the optimal sequence for use in AC magnetometry. This is explored in the experimental section (6.4) below.

6.3 Sensitivity analysis

We denote the dephasing envelope in the presence of the $(n+1)$th pulse sequence as $L^{(n)}(t) = \prod_{k=n}^{\infty} L_k^{(n)}(t)$ [figure. 6.2(a)]. In the presence of background dephasing described by equation (6.2.1), the minimum induced phase from $B_{\text{ext}}(t)$ that may be measured is $\Delta\phi(b) = [C\sqrt{N}L^{(n)}(\tau)]^{-1}$, where C describes photon shot noise and imperfect collection [TCC+08], and N is the number of measurements taken. Typically $C < 0.3$, however vast improvements have recently been demonstrated by entangling the NV spin with proximate nuclear spins, permitting repetitive readout of the NV spin state [SNB+10, JHM+09]. We now discuss the relevant detection protocols and sensitivities for different fields to which these techniques apply.

6.3.1 Sensitivity limits: Controlled telegraph signals

For a telegraph signal (ts) synchronously switching between $\pm B_0$ with each π pulse, the qubit will acquire the maximum possible phase for a given interrogation time,

$\Delta\phi = \gamma B_0 \tau$. This gives a magnetic field sensitivity of

$$\begin{aligned} \eta_{\text{ts}}^{(n)} &= B_0\sqrt{T} \\ &= \left[C\gamma\sqrt{\tau}L^{(n)}(\tau)\right]^{-1}. \end{aligned} \tag{6.3.1}$$

For all cases where $\Theta_{\text{int}} \ll 1$, we have that $\Gamma_k \gg \Gamma_{k+1}$, and $\Gamma_k > \Gamma_k^{(n)}$ [HCHH09], so we may approximate the total dephasing envelope, $L^{(n)}$, by the its leading order contribution. That is $L^{(n)}(t) \sim \exp\left[-\left(\Gamma_{n+1}t\right)^{2n+4}\right]$, implying the optimal interrogation time is $\tau = \Gamma_{n+1}^{-1}\left(4n+8\right)^{1/(2n+4)}$. We then find the sensitivity to be bounded above by

$$\eta_{+}^{(n)} = \frac{1}{C\gamma}\sqrt{f_e\Theta_{\text{int}}^{-1/n}}. \tag{6.3.2}$$

This upper bound, together with the actual sensitivity (see below), is plotted in figure 6.4(a) for an NV. Notice that, as $\Theta_{\text{int}} \to 1$, there is little to be gained by applying UDD.

We now compute the sensitivity of the probe by taking into account the effect of the n^{th} order pulse sequence on the n^{th} order Taylor coefficient. This results in improved sensitivity beyond that indicated above, as a reduction in the a_k leads to a reduction in the total decoherence rate, and hence an extended interrogation time.

The dephasing rates are found via equation (6.2.1), where the σ_j obey the same mapping as the Taylor coefficients in equation 6.2.8.

$$\sigma^{(n)} \mapsto \left|2\sum_{k=1}^{n+1}(-1)^{k-1}\sin^{2j+2}\left(\frac{\pi k}{2n+4}\right) + (-1)^{n+1}\right|\sigma_j \equiv \sigma_j^{(n)}. \tag{6.3.3}$$

The actual dephasing time due to the combined effect of all the $\Gamma_k^{(n)}$ will be given by the solution to $\sum_{k=n+1}^{\infty}\left(\Gamma_k^{(n)}t\right)^{2k+2} - 1 = 0$ for t, and are plotted against the number of pulses used in the sequence in figure 6.2(b). From this we see that dephasing

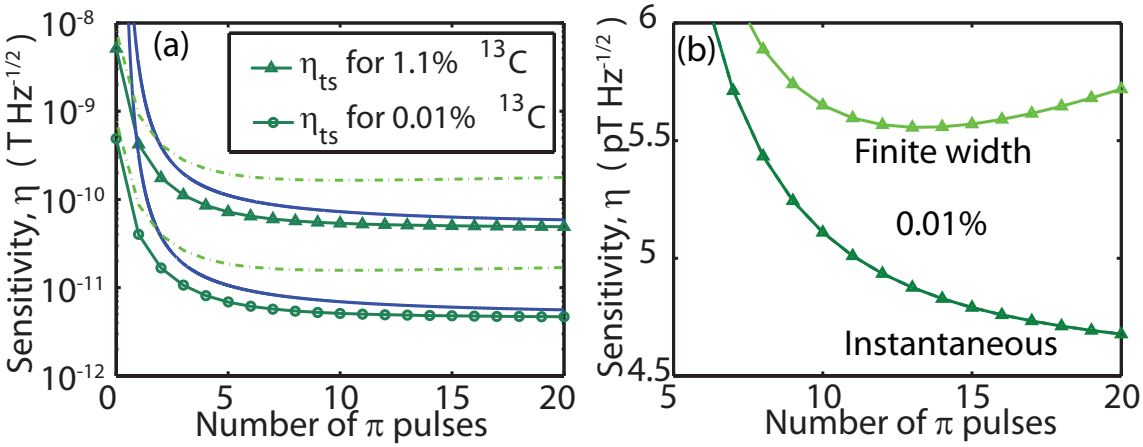

Figure 6.4: (a) Fundamental shot-noise sensitivity limits, $\eta_{\rm ts}$, assuming $C = 1$ for different ^{13}C concentrations. Smooth curves show the analytic bound on $\eta_{\rm ts}$. Dashed lines show the sensitivity to ac fields. (b) Effect of 50 ns pulse widths. The optimal sensitivity occurs for $n = 13$ π pulses.

times asymptote to the correlation time of the bath. This is to be expected, since information lost to the bath cannot be recovered by control of the NV spin alone. Retaining all terms, the sensitivity is then

$$\eta^{(n)}(\tau) \;=\; \frac{1}{\gamma\sqrt{\tau}} \exp\left[\sum_{k=n+1}^{\infty} \left(\Gamma_k^{(n)}\tau\right)^{2k+2}\right]. \tag{6.3.4}$$

By minimising this expression with respect to τ we determine the optimal sensitivity, $\eta_{\rm ts}^{(n)}$, as shown in figure 6.4(a).

6.3.2 AC fields

In many proposals [Deg08, TCC+08] magnetic resonance techniques are used to drive the sample magnetisation at some controlled frequency. For a general sinusoidal field, given by $B_{\rm ac}\sin(\nu t + \chi)$, the corresponding sensitivity with which $B_{\rm ac}$ may be

measured is

$$\eta_{\mathrm{ac}}^{(n)} \;=\; \eta_{\mathrm{ts}}^{(n)}\frac{\pi}{2}\left[\sum_{k=0}^{n}(-1)^k\int_{\tau_{n,k}}^{\tau_{n,k+1}}\sin\left(\nu_n t+\chi_n\right)\,\mathrm{d}t\right]^{-1}, \tag{6.3.5}$$

where ν_n and χ_n are the frequency and ac phase offset that minimise $\eta_{\mathrm{ac}}^{(n)}$. For example, for $n = 1$, the NV spin will acquire maximum phase when $\nu = 2\pi/\tau$ and $\chi = 0$. For $n = 5$, $\nu_5 = 9\pi/2\tau$ and $\chi_5 = 3\pi/4$. The optimal AC sensitivity is plotted as a function of the number of pulses in figure. 6.4(a).

Alternatively, by controlling the power of a proximate microwave field source, we may synchronise environment NMR/ESR control frequencies with the chosen pulse sequence. This allows a piecewise continuous sinusoidal signal to be produced whose nodes coincide with the time of application of each π pulse [figure. 6.1(c)], giving a sensitivity of

$$\eta_{\mathrm{cac}}^{(n)} \;=\; \frac{\pi}{2}\eta_{\mathrm{ts}}^{(n)}. \tag{6.3.6}$$

6.3.3 Randomly fluctuating (FC) fields

Many typical biological samples have a high nuclear spin density, which can result in significant additional dephasing. If the dynamics are fast ($\Theta_{\mathrm{ext}} \gg 1$), as in the case of Brownian motion for example, the additional dephasing may be detected as a perturbation in the dephasing rate [HCHH09]. The dephasing envelope will be modified by a factor of $L_{\mathrm{ext}}(\tau) = \exp(-\Gamma_{\mathrm{ext}}\tau)$, where $\Gamma_{\mathrm{ext}} = \frac{1}{2}\gamma_{\mathrm{p}}^2\sigma_{\mathrm{ext}}^2\tau_{\mathrm{ext}}$. The sensitivity with which $\sigma_{\mathrm{ext}} = \sqrt{\langle B_{\mathrm{ext}}^2\rangle - \langle B_{\mathrm{ext}}\rangle^2}$ may be measured is then [HCHH09]

$$\eta_{\mathrm{fc}} \;=\; 2\Theta_{\mathrm{ext}}\eta_{\mathrm{ts}}^{(n)}, \tag{6.3.7}$$

making the field more difficult to detect as the fluctuation rate increases. This is consistent with motional narrowing phenomena in NMR, in which high frequency

noise is known to have a reduced effect on the sample T_2 as compared with quasi-static noise. If the dynamics are slow ($\Theta_{\text{ext}} \ll 1$), the dephasing will be suppressed, permitting the application of the AC methods outlined above.

6.3.4 Effects of finite width pulses

Coherent manipulation of the NV is achieved via a resonant ESR transition, or Rabi cycle. Instantaneous π pulses cannot be achieved in practice, and lead to additional decoherence effects. For a Rabi frequency of Ω, the decoherence envelope is given by $L_{\text{R}} = [1 + (\gamma^2\sigma_0^2 t/\Omega)^2]^{-1/4}$ (see chapter 3), and typical pulse errors are $\approx 1\%$ [TCC+08]. Hence for n π pulses, the sensitivity will be worsened by a factor of $\sim 0.99^{-n-1}[1 + \frac{n+1}{4}(\sqrt{\pi}\gamma\sigma_0/\Omega)^4]$, as shown in figure. 6.4(b). For a typical pulse width of 50 ns, 13 π pulses is found to be optimal, with $\eta_{\text{ts}}^{(13)} \approx 5.5\,\text{pT}\,\text{Hz}^{-1/2}$.

Cases where the total pulse time is significant compared with the total interrogation time have been considered [UP10], however, since we are dealing with extremely long coherence times and short pulse times, these effects have been neglected in this analysis.

6.4 Experimental Investigation

In this section, we experimentally demonstrate the effects of multi-pulse sequences on both the decoherence and sensitivity of an NV spin based magnetometer. As noted above, by virtue of its comparative ease of experimental implementation and suitability to measuring controlled AC fields (which represent the simplest control case), we consider only CPMG pulse sequences in what follows.

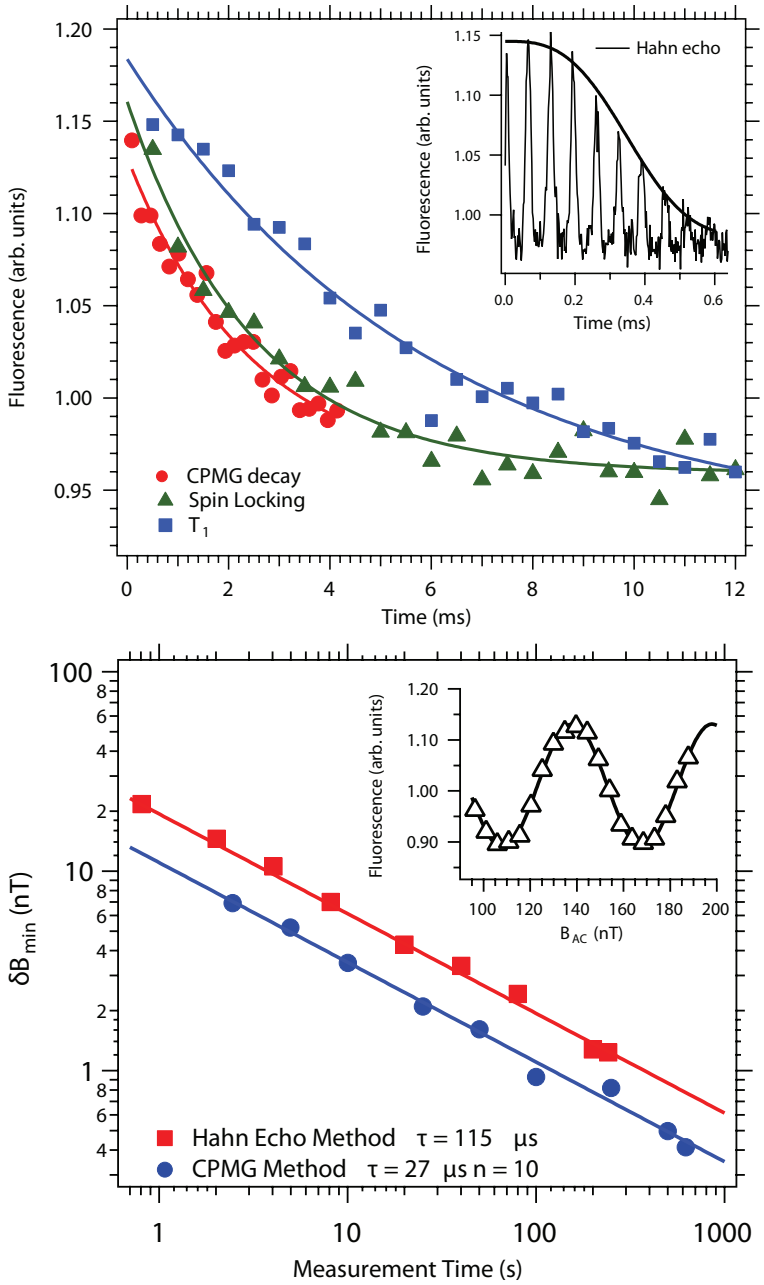

Figure 6.5: (a) Spin echo decay (inset, $T_2^{\mathrm{SE}} = 0.4 \pm 0.16\,\mathrm{ms}$), CPMG (circles, $T_2^{\mathrm{CPMG}} = 2.44 \pm 0.44\,\mathrm{ms}$), spin locking (triangles, $T_{1\rho} = 2.47 \pm 0.27\,\mathrm{ms}$), and spin-lattice relaxation (squares, $T_1 = 5.93 \pm 0.7\,\mathrm{ms}$). The solid curves are fits to the data (see text). (b) Plot of minimum measurable magnetic field, δB_{min}, as a function of the total measurement time per data point in the presence Hahn echo and CPMG based pulse sequences. Solid lines denotes fits to the expected shot-noise scaling with measurement time t, $\delta B_{\mathrm{min}} = k/\sqrt{t}$. Oscillations in the NV fluorescence intensity due to the applied ac magnetic field are shown in the insert.

The diamond sample used was a chemical vapour deposition (CVD) grown with a natural 1.1% ^{13}C abundance and low (less than ppb) nitrogen impurity concentration. The spin echo decay is shown in the inset of figure. 6.5(a), and the decoherence time was measured to be $T_2^{\mathrm{SE}} = 400\,\mu$s, showing excellent agreement with our theoretical prediction (published months before this experiment was conducted) made at the beginning of this chapter. The modulations are the result of strong coupling between the NV spin and proximate ^{13}C spins, and occur at a rate equal to their Larmor frequency.

By increasing the number of pulses from 1 to $n = 90$, we are able to increase the decoherence time to 2.44 ms, as consistent with the hard limit predicted in this work (see figure 6.2), although an upper limit exists to the number of pulses that may be employed. As discussed above, due to finite pulse widths, the total evolution time of the NV under microwave control will eventually dominate the total evolution time. At this point, the NV spin has entered the 'spin locking' regime, meaning that the decoherence is instead limited by the Rabi decay time, T_1^{ρ}. This does not represent a fundamental limit however, and may be increased further by employing a stronger microwave field (see chapter 3). In the limit of an infinite Rabi frequency, T_1^{ρ} simply approaches the true relaxation time of the NV, T_1.

To demonstrate the utility of CPMG sequences in AC magnetometry, a gold nanostructure was deposited onto the diamond surface. An oscillatory current was passed down this structure using an arbitrary waveform generator, and the resulting controllable AC magnetic field was used to determine the sensitivity of the NV. Changes in the NV fluorescence are plotted in the insert of figure 6.5(b) as a function of AC field

amplitude. At points where the slope is steepest, the fluorescence will show a maximal linear dependence on the field strength, corresponding to best possible magnetic field sensitivity. As such, we may write

$$\delta B_{\min} = \frac{\mathrm{d}B}{\mathrm{d}S}\delta S, \tag{6.4.1}$$

where the uncertainty in the measured fluorescence, δS, is determined by the standard deviation associated with its measurement statistics, σ_S, for a given pulse sequence. We expect σ_S to be shot-noise limited, implying a $1/\sqrt{T}$ dependence on the overall measurement time, and this is indeed shown to be the case from the fits in figure 6.5(b). By choosing a free-precession time of $\tau = 2 \times 115\,\mu$s, the magnetic field sensitivity under a spin-echo pulse sequence was found to be $\eta_{\mathrm{SE}} = \delta B_{\min}\sqrt{T} = 19.4 \pm 0.4\,\mathrm{nT\,Hz^{-1/2}}$. Note that this does not represent the optimal operating regime for the spin echo case, for which we would choose $\tau \sim T_2$. A similar analysis of the CPMG case for 10 pulses and a total free precession time of $\tau = 11 \times 27\,\mu$s shows the corresponding sensitivity to be $\eta_{\mathrm{CPMG}_{10}} = 11.0 \pm 0.2\,\mathrm{nT\,Hz^{-1/2}}$. This shows a slight improvement, and is close to what is expected from the analysis (recall that a factor of 4 suppression in the relevant Taylor co-efficient produces only a factor of two in the sensitivity due to the $\sqrt{\tau}$ dependence of the shot noise), as can be seen from the comparison of figures **??** (a) & (f) for the CPMG case.

We note that the sensitivity was not improved by using more than 10 pulses in the CPMG sequence. This is due to a combination of noise inherent in the applied ac magnetic signal, andsub-shot noise (ie sub-$\sqrt{T}$) improvements as the full NV evolution approaches the spin-locking regime. The latter of these is readily addressed by employing UDD instead of CPMG, as significantly less pulses are required to achieve the same degree of decoherence suppression.

The minimum magnetic field detected in this experiment was 0.4 nT, which was performed using a total sensing time of $T = 10$ min, and corresponds to the coupling between the NV spin and that of a proton a distance of 5 nm away. The optimal sensitivity scaling associated with the UDD sequence will result in orders of magnitude improvements to this acquisition time, and hence the sensitivity, even when the proton spin is driven in an ac fashion (see figure 6.4 (a)). Further improvements will be achieved if the Rabi frequency of the proton spin can be dynamically controlled to coincide with the non-uniform spacing of the UDD pulses.

6.5 Conclusions

We have theoretically investigated the improvements associated with the application of UDD and CPMG sequences to an NV-based magnetometer, with UDD proving to be optimal in this case. Results show that dephasing times are ultimately limited by the self correlation time of the fluctuating environment, thus NV magnetometer interrogation times may be extended by nearly four orders of magnitude beyond the free-induction decay time. An experimental investigation was conducted, and results were shown to be consistent with theoretical predictions. In light of these results, we have shown that incorporation of UDD into current single NV magnetometer protocols may yield sensitivities below 5 pT $\mathrm{Hz}^{-1/2}$ at room temperature in the near future. Such techniques have the potential to yield great improvements to nano-scale sensing, particularly nano-biological processes occurring at room temperature.

Chapter 7

Fundamental limits of achievable fidelity in pulsed-wave spin resonance experiments

As detailed in chapter 3, control of the NV spin state is achieved by tuning the frequency of an oscillatory microwave field to one of the transitions within the ground-state $\{|0\rangle, |-1\rangle, |+1\rangle\}$ spin manifold, say $|0\rangle \leftrightarrow |+1\rangle$. To this point, our analysis has assumed that perfect, instantaneous pulses are possible and that we may be completely detuned from the $|0\rangle \leftrightarrow |-1\rangle$ transition. In reality, the presence of the microwave field and the adjacent spin bath results in a broadening of these transitions, meaning that not only is it impossible to perfectly tune to the $|0\rangle \leftrightarrow |+1\rangle$ transition, we also achieve a non-resonant excitation of the $|0\rangle \leftrightarrow |-1\rangle$ transition, leading to a population leakage into the $|-1\rangle$ state. In this chapter, we quantify these effects, and the associated loss of fidelity, in the context of an NV centre coupled to three different proximate spin baths: the ppm nitrogen electron donor spin bath in type 1b diamond, the 1.1% ^{13}C nuclear spin bath in ultra-pure low nitrogen diamond, and the surface electron spin bath of diamond nanocrystals.

7.1 Introduction

In discussing NV spin resonance processes so far, we have assumed that errors in our measurements are solely due to the influence of spin impurities, both within the diamond crystal and on the crystal surface, during the free precession intervals of the NV spin's evolution. In doing so, we have implicitly assumed that no errors are introduced during the relatively short periods of microwave control. From the discussion of ODMR in chapter 3, we know that a broadening of the NV ground state spin transitions are caused by both microwave and laser fields, and the coupling to a proximate spin bath. As we will show, this broadening results in both incomplete spin rotations and population leakage into the third spin sublevel via excitation of the second, non-resonant transition. Suppression of pulsing errors is shown to be achievable by simultaneously employing a sufficiently strong microwave field, capable of exciting the target transition, despite the detunings caused by couplings to adjacent spins; together with a sufficiently strong background magnetic field, capable of detuning the second non-resonant transition beyond any appreciable excitation.

In what follows, we consider the full coherent evolution of the NV spin under FID and spin echo pulse sequences, including a full quantum mechanical description of microwave driven and free precession intervals. The errors are quantified in terms of both experimental parameters and physical properties of the spin bath, and are shown to explain the origin of a number of features whose discussion has been overlooked in the literature to date. This analysis is then applied to three experimentally relevant cases, including a comparison of our findings with experiment[1].

[1] All experiments described in this chapter were performed by L.P. McGuinness and D.A. Simpson at the University of Melbourne.

7.2 Modeling

In order to model this system, we must consider the evolution of the NV spin under both continuous and pulsed microwave sequences. Firstly, we use ODMR to determine the optimal microwave frequency for use in the microwave control of the spin state. A Rabi sequence is then used to determine the pulse duration required to produce π and $\pi/2$ control pulses. The full evolution is then performed using initial and final $\pi/2$ pulses, encapsulating alternating periods of free evolution and π control pulses.

7.2.1 Continuous microwave-driven evolution

We firstly consider cases in which the evolution of the NV spin state is driven by a continuous, oscillating lateral microwave field, namely ODMR and Rabi cycling. When the frequency of the microwave field is resonant with one of the spin transitions, the population of the NV spin will cycle between the two states associated with the transition. However, because of the broadening of these transitions due to both the presence of the surrounding spin bath, and the microwave field itself, not only are we almost never perfectly on resonance with the desired transition, we also manage to excite the non-resonant transition to a lesser degree. ODMR provides us with a convenient protocol by which to quantify these undesired effects prior to discussing pulsed-based microwave evolution, whereas the Rabi protocol allows us to probe the resultant transition rates for a given microwave frequency.

During periods of microwave driven evolution, we take the static, axial Hamiltonian to be $\mathcal{H}_0 = D\mathcal{S}_z^2 + \omega_z \mathcal{S}_z$, where ω_z is the total coupling to the axial component of the NV spin, including the static background field used to split the ± 1 states, B_0,

and all Ising $(z-z)$ type interactions between the NV and the environment. The interaction with the microwave field, whose amplitude and frequency may be controlled externally, is given by $\mathcal{V}=\omega_x\cos(\omega t)\,\mathcal{S}_x$ (taking $\omega>0$). Switching to the interaction picture, we have

$$\begin{aligned}\mathcal{V}_I &= \omega_x\cos(\omega t)\,e^{i\mathcal{H}_0 t}\mathcal{S}_x e^{-i\mathcal{H}_0 t}\\ &\approx \frac{\omega_x}{2\sqrt{2}}\begin{pmatrix}0 & e^{it(D+\omega_0-\omega)} & 0\\ e^{-it(D+\omega_0-\omega)} & 0 & e^{-it(D-\omega_0-\omega)}\\ 0 & e^{it(D-\omega_0-\omega)} & 0\end{pmatrix}\\ &= \frac{\omega_x}{2\sqrt{2}}\begin{pmatrix}0 & e^{-i\delta_+ t} & 0\\ e^{i\delta_+ t} & 0 & e^{i\delta_- t}\\ 0 & e^{-i\delta_- t} & 0\end{pmatrix},\end{aligned} \tag{7.2.1}$$

where $\delta_\pm=\omega-(D\pm\omega_z)$ is the detuning between the qubit transition frequencies $(D\pm\omega_z)$ and the frequency of the microwave field. Note that in this approximation we have we ignored all terms of the form $e^{\pm i(\omega+D\pm\omega_z)t}$, since their rapid oscillation yields corrections of order $\frac{\omega_x}{\omega+D}\ll 1$, which are much lower than the errors with which we concern ourselves in this chapter (which are of the order $\mathcal{O}\left(\omega_x^2/B_0^2\right)$, $\mathcal{O}\left(\delta_\pm^2/\omega_x^2\right)$). In addition, since we are interested in errors accumulated during microwave evolution on timescales of $t\sim 1/\omega_x$, time-dependent perturbation theory is not appropriate, hence we must solve the evolution of the spin state exactly.

The equation of motion of the state in the interaction picture is given by

$$\frac{\mathrm{d}}{\mathrm{d}t}\left|\psi\right\rangle_I = -i\mathcal{H}_I\left|\psi\right\rangle_I, \tag{7.2.2}$$

where $\left|\psi\right\rangle_I=A_+\left|+1\right\rangle+A_0\left|0\right\rangle+A_{-1}\left|-1\right\rangle$. This system may be simplified further by

substituting $A_+ = e^{-i\delta_+ t} a_+$ and $A_- = e^{-i\delta_- t} a_-$, and rescaling with $\tau = \frac{\omega_x}{2\sqrt{2}}\, t$, giving

$$\begin{aligned} \frac{\mathrm{d}a_+}{\mathrm{d}\tau} &= i\kappa_+ a_+ - iA_0 \\ \frac{\mathrm{d}}{\mathrm{d}\tau} A_0 &= -ia_+ - ia_- \\ \frac{\mathrm{d}a_-}{\mathrm{d}\tau} &= i\kappa_- a_- - iA_0, \end{aligned} \tag{7.2.3}$$

where $\kappa_\pm \tau \equiv \delta_\pm t$. This system of three first-order linear differential equations may be reduced to a single third-order differential equation for A_0,

$$\frac{\mathrm{d}^3}{\mathrm{d}\tau^3} A_0 - i\left(\kappa_+ + \kappa_-\right) \frac{\mathrm{d}^2}{\mathrm{d}\tau^2} A_0 + \left(2 - \kappa_+ \kappa_-\right) \frac{\mathrm{d}}{\mathrm{d}\tau} A_0 - i\left(\kappa_+ + \kappa_-\right) A_0 = 0. \tag{7.2.4}$$

We proceed by seeking solutions of the form $A_0 = e^{i\lambda t}$. In the case of either an ODMR or a Rabi experiment, where the system is initially optically polarised in the $|0\rangle$ state ($A_0 = 1,\ A_+ = A_- = 0$), we have

$$A_0(t) = -\frac{e^{i\lambda_1 t}\left(2 + \lambda_2\lambda_3\right)}{\left(\lambda_1 - \lambda_2\right)\left(\lambda_3 - \lambda_1\right)} - \frac{e^{i\lambda_2 t}\left(2 + \lambda_1\lambda_3\right)}{\left(\lambda_1 - \lambda_2\right)\left(\lambda_2 - \lambda_3\right)} - \frac{e^{i\lambda_3 t}\left(2 + \lambda_1\lambda_2\right)}{\left(\lambda_1 - \lambda_3\right)\left(\lambda_3 - \lambda_2\right)}. \tag{7.2.5}$$

For the more general case of an arbitrary initial state, $\big|\psi(0)\big\rangle \equiv a_+\big|{+1}\big\rangle + a_0\big|0\big\rangle + a_-\big|{-1}\big\rangle$, which will be required for discussions regarding pulse-based microwave control, the initial conditions for equation 7.2.4 are

$$\begin{aligned} A_0(0) &= a_0, \\ \left.\frac{dA_0}{dt}\right|_{t=0} &= -ia_+ - ia_-, \\ \left.\frac{d^2A_0}{dt^2}\right|_{t=0} &= \kappa_+ a_+ + \kappa_- a_- - 2a_0, \end{aligned} \tag{7.2.6}$$

giving the following solution for the amplitude of the $|0\rangle$ state,

$$\begin{aligned} A_0(\tau) &= \frac{a_-\left(\kappa_- - \lambda_2 - \lambda_3\right) + a_+\left(\kappa_+ - \lambda_2 - \lambda_3\right) - \left(2 + \lambda_2\lambda_3\right) a_0}{\left(\lambda_1 - \lambda_2\right)\left(\lambda_3 - \lambda_1\right)} e^{i\lambda_1\tau} \\ &+ \frac{a_-\left(\kappa_- - \lambda_1 - \lambda_3\right) + a_+\left(\kappa_+ - \lambda_1 - \lambda_3\right) - \left(2 + \lambda_3\lambda_1\right) a_0}{\left(\lambda_1 - \lambda_2\right)\left(\lambda_2 - \lambda_3\right)} e^{i\lambda_2\tau} \\ &+ \frac{a_-\left(\kappa_- - \lambda_1 - \lambda_2\right) + a_+\left(\kappa_+ - \lambda_1 - \lambda_2\right) - \left(2 + \lambda_1\lambda_2\right) a_0}{\left(\lambda_3 - \lambda_1\right)\left(\lambda_2 - \lambda_3\right)} e^{i\lambda_3\tau}. \end{aligned} \tag{7.2.7}$$

The amplitudes of the other two states may be evaluated using equation 7.2.3,

$$a_\pm(t) = a_\pm(0) - i\exp\left(i\kappa_\pm\tau\right)\int_0^t A_0(\tau')\exp\left(-i\kappa_\pm\tau\right)\mathrm{d}\tau, \tag{7.2.8}$$

where the normal modes of the system are given by

$$\begin{aligned} \lambda_1 &= \frac{1}{3}\left(\kappa_- + \kappa_+\right) + \frac{1}{3}2^{2/3}\alpha\left[\sin\left(\frac{1}{3}\tan^{-1}\beta^3\right)\right] \\ \lambda_2 &= \frac{1}{3}\left(\kappa_- + \kappa_+\right) + \frac{1}{6}2^{2/3}\alpha\left[\sqrt{3}\cos\left(\frac{1}{3}\tan^{-1}\beta^3\right) - \sin\left(\frac{1}{3}\tan^{-1}\beta^3\right)\right] \\ \lambda_3 &= \frac{1}{3}\left(\kappa_- + \kappa_+\right) - \frac{1}{6}2^{2/3}\alpha\left[\sqrt{3}\cos\left(\frac{1}{3}\tan^{-1}\beta^3\right) + \sin\left(\frac{1}{3}\tan^{-1}\beta^3\right)\right], \end{aligned} \tag{7.2.9}$$

and

$$\alpha^2 = 4\left(6 + \kappa_-^2 - \kappa_-\kappa_+ + \kappa_+^2\right) \tag{7.2.10}$$

$$\beta^3 = \left[1 - 4\frac{\left(\kappa_-^2 - \kappa_+\kappa_- + \kappa_+^2 + 6\right)^3}{\left(\kappa_- + \kappa_+\right)^2\left(-2\kappa_-^2 + 5\kappa_+\kappa_- - 2\kappa_+^2 + 9\right)^2}\right]^{-1/2}. \tag{7.2.11}$$

Typically, we are interested in two limiting cases, as dictated by the strength of the static axial field. In the low field limit, $B_0/\omega_x \ll 1$, the degeneracy between the ± 1 states is lifted ever only so slightly by the presence of the spin bath. As such, the microwave field is still able to excite both $|0\rangle \leftrightarrow |+1\rangle$ and $|0\rangle \leftrightarrow |-1\rangle$

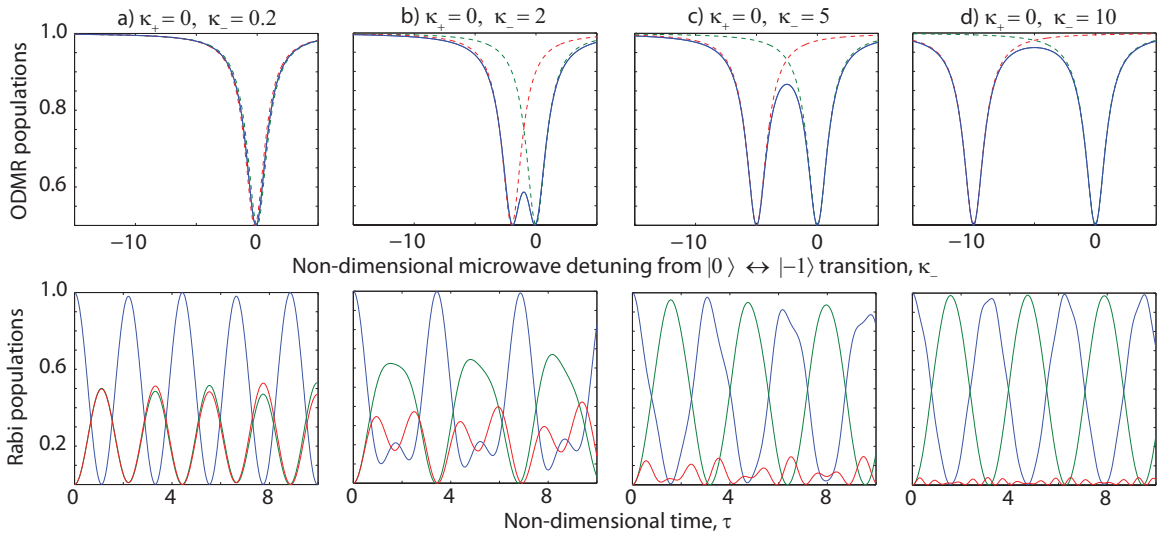

Figure 7.1: ODMR and corresponding Rabi profiles for various detuning parameters, κ_+ and κ_-. The detuning from the adjacent, non-resonant $|0\rangle \leftrightarrow |-1\rangle$ transition increases from left to right, and the Rabi profiles correspondingly show decreasing population of the $|-1\rangle$ state (red curve). Dashed red curves in the upper plots represent the idealised Lorentzian profiles associated with each transition and give an indication of the degree of excitation of the non-resonant transition. In the lower plots, the populations of the $|0\rangle$, $|+1\rangle$ and $|-1\rangle$ states are shown in blue, green and red respectively.

transitions. Pulsing errors arise as a result of the increased broadening, and hence reduced contrast of the transition rate (See figure 7.1 (a) & (b)). In this case, we have $\kappa_+,\ \kappa_- \ll 1$.

More commonly, when the background field is large, the microwave field will be tuned close to resonance with one of the transitions and far detuned from the other, giving $\kappa_+ \ll 1$, $\kappa_- \gg 1$. Pulsing errors will arise not only due to broadening of the $|0\rangle \leftrightarrow |+1\rangle$ transition, but also due to population leakage into the $|-1\rangle$ state via a slight excitation of the $|0\rangle \leftrightarrow |-1\rangle$ transition (See figure 7.1 (c) & (d)).

As the λ_i are real, we simply have $(i\lambda_i)^* = -i\lambda_i$. The time dependent population

at time t is then

$$\begin{aligned} P_0(t) &= A_0^*(t)A_0(t) \qquad (7.2.12)\\ &= \frac{(2+\lambda_2\lambda_3)^2}{(\lambda_1-\lambda_2)^2(\lambda_3-\lambda_1)^2} + \frac{(2+\lambda_1\lambda_3)^2}{(\lambda_1-\lambda_2)^2(\lambda_2-\lambda_3)^2} + \frac{(2+\lambda_1\lambda_2)^2}{(\lambda_3-\lambda_1)^2(\lambda_2-\lambda_3)^2} \\ &\quad + \frac{2(2+\lambda_2\lambda_3)(2+\lambda_1\lambda_3)}{(\lambda_1-\lambda_2)^2(\lambda_3-\lambda_1)(\lambda_2-\lambda_3)}\cos\big[(\lambda_1-\lambda_2)t\big] \\ &\quad + \frac{2(2+\lambda_2\lambda_3)(2+\lambda_1\lambda_2)}{(\lambda_3-\lambda_1)^2(\lambda_1-\lambda_2)(\lambda_2-\lambda_3)}\cos\big[(\lambda_1-\lambda_3)t\big] \\ &\quad + \frac{2(2+\lambda_3\lambda_1)(2+\lambda_1\lambda_2)}{(\lambda_2-\lambda_3)^2(\lambda_1-\lambda_2)(\lambda_3-\lambda_1)}\cos\big[(\lambda_2-\lambda_3)t\big]. \qquad (7.2.13) \end{aligned}$$

Optically detected magnetic resonance

The ODMR spectrum allows us to see the degree to which each of the two transitions will be excited as a function of the microwave frequency, ω. Since the monitored fluorescence is proportional to a long-time ($t \gg 1/\omega_x$) summation over equation 7.2.13, the contribution of the cosine terms vanishes, and we are left with the following DC contribution

$$S_{\text{ODMR}} = \frac{(2+\lambda_2\lambda_3)^2}{(\lambda_1-\lambda_2)^2(\lambda_3-\lambda_1)^2} + \frac{(2+\lambda_1\lambda_3)^2}{(\lambda_1-\lambda_2)^2(\lambda_2-\lambda_3)^2} + \frac{(2+\lambda_1\lambda_2)^2}{(\lambda_3-\lambda_1)^2(\lambda_2-\lambda_3)^2}. \qquad (7.2.14)$$

To illustrate the effect of the detuning, the contrast is plotted in figure 7.1 for a range of values for the detuning parameters, κ_+ and κ_-. These curves show the response for a particular realisation of the axial field, ω_z, however this field will vary slightly about $D \pm B_0$ due to the axial components of the coupling to the spin bath. Computing the ensemble average over these couplings will lead to a broadening of the ODMR curve, and consequently, a reduced contrast. In the case that we are far detuned from one

of the transitions, say $|0\rangle \leftrightarrow |-1\rangle$, we have $\kappa_- \gg \kappa_+$, giving

$$S_{\mathrm{ODMR}} \approx \frac{1}{2}\left(1+\frac{\kappa_+^2}{\kappa_+^2+4}\right)+\frac{4}{\kappa_-}\frac{\kappa_+}{(\kappa_+^2+4)^2}-\frac{2}{\kappa_-^2}\frac{\kappa_+^6+9\kappa_+^4+31\kappa_+^2+28}{(\kappa_+^2+4)^3}, \tag{7.2.15}$$

which shows the correction to the Lorentzian profile associated with the resonant transition to second order in $1/\kappa_-$, resulting from excitation of the non resonant transition.

Rabi Oscillations and determination of pulse duration

Instead of examining the long-time averaged behavior of the NV fluorescence in response to the microwave field under constant optical illumination, we may allow the system to evolve under the action of the microwave field for a predetermined time, and then stop the evolution and readout the population of the $|0\rangle$ state using a pulsed laser (see chapter 3 for a review). By varying the microwave evolution time, we may determine the time dependent population of the $|0\rangle$ state.

As in the ODMR case, the presence of additional axial couplings due to a proximate spin bath leads to a broadening of the effective Rabi frequencies, in turn leading to an eventual decay of the Rabi profile. A full, long-time description of this decay is not necessary for this work, however a description of the behaviour for $t \sim 1/\omega_x$ is sufficient to determine the errors accumulated during pulsed evolution of the system.

In the high field case, the ODMR transitions are split due to the presence of a large static magnetic field, $B_0 \gg \omega_x$, making simultaneous resonant excitation of both transitions impossible. As such, we tune the microwave frequency to the $|0\rangle \leftrightarrow |+1\rangle$ transition. As we will show, leakage of the NV spin population into its $|-1\rangle$ state

via small excitation of the $|0\rangle \leftrightarrow |-1\rangle$ transition is a significant source of error in many practical cases.

For cases where the splitting is large, we may expand equation 7.2.13 for large κ_-, giving

$$\begin{aligned} P_{\text{Rabi}} &= 1 - \frac{4}{\Omega^2}\sin^2\left(\frac{\xi\tau}{2}\right) + \frac{1}{\kappa_-}\frac{8\kappa_+}{\Omega^2}\sin^2\left(\frac{\xi\tau}{2}\right) + \frac{2}{\kappa_-^2}\left[\cos(\kappa_-\tau)\cos\left(\frac{\xi\tau}{2}\right)\right. \\ &\quad \left. -\frac{\kappa_-\sin(\kappa_-\tau)\sin\left(\frac{\xi\tau}{2}\right)}{\Omega} + \frac{2\left(3\Omega^4 - 7\Omega^2 + 16\right)\sin^2\left(\frac{\xi\tau}{2}\right)}{\Omega^6} - 1\right], \end{aligned} \tag{7.2.16}$$

where $\Omega = \sqrt{\kappa_+^2 + 4}$ is the bare 'Rabi' frequency with respect to the $|0\rangle \leftrightarrow |+1\rangle$ transition, and ξ is the modified Rabi frequency, resulting from excitation of the $|0\rangle \leftrightarrow |-1\rangle$ transition. To second order in $1/\kappa_-$, we have

$$\xi = \Omega\left(1 + \frac{2}{\kappa_-^2\Omega^4} + \frac{\kappa_+}{\kappa_-\Omega^2} - \frac{2}{\kappa_-^2\Omega^2}\right). \tag{7.2.17}$$

In addition to being a means by which to demonstrate the quantum coherence of the NV, a Rabi experiment is used to obtain the appropriate pulse widths for pulse based manipulation and control of the quantum state. This is done by using a Fourier transform of the Rabi profile to determine the associated Rabi Frequency, and hence the time required to perform the desired rotation. The Rabi profile in equation 7.2.16 is true for a given realisation of κ_+ and κ_-, however, whilst the detuning with respect to D and B_0 may be controlled externally, the presence of a proximate spin bath introduces a spread in the detuning that cannot be controlled. To determine our best chance of achieving the desired rotation, we must determine the resulting ensemble averaged Rabi profile.

Since the pulse width is typically short on the timescale of the correlation time of the bath, we may assume the spread in the detuning due to the spin bath is quasi

static. Bath dynamics are thus only important for the much longer free-precession intervals, and are dealt with in section 7.2.2 below. Furthermore, owing to the large number of field sources present, the probability density function associated with the detuning will be normally distributed via

$$P(\omega_z) = \frac{1}{2I_N+1}\sum_{k=-I_N}^{k=I_N}\frac{1}{b\sqrt{2\pi}}\exp\left[-\frac{(\omega_z-\omega_0-kA_N)^2}{2b^2}\right], \qquad (7.2.18)$$

where kA_N is the hyperfine shift due to the k^{th} spin state of the spin-I_N nitrogen nuclear spin of the NV centre, which may be either spin-$\frac{1}{2}$ or spin-1 depending on the isotope present, all states of which will be equally populated at room temperature; and b is the spread in coupling strengths from the bath as a whole. We define $\omega_0 \equiv D+B_0$ to be the total static background magnetic field.

Since we are interested in exciting the $|0\rangle \leftrightarrow |+1\rangle$ transition as much as possible, we tune the microwave field to $\omega = \omega_0$. The detuning associated with this transition is then simply $\delta = \omega_z - \omega_0$, and since $\delta \ll \omega_x \ll \omega_0$, we may expand equation 7.2.16 for small κ_+, giving,

$$\begin{aligned} P_{\text{Rabi}} \approx\ & \cos^2\left(\frac{\xi\tau}{2}\right) + \frac{1}{4}\left(\kappa_+ + \frac{1}{\kappa_-}\right)^2 \sin^2\left(\frac{\xi\tau}{2}\right) \\ & + \frac{2}{\kappa_-^2}\left[\cos(\kappa_-\tau) - \cos\left(\frac{\xi\tau}{2}\right)\right]\cos\left(\frac{\xi\tau}{2}\right), \end{aligned} \qquad (7.2.19)$$

from which we see that the corresponding Fourier decomposition will contain three dominant frequency components: one centred near ξ, and two more at $\kappa_- \pm \xi$; however only the former is non-zero for vanishing $1/\kappa_-$. We therefore choose this frequency component to deduce the necessary pulse durations. Since the second order corrections only affect the contrast, and not the Rabi frequency itself, we may determine

the Rabi frequency from the zeroth order component alone,

$$\begin{aligned}\left\langle \frac{1}{2}+\frac{1}{2}\cos(\xi\tau)\right\rangle_{\circlearrowleft} &= \frac{1}{2}+\frac{1}{2}\frac{1}{2I_N+1}\sum_{k=-I_N}^{k=I_N}\frac{1}{\sigma\omega_x\sqrt{2\pi}}\int\exp\left[-\frac{(\kappa_+-k\mu)^2}{2\sigma^2}\right] \\ &\quad\times\cos\left[\left(2+\tfrac{\kappa_+^2}{4}+\tfrac{\kappa_+}{2\kappa_-}-\tfrac{3}{4\kappa_-^2}\right)\tau\right]\mathrm{d}\kappa_+ \\ &\approx \frac{1}{2}+\frac{1}{2}\frac{1}{2I_N+1}\sum_{k=-I_N}^{k=I_N}\cos\left[\tau\left(2-\frac{3}{4\kappa_-^2}+\frac{k\mu}{2\kappa_-}+\frac{k\mu^2}{4}+\frac{\sigma^2}{4}\right)\right],\end{aligned} \tag{7.2.20}$$

where $\sigma = 2\sqrt{2}b/\omega_x$ and $\mu = 2\sqrt{2}A_N/\omega_x$; and the $\circlearrowleft$ subscript denotes an ensemble average over the degrees of freedom present during the application of the microwave field. This will become an important distinction later, when we wish to distinguish between averages over periods of microwave control and periods of free evolution.

Depending on the nitrogen isotope in the NV centre, the Fourier spectrum of the Rabi profile will exhibit two or three peaks, associated with each possible realisation of μ_i, the width of which will be roughly ω_x due to aliasing effects. Since $\omega_x \gg I_n$, the modal component of the spectrum will occur at the centroid of the dominant peaks, namely

$$\bar{\xi} = 2-\frac{3}{4\kappa_-^2}+\frac{\mu^2}{6}+\frac{\sigma^2}{4}, \tag{7.2.21}$$

for the spin-1 ^{14}N nucleus, and

$$\bar{\xi} = 2-\frac{3}{4\kappa_-^2}+\frac{\mu^2}{4}+\frac{\sigma^2}{4}, \tag{7.2.22}$$

for the spin-$\frac{1}{2}$ ^{15}N nucleus. Note also that

$$\frac{1}{\kappa_-} = \frac{\omega_x}{2B_0+b}\approx\frac{\omega_x}{2B_0}. \tag{7.2.23}$$

For comparison with experiments involving diamond nanocrystals and native NV centres in single crystal diamond, we restrict ourselves to the 99.6% abundant ^{14}N

isotope from this point forward. Thus, to achieve a quantum state rotation though an angle of θ, we require a time interval of

$$\begin{aligned} \tau &= \theta/\bar{\xi} \\ &\approx \frac{\theta}{2}\left(1+\frac{3}{8\kappa_-^2}-\frac{\mu^2}{12}-\frac{\sigma^2}{8}\right), \end{aligned} \tag{7.2.24}$$

or in dimensionalised units,

$$t \approx \frac{\theta\sqrt{2}}{\omega_x}\left[1+\frac{3}{32}\left(\frac{\omega_x}{B_0}\right)^2-\frac{2}{3}\left(\frac{A_N}{\omega_x}\right)^2-\left(\frac{b}{\omega_x}\right)^2\right]. \tag{7.2.25}$$

7.2.2 Pulsed microwave-driven evolution

In cases of pulse-based microwave control, the NV spin is typically optically polarised in the $|0\rangle$ state, and subsequently driven into an equal superposition of $|0\rangle$ and $|+1\rangle$ states using using a microwave pulse of suitable length (otherwise known as a $\pi/2$ pulse, or a Hadamard gate in the language of quantum computing). This is followed by $n+1$ (not necessarily equal) periods of evolution separated by n-π pulses, each of which is applied at time t_n. A final $\pi/2$ pulse is used to convert the resulting phase interference into a population difference. The total evolution operator is given by

$$\mathcal{U} = \mathcal{R}_{\frac{\pi}{2}}\mathcal{U}(t,t_n)\mathcal{R}_\pi\ldots\mathcal{R}_\pi\mathcal{U}(0,t_1)\mathcal{R}_{\frac{\pi}{2}}. \tag{7.2.26}$$

Following the optical polarisation of the NV spin in the $|0\rangle$ state, the resultant spin state at time t may be evaluated using

$$|\psi\rangle = \mathcal{U}|0\rangle, \tag{7.2.27}$$

from which we may determine the resulting population of the $|0\rangle$ state after a total free-precession time, t. In this section, we will combine the results for both microwave

driven and free precession intervals, to determine how the pulse errors manifest as abberations in the resulting FID and spin-echo envelopes. For notational clarity we will adopt $\kappa \equiv \langle \kappa_+ \rangle$, $\kappa^2 \equiv \langle \kappa_+^2 \rangle$, $K \equiv \langle 1/\kappa_- \rangle$ and $K^2 \equiv \langle 1/\kappa_-^2 \rangle$.

Periods of imperfect microwave control

Here we consider the effects of the detunings on the evolution of the NV spin under pulsed microwave control. Since we are slightly detuned from the $|0\rangle \leftrightarrow |-1\rangle$ transition and greatly detuned form the $|0\rangle \leftrightarrow |-1\rangle$ transition, we expand the frequency modes of equation 7.2.9 for small κ_+ and large κ_- to second order, giving

$$\lambda_1 \approx 1 + \frac{\kappa_+^2}{8} + \frac{\kappa_+}{4\kappa_-} - \frac{3}{8\kappa_-^2} + \frac{\kappa_+}{2} - \frac{1}{2\kappa_-}, \tag{7.2.28}$$

$$\lambda_2 \approx \kappa_- + \frac{1}{\kappa_-}, \tag{7.2.29}$$

$$\lambda_3 \approx -\left(1 + \frac{1}{8}\kappa_+^2 + \frac{\kappa_+}{4\kappa_-} - \frac{3}{8\kappa_-^2}\right) + \frac{\kappa_+}{2} - \frac{1}{2\kappa_-}. \tag{7.2.30}$$

In the case of the second normal mode, λ_2, we note that the angular frequency grows without bound for an arbitrarily large detuning.

Having determined the Rabi frequency in the previous section, we substitute the pulse duration to achieve a rotation of θ (equation 7.2.24) into the equations of motion (equation 7.2.7 and equation 7.2.8) and make the same asymptotic expansion for small κ^+ and large κ_-, giving a rotation operator of

$$\mathcal{R}(\theta) = \mathcal{R}^{(0)} + \mathcal{R}^{(1)} + \mathcal{R}^{(2)}, \tag{7.2.31}$$

where the zeroth order solution for the transformation matrix is

$$\mathcal{R}^{(0)} = \begin{pmatrix} C & -iS & 0 \\ -iS & C & 0 \\ 0 & 0 & e^{\frac{1}{2}i\theta\kappa_-} \end{pmatrix}, \tag{7.2.32}$$

the first order terms are

$$\begin{aligned}\mathcal{R}^{(1)} &= \frac{\kappa_+}{4}\begin{pmatrix} i(2S+\theta C) & \theta S & 0 \\ \theta S & i(\theta C-2S) & 0 \\ 0 & 0 & 0 \end{pmatrix} \\ &\quad +\frac{1}{4\kappa_-}\begin{pmatrix} 2iS-iC\theta & -S\theta & -4iS \\ -S\theta & -2iS-iC\theta & 4C-4e^{\frac{1}{2}i\theta\kappa_-} \\ -4iS & 4C-4e^{\frac{1}{2}i\theta\kappa_-} & 2ie^{\frac{1}{2}i\theta\kappa_-}\theta \end{pmatrix},\end{aligned} \tag{7.2.33}$$

and the second order terms are

$$\begin{aligned}\mathcal{R}^{(2)} &= \frac{\epsilon^2}{2}\begin{pmatrix} -S\theta & -iC\theta & 0 \\ -iC\theta & -S\theta & 0 \\ 0 & 0 & 0 \end{pmatrix} + \frac{\kappa_+^2}{32}\begin{pmatrix} -\theta(6S+C\theta) & iS\left(\theta^2+4\right)-2iC\theta & 0 \\ iS\left(\theta^2+4\right)-2iC\theta & \theta(2S-C\theta) & 0 \\ 0 & 0 & 0 \end{pmatrix} \\ &+\frac{1}{32\kappa_-^2}\begin{pmatrix} \theta(10S-C\theta) & i\left(6C\theta+S\left(\theta^2+20\right)\right) & -8\left(4C-4e^{\frac{1}{2}i\theta\kappa_-}+S\theta\right) \\ i\left(6C\theta+S\left(\theta^2+20\right)\right) & 2S\theta+32e^{\frac{1}{2}i\theta\kappa_-}-C\left(\theta^2+32\right) & -8i\left(-2S+2e^{\frac{1}{2}i\theta\kappa_-}\theta+C\theta\right) \\ -8\left(4C-4e^{\frac{1}{2}i\theta\kappa_-}+S\theta\right) & -8i\left(-2S+2e^{\frac{1}{2}i\theta\kappa_-}\theta+C\theta\right) & 32C-4e^{\frac{1}{2}i\theta\kappa_-}\left(\theta^2+8\right) \end{pmatrix} \\ &+\frac{\kappa_+}{16\kappa_-}\begin{pmatrix} \theta(C\theta-2S) & -i\left(2C\theta+S\left(\theta^2-4\right)\right) & 4S\theta \\ -i\left(2C\theta+S\left(\theta^2-4\right)\right) & \theta(C\theta-2S) & 4i(C\theta-2S) \\ 4S\theta & 4i(C\theta-2S) & 0 \end{pmatrix}.\end{aligned} \tag{7.2.34}$$

where $\epsilon^2 \equiv \frac{3}{8\kappa_-^2} - \frac{\mu^2}{12} - \frac{\sigma^2}{8}$ is the error in the pulse duration from equation 7.2.24, $C \equiv \cos(\theta/2)$ and $S \equiv \sin(\theta/2)$. To zeroth order, we can see that $\theta = \pi/2$ and $\theta = \pi$ correspond to the Hadamard and bit-flip operations between $|0\rangle$ and $|+1\rangle$ states, as required.

Periods of free precession

Following any fixed period of microwave evolution, the NV spin state will be in a superposition of its magnetic sublevels. The compartiviely weak couplings to the lateral components of the environmental magnetic fields are unable to induce transitions

between these states, and are therefore ignored. As such, free evolution under the axial couplings to the proximate environment will not change the population of the magnetic sublevels, but will change the relative phase between each of them.

The true nature of this free evolution under the influence of a proximate spin bath has been the focus of an extensive research effort in recent years and is the subject of chapter 12. Since, for the purposes of this chapter, we are only interested in modeling the effect of imperfect pulsing on the free evolution, rather than the underlying cause of the free evolution itself, we do not attempt to reproduce these results here. Instead, we are content to subsume the cause of the evolution into an overall effective semi-classical axial field, $B(t)$. The time-dependent free evolution Hamiltonian is then $\mathcal{H} = B(t)\mathcal{S}_z$, giving a corresponding evolution operator of

$$\mathcal{U} = \begin{pmatrix} e^{-i\phi} & 0 & 0 \\ 0 & 1 & 0 \\ 0 & 0 & e^{i\phi} \end{pmatrix}, \tag{7.2.35}$$

where $\phi = \int B(t)\, dt$ is the resulting phase accumulation during some time interval. For cases of higher order pulse sequences, there will be two or more periods of free evolution separated by (not necessarily ideal) π pulses. We denote the phase accumulation of the n^{th} free evolution period ϕ_n. Depending on the pulse sequence chosen, the overall evolution of the quantum state will involve linear combinations of these phases, which must be averaged over the statistical properties of the effective axial field, as detailed below in section 7.2.3.

The imperfect free induction decay pulse sequence

An ideal free induction decay (FID) sequence involves the initialisation of the NV spin into the $|0\rangle$ state followed by a $\pi/2$ rotation to produce an equal superposition of $|0\rangle$ and $|+1\rangle$ states. A phase shift of ϕ_1 then develops on the $|+1\rangle$ state during the free-precession interval, which is followed by a second $\pi/2$ pulse to convert this phase shift into a population difference. Using equations 7.2.26 and 7.2.27 we find the subsequent population of $|0\rangle$ state, to order $\mathcal{O}(\kappa^2, K^2)$, to be

$$\begin{aligned}
\left\langle P_0^{\text{fid}} \right\rangle_{\circlearrowleft}^{(0)} &= \frac{1}{2} - \frac{\cos(\phi_1)}{2} \\
\left\langle P_0^{\text{fid}} \right\rangle_{\circlearrowleft}^{(K,1)} &= \frac{1}{2} K \sin(\phi_1) \\
\left\langle P_0^{\text{fid}} \right\rangle_{\circlearrowleft}^{(\kappa,2)} &= -\frac{1}{4}\kappa^2 \cos(\phi_1) \\
\left\langle P_0^{\text{fid}} \right\rangle_{\circlearrowleft}^{(K,2)} &= -K^2 \left[\sqrt{2}\cos\left(\frac{\pi}{4K} + 2\phi_1\right) - 2\sqrt{2}\cos\left(\frac{\pi}{4K} + \phi_1\right) + \cos\left(\frac{\pi}{2K} + \phi_1\right) \right. \\
&\quad \left. - \cos\left(\frac{\pi}{2K} + 2\phi_1\right) + \sqrt{2}\cos\left(\frac{\pi}{4K}\right) + \frac{9\cos(\phi_1)}{4} - \frac{1}{2}\cos(2\phi_1) - \frac{3}{2} \right],
\end{aligned} \tag{7.2.36}$$

where the $\circlearrowleft$ subscript denotes an ensemble average being taken over the CW degrees of freedom *only*. In the absence of any errors ($\kappa = K = 0$), the population of the $|0\rangle$ state simply oscillates between 1 and 0. Decoherence caused by the external environment will result in this oscillation being damped on a timescale of T_2^*, driving the population of the $|0\rangle$ state to a steady state value of 1/2.

The magnitudes of the $\mathcal{O}(K^2)$ error changes with with the particular realisations of ϕ_1 and K, as shown in figure 7.2, with the extreme error cases occurring for $\phi_1 = \pi$ and $\phi_1 = \pm\pi/2$. Thus, we find the $\mathcal{O}(K^2)$ error to be enclosed within an envelope

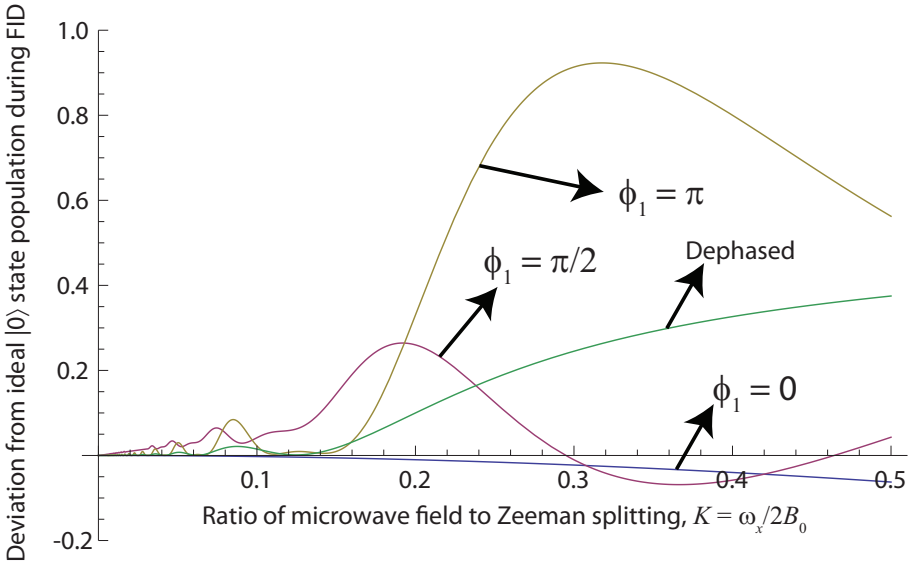

Figure 7.2: Errors introduced during a FID pulse sequence due to excitation of the $|0\rangle \leftrightarrow |-1\rangle$ transition. Different curves represent contours of constant phase accumulation, ϕ, during the free precession interval. When no phase is accumulated ($t = 0$, or $\phi_1 = 0$), this excitation causes an immediate reduction in the $|0\rangle$ state population by an amount $K^2/4$. At points where the population should have ideally transferred entirely to the $|+1\rangle$ state ($\phi_1 = \pi$), the deviation can be as large as $12K^2$. At points where the population should be ideally shared equally between $|0\rangle$ and $|+1\rangle$ states ($\phi_1 = \pi/2$), the associated error is between $K/2 - 2K^2$ and $K/2 + 5K^2$. Finally, when the system has completely dephased, and population is again shared equally between the $|0\rangle$ and $|+1\rangle$ states (but without any phase coherence) the error is between $\frac{K^2}{2}\left(3 - 2\sqrt{2}\right)$ and $\frac{K^2}{2}\left(3 + 2\sqrt{2}\right)$.

given by

$$\max\left\{\left\langle P_0^{\text{fid}}\right\rangle_{\circlearrowleft}^{(K,2)}\right\} = 2K^2 \tag{7.2.37}$$

$$\min\left\{\left\langle P_0^{\text{fid}}\right\rangle_{\circlearrowleft}^{(K,2)}\right\} = -12K^2. \tag{7.2.38}$$

We note some important cases of the error behaviour in an FID sequence. In the absence of any phase accumulation due to free-precession (ie, where $\phi_1 = 0$), we have

$$\left\langle P_0^{\text{fid}}\right\rangle_{\circlearrowleft} = 1 - \frac{K^2}{4} - \frac{\kappa^2}{4}. \tag{7.2.39}$$

This shows an immediate reduction in contrast by an amount $(K^2+\kappa^2)/4$, due to both broadening of the $|0\rangle \leftrightarrow |+1\rangle$ transition, and leakage into the $|0\rangle$ state via the $|0\rangle \leftrightarrow |-1\rangle$ transition during the pulsing intervals.

At points of maximal phase interference, where $\phi_1 = \pi$, we find

$$\left\langle P_0^{\text{fid}} \right\rangle_{\circlearrowleft} = \frac{1}{4}\kappa^2 + \frac{1}{4}K^2\left[17 - 16\sqrt{2}\cos\left(\frac{\pi}{4K}\right) + 8\cos\left(\frac{\pi}{2K}\right)\right], \quad (7.2.40)$$

which, depending on the exact value of K, lies somewhere between a lower bound of $(\kappa^2+K^2)/4$ and an upper bound of $\kappa^2/4 + 12K^2$. Whereas before, in the absence of any pulsing errors, we had $0 \leq \left\langle P_0^{\text{fid}} \right\rangle \leq 1$, these results show that in a best case scenario, we now have that the FID profile will oscillate between

$$0 + \frac{K^2}{4} + \frac{\kappa^2}{4} \leq \left\langle P_0^{\text{fid}} \right\rangle_{\circlearrowleft} \leq 1 - \frac{K^2}{4} - \frac{\kappa^2}{4}, \quad (7.2.41)$$

and in a worst case scenario we have

$$0 + 12K^2 + \frac{\kappa^2}{4} \leq \left\langle P_0^{\text{fid}} \right\rangle_{\circlearrowleft} \leq 1 - \frac{K^2}{4} - \frac{\kappa^2}{4}. \quad (7.2.42)$$

When the system has fully dephased, all sine and cosine terms involving ϕ_1 will have averaged to zero, giving

$$\left\langle P_0^{\text{fid}} \right\rangle_{\circlearrowleft}^{t\to\infty} = \frac{1}{2} + \frac{K^2}{2}\left(3 - 2\sqrt{2}\cos\left(\frac{\pi}{4K}\right)\right). \quad (7.2.43)$$

This implies that the steady state population of the $|0\rangle$ state will be somewhere between $\frac{1}{2} + \frac{K^2}{2}\left(3 \pm 2\sqrt{2}\right)$, instead of $\frac{1}{2}$.

The imperfect spin-echo pulse sequence

An ideal spin-echo pulse sequence is essentially a concatenation of two FID sequences, resulting in two equal periods of free evolution, separated by a π pulse, whose presence

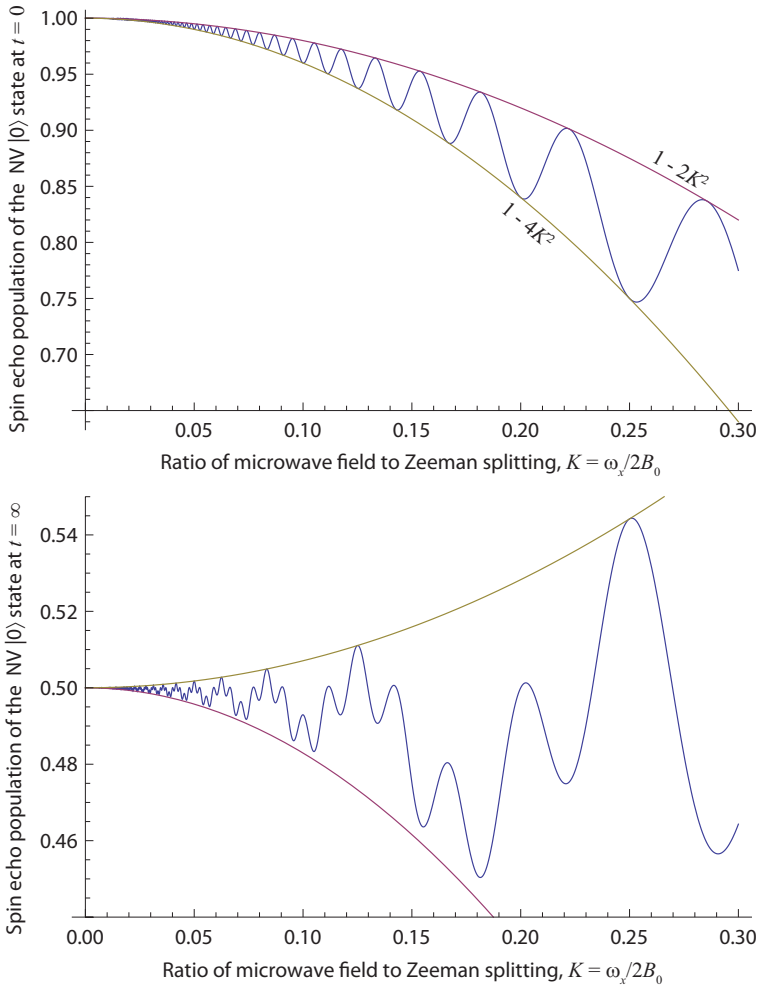

Figure 7.3: Spin echo errors due to population leakage of the NV spin into its $|-1\rangle$ state. (a) Magnitude of the error introduced in the absence of any free precession ($t = 0$) as a function of $K = \omega_x/2B_0$. (b) Steady state value of the population of the $|0\rangle$ state after the NV spin has completely dephased, as a function of $K = \omega_x/2B_0$. In the absence of any errors, the steady state value would be 1/2.

refocuses the effect of any static magnetic noise, thereby increasing the coherence time from T_2^* to T_2. As we will show, pulse errors result in a non-trivial component of the spin-echo profile behaving as a FID, which decays on a timescale of T_2^*, resulting in a further reduction in contrast.

Using equations 7.2.26 and 7.2.27 we find the subsequent population of $|0\rangle$ state, to order $\mathcal{O}\left(\kappa^2, K^2\right)$, to be

$$\begin{aligned}
\langle P_0^{\mathrm{se}}\rangle_{\circlearrowleft}^{(0)} &= \frac{1}{2}+\frac{1}{2}\cos\left(\phi_1-\phi_2\right)\\
\langle P_0^{\mathrm{se}}\rangle_{\circlearrowleft}^{(\kappa,2)} &= \frac{\kappa^2}{8}\Big[\cos\left(\phi_1+\phi_2\right)-\cos\left(\phi_1-\phi_2\right)\Big]\\
\langle P_0^{\mathrm{se}}\rangle_{\circlearrowleft}^{(K,2)} &= \frac{K^2}{8}\Big[-4\sqrt{2}\cos\left(\tfrac{\pi}{4K}+\phi_1\right)-4\cos\left(\tfrac{\pi}{2K}+\phi_1\right)+4\cos\left(\tfrac{\pi}{2K}+2\phi_1\right)\\
&+4\sqrt{2}\cos\left(\tfrac{\pi}{4K}+\phi_1-\phi_2\right)-4\sqrt{2}\cos\left(\tfrac{\pi}{4K}+2\phi_1-\phi_2\right)+4\sqrt{2}\cos\left(\tfrac{\pi}{4K}-\phi_1+\phi_2\right)\\
&-4\sqrt{2}\cos\left(\tfrac{3\pi}{4K}+2\phi_1\right)-4\sqrt{2}\cos\left(\tfrac{\pi}{4K}+\phi_2\right)-4\cos\left(\tfrac{\pi}{2K}+\phi_2\right)+4\cos\left(\tfrac{\pi}{2K}+2\phi_2\right)\\
&+8\cos\left(\tfrac{\pi}{2K}+\phi_1+\phi_2\right)-8\sqrt{2}\cos\left(\tfrac{3\pi}{4K}+\phi_1+\phi_2\right)-4\cos\left(\tfrac{\pi}{2K}+2\phi_1+\phi_2\right)\\
&+8\sqrt{2}\cos\left(\tfrac{3\pi}{4K}+2\phi_1+\phi_2\right)-8\cos\left(\tfrac{\pi}{K}+2\phi_1+\phi_2\right)-4\sqrt{2}\cos\left(\tfrac{\pi}{4K}-\phi_1+2\phi_2\right)\\
&-4\cos\left(\tfrac{\pi}{2K}+\phi_1+2\phi_2\right)+8\sqrt{2}\cos\left(\tfrac{3\pi}{4K}+\phi_1+2\phi_2\right)-8\cos\left(\tfrac{\pi}{K}+\phi_1+2\phi_2\right)\\
&-4\sqrt{2}\cos\left(\tfrac{3\pi}{4K}+2\phi_2\right)+8\sqrt{2}\cos\left(\tfrac{\pi}{4K}\right)+4\cos\left(\phi_1\right)+4\cos\left(\phi_1-2\phi_2\right)\\
&-17\cos\left(\phi_1-\phi_2\right)+4\cos\left(2\phi_1-\phi_2\right)+4\cos\left(\phi_2\right)+\cos\left(\phi_1+\phi_2\right)-16\Big].
\end{aligned} \tag{7.2.44}$$

Errors of order $\mathcal{O}(\kappa)$ and $\mathcal{O}(K)$ are zero. The error arising in the absence of any free precession ($\phi_1=\phi_2=0$) is

$$\langle P_0^{\mathrm{se}}(0)\rangle_{\circlearrowleft} = 1-2K^2-2K^2\cos^2\left(\frac{\pi}{K}\right), \tag{7.2.45}$$

yielding a worst-case error and corresponding decrease in contrast of $-4K^2$. When

the system has fully dephased, it will do so to a final value of

$$\lim_{t\to\infty}\langle P_0^{\rm se}\rangle_{\circlearrowleft} \;=\; \frac{1}{2}+\frac{1}{2}K^2\left(\sqrt{2}\cos\left(\frac{\pi}{2K}\right)+\cos\left(\frac{2\pi}{K}\right)-1\right), \qquad (7.2.46)$$

yielding an error range of $\frac{1}{\sqrt{2}}\left(\frac{\omega_x}{B_0}\right)^2\left[-(1+\sqrt{2}),\,1\right]$. As κ does not appear in either of the $t=0$ or $t=\infty$ expressions, both of the associated errors are directly attributable to population of the $|-1\rangle$ state.

Of perhaps more interest however, is the non-zero DC phase accumulation that arises due to the non-ideal pulses. Whereas in an ideal spin-echo experiment, the π pulse is used to refocus any DC couplings, the imperfect π-pulse causes a small component of the otherwise ideal spin-echo sequence to behave as a FID sequence. This effect can be seen in equation 7.2.44 in all terms that do not have a phase accumulation of $\phi_1-\phi_2$, ensuring the DC phase accumulation is non-zero. The phases alone, ϕ_1 and ϕ_2, as well as their sum, $\phi_1+\phi_2$, however, contain static contributions involving frequency components of order B_0, I, etc. As such, the spin-echo curve will show rapid oscillations at these frequencies with amplitudes of order $\langle\kappa^2\rangle$ and $\langle K^2\rangle$. Such behaviour has been observed in experiments, particularly those detailed in chapter 5, and is discussed in the following section.

By definition, this FID like behaviour decays on timescales of T_2^*, beyond which, but prior to complete decoherence ($T_2^*<t<T_2$) we are left only with terms involving differences in ϕ_1 and ϕ_2,

$$\begin{aligned}
\langle P_0^{\rm se}\rangle_{\circlearrowleft}^{(0)} &= 1\\
\langle P_0^{\rm se}\rangle_{\circlearrowleft}^{(\kappa,2)} &= -\frac{\kappa^2}{8}\\
\langle P_0^{\rm se}\rangle_{\circlearrowleft}^{(K,2)} &= \frac{K^2}{8}\left[16\sqrt{2}\cos\left(\tfrac{\pi}{4K}\right)-17-16\right].
\end{aligned} \qquad (7.2.47)$$

To see the effects of errors at all timescales in full detail, we must include a model

of decoherence to account for the dynamic behaviour of the phase accumulations arising from the surrounding spin bath during periods of free precession.

7.2.3 Including decoherence

As the pulse times are extremely short compared with the environmental correlation time, we may assume the environment is effectively quasi static over each pulse duration, and employ the same probability distribution for the bath-induced detunings as was used in the Rabi analysis (equation 7.2.18). For evaluation of the phase interferences that develop during free precession, we are interested in evaluating the ensemble averages of quantities of the form $\cos(a_\kappa + \Phi)$ (see equations 7.2.36 and 7.2.44), where a_K is an additional phase shift (possibly 0) resulting from population leakage of the NV spin into the $|-1\rangle$ state; and Φ may represent any linear combination of the ϕ_n (this statement will be made exact in what follows).

Because the effective field arises from a large number of individual sources, by the central limit theorem, the amplitude of the resulting phase shift will be normally distributed, by definition, according to

$$\Pr(\Phi) = \frac{1}{\Delta\Phi\sqrt{2\pi}} \exp\left[-\frac{(\Phi - \langle\Phi\rangle)^2}{2\Delta\Phi^2}\right], \tag{7.2.48}$$

where $\Delta\Phi^2 = \langle\Phi^2\rangle - \langle\Phi\rangle^2$. Thus

$$\begin{aligned}\left\langle\cos(a_\kappa + \Phi)\right\rangle &= \frac{1}{\Delta\Phi\sqrt{2\pi}} \int_{-\infty}^{\infty} \exp\left[-\frac{(\Phi - \langle\Phi\rangle)^2}{2\Delta\Phi^2}\right] \cos(a_\kappa + \Phi)\, \mathrm{d}\Phi \\ &= \exp\left(-\frac{\langle\Phi^2\rangle - \langle\Phi\rangle^2}{2}\right) \cos\big(a_\kappa + \langle\Phi\rangle\big),\end{aligned} \tag{7.2.49}$$

We therefore wish to relate the statistical moments of the phase shifts developed during the free-precession intervals, Φ, to the dynamic properties of the field. To

do this, we decompose the field into its static and fluctuating components, $B(t) = B_{\rm dc} + \sum_i b_i(t)$, where $b_i(t)$ is normally distributed with zero mean at any instant in time, t, as above. The summation index represents the fact that more than one fluctuating field may be present, for example, due to the internal spin bath, surface spins, and external target systems. In the case of electron spin baths, the associated autocorrelation function will exhibit an exponential decay[2],

$$\big\langle b_{\rm e}(t')b_{\rm e}(t'')\big\rangle \;=\; \big\langle b_e^2\big\rangle e^{-f_e|\,t'-t''|}, \tag{7.2.50}$$

where $1/f_e$ is the correlation time for the electron bath. This is not true for nuclear spin baths however, where, for reasons detailed in chapter 12, a linear exponential decay does not describe the autocorrelation function of the environment. For this case, following the analysis of chapter 4, we employ a Gaussian shaped autocorrelation function

$$\big\langle b_{\rm n}(t')b_{\rm n}(t'')\big\rangle \;=\; \big\langle b_n^2\big\rangle e^{-f_n^2(\,t'-t'')^2}, \tag{7.2.51}$$

If we restrict ourselves to FID and spin-echo pulse sequences, we will only be interested in evaluating sums and differences of at most two phase shifts, ϕ_1 and ϕ_2. For the first moments of the phase shifts, we have

$$\begin{aligned}
\big\langle\phi_1\big\rangle = \big\langle\phi_2\big\rangle = \big\langle 2\phi_1-\phi_2\big\rangle = \big\langle 2\phi_2-\phi_1\big\rangle &= \frac{1}{2}B_{\rm dc}t,\\
\big\langle\phi_1+\phi_2\big\rangle = 2\big\langle\phi_1\big\rangle = 2\big\langle\phi_2\big\rangle &= B_{\rm dc}t,\\
\big\langle\phi_1-\phi_2\big\rangle = \big\langle\phi_2-\phi_1\big\rangle &= 0,\\
\big\langle\phi_1+2\phi_2\big\rangle = \big\langle 2\phi_1+\phi_2\big\rangle &= \frac{3}{2}B_{\rm dc}t,
\end{aligned}$$

[2]This is a commonly accepted result in the literature (see, for example, refs. [dSD03a, dSD03b, TCC+08, HDF+08, DFHA09, HHCH10, LWR+10]), although a complete quantum mechanical proof has never been produced. Such a proof is given in chapter 12

and for the second moments, we assume that the distinct spin baths are uncorrelated with each other, ie $\langle b_i(t')b_j(t'')\rangle = 0$ if $i \neq j$. Thus, for an electron spin bath we find

$$\begin{aligned}\langle B(t')B(t'')\rangle &= \langle [B_{\rm dc} + b(t')]\,[B_{\rm dc} + b(t'')]\rangle \\ &= B_{\rm dc}^2 + \left\langle b_{\rm e}^2\right\rangle e^{-f_{\rm e}|\,t'-t''|}, \end{aligned} \tag{7.2.52}$$

Hence, the resulting second moments of the phase shifts are given by

$$\begin{aligned}\left\langle \phi_1^2\right\rangle = \left\langle \phi_2^2\right\rangle &= \left\langle \phi_1\right\rangle^2 - \frac{\left\langle b_{\rm e}^2\right\rangle}{f_{\rm e}^2}\Big(2 - f_{\rm e}t - 2e^{-f_{\rm e}t/2}\Big), \\ \left\langle (\phi_1+\phi_2)^2\right\rangle &= \left\langle \phi_1+\phi_2\right\rangle^2 - \frac{\left\langle b_{\rm e}^2\right\rangle}{f_{\rm e}^2}\Big(2 - 2f_{\rm e}t - 2e^{-f_{\rm e}t}\Big), \\ \left\langle (\phi_1-\phi_2)^2\right\rangle &= -\frac{\left\langle b_{\rm e}^2\right\rangle}{f_{\rm e}^2}\Big(6 - 2f_{\rm e}t + 2e^{-f_{\rm e}t} - 8e^{-f_{\rm e}t/2}\Big), \\ \left\langle (2\phi_1+\phi_2)^2\right\rangle &= \left\langle 2\phi_1+\phi_2\right\rangle^2 - \frac{\left\langle b_{\rm e}^2\right\rangle}{f_{\rm e}^2}\Big(6 - 5f_{\rm e}t - 4e^{-f_{\rm e}t} - 2e^{-f_{\rm e}t/2}\Big), \\ \left\langle (2\phi_1-\phi_2)^2\right\rangle &= \left\langle 2\phi_1-\phi_2\right\rangle^2 - \frac{\left\langle b_{\rm e}^2\right\rangle}{f_{\rm e}^2}\Big(14 - 5f_{\rm e}t + 4e^{-f_{\rm e}t} - 18e^{-f_{\rm e}t/2}\Big). \end{aligned} \tag{7.2.53}$$

This approach gives us all of the tools required to perform a full analysis of the errors exhibited by pulse-based NV experiments, which is the focus of the following section.

7.3 Applications to physical systems and comparison with experiment

We now apply the analysis developed in the preceding sections to three practically relevant NV based systems: the ppm nitrogen electron donor spin bath in type 1b diamond, the 1.1% ^{13}C nuclear spin bath in ultra-pure low nitrogen diamond, and the surface electron spin bath of diamond nanocrystals. In the case of the latter,

we make a direct comparison between theory and experiment, which demonstrate excellent agreement.

7.3.1 Type 1-b bulk diamond crystal (ppm nitrogen-donor electron spin bath)

In this section, we focus on the specific case of a spin echo experiment in the presence of a naturally occurring electron bath. This bath arises due to the presence of naturally occurring nitrogen electron donor impurities, and yields an inhomogenous linewidth of approximately $b_e \approx 2\,\mathrm{MHz}$ (see chapter 3). Similarly, the width of the frequency spectrum will be of roughly the same magnitude, $f_e \approx 1\,\mathrm{MHz}$, due to the distance between nearest neighbour pairs of electrons having the same spatial distribution as that from the NV to its nearest electron.

The choice of microwave field strength, ω_x, will have complementary effects on the two sources of error. For a given B_0, increasing ω_x will broaden the Rabi frequency, thereby more broadly encompassing the detunings associated with the $|0\rangle \rightarrow |+1\rangle$ transition, and reducing κ. On the other hand, having a broader excitation range will increase the overlap between the two NV spin state transitions, increasing K, and consequently, the probability of leakage into, the $|-1\rangle$ state. Typical π pulse times are of the order of $0.1\,\mu\mathrm{s}$, but may be as fast as a few nanoseconds [FDT+09]. We firstly consider two limiting test cases in which errors may be exclusively attributed to either detuning or population leakage effects, as depicted by figures 7.4(a) and (b) respectively, and then follow with an example employing a typical experimental parameter regime.

In the first case (figure 7.4(a)), we choose a sufficiently large magnetic field strength

(1000 G, or 2800 MHz) to almost completely detune the $|0\rangle \leftrightarrow |-1\rangle$ transition from excitation by the 50 MHz microwave field. As such, we see that the steady state population of the $|0\rangle$ and $|+1\rangle$ states are both effectively 0.5, meaning the population of the $|-1\rangle$ state is negligible. Additionally, the choice of a narrow microwave field only just encompasses the dipolar-broadened $|0\rangle \leftrightarrow |+1\rangle$ transition, leading to significant detuning errors, and a significant reduction in contrast for times of $T_2^* < t < T_2$ (recall from chapter 4 that $T_2^* = \sqrt{2}/b_e = 700\,\text{ns}$).

In the second case (figure 7.4(b)), we choose a comparatively large microwave field (200 MHz), and small magnetic field (150 G, or 420 MHz). In this cased we manage to sufficiently encompass the dipolar-broadened $|0\rangle \leftrightarrow |+1\rangle$ transition, meaning that detuning errors are suppressed to a large degree, as evidenced by the fact that the rapid oscillations persist for times greater than $T_2^* = 700\,\text{ns}$. At the same time, we achieve an appreciable excitation of the $|0\rangle \leftrightarrow |-1\rangle$ transition, leading to significant population of $|-1\rangle$ state, to the point where the population is appreciably shared amongst the three NV spin states ($P_{+1} = P_0 = 0.44$, $P_{-1} = 0.12$).

As our final example in type 1-b diamond (figure 7.4(c)-(e)), we take the π pulse time to be $t_\pi = 72\,\text{ns}$, and $\frac{\pi}{2} = 36\,\text{ns}$, giving a microwave field strength of $\omega_x \approx 2\sqrt{2}\frac{\pi}{t_\pi} = 123\,\text{MHz}$, together with a background field strength of $80\,\text{G} = 225\,\text{MHz}$. This regime shows that both sources of error are present under typical experimental conditions, resulting in both a large reduction in contrast and a large population leakage into the $|-1\rangle$ state.

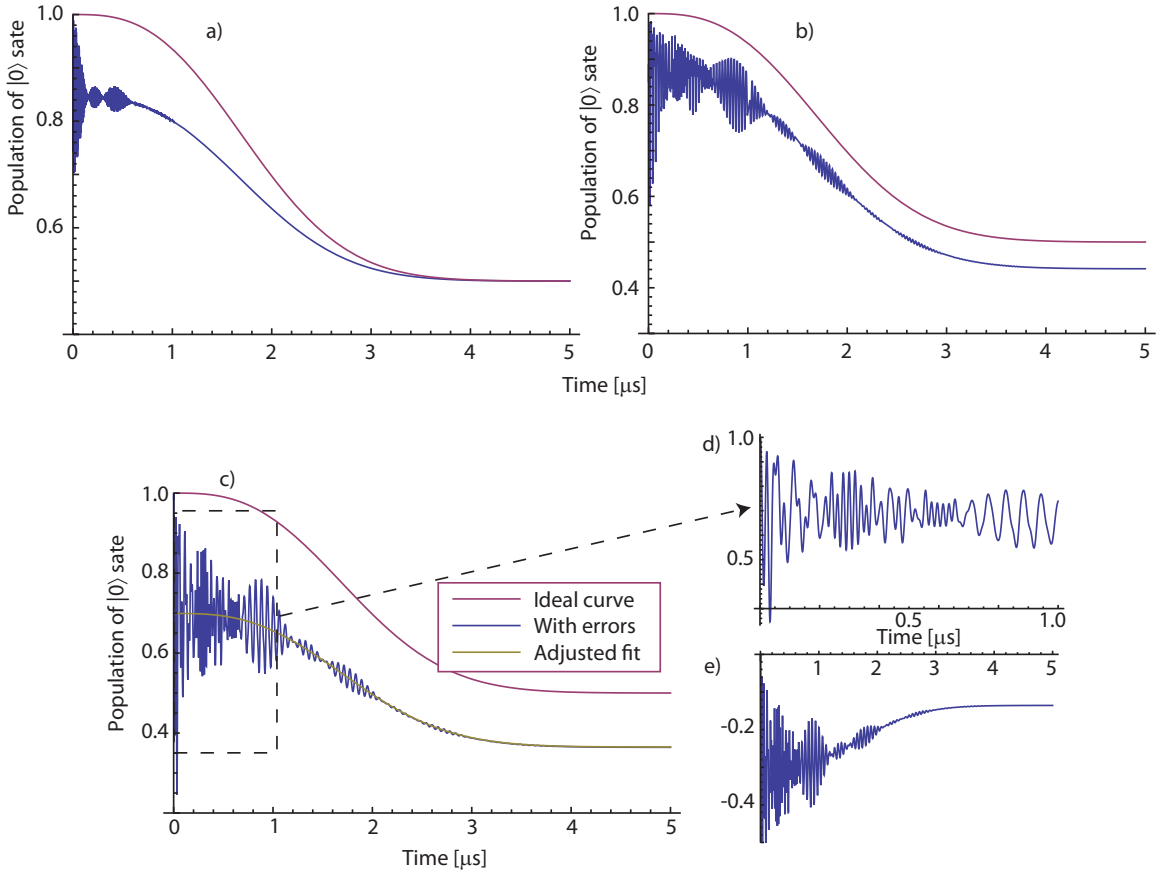

Figure 7.4: Analytic spin-echo profiles for a typical nitrogen spin bath, with $b = 2\,\mathrm{MHz}$ $f = 0.5\,\mathrm{MHz}$. (a) Spin echo profile for the case of $\omega_x = 50\,\mathrm{MHz}$, and $B_0 = 2800\,\mathrm{MHz}$ (1000 G), demonstrating a large detuning error, but negligible population leakage into the NV $|-1\rangle$ state. (b) Spin echo profile for the case of $\omega_x = 200\,\mathrm{MHz}$, and $B_0 = 420\,\mathrm{MHz}$ (150 G), demonstrating a very small detuning error, but a significant population leakage into the NV $|-1\rangle$ state. (c) Spin echo profile for the experimentally relevant case of $\omega_x = 123\,\mathrm{MHz}$ ($t_\pi = 72\,\mathrm{ns}$), and $B_0 = 225\,\mathrm{MHz}$ (80 G), showing the contrast between the ideal cases and that with errors introduced via broadening of the resonant transition and excitation of the non-resonant transition. (d) Close up of the short time modulation of the spin echo profile from (c). (e) Error introduced to the spin echo profile. Whist the full profile decays on a timescale of T_2, the majority of the error decays on a timescale of $T_2^* = 0.7\,\mu\mathrm{s}$ due to the imperfect π pulse.

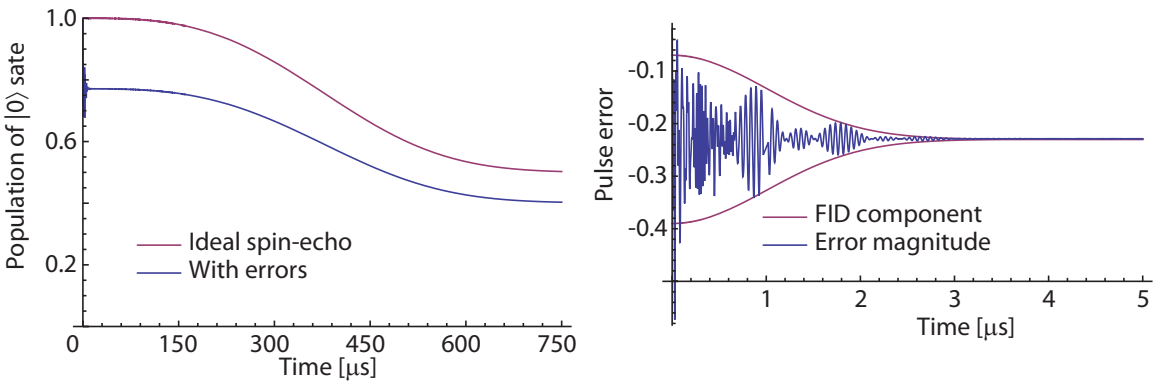

Figure 7.5: Results for a naturally occurring ^{13}C spin bath with $b = 1\,\text{MHz}$ $f = 0.5\,\text{MHz}$, $\omega_x = 123\,\text{MHz}$ ($t_\pi = 72\,\text{ns}$), and $B_0 = 80\,\text{MHz}$ (12 G), showing the contrast between the ideal cases and that with errors introduced via broadening of the resonant transition and excitation of the non-resonant transition. (b) Error introduced to the spin echo profile. Whist the full profile decays on a timescale of T_2, the majority of the error decays on a timescale of $T_2^* = 0.7\,\mu\text{s}$ due to the imperfect π pulse.

7.3.2 Ultra-pure bulk diamond (^{13}C nuclear spin bath)

As a second example system, we consider the case of a naturally occurring 1.1% ^{13}C nuclear spin bath in ultra-pure diamond crystal. Despite having a similar NV-bath couplings as the nitrogen case considered above, the intra-bath couplings are roughly 4 orders of magnitude slower. As a result, spin-echo decay times, T_2, are 2 orders of magnitude longer than FID times, T_2^*, allowing us to make a clear distinction between errors associated with microwave detuning and those associate with population leakage.

The analytic spin-echo results for the ^{13}C nuclear spin bath are plotted in figure 7.5(a) for the case of microwave and background field strengths of $\omega_x = 123\,\text{MHz}$ and $B_0 = 80\,\text{G} = 225\,\text{MHz}$ respectively. In this case, we can see that the rapid oscillatory motion decays on a timescale of $T_2^* = 1.4\,\mu\text{s}$ (figure 7.5(b)), and the full

profile decays to a final value of $P_0(t \to \infty) = 0.404$, implying a resulting $|-1\rangle$ state population of $P_{-1}(t \to \infty) = 0.192$.

7.3.3 Diamond nanocrystals

As a final example, we consider the case of an NV centre residing sufficiently close to a nanodiamond surface, such that the surface spin bath is predominantly responsible for its decoherence. Following the investigation conducted in chapter 5, we choose a surface spin relaxation rate of 200 MHz and an RMS surface field strength of 10 MHz, corresponding to an effective surface spin density of $10\,\mathrm{nm}^{-2}$ and an NV depth of 4 nm. The experimental results are shown in figure 7.6(a) for the case of $\omega_x = 123\,\mathrm{MHz}$ and $B_0 = 100\,\mathrm{G} = 280\,\mathrm{MHz}$, and the corresponding analytic results for these conditions are shown in figure 7.6(b). From this we can see that the non-resonant $|0\rangle \leftrightarrow |-1\rangle$ transition has been sufficiently excited to give a final $|-1\rangle$ state population of $P_{-1}(t \to \infty) = 0.06$. By evaluating the analytic result at the same timepoints used in the experiment (multiples of 49 ns), as shown in figure 7.6(c), we see excellent agreement between theory an experiment.

7.4 Discussion and conclusions

In this chapter, we have investigated the effects of non-ideal pulses on ODMR, Rabi, FID and spin-echo based protocols as applied to the NV spin. The associated errors were found to arise from two effects:

1. Detuning errors arising from the presence of both the nitrogen nuclear spin in the NV centre and the surrounding spin bath, resulting in incomplete $\pi/2$ and

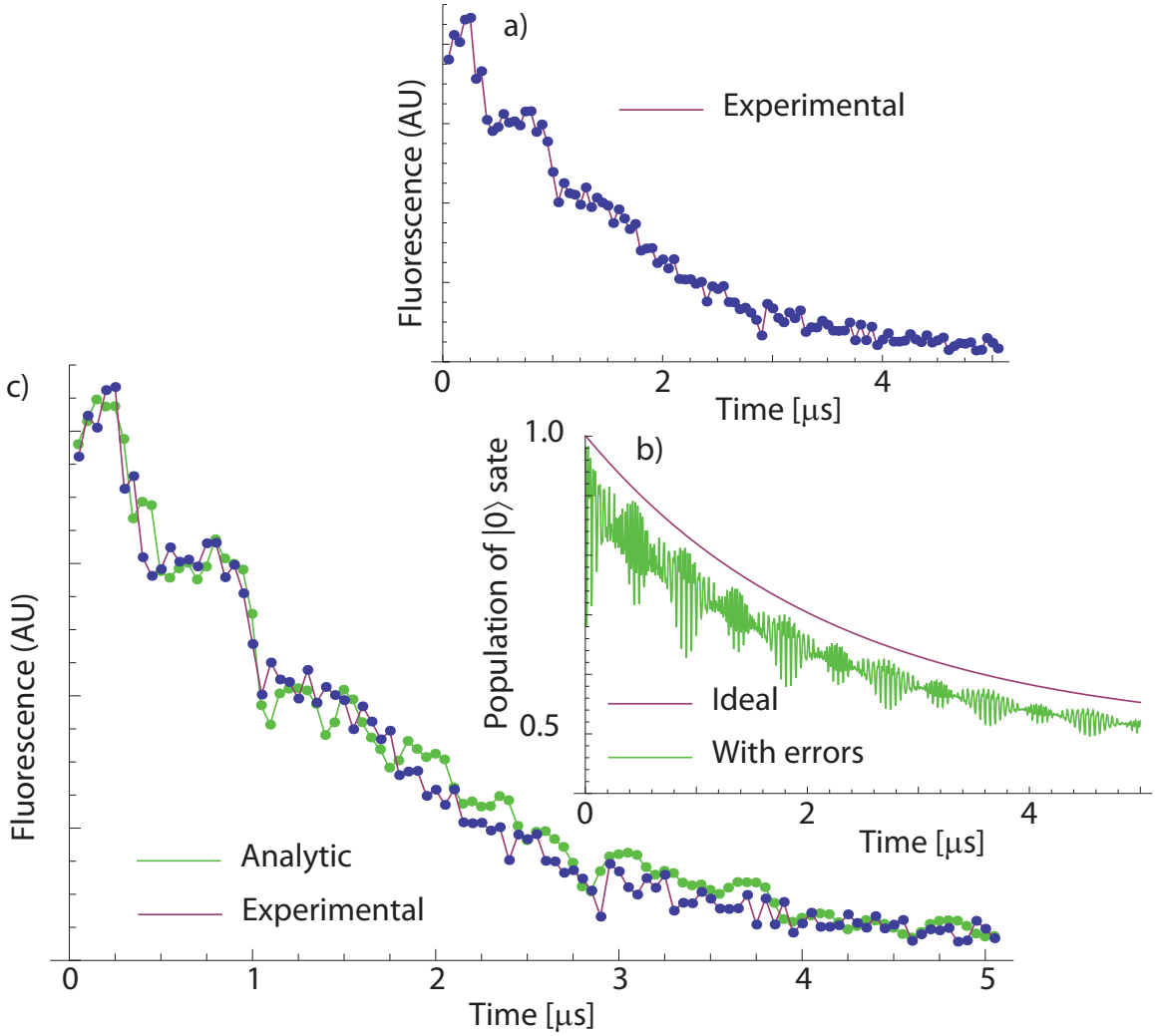

Figure 7.6: Comparison of analytic and experimental spin-echo results for the case of a diamond nanocrystal with $\omega_x = 123\,\mathrm{MHz}$, and $B_0 = 100\,\mathrm{G}$. (a) Analytic results showing the discrepancy between an ideal spin-echo pulse sequence (purple), and that containing pulse errors due to population leakage and microwave detuning (green). (b)Experimental results for a spin-echo pulse sequence conducted on an NV centre in a diamond nanocrystal at $\omega_x = 123\,\mathrm{MHz}$, and $B_0 = 100\,\mathrm{G}$. (c) Analytic curve (green), as evaluated at the same time points as the experimental curve (purple), showing excellent agreement between experiment and theory.

π pulses in the $\{|0\rangle, |+1\rangle\}$ manifold, leading to a small component of the spin-echo sequence behaving as a FID. As such, the resulting spin-echo envelope will contain rapidly oscillating components associated with DC shifts due to the hyperfine coupling to the adjacent nitrogen nuclear spin, eventually leading to a reduction in contrast on timescales beyond which the FID component has decayed ($t > T_2^*$).

2. Population leakage into the NV $|-1\rangle$ state due to non-resonant excitation of the $|0\rangle \leftrightarrow |-1\rangle$ transition, resulting in an overall reduction in the population associated with the $\{|0\rangle, |+1\rangle\}$ manifold, and hence a reduction in measurement contrast.

The results of this chapter not only give a accurate description of previously unexplained experimental artifacts, but also detail the manner in which these artifacts, and the associated errors, may be suppressed. Namely, we have shown that, by using a large microwave field to encompass the broadened features of $|0\rangle \leftrightarrow |+1\rangle$ transition, we may eliminate the likelyhood of incomplete control pulses; and by simultaneously incorporating a sufficiently large DC field, we may detune the $|0\rangle \leftrightarrow |-1\rangle$ transition, thereby suppressing population leakage into the $|-1\rangle$ state.

Chapter 8

Monitoring ion channel function in real time through quantum decoherence

In drug discovery there is a clear and urgent need for detection of cell membrane ion-channel operation with wide-field capability. Existing techniques are generally invasive, or require specialized nano-structures. This is an important problem in biology and which may lend itself to the sensing capabilities of the NV centre. In previous chapters we have shown the nitrogen-vacancy (NV) centre in nano-diamond to be of great interest as a single-atom quantum probe for nanoscale processes. However, until now we have not addressed the quantum behaviour of a NV probe in a complex biological environment. In this chapter we explore the quantum dynamics of a NV probe in proximity to the ion channel, lipid bilayer and surrounding aqueous environment. Our theoretical results indicate that real-time detection of ion channel operation at millisecond resolution is possible by directly monitoring the quantum decoherence of the NV probe. With the potential to scan and scale-up to an array-based system this conclusion may have wide ranging implications for nanoscale biology and drug discovery. The results of this chapter have been published in reference [HHC+10].

8.1 Introduction

The cell membrane is a critical regulator of life. Its importance is reflected by the fact that the majority of drugs target membrane interactions [RTL+08]. Ion channels allow for passive and selective diffusion of ions across the cell membrane [ITAY02], while ion pumps actively create and maintain the potential gradients across the membranes of living cells [BSS+08]. To monitor the effect of new drugs and drug delivery mechanisms a wide field ion channel monitoring capability is essential [Lun06]. However, there are significant challenges facing existing techniques stemming from the fact that membrane proteins, hosted in a lipid bilayer, require a complex environment to preserve their structural and functional integrity [RTL+08, FFL02, YSS+05, JS09]. Patch clamp techniques are generally invasive, quantitatively inaccurate, and difficult to scale up [Dam05, Qui02], while black lipid membranes [MRTW62, MWRT63] often suffer from stability issues and can only host a limited number of membrane proteins.

Instead of altering the way ion channels and the lipid membrane are presented or even assembled for detection, our approach is to consider a novel and inherently non-invasive in-situ detection method based on the quantum properties of a single-atom probe. The atomic probe is a single nitrogen-vacancy (NV) centre in a nanodiamond crystal which is highly sensitive to magnetic fields, and shows great promise as a magnetometer for nano-bio sensing (see chapters 2 and 3 for a review, and chapter 4 for the specific case of fluctuating magnetic fields). The NV centre in nanodiamond has already been used as a fluorescence marker in biological systems [YKC+05, NZJ+07, FLC+07, CPC+07, FGJ+08]. However, up to now there has been no analysis of the effect of the biological environment on the quantum dynamics of the NV centre – such considerations are critical to nano-bio magnetometry applications.

We explore these issues in detail, and furthermore show that the rate of quantum decoherence of the NV centre is sufficiently sensitive to the flow of ions through the channel to allow real-time detection, over and above the myriad background effects. In this context, decoherence refers to the loss of quantum coherence between magnetic sub-levels of the NV atomic system due to interactions with an environment. Such superpositions of quantum states are generally fleeting in nature due to interactions with the environment, and the degree and timescale over which such quantum coherence is lost can be measured precisely. The immediate consequence of the fragility of the quantum coherence phenomenon is that detecting the loss of quantum coherence (decoherence) in such a single atom probe offers a unique monitor of biological function at the nanoscale.

The NV probe (figure 8.1) consists of a diamond nano-crystal containing a nitrogen-vacancy (NV) defect at the end of an AFM tip, as recently demonstrated [BCK$^+$08]. For biological applications a quantum probe must be submersible to be brought within nanometers of the sample structure, hence the NV system locked and protected in the ultra-stable diamond matrix (figure 8.1 (a)) is the system of choice. The NV centre alone offers the controllable, robust and persistent quantum properties such room temperature nano-sensing applications will demand, as well as zero toxicity in a biological environment [YKC$^+$05, NZJ$^+$07, FLC$^+$07]. As has been discussed in previous chapters, theoretical proposals for the use of diamond nanocrystals as sensitive nanoscale magnetometers [CB05, Deg08, TCC$^+$08] have been followed by proof-of-principle experiments [MSH$^+$08, BCK$^+$08, BNT$^+$09]. However, such nanoscale magnetometers employ only a fraction of the quantum resources at hand and do not have the sensitivity to detect the minute magnetic moment fluctuations associated with ion channel

operation. In contrast, our results show that measuring the quantum decoherence of the NV induced by the ion flux provides a highly sensitive monitoring capability for the ion channel problem, well beyond the limits of magnetometer time-averaged field sensitivity [HCHH09]. To determine the sensitivity of the NV probe to the ion channel signal we describe the lipid membrane, embedded ion channels, and the immediate surroundings as a fluctuating electromagnetic environment and quantitatively assess each effect on the quantum coherence of the NV centre. We consider the diffusion of nuclei, atoms and molecules in the immediate surroundings of the nanocrystal and the extent to which each source will decohere the quantum state of the NV. We find that, over and above these background sources, the decoherence of the NV spin levels is highly sensitive to the ion flux through a single ion channel. Our theoretical findings demonstrate the potential of this approach to revolutionize the way ion channels and potentially other membrane bound proteins or interacting species are characterized and measured, particularly when scale-up and scanning capabilities are considered.

This chapter is organized as follows. We begin by describing the quantum decoherence imaging system (figure 8.1) implemented using an NV centre in a realistic technology platform. The biological system is described in detail, and estimates of the sensitivity of the NV decoherence to various magnetic field sources are made which indicate the ability to detect ion channel switch-on/off events. Finally, we conduct large scale numerical simulations of the time evolution of the NV spin system including all magnetic field generating processes. This acts to verify the analytic picture, and provides quantitative results for the monitoring and scanning capabilities of the system.

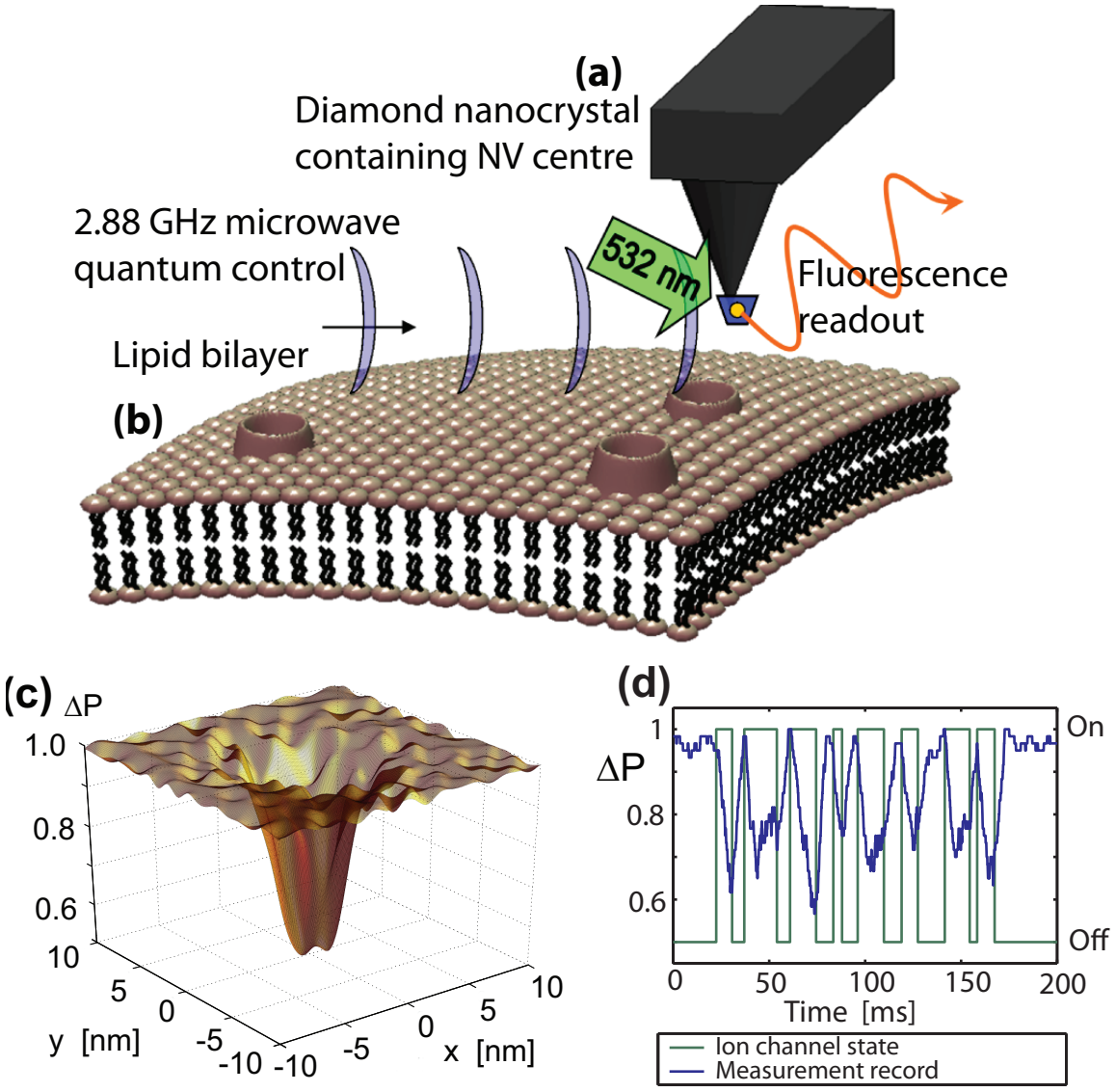

Figure 8.1: Quantum decoherence imaging of ion channel operation (simulations). (a) A single nitrogen-vacancy (NV) defect in a diamond nanocrystal is placed on an AFM tip. The unique properties of the NV atomic level scheme allow for optically induced readout and microwave control of magnetic (spin) sub-levels. (b) The nearby cell membrane is host to channels permitting the flow of ions across the surface. The ion motion results in an effective fluctuating magnetic field at the NV position which decoheres the quantum state of the NV system. (c) This decoherence results in a decrease in fluorescence, which is most pronounced in regions close to the ion channel opening. (d) Changes in fluorescence also permit the temporal tracking of ion channel dynamics.

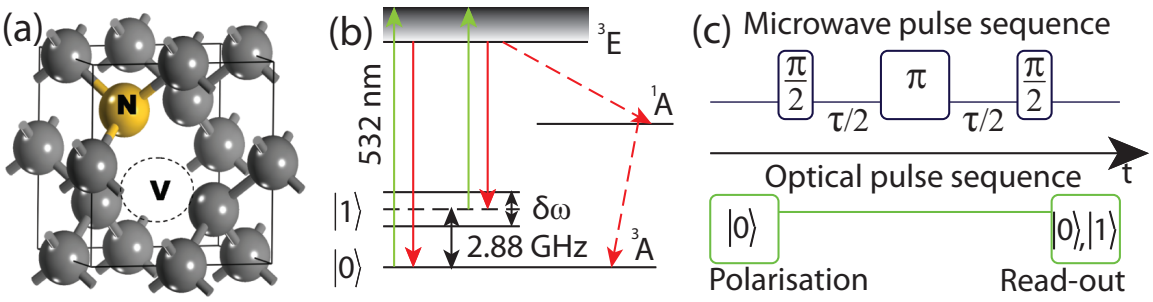

Figure 8.2: (a) NV-centre diamond lattice defect. (b) NV spin detection through optical excitation and emission cycle. Magnetic sublevels $|0\rangle$ and $|\pm 1\rangle$ are split by a D=2.88 GHz crystal field. Degeneracy between the $|\pm 1\rangle$ sublevels is lifted by a Zeeman shift, $\delta\omega$. Application of 532 nm green light induces a spin-dependent photoluminescence and pumping into the $|0\rangle$ ground state. (c) Microwave and optical pulse sequences for coherent control and readout.

8.2 Modelling

Typical ion channel species K^+, Ca^{2+}, Na^+, and nearby water molecules are electron spin paired, so any magnetic signal due to ion channel operation will be primarily from the motion of nuclear spins. Ions and water molecules enter the channel in thermal equilibrium with random spin orientations, and move through the channel over a μs timescale. The monitoring of ion channel activity occurs via measurement of the contrast in probe behavior between the on and off states of the ion channel. This requires the dephasing due to ion channel activity to be at least comparable to that due to the fluctuating background magnetic signal. We must therefore account for the decoherence due to the diffusion of water molecules, buffer molecules, saline components as well as the transversal diffusion of lipid molecules in the cell membrane.

The nth nuclear spin with charge q_n, gyromagnetic ratio γ_n, velocity $\vec{v}_n$ and spin vector $\vec{S}_n$, interacts with the NV spin vector $\vec{P}$ and gyromagnetic ratio $\gamma_{\rm p}$ through

the time-dependent dipole dominated interaction:

$$\mathcal{H}_{\rm int}(t) \;=\; \sum_{n=1}^{N} \kappa_{\rm dip}^{(n)} \left[\frac{\vec{P}\cdot\vec{S}_n}{r_n^3(t)} - 3\frac{\vec{P}\cdot\vec{r}_n(t)\vec{S}_n\cdot\vec{r}_n(t)}{r_n^5(t)} \right] \tag{8.2.1}$$

where $\kappa_{\rm dip}^{(n)} \equiv \frac{\mu_0}{4\pi}\hbar^2\gamma_{\rm p}\gamma_n$ are the probe-ion coupling strengths, and $\vec{r}_n(t)$ is the time-dependent ion-probe separation. Additional Biot-Savart fields generated by the ion motion, both in the channel and the extracellular environment, are several orders of magnitude smaller than this dipole interaction and are neglected here. Any macroscopic fields due to intracellular ion currents are of nano-Tesla (nT) order and are effectively static over T_2 timescales. These effects will thus be suppressed by the spin-echo pulse sequence.

In figure 8.3(a) we show typical field traces at a probe height of 1-10nm above the ion channel, generated by the ambient environment and the on-set of ion-flow as the channel opens. The contribution to the net field at the NV probe position from the various background diffusion processes dominate the ion channel signal in terms of their amplitude. Critically, since the magnetometer mode detects the field by acquiring phase over the coherence time of the NV centre, both the ion channel signal and background are well below the $\mathrm{nT\,Hz^{-1/2}}$ sensitivity limit of the magnetometer over the ($\sim 1\,\mathrm{ns}$) self-correlated timescales of the environment. However, the effect of the various sources on the decoherence rate of the NV centre are distinguishable because the amplitude-fluctuation frequency scales are very different, leading to remarkably different dephasing behaviour [HCHH09].

To understand this effect, we need to consider the full quantum evolution of the NV probe. In the midst of this environment the probe's quantum state, described by

the density matrix $\rho(t)$, evolves according to the Liouville equation,

$$\frac{\mathrm{d}}{\mathrm{d}t}\rho(t) = -\frac{i}{\hbar}\big[\mathcal{H}(t)\rho(t) - \rho(t)\mathcal{H}(t)\big], \tag{8.2.2}$$

where $\rho(t)$ is the incoherent thermal average over all possible unitary evolutions of the entire system, as described by the full Hamiltonian,

$$\mathcal{H} = \mathcal{H}_{\mathrm{nv}} + \mathcal{H}_{\mathrm{int}} + \mathcal{H}_{\mathrm{bg}}, \tag{8.2.3}$$

where $\mathcal{H}_{\mathrm{nv}}$ is the Hamiltonian of the NV system, and $\mathcal{H}_{\mathrm{int}}$ describes the interaction of the NV system with the background environment (e.g. diffusion of ortho spin water species and ions in solution) and any intrinsic coupling to the local crystal environment. The self evolution of the background system is described by $\mathcal{H}_{\mathrm{bg}}$, which, in the present methodology, is used to obtain the noise spectra of the various background processes. We note that the following analysis assumes dephasing to be the dominant decoherence channel in the system. We ignore relaxation processes since the frequencies of all magnetic fields considered are at least 4 orders of magnitude less than 2.88 GHz, and are hence unable to flip the probe spin over relevant timescales. Phonon excitation in the diamond crystal may also be neglected [BNT$^+$09] . Before moving onto the numerical simulations we consider some important features of the problem.

8.2.1 Decoherence from ion-channel dynamics

The decoherence rate of the NV centre is governed by the accumulated phase variance during the control cycle. Maximal dephasing due to a fluctuating field will occur at the cross-over point between the fast (FFL) and slow (SFL) fluctuation regimes [HCHH09]. A measure of this point is the dimensionless ratio $\Theta \equiv f_{\mathrm{e}}/\gamma_{\mathrm{p}}\sigma_B$, where

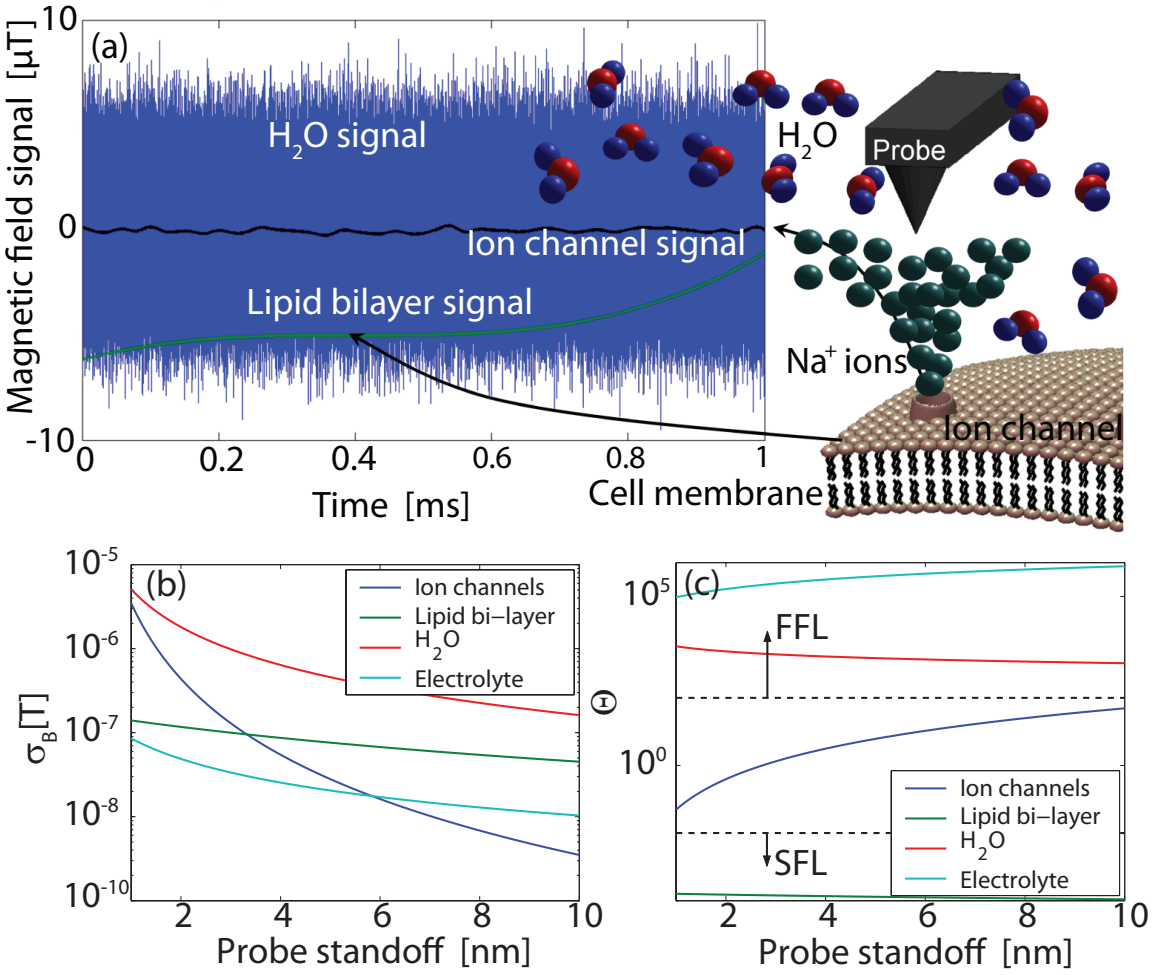

Figure 8.3: (a) Typical realisations of the stochastic magnetic fields arising from the motion of nuclear magnetic dipoles in water (blue), the lipid bi-layer (green), and ions passing through the ion channel (black). These signals are generated using the dynamic properties derived in section 8.2, using a probe standoff of 4 nm over a 1 ms timescale. (b) Comparison of σ_B for various sources of magnetic fields. (c) Fluctuation regime, $\Theta = f_e/\gamma_p\sigma_B$, for magnetic field sources vs probe standoff. Rapidly fluctuating fields ($\Theta \gg 1$) are said to be in the fast-fluctuating limit (FFL). Slowly fluctuating fields ($\Theta \ll 1$) are in the slow fluctuation limit (SFL). The ion channel signal exists in the $\Theta \sim 1$ regime, and therefore has an optimal dephasing effect on the NV probe.

$\tau_{\rm e} = 1/f_{\rm e}$ is the correlation time of the fluctuating signal, with cross-over at $\Theta \sim 1$ (see chapter 4).

In what follows, we consider exclusively the behaviour of a sodium ion channel. Sodium-23 has an effective abundance of 100%, and a nuclear magnetic moment of $\mu_{\rm Na} = 2.22\mu_N$, where $\mu_N = 5.05\times10^{-27}\,{\rm J\,T^{-1}}$ is the nuclear magneton. Other magnetically active ion channel species include potassium-39, having a 93.1% abundance and a nuclear magnetic moment of $0.391\mu_N$, and chlorine-35, having a 75.4% abundance and a nuclear magnetic moment of $0.821\mu_N$, ensuring sodium ions will interact most strongly with the NV centre. We can estimate the standard deviation of the magnetic field strength, $\sigma_B^{\rm ic}$, due to the random nuclear spin projections of ions and bound water molecules moving through an ion channel (ic) as $\sigma_B^{\rm ic} \sim \frac{\mu_0}{4\pi}\frac{1}{h_p^3}\sqrt{N_{\rm Na}\mu_{\rm Na}^2 + N_{\rm H_2O}\mu_{\rm H_2O}^2}$, where $N_{\rm Na}$ and $N_{\rm H_2O}$ are the average numbers of sodium ions and water molecules inside the channel. By modeling the channel as a cylinder with typical sodium channel influx/outflux rates [LMM07], we may numerically calculate the RMS fluctuation strength of the ion channel magnetic field, $\sigma_B^{\rm ic}$, as a function of the probe stand-off distance h_p, as shown in figure 8.3(b). The fluctuation rate is defined by the rate at which ions move through the channel, and is independent of whether the ions are moving in to or out of the cell. However, in typical physiological processes (neuronal firing for example) the sodium flux will be inward. Ion flux rates give an effective fluctuation rate of $f_e^{\rm ic} \sim 3\,{\rm MHz}$ [LMM07]. For probe-channel separations of 2-8nm, values of Θ range from 0.4 to 40 (figure 8.3(c)). Thus, the ion channel flow hovers near the cross-over point, with an induced dephasing rate of $\Gamma_{\rm ic} \sim 10^4 - 10^5$ Hz.

At these separation distances, the presence of the diamond surface is expected to have a negligible effect on the ion channel dynamics. To reduce the decoherence effects

of surface spins on the NV, the surface may be terminated with H or OH moieties. This essentially replaces the electron spins associated with the sp2 hybridised orbitals, with weaker nuclear spins [BGN$^+$10]. The ions in the channel, also being nuclear spins, couple very weakly to their surrounding environment. We may estimate their coupling to the diamond surface as $f \sim \frac{\mu_0}{4\pi\hbar}\mu_N^2 h_p^{-3} \sim 1\,\mathrm{Hz}$, which is negligible compared to the fluctuation rate of the channel itself. Additionally, we may approximate the ratio between the magnetic force on the ions due to the surface spins and the electric force due to adjacent ions as $F_B/F_E \sim \left(3\frac{\mu_0}{4\pi}\mu_N^2 h_p^{-4}\right) / \left(\frac{e^2}{4\pi\varepsilon_0}\Delta r^{-2}\right) \sim 10^{-15}$, where Δr is the typical distance between adjacent ions in the channel. Similarly, the ratio between the magnetic force due to the NV spin and the electric force is $F_B/F_E \sim \left(3\frac{\mu_0}{4\pi}\mu_B\mu_N h_p^{-4}\right) / \left(\frac{e^2}{4\pi\varepsilon_0}\Delta r^{-2}\right) \sim 10^{-12}$, thus we expect the presence of the probe to be truly non-invasive.

8.2.2 Decoherence from background sources

We now consider the dephasing effects of the various sources of background magnetic fields. The first source of background noise are the fields arising from the motion of the water molecules and ions throughout the aqueous solution. Due to the nuclear spins of the hydrogen atoms, liquid water consists of a mixture of spin neutral (para) and spin-1 (ortho) molecules. The equilibrium ratio of ortho to para molecules (OP ratio) is 3:1 [TV02], making 75% of water molecules magnetically active. In biological conditions, dissolved ions occur in concentrations 2-3 orders of magnitude below this and are ignored here (they are important however for calculations of the induced Stark shift, see below). The RMS strength of the field due to the aqueous solution is $\sigma_B^{\mathrm{H_2O}} \sim g_{\mathrm{H}}\mu_{\mathrm{N}}\frac{\mu_0}{2\pi}\sqrt{n_{\mathrm{H_2O}}\frac{\pi}{h_p^3}}$. This magnetic field is therefore 1-2 orders of magnitude

stronger than the field from the ion channel (figure 8.3(a,b)). The fluctuation rate of the aqueous environment is dependent on the self diffusion rate of the water molecules. Using $D_{\mathrm{H_2O}} = 3 \times 10^{-9}\ \mathrm{m^2\,s^{-1}}$, the fluctuation rate is $f_e^{\mathrm{H_2O}} \sim D_{\mathrm{H_2O}} / (2h_{\mathrm{p}})^2$. This places the magnetic field due to the aqueous solution in the fast-fluctuation regime, with $\Theta_{\mathrm{H_2O}} \sim 10^3 - 10^4$ (figure 8.3(b)), giving a comparatively slow dephasing rate of $\Gamma_{\mathrm{H_2O}} \sim f_e^{\mathrm{H_2O}} \Theta_{\mathrm{H_2O}}^{-2} \sim 100$ Hz and corresponding dephasing envelope $L_{\mathrm{H_2O}} = e^{-\Gamma_{\mathrm{H_2O}} t}$.

An additional source of background dephasing is the lipid molecules comprising the cell membrane. Assuming magnetic contributions from hydrogen nuclei in the lipid molecules, lateral diffusion in the cell membrane gives rise to a fluctuating B-field, with a characteristic frequency related to the diffusion rate. Atomic hydrogen densities in the membrane are $n_{\mathrm{H}} \sim 3 \times 10^{28}\,\mathrm{m^{-3}}$. At room temperature, the populations of the spin states of hydrogen will be equal, thus the RMS field strength is given by $\sigma_B^{\mathrm{L}} \sim g_H \mu_N \frac{\mu_0}{8\pi} \sqrt{n \frac{5\pi}{4h_{\mathrm{p}}^3}}$. The strength of the fluctuating field due to the lipid bilayer is of the order of $10^{-7}\,\mathrm{T}$ (figure 8.3(a)). The diffusion constant for lateral Brownian motion of lipid molecules in lipid bilayers is $D_{\mathrm{L}} = 2 \times 10^{-15}\,\mathrm{m^2 s^{-1}}$ [BLS+06], giving a fluctuation frequency of $f_e^{\mathrm{L}} \sim 125$ Hz and $\Theta_{\mathrm{L}} \sim 10^{-4}$ (figure 8.3(d)). At this frequency, any quasi-static field effects will be predominantly suppressed by the spin-echo refocusing. The leading-order (gradient-channel) dephasing rate is given by [HCHH09], $\Gamma_{\mathrm{L}} \sim \frac{1}{2\sqrt{2\sqrt{2}}} \Theta_{\mathrm{L}}^{-1/2} f_e^{\mathrm{L}} + \mathcal{O}\left(\Theta_{\mathrm{L}}^{-1/3} f_e^{\mathrm{L}}\right)$, giving rise to dephasing rates of the order $\Gamma_{\mathrm{L}} \sim 100\,\mathrm{Hz}$, with corresponding dephasing envelope $L_{\mathrm{L}}(t) = e^{-\Gamma_{\mathrm{L}}^4 t^4}$.

The electric fields associated with the dissolved ions also interact with the NV centre via the ground state Stark effect. The coefficient for the frequency shift as a function of the electric field applied along the dominant (z) axis is given by $R_{3D} = 3.5 \times 10^{-3}\ \mathrm{Hz\,m\,V^{-1}}$ [vOG90]. Fluctuations in the electric field may be related to

an effective magnetic field via $B_z^{\text{eff}} = R_{3D}E_z/\gamma_p$, which may be used in an analysis similar to that above. An analysis using Debye-Hückel theory [KF08] shows charge fluctuations of an ionic solutions in a spherical region Λ of radius R behave as $\langle Q_\Lambda^2 \rangle = D_{\text{E}} k_{\text{B}} T \left(1 + \kappa R\right) e^{-\kappa R} \left[R \cosh\left(\kappa R\right) - \frac{\sinh(\kappa R)}{\kappa} \right]$, where D_{E} is the diffusion coefficient of the electrolyte, and κ is the inverse Debye length (l_{D}); $l_{\text{D}} = 1/\kappa = 1.3$ nm for biological conditions. Whilst this analysis applies to a region Λ embedded in an infinite bulk electrolyte system, simulation results discussed below show very good agreement when applied to the system considered here. The electric field variance may be obtained from $\langle Q_\Lambda^2 \rangle$, giving $\sigma_{\text{E}} = \sqrt{\langle E^2 \rangle - \langle E \rangle^2} \sim 10^6\,\text{Vm}^{-1}$, as a function of h_{p}. Relaxation times for electric field fluctuations are $\tau_e^{\text{E}} = \epsilon\epsilon_0\rho_{\text{E}}$ [For00], where ρ_{E} is the resistivity of the electrolyte, giving $f_e^{\text{E}} \sim 1/\tau_e^{\text{E}} = 1.4\,\text{GHz}$ under biological conditions. Given the relatively low strength (figure 8.3(a)) and short relaxation time of the effective Stark induced magnetic field fluctuations ($\Theta \sim 10^5$) (figure 8.3(b)), we expect the charge fluctuations associated with ions in solution to have little effect on the evolution of the probe.

8.3 Results and discussion

8.3.1 Lateral scanning and spatial resolution

We now turn to the problem of non-invasively resolving the location of a sodium ion channel in a lipid bilayer membrane. When the channel is closed (off), the dephasing is the result of the background activity, and is defined by $L_{\text{off}} = L_{\text{H}_2\text{O}} L_{\text{L}} L_{\text{E}} L_{^{13}\text{C}}$. When the channel is open (on), the dephasing envelope is defined by $L_{\text{on}} = L_{\text{off}} L_{\text{ic}}$. Maximum contrast will be achieved by optimising the spin-echo interrogation time, τ,

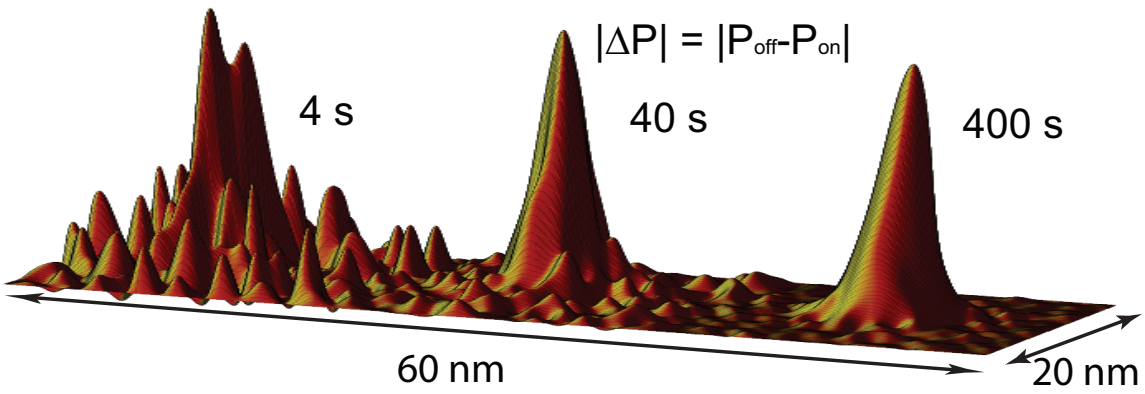

Figure 8.4: Simulated spatial scans based on the ion channel as a dephasing source. Relative population differences are plotted for pixel dwell times of 10, 100 and 1000 ms. Corresponding image acquisition times are 4, 40 and 400 s.

to ensure $L_{\text{off}} - L_{\text{on}}$ is maximal. Thus in the vicinity of an open channel at the point of optimal contrast, $\tau \approx T_2/2$, we expect an ensemble ground state population of $P_{\text{on}}(\frac{T_2}{2}) = \frac{1}{2}\left[1 + L_{\text{on}}\left(\frac{T_2}{2}\right)\right] = 0.61$, and $P_{\text{off}}(\frac{T_2}{2}) = \frac{1}{2}\left[1 + L_{\text{off}}\left(\frac{T_2}{2}\right)\right] = 0.93$ otherwise. By scanning over an open ion channel and monitoring the probe via repeated measurements of the spin state, we may build up a population ensemble for each lateral point in the sample. The signal to noise ratio improves with the dwell time at each point. Figure 8.4 shows simulated scans of a sodium ion channel with corresponding image acquisition times of 4, 40 and 400 s. It should be noted here that the spatial resolution available with this technique is beyond that achievable by magnetic field measurements alone, since for large Θ, $\Delta P \propto B^2 \propto h_p^{-6}$.

8.3.2 Temporal resolution and tracking ion channel activity

We may employ similar techniques to temporally resolve a sodium ion channel switch-on event. By monitoring a single point, we may build up a measurement record, $\mathcal{I}$. In an experimental situation, measurement frequency has an upper limit of

$f_{\mathrm{m}} = (\tau + \tau_{\mathrm{m}} + \tau_{2\pi})^{-1}$, where $\tau_{\mathrm{m}} \approx 900$ ns is the time required for photon collection, and $\tau_{2\pi}$ is the time required for all 3 microwave pulses. A trade-off exists between the increased dephasing due to longer interrogation times and the corresponding reduction in measurement frequency. Interrogation times are limited by the intrinsic T_2 time of the crystal. A second trade-off exists between the variance of a given set of N_τ consecutive measurements and the temporal resolution of the probe. For the monitoring of a switching event, the spin state may be inferred with increased confidence by performing a running average over a larger number of data points, N_τ. However increasing N_τ will lead to a longer time lag before a definitive result is obtained. The uncertainty in the ion channel state goes as $\delta P \sim \left(\sqrt{N_\tau}\right)^{-1}$, where N_τ is the number of points included in the dynamic averaging. We must take sufficient N_τ to ensure that $\delta P < \Delta P(\tau, h_{\mathrm{p}}, T_2) = P_{\mathrm{off}} - P_{\mathrm{on}}$. The temporal resolution depends on the width of the dynamic average and is given by $\delta t \sim N_\tau(\tau + \tau_m)$, giving the relationship $\delta t = \frac{\tau+\tau_m}{\delta P^2} > \frac{\tau+\tau_m}{[\Delta P(\tau,h_{\mathrm{p}},T_2)]^2}$. We wish to minimise this function with respect to τ for a given stand-off (h_{p}) and T_2 time.

In reality, not all crystals are manufactured with equal T_2 times. An important question is therefore, for a given T_2, what is the best temporal resolution we may hope to achieve? Figure 8.5(b) shows the optimal temporal resolution as a function of T_2. It can be seen that δt improves monotonically with T_2 until T_2 exceeds the dephasing time due the fluctuating background fields (figure 8.5(a)). Beyond this point no advantage is found from extending T_2.

A plot of δt as a function of τ is given in figure 8.5(c) for standoffs of 2-6 nm. Solid lines depict the resolution that maybe achieved with $T_2 = 300\,\mu$s. Dashed lines represent the resolution that may be achieved by extending T_2 beyond the dephasing

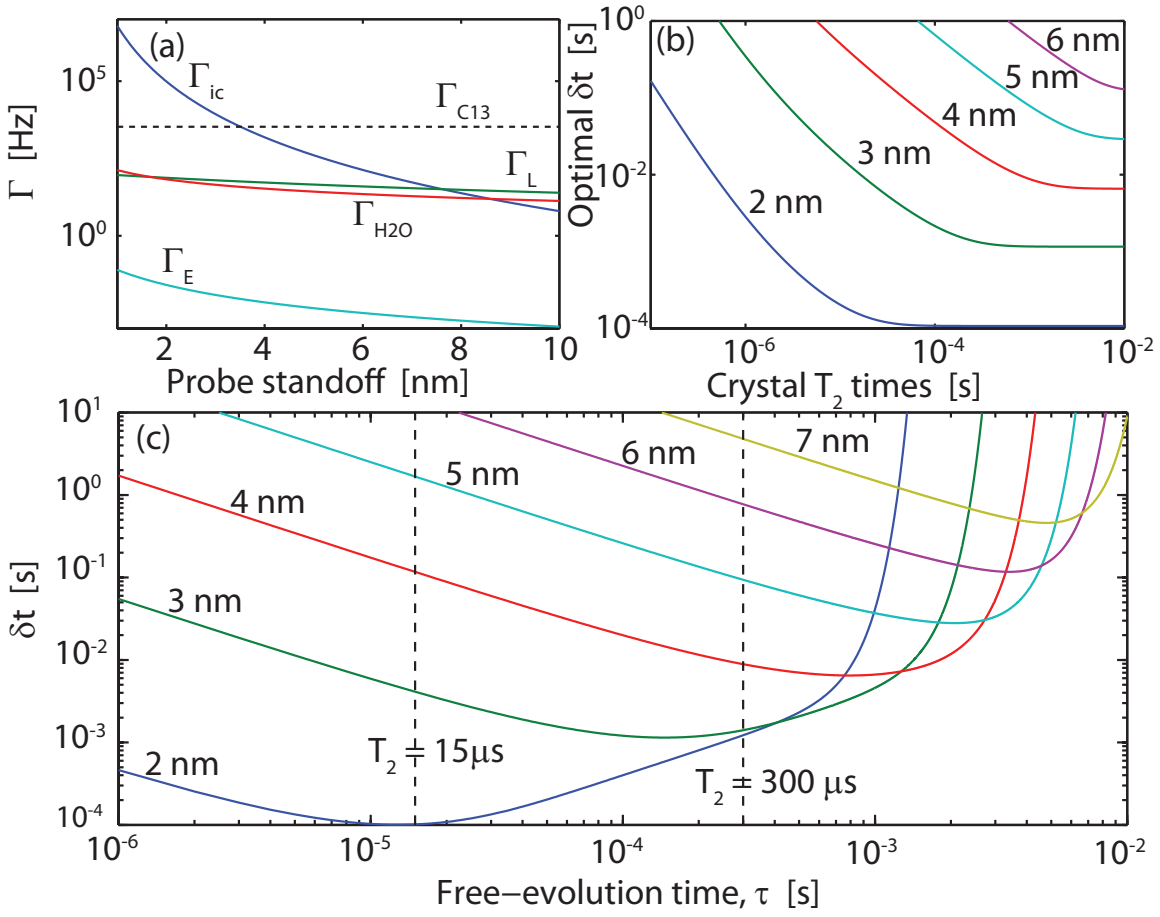

Figure 8.5: (a) Dephasing rates due to the sources of magnetic field plotted as a function of probe standoff, h_p. (b) Optimum temporal resolution as a function of crystal T_2 times for $h_p = 2 - 6$ nm. (c) Temporal resolution as a function of interrogation time, τ, for separations of 2-7 nm and $T_2 = 15\,\mu$s and $T_2 = 300\,\mu$s. Dashed lines show expected improvements from much longer T_2 times, $T_2 \gg \tau$.

times of background fields. We see that δt diverges as $\tau \to T_2$, and is optimal for $\tau \to 1/\Gamma_{\rm ic}$.

As an example of monitoring of ion channel behaviour, we consider a crystal with a T_2 time of 300 μs at a standoff of 3 nm. Figure 8.5(c) tells us that an optimal temporal resolution of $\delta t \sim 1.1$ ms may be achieved by choosing $\tau \sim 100\,\mu$s. This in turn suggests an optimal running average will employ $N_\tau = \delta t\,(\tau + \tau_{\rm m})^{-1} \approx 11$ data points. Figure 8.6(a) shows a simulated detection of a sodium ion channel switch-on event using $N_\tau = 20,\ 50$ and 100 points. The effect of increasing N_τ is shown to give poorer temporal resolution but also produces a lower variance in the signal. This may be necessary if there is little contrast between $P_{\rm off}$ and $P_{\rm on}$. Conversely, decreasing N_τ results in an improvement to the temporal resolution but leads to a larger signal variation.

We now consider an ion channel switching between states after an average waiting time of 5 ms (200 Hz) (figure 8.6(b)). To ensure the condition $\delta P < \Delta P$ is satisfied, we perform the analysis using $N_\tau = 20$, giving a resolution of $\delta t \approx 2$ ms. The blue curve shows the response of the NV population to changes in the ion channel state. Fourier transforms of the measurement record, $\mathcal{F}(\mathcal{I})$, are shown in figure 8.6(c)-(e). The switching dynamics are clearly resolvable for heights less than 6 nm. The dominant spectral frequency is 100 Hz which is half the 200 Hz switching rate as expected. Beyond 6 nm, the contrast between $P_{\rm off}$ and $P_{\rm on}$ is too small to be resolvable due to the T_2 limited temporal resolution, as given in figure 8.5(b). This may be improved via the manufacturing of nanocrystals with improved T_2 times, allowing for longer interrogation times [dashed curves, figure 8.5(c)].

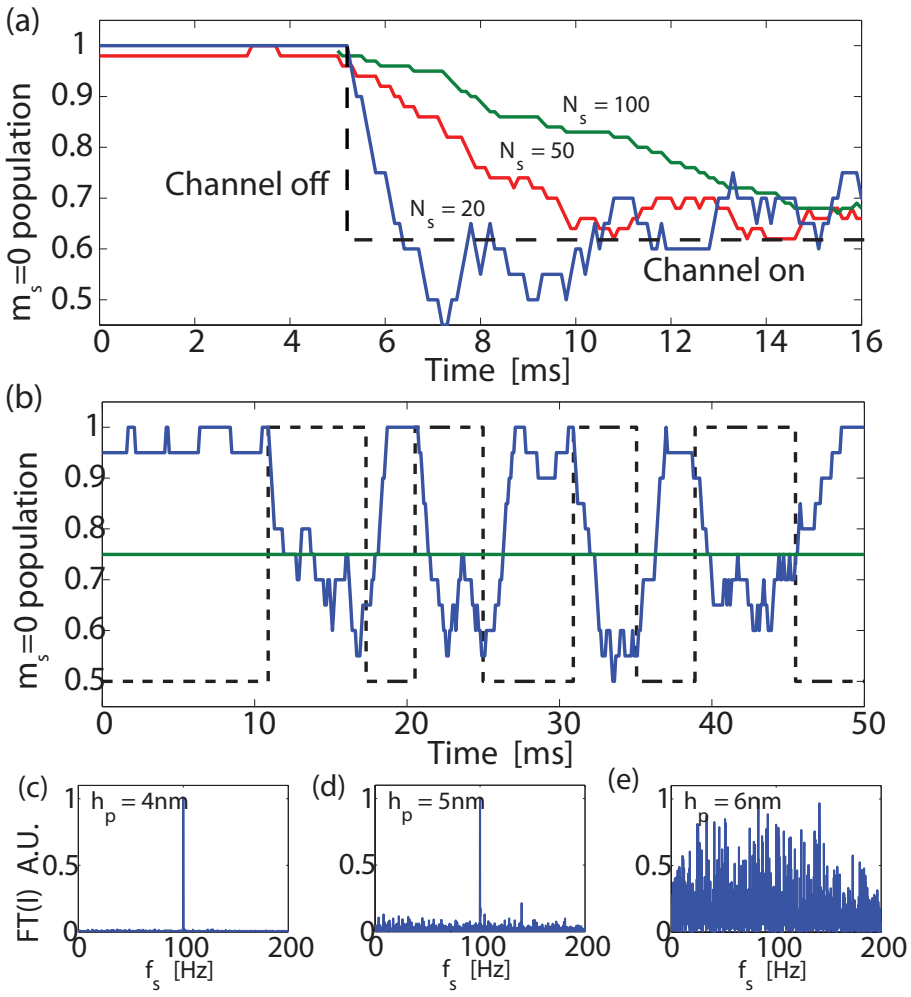

Figure 8.6: Theoretical results for the detection of ion channel operation. (a) Plot illustrating the dependence of temporal resolution (δt) and signal variance (δP) on the number of data points included in the running average (N_s). (b) Simulated reconstruction of a sodium ion channel signal with a 200 Hz switching rate using optical readout of an NV centre (blue curve). The actual ion channel state (on/off) is depicted by the dashed line, and the green line depicts the analytic confidence threshold. Fourier transforms of measurement records are shown in (c)-(e) for stand-offs of 4, 5 and 6 nm respectively. Switching dynamics are clearly resolvable for $h_p < 6$ nm, beyond which there is little contrast between decoherence due to the ion channel signal and the background.

8.3.3 Wide-field operation

With regard to scale-up to a wide field imaging capability, beyond the obvious extrinsic scaling of the number of single channel detection elements (in conjunction with micro-confocal arrays), we consider an intrinsic scale-up strategy using many NV centres in a bulk diamond probe [SDN$^+$10], with photons collected in a pixel arrangement. Since the activity of adjacent ion channels is correlated by the μm scale activity of the membrane, the fluorescence of adjacent NV centres will likewise be correlated, thus wide field detection will occur via a fluorescence contrast across the pixel. Implementation of this scheme involves a random distribution of NV centres in a bulk diamond crystal. The highest reported NV density is 2.8×10^{24} m^{-3} [ABL$^+$09], giving typical NV- NV couplings of < 10 MHz which are strong enough to introduce significant additional decoherence. We seek a compromise between increased population contrast and increased decoherence rates due to higher NV densities, $n_{\rm nv}$, given by $\Gamma_{\rm nv} \sim \frac{\sqrt{2\pi}}{3}\frac{\hbar\mu_0}{4\pi}\gamma_{\rm p}^2 n_{\rm nv}$[HCHH09].

For ion channel operation correlated across each pixel, the total population contrast $\Delta\Phi$ between off and on states is obtained by averaging the local NV state population change $\Delta\Phi(\tau) = P_{\rm off}(\vec{r}_i, \vec{r}_c, \tau) - P_{\rm on}(\vec{r}_i, \vec{r}_c, \tau)$ over all NV positions $\vec{r}_i$ and orientations; and ion channel positions $\vec{r}_c$ and species; and maximizing with respect to τ. As an example, consider a crystal with $n_{\rm nv} = 10^{24}\,$m^{-3} whose surface is brought within 3 nm of the cell membrane containing an sodium and potassium ion channel densities of $\sim 2 \times 10^{15}\,$m^{-2}[AB07]. Higher densities will yield better results, however these have not been realised experimentally as yet, and electron spins in residual nitrogen will begin to induce NV spin flips. We expect ion channel activity to be correlated across pixel areas of $1\,\mu$m $\times\, 1\,\mu$m, so the population contrast between off and

on states is $\Delta\Phi \approx 15$. At these densities, the optimal interrogation time is $\tau \sim 0.8\,\mu$s, yielding an improvement in the temporal resolution by a factor of 10,000, opening up the potential for single-shot measurements of ion channel activity across each pixel.

8.4 Conclusion

We have carried out an extensive analysis of the quantum dynamics of a NV diamond probe in the cell-membrane environment and determined the theoretical sensitivity for the detection, monitoring and imaging of single ion channel function through quantum decoherence. Using current demonstrated technology a temporal resolution in the 1-10 ms range is possible, with spatial resolution at the nanometer level. With the scope for scale-up and novel scanning modes, this fundamentally new detection mode has the potential to revolutionize the characterization of ion channel action, and possibly other membrane proteins, with important implications for molecular biology and drug discovery.

Chapter 9

High spatial and temporal resolution wide-field imaging of neuron activity using quantum NV-diamond

A quantitative understanding of the dynamics of biological neural networks is fundamental to gaining insight into information processing in the brain. While techniques exist to measure spatial or temporal properties of these networks, it remains a significant challenge to resolve the neural dynamics with sub-cellular spatial resolution. In this chapter we consider a fundamentally new form of wide-field imaging for neuronal networks based on the nanoscale magnetic field sensing properties of optically active spins in a diamond substrate. We analyse the sensitivity of the system to the magnetic field generated by an axon transmembrane potential and confirm these predictions experimentally using electronically-generated neuron signals. By numerical simulation of the time dependent transmembrane potential of a morphologically reconstructed hippocampal CA1 pyramidal neuron, we show that the imaging system is capable of imaging planar neuron activity non-invasively at millisecond temporal resolution and micron spatial resolution over wide-fields. The results of this chapter

have been published in reference [HBT+12].

9.1 Introduction

Information processing in the brain is presumed to arise from interactions and correlations across several orders of magnitude of temporal and spatial scales and tens of thousands to billions of computational units. The smallest computational unit is the synapse, with sub-micron structures involved in chemical and electrical signalling. Changes in synaptic dynamics are the basis of learning and memory. While local conditions in the neuron determine signal flow into and out of synapses, complex signal integration and filtering occurs independently in different branches in the dendritic tree (the neuronal input structure). The decision to trigger an output is made in another structure - the axon. Neurons are organized in networks with complex, and largely unknown, connection rules. Networks may contain over a dozen different neuron types, each with their own dynamics and connection rules. Understanding the behaviour of these systems requires understanding the interactions between computational units at different scales in the system [CK11, GMDS+05].

Current diagnostic techniques are limited in the number of computational units that can be recorded simultaneously at sufficiently high spatial and temporal resolution. New techniques in optogenetics are enabling the manipulation of networks at some of these scales [FYD11] however technology to read neuronal networks lags considerably. Voltage sensitive dyes allow readout of the neuron membrane potential, but have poor signal to noise properties and are toxic, making them unsuitable for long term recording [BKV+05, HBJ+09]. Voltage sensitive fluorescent proteins show promise, but also have poor signal to noise properties and limited temporal and

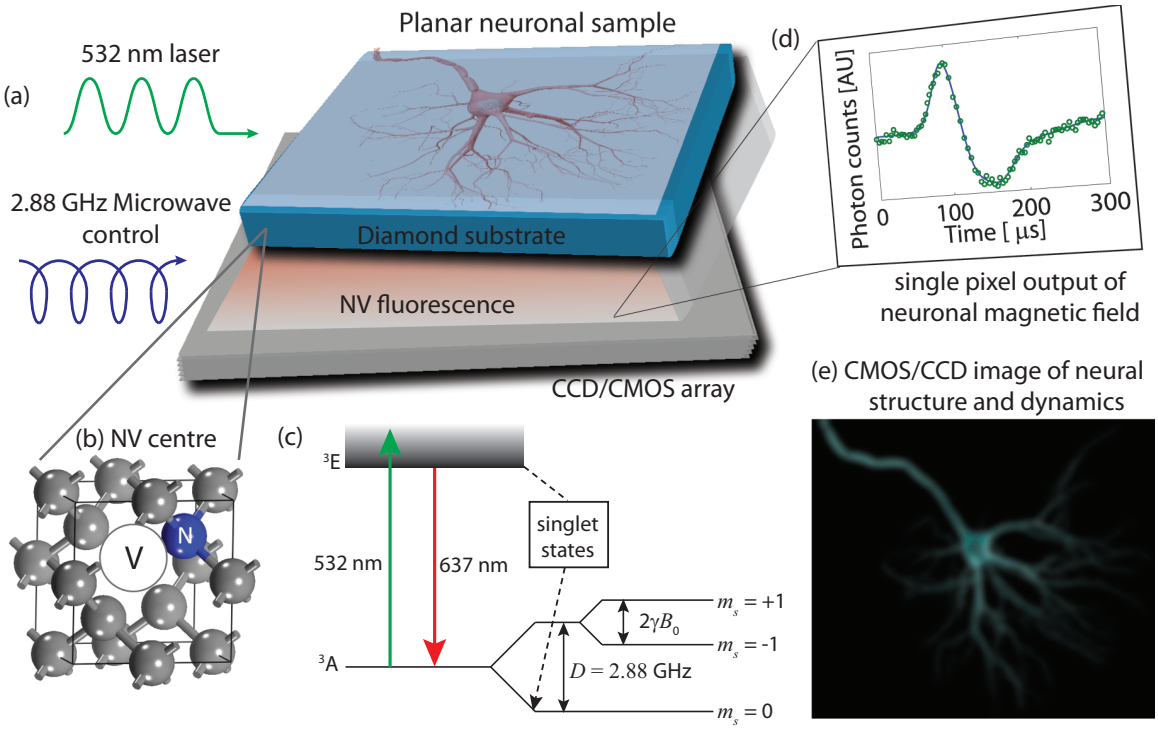

Figure 9.1: Schematic of the nitrogen-vacancy (NV) in diamond neuron detection system showing a neural network component (in this case an axon) on a diamond substrate containing fluorescent NV centres. (a) The quantum state may be controlled via application of 2.88 GHz microwave radiation, and is dependent on the strength of the field produced by the axon. (b) Atomic lattice structure of the NV centre. (c). Upon optical excitation at 532 nm, the NV centre spin state may be measured (readout) by monitoring the intensity of the emitted red light using a CCD or CMOS camera. (d) Simulated dynamic output from a single CMOS pixel. (e) By monitoring many pixels, we may obtain a dynamic widefield image of the neural dynamics and network structure.

spatial resolution [PMA+09]. Direct invasive techniques such as electrophysiological probes are fundamentally limited by the number of electrodes that can be placed in the tissue. Progress in silicon nanowire field-effect transistors have demonstrated sub millisecond temporal resolution, however spatial resolution is limited by the 60 μm distance between adjacent devices [QPT+10].

The detection method we consider here is based on non-invasive magnetic field detection and is therefore fundamentally different to approaches based on detection of electric fields. While the techniques may ultimately complement each other, our magnetic field based technique will not suffer from some of the drawbacks of electrically-based detection, such as probe positioning with respect to the Debye length and background electrical noise sources at the nanoscale. Furthermore, the detection is inherently non-invasive and issues such as the compatibility of quantum measurements of the NV defect with biological systems are now well established in terms of the low toxicity of diamond and the low photo and microwave powers involved.

The detection set-up we consider consists of a commercial grade single crystal ultra-pure diamond membrane substrate containing a fabricated layer of negatively charged nitrogen-vacancy (NV) defect centres (figure 9.1). Neurons can be grown directly on the diamond surface [SWJS04] whose low toxicity is ideal for biological applications [YKC+05]. As we show, the ensemble of NV centres provides high sensitivity to the magnetic field fluctuations resulting directly from the transmembrane potentials generated by the neural activity at sub-millisecond time-scales, and the spatial attenuation of the magnetic field at a 100nm standoff provides micron spatial resolution. This standoff is conservative, as implantation techniques permit the creation of NV centres within a few nm of the diamond surface. Employing a

physical model of the hippocampal CA1 pyramidal neuron, developed by Royeck et al [RHR$^+$08] and modified by Wimmer et al [WRS$^+$10, WRM$^+$10], we show that the NV detection system is able to non-invasively capture the transmembrane potential activity in a series of near real-time images, with spatial resolution at the level of the individual neural compartments. The data obtained will allow both the planar morphology and function connectivity to be determined. The realisation of this detection system using available technology would represent a significant step forward in measuring and understanding the dynamics of whole-scale neuronal networks.

In what follows, we first outline how transmembrane potentials generate magnetic fields, their typical strength and detection using the NV centre as a nanoscale magnetometer. We then analyse the detection sensitivity for a single axon case. We experimentally verify this sensitivity by propagating a simulated axon pulse along a micro-wire and detecting the resulting magnetic field signal with a proximate NV centre. Finally, we employ a model of a hippocampal CA1 pyramidal neuron under a typical excitatory regime in which distal dendrites undergo current injections of roughly 2nA. By direct simulation of the magnetic fields generated at the soma, axon and dendrites in response to this stimulation, we produce the corresponding image output (assuming current CMOS imaging technology [Sab11]) and determine the effective spatial and temporal resolution of the system.

9.2 Modelling

The advent of widefield NV magnetometry based on CCD detection of a high NV density diamond substrate has yielded the ability to spatially reconstruct magnetic fields at the μm scale together with improved sensitivity over that obtainable with a single

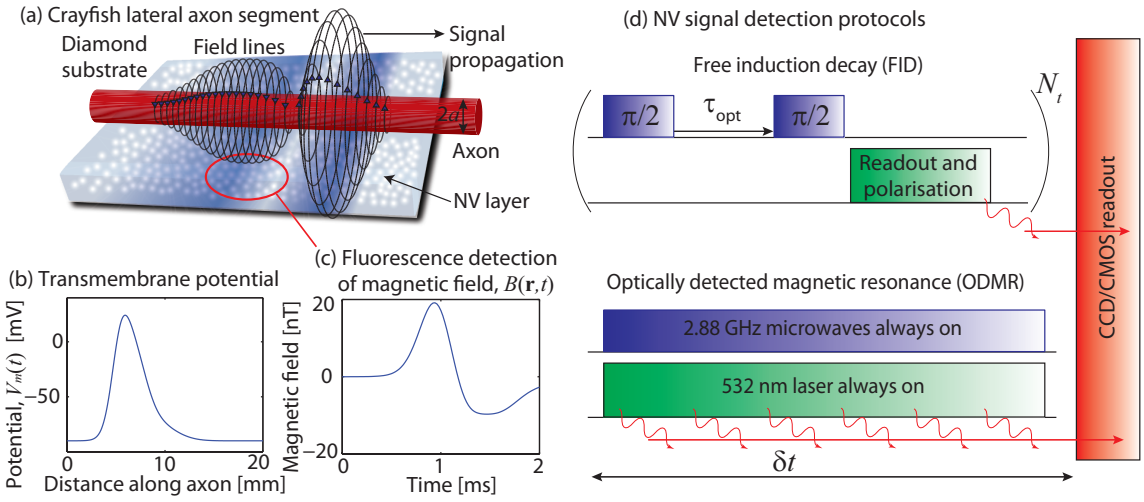

Figure 9.2: (a) Schematic of the NV-diamond neuron detection system showing a neural network component (in this case an axon) on a diamond substrate containing fluorescent NV centres. For a FID based protocol, regions where the field is greatest produce the least fluorescence. For and ODMR based protocol, the converse is true. (b) Longitudinal variation of the transmembrane potential, V_m, of a crayfish lateral axon as taken from Ref. [WG61]. As this excitation propagates along the axon, it produces a time dependent magnetic field like that shown in (c) for a standoff of 100 nm. (d) Temporal arrangement of microwave and optical pulse sequences. For the FID based protocol, $\pi/2$ microwave pulses are used to prepare the NV in a superposition of $|0\rangle$ and $|1\rangle$ states which accumulate a relative phase shift during the free evolution period due to the presence of a neural field. A second $\pi/2$ pulse transforms this phase into a population difference which is read out using a 532 nm laser. Application of this laser also acts to re-polarise the NV in the $|0\rangle$ state. The decreased intensity of the collected fluorescence permits the determination of the phase shift and hence the strength of the neural magnetic field. In the case of an ODMR based protocol, the constantly applied microwaves drive transitions between the paramagnetic sublevels of the ground states, whose relative energies are altered by the presence of a neural field, making the $|0\rangle \rightarrow |1\rangle$ transition less likely, resulting in an increased fluorescence.

NV centre whilst retaining the necessary quantum coherence properties [SPM+10]. Further improvements are expected in the near future, with nitrogen to NV^- conversion efficiencies in excess of 50% having been recently reported [NRB+10, PNJ+10].

9.2.1 Calculation of the magnetic field from a transmembrane potential

In order to establish our detection regime and required sensitivity we determine theoretically the magnetic fields generated by a transmembrane potential. We model an axon segment as a cylinder of radius a and length L aligned along the z axis (figure 9.2(a)). These segments form the building blocks of more complicated neuron models to be considered later. Let $\Phi(r, z, t)$ denote the radially-symmetric electric potential at radius r, longitudinal distance z and time t. Approximating the width of the cell membrane to be infinitesimally small, there is a step-change in the potential as it goes from just within the cell, $\Phi(a_-, z, t)$, to just outside the cell, $\Phi(a_+, z, t)$. The transmembrane potential, given by the difference $V_m(z, t) = \Phi(a_-, z, t) - \Phi(a_+, z, t)$, therefore represents the voltage drop across the cell membrane at longitudinal position z and time t. Using data for V_m, one can reconstruct the $\Phi(\mathbf{r}, t)$ in the regions inside and outside a given component via the solution of Laplace's equation with boundary conditions set by V_m (see Methods section). By solving for the potentials in both regions, we determine the electric field and hence current densities using Ohm's law, $\mathbf{J}(\mathbf{r}, t) = \vec{\sigma}(\mathbf{r}, t) \cdot \nabla\Phi(\mathbf{r}, t)$, which is integrated using the Biot-Savart law,

$$\mathbf{B}(\mathbf{r}, t) = \frac{\mu_0}{4\pi} \int \mathbf{J}(\mathbf{r}', t) \times \frac{\mathbf{r} - \mathbf{r}'}{|\mathbf{r} - \mathbf{r}'|^3} \, \mathrm{d}^3\mathbf{r}' \tag{9.2.1}$$

to obtain the resulting magnetic fields, $\mathbf{B}(\mathbf{r}, t)$. In figure 9.2 we show this for the case of a crayfish lateral axon using the measured transmembrane potential (figure 9.2(b)) taken from Ref. [WG61]. The resulting magnetic field signal calculated at the NV position is shown in figure 9.2(c) for a 100nm standoff. Typically, the magnetic fields generated by the transmembrane potential are at the nT scale. We will show that the quantum detection system based on optically detected magnetic resonance (ODMR) of the NV centre in diamond has the combination of sensitivity and the appropriate spatial scale to enable detection of the neuronal magnetic fields at the high temporal-spatial resolution required.

9.2.2 Sensitivity Analysis

We envisage two detection protocols based on either directly monitoring the coherent phase difference between the sublevels of the NV centre using free induction decay (FID) experiment; or by measuring the location of the resonance peak in a continuous wave ODMR experiment (figure 9.2(d)). The sensitivities of the two methods are essentially equivalent [SH11], however for definiteness (and brevity) we describe in more detail the former. At fiducial $\tau = 0$, following optical polarisation into the $|0\rangle$ state, the application of a $\pi/2$ microwave pulse places each NV centre into an even superposition of $|0\rangle$ and $|+1\rangle$ Zeeman levels. After a free evolution time of τ, another $\pi/2$ pulse is applied and the system's state is read out optically. In the absence of any magnetic disturbances the system remains coherent, and the probability of finding the NV system in the $|0\rangle$ magnetic level after the second $\pi/2$ pulse, measured directly from its fluorescence, will oscillate between 0 and 1 at a frequency given by the energy difference of the two levels. However, in reality such coherent

superpositions of quantum states are highly sensitive to magnetic field fluctuations in the immediate crystalline environment due to mutual spin flipping of electronic nitrogen defects and/or ^{13}C nuclear spins. Thus, depending on the material composition, one typically measures a decay of these coherent oscillations between the magnetic levels as a function of the evolution time τ. For isotopically pure diamond the timescale of this decoherence, referred to as the FID time T_2^*, is typically of order 1 to 10 μs and ultimately sets the sensitivity limits for an NV based magnetometer. By employing a spin-echo pulse sequence in which an additional π-pulse is applied at time $\tau/2$, coherence times may be extended by more than 2 orders of magnitude, and further improvements may be realised by employing higher order decoupling schemes such as CPMG[TCC$^+$08, NDH$^+$11] or Uhrig[Uhr07, HHCH10] pulse sequences. Such decoupling schemes achieve improvements to the sensitivity by suppressing the effect of low frequency noise on the NV centre, and are hence not suited to measuring neural magnetic fields which fluctuate on T =1 to 10 ms timescales. To ensure maximal sensitivity to low frequency noise we must employ some N_t repetitions of the FID or ODMR protocols in the time interval $[t, t + \delta t]$. As such, δt serves to define the temporal resolution of the system, and must satisfy $\delta t < T$. Furthermore, each protocol cycle must be sufficiently sensitive that $N_t \lesssim T/T_2^*$ measurements may be taken within the timescales associated with the neuronal dynamics, whilst maintaining an acceptable signal to noise ratio (SNR).

During its evolution under the neural magnetic field $B(\mathbf{r}, t)$, the coherent phase accumulation is of an NV centre at position $\mathbf{r}_i$ during time interval τ, is given by $\Delta\phi(\mathbf{r}_i) = \gamma \int_0^\tau B_i(\mathbf{r}_i, t)\,\mathrm{d}t$, where γ is the NV gyromagnetic ratio and B_i is the component of $\mathbf{B}$ parallel to the t^{th} N-V axis. The signal change we are interested in

measuring is the resulting change in fluorescence due to this phase accumulation, which is proportional to $\sin(\Delta\phi)$. Since the neural magnetic fields considered here are typically less than 10 nT, and are essentially constant over the timescale of a single measurement protocol, we have that $\Delta\phi \ll 1$, thus the signal change at a single defect site is given by $\mathcal{S}_i \approx \gamma\tau B_i(\mathbf{r}_i)L(\mathbf{r}_i,\tau)$, where $L(\mathbf{r}_i,\tau)$ is the decoherence envelope of the NV defect at position $\mathbf{r}_i$ as a function of the interrogation time, τ. This envelope represents the decay of quantum coherence of defect i due to interactions with the surrounding magnetic environment, including ^{13}C nuclei, nitrogen electron spins, and other proximal NV centres. As we are considering an FID sequence, the shape of each envelope is assumed to be Gaussian, and is given by

$$L(\tau) \;=\; \exp\left[-\left(\Gamma^i_{\mathrm{C}_{13}}\tau\right)^2 - \left(\Gamma^i_{\mathrm{N}}\tau\right)^2\right], \tag{9.2.2}$$

where $\Gamma^i \equiv \Gamma(\mathbf{r}_i)$ is the intrinsic decoherence rate of NV centre i, and $\Gamma_{\mathrm{C}_{13}} \sim 100\,\mathrm{kHz}$. The decoherence rate due to nitrogen impurities, Γ_{n} will explicitly depend on the nitrogen density and must be optimised, as shown below. The total signal from a single FID protocol cycle, $\mathcal{S} = \sum_i \mathcal{S}_i$, is the sum of the signals from all NV centres, and in the high NV density limit, is given by

$$\mathcal{S}(\tau) \;=\; \alpha\gamma\tau n \int_{V_p} B(\mathbf{r},\tau)\, L(\mathbf{r},\tau)\, \mathrm{d}^3\mathbf{r}, \tag{9.2.3}$$

where n is the total electron spin density due to both nitrogen and NV defect centres (assumed uniform for chemical vapor deposition grown samples, and an axially-symmetric Gaussian for implanted samples), α is the nitrogen-NV conversion efficiency, and V_p is the volume of a given pixel. Since the measurement of each NV centres is projective, the total signal distribution follows the central limit theorem

and the uncertainty in the signal is given by

$$\delta\mathcal{S} \;=\; \frac{1}{C}\sqrt{\frac{N_p}{N_t}}, \tag{9.2.4}$$

where C is an experimental parameter accounting for imperfect photon collection (including non-unity quantum efficiency of the detector) and signal contrast, and N_p is the effective number of NV defects (probes) in V_p, given by $N_p \approx \alpha n V_p$. To measure the magnetic field of an axon, ultimately we require $\mathcal{S} \gtrsim \delta\mathcal{S}$.

We now consider a simple, analytically solvable case where the axon dimensions are large ($\sim 60\,\mu$m, as in the case of a crayfish lateral axon [WG61]) compared with a sensing volume of $V_p \sim (1\,\mu\,\mathrm{m})^3$, ensuring there is little variation in the magnetic field strength over the sensing volume (i.e. $B_i \equiv B \forall i$). The signal is then $\mathcal{S} \approx \alpha n V_p \gamma B \tau$. The minimum detectable magnetic field is then

$$\delta B \;=\; \frac{1}{\gamma C\sqrt{\alpha N_t V_\mathrm{p}}}\frac{\exp\left[\tau^2\left(\Gamma_{\mathrm{c}_{13}}^2+\Gamma_\mathrm{n}^2\right)\right]}{t\sqrt{n}}, \tag{9.2.5}$$

which we wish to optimise for n and τ, giving firstly $\tau_\mathrm{opt} = \left(2\Gamma_{\mathrm{c}_{13}}^2 + 2\Gamma_\mathrm{n}^2\right)^{-1/2}$. The dephasing due to nitrogen is given by $\Gamma_\mathrm{n} = \kappa n$ [HHCH10], where $\kappa = \sqrt{\frac{\pi}{3}}\frac{\mu_0}{4\pi}\hbar\gamma^2$. Setting $\frac{\partial}{\partial n}\delta B = 0$ gives $\Gamma_{\mathrm{c}_{13}} = \Gamma_\mathrm{n}$, hence $n = \Gamma_{\mathrm{c}_{13}}/\kappa = 2.3 \times 10^{23}\,\mathrm{m}^{-3} = 1.3\,\mathrm{ppm}$, an order of magnitude below the maximum reported density achieved in practice to date of $2.8 \times 10^{24}\,\mathrm{m}^{-3}$ [ABL$^+$09]. The minimum detectable field by a pixel of volume V_p is then

$$\delta B \;=\; \frac{3.3\,\mathrm{nT}\,\mu\mathrm{m}^{3/2}}{C\sqrt{\alpha N_t V_\mathrm{p}}}.$$

For example, an implementation with $C = 0.3$ and an N-NV conversion ratio of $\alpha = 0.1$ would be capable of resolving a magnetic field to an accuracy of 3.5 nT in an integration time of 1 ms ($N_t = 100$).

In the large axon case considered here, increasing V_p will result in an improved sensitivity, however this will not be true in general. As V_p becomes comparable to the axon dimensions, the field felt by distant NV centres will be significantly less than that felt by those proximate to the axon, and the integral in equation 9.2.3 will no longer scale linearly with V_p. The noise amplitude however (equation 9.2.4) will grow with the square root of the sensing volume, regardless of the axon field characteristics. If the sensing volume is sufficiently large that the signal exhibits sub-square root scaling with the sensing volume, there will be no advantage in having a larger V_p. As such, better results for smaller neural components will be achieved by optimising the V_p for the task at hand.

The maximum frequency with which measurements may be taken is

$$f_{\mathrm{m}} \;=\; (\tau_{\mathrm{opt}} + \tau_{\mathrm{m}})^{-1}\,, \tag{9.2.6}$$

where $\tau_{\mathrm{opt}} = (2\Gamma_c)^{-1}$ from above, and $\tau_{\mathrm{m}} \sim 350\,\mathrm{ns}$ is the time required for photon collection and subsequent re-polarisation of the NV spin state. To gain further improvements to the SNR, we envisage taking numerous measurements with frequency f_{m}, and applying a low-pass filter to the measurement record. Incorporating a greater number of timepoints in this process will improve the sensitivity, however this comes at a cost of decreased temporal resolution, $\delta t = N_t/f_m$. A faithful reconstruction of the field dynamics with time-lag δt will be possible provided δt is less than the characteristic timescales of the neural dynamics.

$$\delta t \;=\; \left(\frac{3.3\,\mathrm{nT}}{B}\right)^2 \frac{\tau_{\mathrm{opt}} + \tau_{\mathrm{m}}}{C\sqrt{\alpha V_{\mathrm{p}}}\,\mu\mathrm{m}^{3/2}}. \tag{9.2.7}$$

The effect of averaging over different ranges of measurements and the trade-off that exists between a high SNR and high temporal and spatial resolution is considered

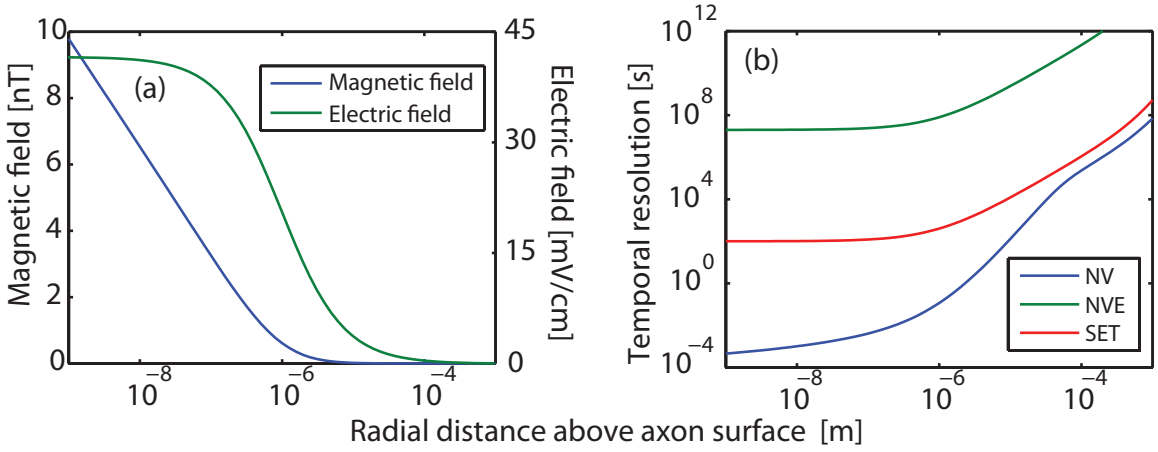

Figure 9.3: (a) Dependence of magnetic and electric field strength on radial distance above the axon surface. The more immediate attenuation of the magnetic field permits roughly an order of magnitude better spatial imaging resolution as compared with the electric field. Note the different axes used for electric and magnetic fields. (b) Comparison of the temporal resolution corresponding to sensing the magnetic field using diamond crystal containing a high NV centre density (NV, blue), and sensing the electric field using the same NV centre density (NVE, green) and a single electron transistor (SET, red).

later for the case of the hippocampal CA1 pyramidal neuron.

9.3 Results

9.3.1 Comparison of magnetic and electric field detection

This method of monitoring neuron function through the magnetic fields generated offers a distinct advantage over consideration of the resulting electric fields. The electric field is a consequence of the local gradient of the electric potential, whereas magnetic field detection is sensitive to non-local field sources. That is, the external magnetic field is a consequence of both the internal and external electric fields, the

strength of the former being some 3 orders of magnitude larger than the latter.

Electric field detection protocols using single electron transistors (SETs) have sensitivities of $2\,\mathrm{V\,cm^{-1}\,Hz^{-1/2}}$ at standoffs of 100 nm [DS00], however there are significant practical compatibility issues associated with real neural samples and the need for cryogenic sensing operation. Electric field sensing using NV centres does allow for room temperature operation, however the associated DC field sensitivity was recently demonstrated at $613\,\mathrm{V\,cm^{-1}\,Hz^{-1/2}}$ [DFD+11], whereas single NV sensitivities to DC magnetic fields have been demonstrated at $43\,\mathrm{nT\,Hz^{-1/2}}$ [BNT+09]. The peak magnitudes of magnetic and electric fields around a typical axon are shown in figure 9.3(a), yielding 3 nT and $40\times10^{-3}\,\mathrm{V\,cm^{-1}}$, respectively, at a standoff of 100 nm. For the sake of comparison, figure 9.3(b) shows the time required for a single NV centre to resolve the magnetic and electric field strengths in the region surrounding a typical axon. Clearly local magnetic detection offers an advantage in terms of both spatial and temporal resolution.

9.3.2 Experimental verification of detection protocol

To experimentally demonstrate the effectiveness of the proposed detection protocol for neuron specific signals, and quantitatively verify the theoretical analysis, we replicated the magnetic field produced by a single axon using a microwire on the surface of a diamond substrate (figure 9.4(a)). The pulses were constructed such that the resulting Biot-Savart field emulates the temporal dynamics of the axon considered in the preceding section (figure 9.4(b)). A single NV centre, located at a lateral distance of approximately $10\,\mu$m from the wire, was used as the sensor.

We simulated the detection gain of N_p centres by repeating the measurement

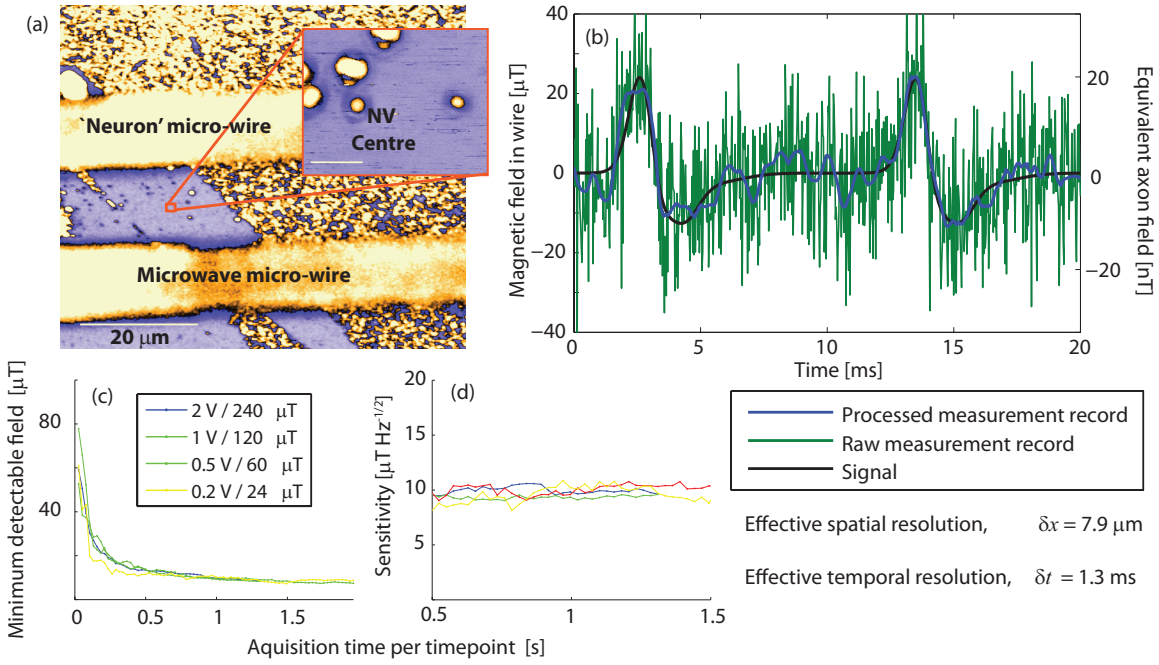

Figure 9.4: Detection of experimentally simulated neuron signals using the ODMR detection protocol on a single NV centre. (a) Confocal fluorescence image showing the spatial arrangement of the NV with respect to the microwave and artificial neuron signal micro-wires. (b) Experimental measurement of the electronically generated neuron pulse together with the extrapolated effective spatial and temporal resolution corresponding to a high NV density widefield detection system. Optimisation of this protocol to achieve higher resolutions is discussed in the main text. (c) Experimental minimum detectable magnetic field, δB vs total photon integration time, T, showing a $\delta B \propto T^{-1/2}$ dependence. This dependence is verified by plotting the corresponding sensitivity, $\eta = \delta B\sqrt{T}$, in (d), showing the sensitivity is effectively constant.

process N_s times. The binning widths for the photon integration times were $t_p = 24.2\mu$s, and the total time taken to send two successive pulses down the wire was 20 ms (figure 9.4(d)). The dynamics of this signal place a limit on the permissable temporal resolution, $\delta t \approx 1 - 2$ ms, hence the maximum number of data points employed in the low-pass filtering process is $N_t = \delta t / t_p \approx 50$. Assuming a constant sensitivity, the effective number of centres involved in the detection may then be determined from $N_p = \frac{N_s}{N_t} \left(\frac{B_w}{B_a}\right)^2$, where B_w is the peak magnetic field strength due to the pulse in the wire, and B_a is the peak magnetic field strength due to the axon. This assumption was experimentally verified by measuring the minimum detectable magnetic field for a range of photon integration times (figure 9.4(c)), from which a corresponding sensitivity of $10\,\mu\mathrm{T\,Hz}^{-1/2}$ was determined (figure 9.4(d)), for this (non-optimised) system.

The figures of merit are the effective spatial and temporal resolutions, given by $\delta x = (N_p/n)^{1/3}$ and $\delta t = N_t t_p$ respectively. The measurement record obtained by monitoring a pulse with $B_w = 24\,\mu$T, and $N_s = 5,000$ cycles is given by the green trace in figure 9.4(b). From the above scaling, this is equivalent to a pixel volume of $V_p = (7.9\,\mu\mathrm{m})^3$ at a temporal resolution of $\delta t = 1.3$ ms. Sacrifices in the temporal resolution will allow for decreases in the required pixel volume, for example, a pixel volume of $V_p = (1\,\mu\mathrm{m})^3$ has a corresponding temporal resolution of $\delta t = 2$ ms. These figures clearly demonstrate, experimentally, that NV are centres are capable of simultaneously resolving both the spatial structure and temporal dynamics of neuronal magnetic fields, even in their current, unoptomised implementation. Further improvements may be achieved with the use of higher grades of isotopocially pure diamond crystal, as used in [BNT+09], where single-spin DC magnetic field sensitivities

of $43\,\mathrm{nT\,Hz^{-1/2}}$ were demonstrated. Extrapolating this to the present context, such sensitivities would permit a pixel volume of $V_p = (0.2\,\mu\mathrm{m})^3$ at a temporal resolution of 1.3 ms. How these capabilities relate to the spatial and temporal characteristics of a biological neuronal network are discussed in the following section.

9.3.3 Imaging simulation: the hippocampal CA1 pyramidal neuron

In order to quantitatively describe how the device would sense and image neural activity we simulated the magnetic fields that would be produced by a neuron while it receives synaptic input and generates and fires an action potential output. The neuron model we used was of a morphologically reconstructed hippocampal CA1 pyramidal neuron. Hippocampal CA1 pyramidal neurons have an extended morphology, show a rich repertoire of dynamics and are involved in networks that underlie important behaviour such as learning and memory. Study of these neurons and the networks they reside in will be a major target of the techniques described here.

Typically such an experiment would be performed in vitro using a buffer solution of phosphate buffered saline (PBS), or equivalent. Such solutions contain dissolved sodium and potassium salts at concentrations of roughly $150\,\mathrm{mmol\,L^{-1}}$, giving rise to nuclear spin concentrations of roughly $10^{25}\,\mathrm{m^{-3}}$, some 5 orders of magnitude less than the hydrogen nuclear spin concentration due to water molecules. The hydrogen spins themselves produce an effective stochastic magnetic field with fluctuations caused by molecular self-diffusion. This would cause the decoherence rates of NV centres at even a few nanometres from the diamond surface to increase by approximately 100 Hz-1 kHz [HHC+10], some 2-3 orders of magnitude less than that due to intrinsic

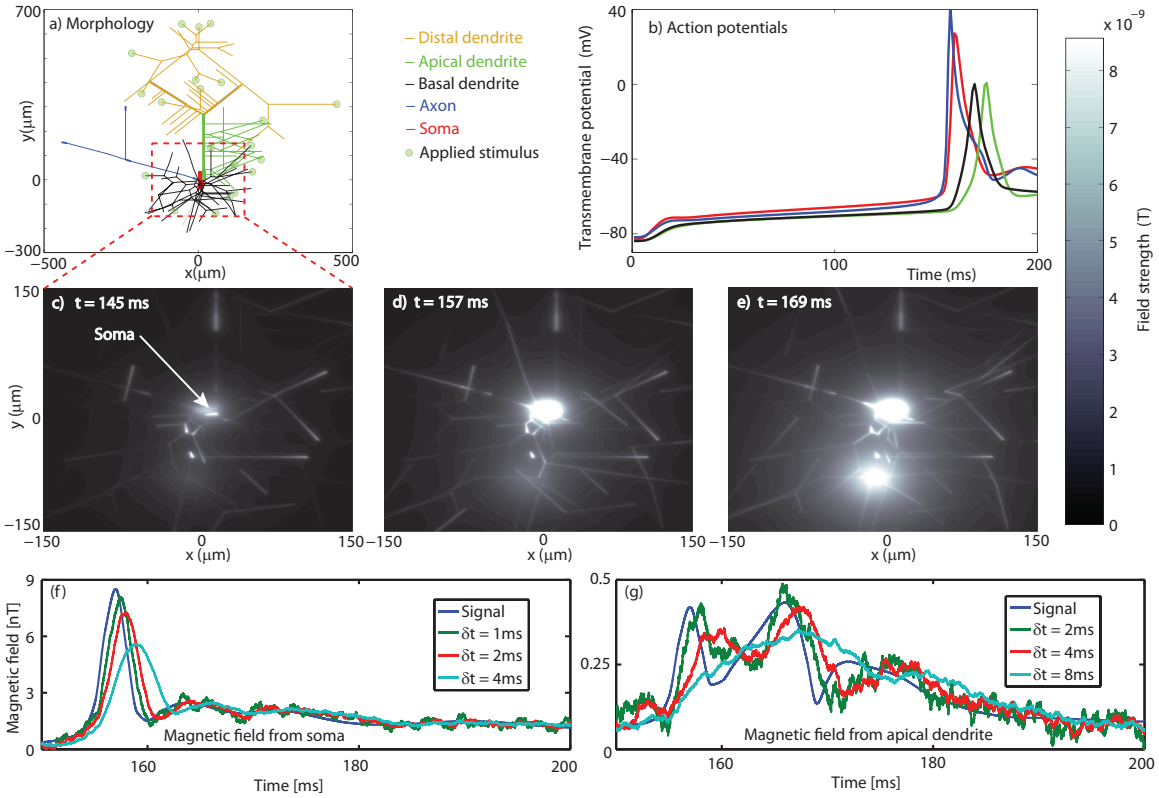

Figure 9.5: (a) Morphology of the Royeck-Wimmer model and input excitation sites. (b) Transmembrane potentials generated at the soma, axon and dendrites shown in (a). (c-e) Zoomed plots of magnetic field strength at 100 nm standoff showing the integrate and fire effect of the central soma and the reactionary dynamics in the dendritic region below. Simulated measurements taken at (f) $0\,\mu$m and (g) $45\,\mu$m along the apical dendrite directly above the soma, as shown in (a) for a detection volume of $V_p = (2\,\mu\text{m})^3$ and a range of integration times, δt. Note the change of magnetic field strength scale in (f) and (g), resulting in the latter requiring longer integration times. Assumed parameter values are $C = 0.05$, and $\alpha = 0.1$.

decoherence sources, and can therefore be ignored.

The model consists of 265 anatomical sections (figure 9.5(a)) and 15 voltage and calcium activated conductances with a non-uniform distribution across the morphology. We stimulated the model neuron with 2nA current injections into 21 sites on distal dendrites. The associated transmembrane potentials at specific locations are shown in figure 9.5(b). As the distal dendrites are stimulated current flows along these processes towards the soma. The associated magnetic field strength changes are readily seen in the sequence of time snapshots, figure 9.5(c-e). As the membrane potential increases the soma current flow along the dendrites decreases, reducing the magnetic field strength (figure 9.5(c)). As active conductances in the soma and axon are recruited, current flow increases in these compartments and the field strength increases. Eventually an action potential is triggered in the soma and distal axon (figure 9.5(d)). The initiation point in the distal axon is not as bright as the soma because the technique is sensitive to longitudinal currents, not voltage. A back propagating action potential is also triggered in the basal dendritic tree (figure 9.5(e)).

In figure 9.5(f)&(g) we show the single ($2\,\mu$m) pixel detection trace of the neuronal magnetic field at two locations below the neuron structure in response to the applied stimuli, assuming experimentally realised values of $C = 0.05$[CDT^{+}06], and $\alpha = 0.1$. The magnetic field signal is plotted together with the simulated measurement output for a range of integration times, δt. As the integration time is increased the SNR improves, at the cost of temporal resolution in the neuronal signal itself. However, it is evident that a minimal time-lag of 1ms gives an acceptable account of the neuron signal in all three cases.

Finally, we determine the overall spatial-temporal resolution of the imaging system

by explicitly considering the trade-off between integration time and detection volume. In figure 9.6 we show the simulated CMOS/CCD output (assuming a readout rate of 500 fps, as available with current technology [Sab11]) for a snap-shot of the neuron activity at $t = 157$ ms for a range of integration times δt and spatial detection volumes δx. It is clear that the neuronal magnetic field structure is apparent at $[\delta x, \delta t] = [2\,\mu\text{m}, 1\,\text{ms}]$, showing the imaging system has the temporal resolution to fully map the magnetic field dynamics of a neuronal network, whilst simultaneously reproducing the structural morphology at the sub-cellular level.

9.4 Discussion

We have investigated the use of the magnetic field sensing properties of NV-ensembles in diamond for imaging neural activity. Using published crayfish lateral axon biophysical data we determined the magnetic field signal at 100nm from the axon surface to demonstrate that it lies within the sensitivity range of our detection system. The sensitivity regime for detection of the magnetic field dynamics generated in the axon structure was determined based on both pulsed (FID) and continuous wave (ODMR) sequences. Direct measurement of axon-scale magnetic fields, produced by passing current in a proximate microwire, verified that the sensitivity limits fell within the range needed to detect neuronal signals. To explore the potential utility of NV arrays as wide field detectors of neuronal network activity we simulated the three dimensional magnetic fields associated with action potential propagation in a morphologically realistic hippocampal CA1 pyramidal neuron placed 100nm from the NV detection layer. The simulated photon emission of our model neuron/NV-layer combination

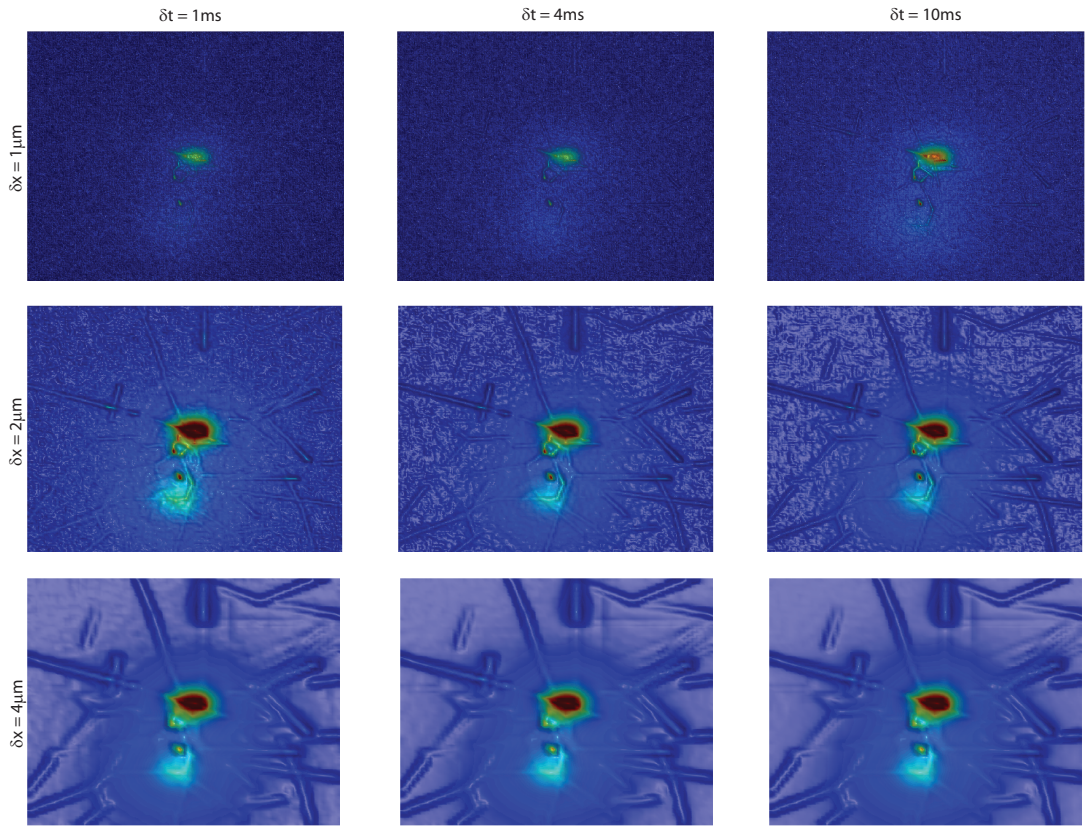

Figure 9.6: Simulated snapshot of the CCD output at $t = 157\,\mathrm{ms}$ and for a range of detection volumes, $V_p = (\delta x)^3$ and integration times δt. Assumed parameter values are $C = 0.05$, and $\alpha = 0.1$.

was projected onto a virtual CMOS array to investigate the performance of the sensor in detecting local and wide-field neuronal structure and dynamics. By exploring different combinations of integration times, δt, and detection regions, δx, we found that the performance of the sensor enabled simultaneously high temporal and spatial resolution of extracellular field potentials in regimes beyond those obtained by current methodologies. In summary, our experimental results and theoretical work establish the significant potential of this quantum based technique to visualise the key components of neuronal network activity, subthreshold signalling, action potential initiation and propagation in axons, soma and dendritic compartments, at relevant scales to provide new views into network function. To bring this imaging concept to reality one must assemble all the individual and non-trivial components, such as sufficiently dense near-surface NV layer structures in high grade diamond material, neuron growth on these diamond surfaces, and microwave quantum control and optical wide-field readout commensurate with long term integrity and function of the biological structure. Precursor experiments based on well characterized biological systems will extend the experimental work carried out here on model neuronal signals.

Chapter 10

Sensing of Fluctuating Nanoscale Magnetic Fields via Relaxation of Electron Spins in solids

In this chapter we shift our focus from pure dephasing (T_2) processes to those resulting in the relaxation (T_1) of an NV spin coupled to some proximate magnetic environment. Where T_2 based sensing was sensitive to a broad range of frequencies centred about $\omega = 0$, T_1 based sensing requires a resonant energy exchange with the environment, and hence only couples to frequencies close to the transition frequencies of the NV spin-1 system. This makes T_1 based sensing inherently more sensitive to high frequency phenomena, and therefore well suited to characterising electron spin systems. In what follows we discuss not only how this selectivity arises, but how it may be tuned to measure specific regions of the environmental spectrum, and consequently, how this spectrum may be reconstructed in practice from an arbitrary environment. We perform a detailed theoretical analysis of two experiments, which demonstrate excellent agreement between experimental results and the theory developed here.

10.1 Introduction

To this point, we have considered the detection of magnetic processes based exclusively on monitoring the dephasing of the NV electron spin. As such, dephasing based sensing is only appreciably sensitive to processes occurring with frequencies of less than a few MHz, and are thus well suited to characterising nuclear spin based environments. However, to achieve the desired sensitivity to rapidly fluctuating fields, and more importantly, the ability to be selective, we have seen that extremely complex pulse sequences are necessary.

On the other hand, given the GHz transition frequencies associated with the NV spin in its orbital ground state, we would expect the comparatively rapid electron based environments to be capable of exchanging energy with the NV spin, thereby enabling a relaxation, or T_1 based sensing approach. This is particularly enticing, as both the energy levels of environmental spins, $\omega_{\mathrm{E}} = \gamma B_0$, and the NV spin, $\omega_{\mathrm{NV}} = D \pm \gamma B_0$, can be tuned via the Zeeman effect through control of the background magnetic field, B_0. This makes T_1 based sensing a selective, tunable protocol that allows regions of the frequency spectrum to be filtered out as desired.

Another advantage of T_1 based imaging stems from the fact that T_1 times of an NV centre can be up to 3 orders magnitude longer than spin-echo based T_2 times. This corresponds to an improvement in sensitivity by a factor of $\sqrt{T_2/T_1}$ over T_2 based protocols. This allows for a much greater contrast, particularly in detection setups based on an NV array where intrinsic T_2 times of a few μs make relaxation rates of MHz or slower difficult to detect. Such processes are readily detectable when intrinsic T_1 times are greater than a few ms.

In this chapter, we develop the theory of relaxation based sensing by considering

the simple case of a spin-$\frac{1}{2}$ electron system. This is then extended to the more complex spin-1 system, allowing the relevant properties of the NV spin to be described. We then discuss how this protocol can be tuned to different regions of the target system's fluctuation spectrum, and consequently, how this spectrum may be experimentally reconstructed. We conclude this chapter by using the techniques developed here to analyse two recent experiments.

10.2 Modeling

The time evolution of the density matrix is described by

$$\frac{\mathrm{d}\rho_T}{\mathrm{d}t} = -i\big[\mathcal{H}_T(t), \rho_T\big], \tag{10.2.1}$$

where ρ_T represents the combined density matrix of the entire spin + environment system. The full Hamiltonian is given by $\mathcal{H}_T = \mathcal{H}_0 + \mathcal{V} + \mathcal{H}_E$ where $\mathcal{H}_0$ and $\mathcal{H}_E$ are the self Hamiltonians of the NV centre and environment respectively. The coupling of the environment to the NV is described by the full dipolar interaction due to all spins in the environment:

$$\mathcal{V} = \frac{\mu_0}{4\pi}\hbar\gamma_{nv}\gamma_E \sum_i \frac{1}{R_i^3}\left[\vec{\mathcal{S}}_{\mathrm{nv}} \cdot \vec{\mathcal{S}}_i + \frac{1}{R_i^2}\left(\vec{\mathcal{S}}_{\mathrm{nv}} \cdot \mathbf{R}_i\right)\left(\mathbf{R}_i \cdot \vec{\mathcal{S}}_i\right)\right], \tag{10.2.2}$$

which includes both transverse and longitudinal components, proportional to $\mathcal{S}_{x,y}$ and $\mathcal{S}_z$ of the NV spin respectively. The latter have a pure dephasing effect, resulting in an additional contribution to the intrinsic dephasing rate of the NV. As the environmental constituents are assumed to strongly interact with each other and only weakly with the NV, the dephasing will be purely exponential (see chapter 4). These effects may thus be modeled using a master equation approach for the reduced density

matrix for the ensemble averaged dynamics of the NV, ρ, as follows

$$\frac{\mathrm{d}\rho}{\mathrm{d}t} = -i\big[\mathcal{H}(t),\rho\big] + \mathcal{L}\rho\mathcal{L}^{\dagger} - \frac{1}{2}\left\{\mathcal{L}^{\dagger}\mathcal{L},\rho\right\}, \tag{10.2.3}$$

where, in the present context, $\mathcal{L}$ is the Lindbladian operator corresponding to a pure dephasing process, and is given by $\mathcal{L} = \sqrt{\Gamma}_2\sigma_z$. The total dephasing rate due to both the local crystal environment and the longitudinal coupling to the environment is given by $\Gamma_2 = (T_2^*)^{-1} + \Gamma_2^{\mathrm{nv-E}}$. The timescale of the intrinsic dephasing process is described using the inhomogeneous linewidth, $(T_2^*)^{-1}$, since the lateral phase accumulation occurs in the absence of any pulsed microwave control. Subtle tuning effects that modify the sensitivity of this technique to various parts of the environmental spectral density may be achieved by changing the intrinsic dephasing rate via dynamic decoupling techniques.

In what follows, owing to the strong intra-environment and comparatively weak NV-environment couplings, we will treat the coupling of the environment to the transverse components of the NV spin as a semiclassical oscillatory field,

$$\mathcal{V} = \mathcal{B}e^{i\omega t} + \mathcal{B}^{\dagger}e^{-i\omega t}, \tag{10.2.4}$$

where $\mathcal{B} = B_x(\omega)\mathcal{S}_x + B_y(\omega)\mathcal{S}_y$; and B_x and B_y are the x and y components of the magnetic field. The frequency spectrum is determined by analysing the interaction between environmental constituents, as described by $\mathcal{H}_E$. The details of this approach are discussed in chapter 12, section 12.5.

To make the solution tractable, we change to the interaction picture (see appendix A). The transformed equation of motion is given by

$$\frac{\mathrm{d}}{\mathrm{d}t}\rho_I(t) = -i\big[\mathcal{V}_I(t),\rho_I(t)\big] + \Gamma_2\big(\sigma_z\rho_I(t)\sigma_z - \rho_I(t)\big), \tag{10.2.5}$$

with the interaction Hamiltionian given by $\mathcal{V}_I = e^{i\mathcal{H}_0 t}\mathcal{V}e^{-i\mathcal{H}_0 t}$.

We are then interested in determining the rate at which the NV spin relaxes to its equilibrium state under the influence of the environment. We proceed by reducing the 3×3 system of first order linear differential equations described by equation 10.2.5 to a higher order differential equation for ρ_{00}. We then wish to solve this equation, together with the initial conditions of $\rho_{ij} = 0$ unless $i = j = 0$, in which case we have $\rho_{00} = 1$, representing the initial polarisation of the NV spin in the $|0\rangle$ state.

10.2.1 A simplified example: one excited transition

To gain insight into the expected analytic solution for the spin-1 NV centre, we consider the simplified case in which only one of the transitions of the NV centre is excited by the environment, and the other is assumed to be too far detuned to have any effect on the population of the spin states. This simplifies the analysis dramatically, yet demonstrates the main properties of relaxation based detection. Incidentally, this simplification is still applicable to a spin-1 system for cases of significantly strong Zeeman splittings between the $|\pm1\rangle$ states. This ensures that one transition will be excited by the environment, whilst the other is not. This forms the basis of the technique by which environmental spectra may be mapped, as outlined in section 10.3.

Resonant case

For the case where the frequency of the environment is resonant with the transition frequency between the probe's spin states, the equation of motion for $z = P_0 - \frac{1}{2}$ is

$$\frac{\mathrm{d}^2 z}{\mathrm{d}t^2} + \Gamma_2 \frac{\mathrm{d}z}{dt} + B^2 z \;=\; 0, \tag{10.2.6}$$

where $B \equiv \langle \mathcal{B}^2 \rangle^{\frac{1}{2}}$, the solution of which is

$$\begin{aligned} z(t) &= \frac{1}{4}\left[\exp\left(-\Gamma_2 t + \Gamma_2 t\sqrt{1-4\frac{B^2}{\Gamma_2^2}}\right) + \exp\left(-\Gamma_2 t - \Gamma_2 t\sqrt{1-4\frac{B^2}{\Gamma_2^2}}\right)\right] \\ &\quad + \frac{1}{4}\frac{\Gamma_2}{\sqrt{\Gamma_2^2 - 4B^2}}\left[\exp\left(-\Gamma_2 t + \Gamma_2 t\sqrt{1-4\frac{B^2}{\Gamma_2^2}}\right)\right. \\ &\quad \left. - \exp\left(-\Gamma_2 t - \Gamma_2 t\sqrt{1-4\frac{B^2}{\Gamma_2^2}}\right)\right]. \end{aligned} \tag{10.2.7}$$

Typically the spin based environments in which we are interested couple weakly to the NV spin as compared with its intrinsic dephasing rate, giving $\Gamma_2 \gg B$. In fact, even a strong coupling will also induce additional dephasing, so even in a worst case scenario we are guaranteed $\Gamma_2 > B$. In this limit, we have

$$P_0(t) = \frac{1}{2} + \frac{1}{2}\exp\left(-\frac{B^2}{\Gamma_2}t\right). \tag{10.2.8}$$

Hence the longitudinal relaxation rate is given by

$$\Gamma_1 = \frac{1}{T_1} = \frac{B^2}{\Gamma_2} = T_2 \left\langle \mathcal{B}^2 \right\rangle. \tag{10.2.9}$$

Off resonance

When a finite detuning, δ, exists, the equation of motion becomes

$$\cos(\delta t)\frac{\mathrm{d}^2 z}{\mathrm{d}t^2} + \left[\Gamma_2 \cos(\delta t) + \delta \sin(\delta t)\right]\frac{\mathrm{d}z}{\mathrm{d}t} + B^2 \cos(\delta t)\, z = 0 \tag{10.2.10}$$

To determine the relative importance of the terms within this equation, we rescale t in terms of the decay time from the resonant solution. That is, if we consider the dimensionless variable $T = \Gamma_1 t$, the equation of motion becomes

$$R^2 \cos(\kappa_1 T)\frac{\mathrm{d}^2 z}{\mathrm{d}T^2} + \left[\cos(\kappa_1 T) + \kappa_2 \sin(\kappa_1 T)\right]\frac{\mathrm{d}z}{\mathrm{d}T} + \cos(\kappa_1 T)\, z = 0, \tag{10.2.11}$$

where $R = B/\Gamma_2 \ll 1$, $\kappa_1 = \frac{\delta}{\Gamma_1}$ and $\kappa_2 = \frac{\delta}{\Gamma_2}$. In light of this, we may treat the term with the second derivative as a perturbation. The zeroth order solution is given by

$$z(T) = \frac{1}{2} e^{-\frac{T}{\kappa_2^2+1}} \left(\frac{\delta}{\Gamma} \sin(\delta t) + \cos(\delta t) \right)^{-\frac{\kappa_2}{\kappa_1 \kappa_2^2 + \kappa_1}}, \tag{10.2.12}$$

which, for small δ, becomes

$$P_0(t) = \frac{1}{2} + \frac{1}{2} \exp\left(-\Gamma_1 t \frac{\Gamma_2^2}{\delta^2 + \Gamma_2^2} \right). \tag{10.2.13}$$

For zero detuning, we recover the previous result (equation 10.2.9). For finite detuning, the relaxation rate is modified by a Lorentzian factor with a FWHM of Γ_2. The complete decay profile is then obtained by integrating this expression over the spectral density of the environment.

10.2.2 General case: Two excited transitions

To find the solution for the spin 1 case, we follow the same analysis as above. Let $\omega_+ \equiv D + B_0$ and $\omega_- \equiv D - B_0$ denote the energy differences between the $|0\rangle$, $|+1\rangle$ and $|0\rangle$, $|-1\rangle$ states respectively. The corresponding detunings are then $\delta_+ = \omega - \omega_+$ and $\delta_- = \omega - \omega_-$; and the corresponding decay rates are

$$\Gamma_1^+ = 2\Gamma_1 \frac{\Gamma_2^2}{\delta_+^2 + \Gamma_2^2}, \tag{10.2.14}$$

$$\Gamma_1^- = 2\Gamma_1 \frac{\Gamma_2^2}{\delta_-^2 + \Gamma_2^2}, \tag{10.2.15}$$

where $\Gamma_1 = B^2/\Gamma_2$. The probability of finding the NV in the $|0\rangle$ state is given by

$$P_0 = \frac{1}{6} \left(2 + e^{-\Gamma_1^+ t} + e^{-\Gamma_1^- t} + 2e^{-\left(\Gamma_1^+ + \Gamma_1^-\right)t} \right). \tag{10.2.16}$$

To consider some of the interesting relaxation regimes described by this expression, suppose firstly that the splitting between the $|\pm 1\rangle$ levels is large relative to Γ_2,

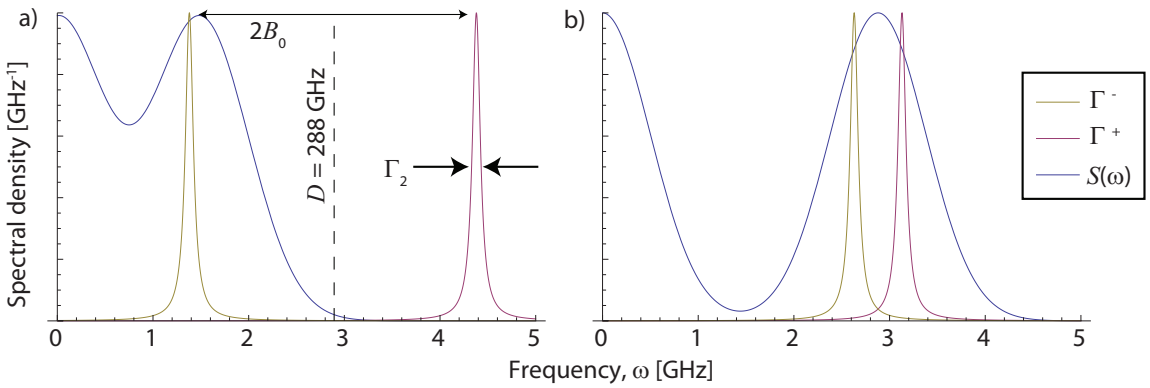

Figure 10.1: Illustration of the way in which the NV relaxation filter functions, Γ_1^+ and Γ_1^- filter specific regions of the environmental spectral density. (a) One of the NV transitions is significantly detuned from the environment and hence cannot be excited. The NV spin thus behaves as a spin-$\frac{1}{2}$ qubit and the steady state of the NV spin will be an equal mixture of only the two states associated with the excited transition, with the third state remaining unpopulated. (b) Both transitions are appreciably excited, meaning the steady state of the NV spin will be an equal mixture of all three magnetic sublevels.

and that the $|0\rangle \rightarrow |-1\rangle$ transition is significantly excited by the environmental spectrum, whereas the $|0\rangle \rightarrow |+1\rangle$ transition is sufficiently detuned that it is not excited (see figure 10.1 (a)). In this case, we have $\Gamma^+ \sim 0$ for all frequencies of the spectrum, giving

$$P_0 = \frac{1}{2}\left(1 + e^{-\Gamma_1^- t}\right), \tag{10.2.17}$$

which is equivalent to the spin-$\frac{1}{2}$ case. On the other hand, if both transitions are appreciably excited (figure 10.1 (b)), the system will decay to an equal mixture of all 3 spin states. This can be seen by taking $\Gamma_+ \approx \Gamma_-$, giving

$$P_0 = \frac{1}{3}\left(1 + e^{-\Gamma_1^+ t} + e^{-2\Gamma_1^+ t}\right). \tag{10.2.18}$$

To find the overall relaxation rate of the $|0\rangle$ spin state in the presence of an arbitrary environment, we must integrate the expression in equation 10.2.16 over the

corresponding spectral density. In the following, we consider the effects of two limiting spectral regimes on the relaxation rate of the NV spin.

Quasi white Noise/Broad spectrum

Consider the case of a broad spectral density given by $S(\omega) = 1/f_e$, where $f_e \gg D + B_0 + \Gamma_2$ is some high frequency cutoff, or effective spectral linewidth. The corresponding ensemble averaged population of the $|0\rangle$ spin state is given by

$$\begin{aligned} \langle \mathrm{P}_0 \rangle &= \int_{-\infty}^{\infty} S(\omega) \left[\exp\left(-\Gamma_1 t \frac{\Gamma_2^2}{\delta^2 + \Gamma_2^2} \right) \right] \mathrm{d}\delta \\ &\sim \exp\left(-\pi \frac{B^2}{f_e} t \right), \end{aligned} \tag{10.2.19}$$

for $t < B^2/f_e$. The initial ensemble decay rate of the population of the $|0\rangle$ spin state in the presence of an environment defined by a high frequency cutoff f_e is therefore given by

$$\left\langle \Gamma_1 \right\rangle = \frac{1}{T_1} = \pi \frac{B^2}{f_e} \tag{10.2.20}$$

Despite the apparent simplicity of this anaysis, this turns out to be an excellent approximation for electron environments (see the experimental investigation in section 10.4 below) due to their broad spectral density. Notice also that Γ_2 does not appear in the final expression.

Black noise/narrow spectrum

In cases where the linewidth is much smaller than Γ_2, the spectrum approaches a small number of infinitesimally thin bands and may be approximated by one (or more) delta function(s) about the characteristic frequency of the environment, f_e. In

the case of a single band, we may thus simply replace ω with f_e. If the peak splitting is much greater than the dephasing rate ($B_0 \gg \Gamma_2$), this reduces to

$$\begin{aligned} \langle \mathrm{P}_0 \rangle &= \int S(\omega) P_0 \, \mathrm{d}\omega \\ &\approx \frac{1}{2}\left(1 + e^{-\Gamma_1 t}\right), \end{aligned} \tag{10.2.21}$$

and the ensemble relaxation rate is given by

$$\left\langle \Gamma_1 \right\rangle = \Gamma_1 = \frac{B^2}{\Gamma_2}, \tag{10.2.22}$$

which is just the resonant case from above.

10.3 Reconstruction of the environmental spectral density

As noted above, the region of the spectral density filtered by the NV filter functions may be tuned by controlling the strength of the static background field. This suggests that, by sweeping the filter function across the entire spectrum, we should be able to reconstruct it by measuring the relaxation rate of the NV spin.

We denote an arbitrary given noise spectrum at zero field by $S_0(\omega)$. The distribution at some finite background field ω_0 is then $S_0(\omega - \omega_0)$. For simplicity we assume the shape of the distribution does not change with ω_0, although this case is easily handled by extension. Furthermore, we also assume that one of the NV transitions is sufficiently detuned that it is not sensitive to the environment. When this is not true, the detuned filter function will translate with ω_0 at the same rate as $S_0(\omega - \omega_0)$, and thus produce a constant shift in the overall measurement that does not change

with ω_0, which may be later subtracted. We denote the non-trivial filter function by

$$G(\omega) \;=\; 2B^2 \frac{\Gamma_2}{\omega^2 + \Gamma_2^2}\,. \tag{10.3.1}$$

The response of the NV to the arbitrary spectrum is given by

$$M(\omega_0) \;=\; \int_{-\infty}^{\infty} S_0(\omega - \omega_0) G(\omega - D + \omega_0)\,\mathrm{d}\omega. \tag{10.3.2}$$

By introducing the frequency-space variable $\Omega = \omega - \omega_0$, and the parameter, $\Omega_0 = D - 2\omega_0$, and making use of the symmetry properties of the Lorentzian function, we may write this integral as a Fourier-space convolution,

$$\begin{aligned} M(\Omega_0) \;&=\; \int_{-\infty}^{\infty} S_0(\Omega) G(\Omega_0 - \Omega)\,\mathrm{d}\Omega \\ &=\; (S_0 * G)\,(\Omega_0). \end{aligned} \tag{10.3.3}$$

Given that the filter function is known, and can be measured to arbitrary precision using ODMR at low laser and microwave powers (see chapter 3), the spectral density may thus be reconstructed using an appropriate deconvolution algorithm or numerical routine (MATLAB's `deconv`, for example).

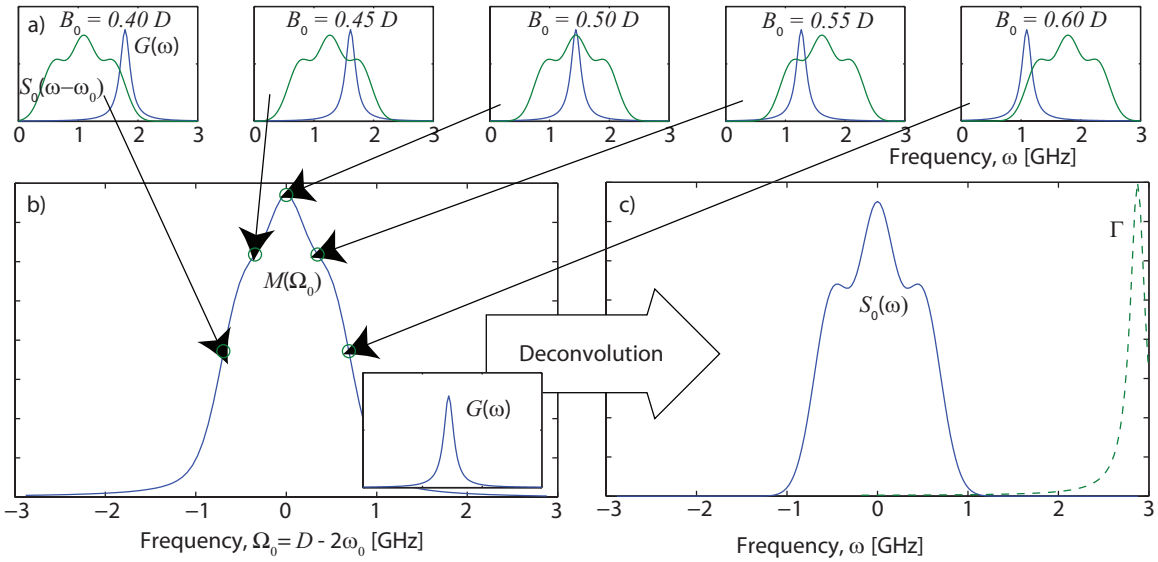

Figure 10.2: Sequence (a) By controlling the background field strength, B_0, the NV filter function, G may be tuned to filter specific regions of the spectral density, S. (b) The resulting measured signal, $M(\Omega_0)$, is the convolution of the NV filter function, G, and the spectral density of the environment, S. (c) Given that G is known, the spectral density, S, may be reconstructed by deconvolving S and G from M.

10.4 Experimental Investigation I: Nanoscale detection of stochastic spin fluctuations

In order to demonstrate the effect of a widefield ensemble array of NV centres coupling to an aqueous environment of electron spins, an experiment was conceived and performed at the University of Stuttgart[1] in which the concentration of the aqueous solution could be controlled with precision. Paramagnetic Gd^{3+}, in the form of the Gadobutrol complex, was chosen due to its seven unpaired electron giving rise to an overall spin of $S = \frac{7}{2}$. As was the case in chapter 5, the internal dynamics of the aqueous environment result in stochastic fluctuations of the effective magnetic field felt by the NV spin ensemble, however here we focus on the effect of the environment on the longitudinal component, and hence relaxation rate, of the NV spins. This effect is facilitated by the extremely fast dynamics occurring both within and between each Gadobutrol complex, yielding an extremely broad spectral distribution (10-100 GHz) capable of flipping the 2.88 GHz-split NV spins.

To detect the Gd environment, an array of NV centres was created using a $\sim 10^{13}\,\mathrm{cm}^{-2}$ 4 keV implant of ^{15}N atoms into an ultra-pure diamond substrate. The substrate was subsequently electron irradiated to produce a lateral NV density of $\sim 1000\,\mu\mathrm{m}^{-2}$ at a depth of 6.7 nm. A transparent microfluidic channel was engineered on top of the diamond substrate, allowing the NV layer to be addressed by the 532 nm laser through the sample (see figure 10.3 (a)). The effect of Gd fluctuations on the NV ensemble is then monitored using a CCD camera to detect changes in NV fluorescence.

[1] All experiments described in this section were performed by S. Steinert at the University of Stuttgart, and together with the theoretical analysis of this section, have been published in reference [SZH$^+$]

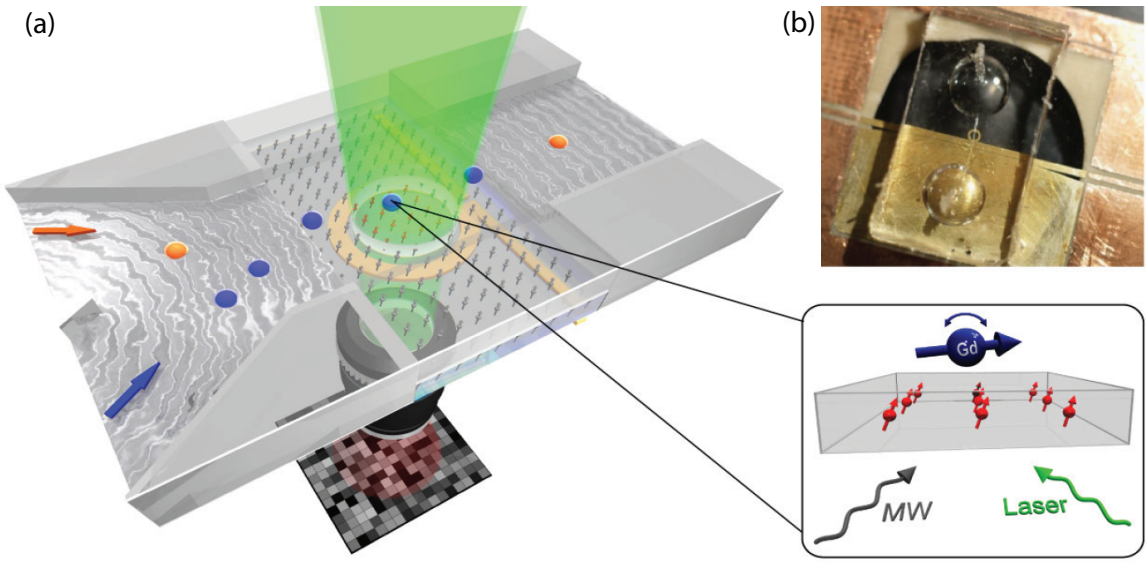

Figure 10.3: Schematic of widefield microfluidic detection setup, as taken from reference [SZH+]. (a) A 532 nm (green) laser is used to excite the ensemble of NV spins (red arrows) and the resulting fluorescence is readout using the CCD camera, yielding a spatially dependent image of the response of the NV spins to the dynamics of the sample. The strong magnetic dipole coupling between Gd^{3+} ions in the sample results in an appreciable fraction of them having the same 2.88 GHz Zeeman splitting as the NV spins, thus allowing them to exchange energy, and ultimately resulting in the relaxation of the NV spin ensemble. (b) Photograph of the experimental setup consisting of the PCB board, the lithographic microcoil, diamond substrate and microfluidic flow cell.

10.4.1 Determination of dynamic parameters

As we are measuring the *longitudinal* relaxation rate of the NV spin, we are interested in the spectrum of the effective field that couples to the $\mathcal{S}_x$ and $\mathcal{S}_y$ components of the NV spin.

Gd-NV interaction

The RMS strength (in Hz, not T) of the lateral components of the magnetic field operators is given by,

$$B \equiv \sqrt{\langle \mathcal{B}_x^2 \rangle + \langle \mathcal{B}_y^2 \rangle}, \tag{10.4.1}$$

where $\mathcal{B}_x$ and $\mathcal{B}_y$ are defined by the total dipolar coupling to the S_x and S_y components of the NV centre respectively.

$$\mathcal{B}_x^i = \frac{\mu_0}{4\pi}\frac{\gamma_{\rm nv} g_G \mu_B}{R^3}\left[\mathcal{S}_x^i - \frac{3}{R}\sin(\Theta)\cos(\Phi)\left(\mathbf{R}\cdot\vec{\mathcal{S}}_i\right)\right], \tag{10.4.2}$$

$$\mathcal{B}_y^i = \frac{\mu_0}{4\pi}\frac{\gamma_{\rm nv} g_G \mu_B}{R^3}\left[\mathcal{S}_y^i - \frac{3}{R}\sin(\Theta)\sin(\Phi)\left(\mathbf{R}\cdot\vec{\mathcal{S}}_i\right)\right], \tag{10.4.3}$$

where $\mathbf{R} = R\big(\sin\Theta\cos\Phi, \sin\Theta\sin\Phi, \cos\Theta\big)$ denotes the separation vector between a given NV-Gd pair, and $\mathcal{S}$ again denotes the spin vector of the Gd spin. Integrating x and y from $-\infty$ to ∞, and z from h to ∞, we have

$$\mathcal{B}_x^2 + \mathcal{B}_y^2 = \frac{n\pi}{8h^3}\left(\frac{\mu_0}{4\pi}\gamma_{\rm nv} g_G \mu_B\right)^2\left[\mathcal{S}_x^2 + \mathcal{S}_y^2 + 2\mathcal{S}_z^2\right], \tag{10.4.4}$$

and taking the trace over a purely mixed state, we find

$$\begin{aligned} B^2 &= \frac{21n\pi}{16h^3}\left(\frac{\mu_0}{4\pi}\gamma_{\rm nv} g_G \mu_B\right)^2 \\ &= 1.0\times 10^3\,\mathrm{MHz^2\,M^{-1}}\times[\mathrm{Gd}], \end{aligned} \tag{10.4.5}$$

where [Gd] is the concentration of Gd ions, measured in mol/L.

Gd-Gd dipolar Interaction

The analysis of spatial and rotational diffusion and Gd-Gd dipolar interactions is identical to that performed for Mn^{2+} spins in chapter 5 and is therefore not repeated here. The magnetic dipole-dipole mediated fluctuation rate, in terms of the concentration Gd concentration, [Gd], is given by

$$f_{\text{dip}} = 77\,\text{GHz}\,\text{M}^{-1} \times [\text{Gd}], \tag{10.4.6}$$

where the concentrations in the experiment varies from 0 to 1 M.

Gadobutrol molecular lattice effects

In addition to the concentration dependent dipole mediated relaxation caused by adjacent Gd spins, relaxation is also caused by dynamic processes taking place within the gadobutrol molecules. Specifically, this relaxation is caused by modulations of the zero-field splitting by damped quantum mechanical vibrations, resulting in the dissipation of the electron spin's energy into the lattice. For magnetic fields below 1 T, the electron spin relaxation rate has a constant value of $f_{\text{mol}} = 50\,\text{GHz}$ [KKW04].

Combined dynamics

Given the extremely high Gd fluctuation rates due to gadobutrol lattice effects and the dipolar coupling between Gd spins, we ignore the comparatively slow effects of spatial and rotational diffusion.The total autocorrelation function of the effective lateral field of the Gd is the product of the functions associated with dipolar and molecular lattice effects,

$$\langle \mathcal{B}(t)\mathcal{B}(t')\rangle = \left\langle \mathcal{B}^2 \right\rangle \exp\left[f_e(t-t')\right] \cos\left(\omega_0 t\right), \tag{10.4.7}$$

where ω_0 is the Larmor frequency of the Gd spins, and the total decay rate is given by the sum of the respective decay rates, $f_e = f_{\rm dip} + f_{\rm mol}$. The corresponding normalised spectral density is then given by

$$S(\omega) = \sqrt{\frac{2}{\pi}} \frac{f_{\rm dip} + f_{\rm mol}}{(\omega - \omega_0)^2 + (f_{\rm dip} + f_{\rm mol})^2}. \tag{10.4.8}$$

The width of this distribution is dependent of the concentration of Gd spins, $f_e = 50\,\text{GHz} + 77\,\text{GHz}\,\text{M}^{-1} \times [\text{Gd}]$.

10.4.2 Results and discussion

The ESR spectrum of Gadobutrol shows a single peak at 9.785 GHz at a field of 3500 G. The NV detection experiment was conducted at 200 G, from which we expect an ESR peak at $\omega_0 = 600\,\text{MHz}$. Rewriting the expressions for the decay rates of the $|0\rangle$ state of the NV centre into its $|\pm 1\rangle$ states in terms of Lorentzian distributions, we find that the NV spin essentially 'filters' regions of the Gd spectrum according to

$$\Gamma_1^+ = 2\pi B^2 \left(\frac{1}{\pi} \frac{\Gamma_2}{\delta_+^2 + \Gamma_2^2} \right), \tag{10.4.9}$$

$$\Gamma_1^- = 2\pi B^2 \left(\frac{1}{\pi} \frac{\Gamma_2}{\delta_-^2 + \Gamma_2^2} \right). \tag{10.4.10}$$

Given this value of ω_0, we have that $\omega_+ = 3.24\,\text{GHz}$ and $\omega_- = 2.28\,\text{GHz}$, ensuring that both the centroids and widths of these filter functions are much less than the width of the Gd spectral density. As such, the Lorentzian distributions describing Γ_1^+ and Γ_1^- are effectively delta functions,

$$\Gamma_1^+ \approx 2\pi B^2 \delta(\omega - \omega_+), \tag{10.4.11}$$

$$\Gamma_1^- \approx 2\pi B^2 \delta(\omega - \omega_-). \tag{10.4.12}$$

To find the ensemble averaged response of the NV centre, we must integrate the expression in equation 10.2.16 over the spectral density of the Gd environment, equation 10.4.8. We note that this integral has no analytic solution

$$\begin{aligned}\int S(\omega)e^{-\Gamma_1^+ t}\,d\omega &= 1+\int S(\omega)\sum_{k=1}^{\infty}(-1)^k\frac{\left(\Gamma_1^+ t\right)^k}{k!}\,d\omega \\ &= 1+\sum_{k=1}^{\infty}(-1)^k\frac{(2B^2t)^k}{k!}\int S(\omega)\left(\frac{1}{\pi}\frac{\Gamma_2}{\delta_+^2+\Gamma_2^2}\right)^k d\omega \\ &\approx 1+S(D+\omega_0)\sum_{k=1}^{\infty}(-1)^k\frac{(2B^2t)^k}{k!}\int\left(\frac{1}{\pi}\frac{\Gamma_2}{\delta_+^2+\Gamma_2^2}\right)^k d\omega.\end{aligned}$$

Retaining first order terms in the formal expansion above, we find

$$\begin{aligned}\left\langle\Gamma_1^+\right\rangle &\approx 2\pi B^2 S(D+\omega_0) \\ &\approx 2\frac{f_e B^2}{f_e^2+D^2}, \qquad (10.4.13)\\ \left\langle\Gamma_1^-\right\rangle &\approx 2\pi B^2 S(D-\omega_0) \\ &\approx 2\frac{f_e B^2}{f_e^2+D^2}. \qquad (10.4.14)\end{aligned}$$

Hence, the overall relaxation rate of the NV spin is given by

$$\begin{aligned}\frac{1}{T_1} = \left\langle\frac{d}{dt}P_0\Big|_{t=0}\right\rangle &= \frac{1}{6}\left[\left\langle\Gamma_1^+\right\rangle+\left\langle\Gamma_1^-\right\rangle+2\left(\left\langle\Gamma_1^+\right\rangle+\left\langle\Gamma_1^-\right\rangle\right)\right] \\ &\approx -2\left[\frac{f_e B^2}{f_e^2+D^2}\right]. \qquad (10.4.15)\end{aligned}$$

It is interesting to note that, given $f_e \gg D$, we may make the following approximation,

$$\begin{aligned}\frac{1}{T_1} &\approx 2\frac{B^2}{f_e} \\ &= 40\,\text{kHz}\times\frac{[\text{Gd}]}{1.0\,\text{M}+1.5\times[\text{Gd}]},\end{aligned}$$

which shows the NV spin relaxation rate to have a very similar form to the dephasing rates obtained for rapidly fluctuating fields, a similarity that was discussed briefly in

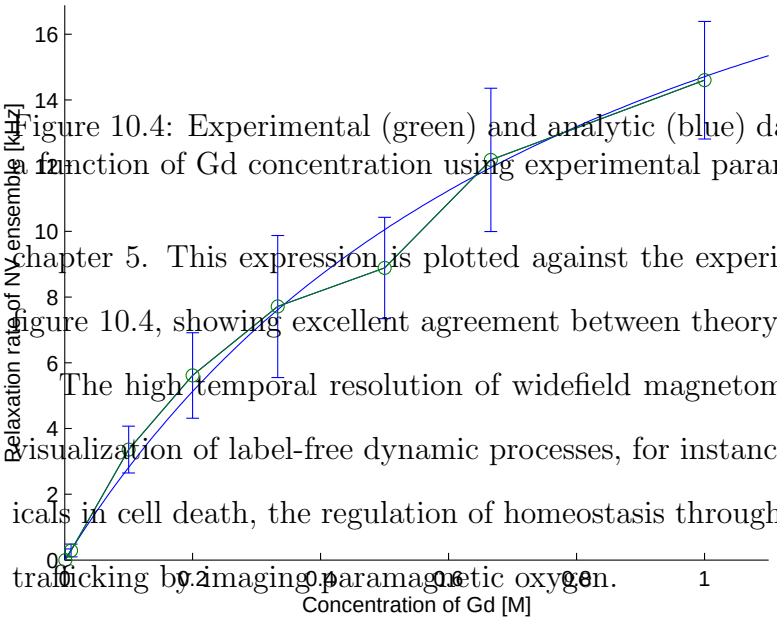

Figure 10.4: Experimental (green) and analytic (blue) data for the relaxation rate as a function of Gd concentration using experimental parameters only (ie, no fitting).

chapter 5. This expression is plotted against the experimentally obtained results in figure 10.4, showing excellent agreement between theory and experiment.

The high temporal resolution of widefield magnetometry also favors sub-cellular visualization of label-free dynamic processes, for instance the production of free radicals in cell death, the regulation of homeostasis through ion channels or hemoglobin trafficking by imaging paramagnetic oxygen.

10.5 Experimental Investigation II: Ultra-high resolution detection of spins in an artificial cell membrane

In the previous experimental investigation, a high density NV ensemble together with a widefield CCD camera arrangement was employed to obtain a better signal to noise ratio for measurement of the ensemble NV spin state. This improvement, however, comes at the cost of the highly local magnetic detection capabilities of a single NV, which in many situations is a desirable property to retain. In this example, we consider an arrangement of single gadolinium atoms in an artificial cell membrane whose detection and characterisation is facilitated by a distribution of individually addressable nanodiamonds containing single NV centres[2].

10.5.1 Determination of dynamic parameters

In analysing this system, we follow a similar methodology as that used in the manganese immersion (chapter 5) and Gd flow cell (section 10.4) experiments. Where this sytem differs however is that we are now detecting a two-dimensional distribution of target spins rather than a three-dimensional bulk system. This has a number of significant physical consequences, and leads to very different NV spin relaxation behaviour than observed previously.

[2]All experiments described in this section were performed by S. Kaufmann and D.A. Simpson at the University of Melbourne, and together with the theoretical analysis of this section, have been published in reference [KSH+13]

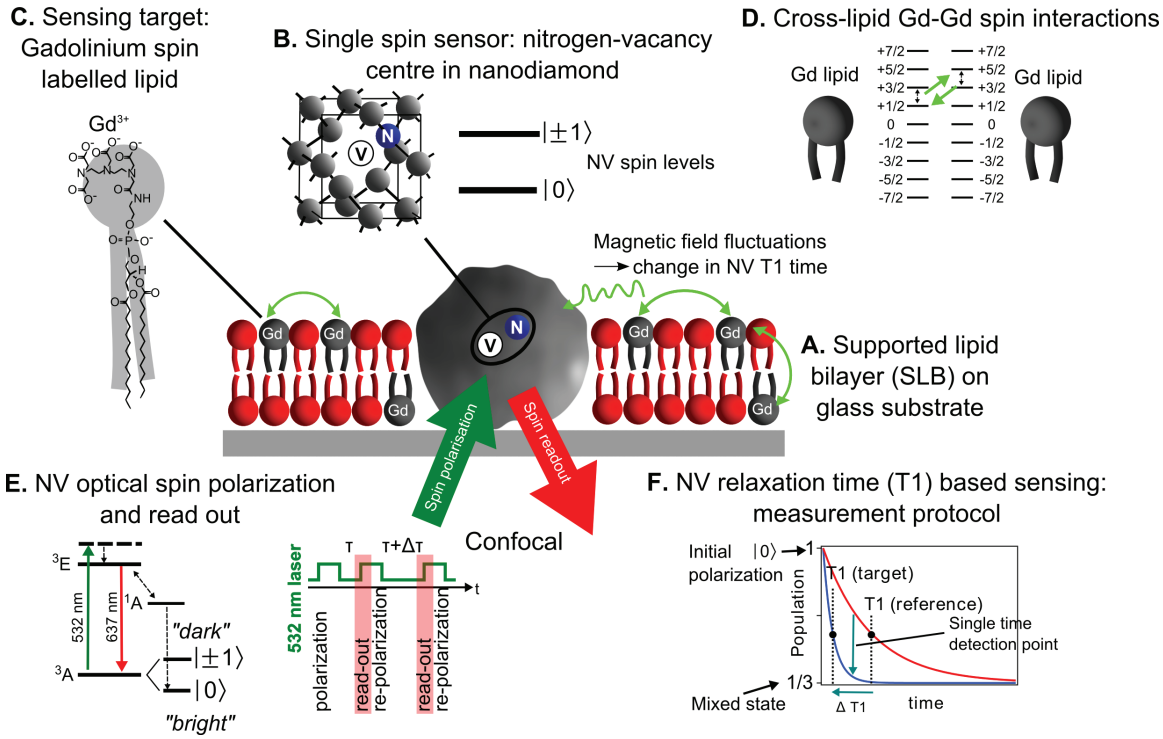

Figure 10.5: Schematic of nanoscopic detection of spin labels in an artificial cell membrane using a single-spin nanodiamond sensor, as taken from ref. [KSH+13]. (a) A supported lipid bilayer (SLB) is formed around a nanodiamond immobilized on a glass substrate. (b) The nanodiamond contains a single nitrogen-vacancy (NV) optical centre which acts as a single spin sensor by virtue of the magnetic levels in the ground state. (c) Gadolinium (Gd) spin labelled lipids are introduced into the SBL. (d) Magnetic field fluctuations arising from Gd spin labels affect the quantum state of the NV spin, measured through the NV relaxation time, T_1. (e) The electronic energy structure of the NV centre showing the fluorescent cycle and optical spin readout of the spin states $|0\rangle$ and $|+1\rangle$, and the protocol for the T_1 measurement. (f) A schematic illustration of the T_1 measurement. The relaxation of the NV spin in the target environment is compared to that in the reference environment. Measurement at a single time point in the evolution allows faster detection.

Gd-NV interaction

In the following we employ a similar analysis to that of the flow cell case, except here the Gd spins are confined to a 2-dimensional planar distribution. Integrating expression 10.4.3 over x and y from $-\infty$ to ∞, and z from h to ∞ over a planar spin density of σ, and taking the trace over a purely mixed state,

$$\begin{aligned} B^2 &\equiv \left\langle \mathcal{B}_x^2 \right\rangle + \left\langle \mathcal{B}_y^2 \right\rangle = \frac{63\pi\sigma}{8z^4} \left(\frac{\mu_0}{4\pi} \gamma_{\mathrm{nv}} g_G \mu_B \right)^2 \\ &= 3.1\,\mathrm{GHz}^2\,\mathrm{nm}^6 \times \frac{\sigma}{z^4}. \end{aligned} \tag{10.5.1}$$

Strictly speaking, the NV-Gd standoff, z, is not necessarily simply the depth of the NV centre below the nanodiamond surface, h, as the likelihood of finding Gd atoms close to the nanodiamond surface decreases with decreasing Gd concentration. As such, we take standoff to be the greater of the NV depth, and the radius of the circle in which we expect to find a single Gd atom given a lateral density of σ,

$$z \sim h + \frac{1}{\sqrt{\pi\sigma}}. \tag{10.5.2}$$

Note that we may relate the lateral density of Gd, σ, to the percentage of total lipid weight comprised by Gd, w, via $\sigma = 2.63 \times 10^{-2}\,\mathrm{nm}^{-2} \times w$. A plot of the RMS field strength, B, is shown in figure 10.6 (a). Given that we are in an experimental regime in which $1 \leq w \leq 10$, we take $z \sim h$.

To find the effective number of spins that interact with the NV, we note that the variance of the axial field is

$$\left\langle \mathcal{B}_z^2 \right\rangle = \frac{63\pi\sigma}{8h^4} \left(\frac{\mu_0}{4\pi} \gamma_{\mathrm{nv}} g_G \mu_B \right)^2, \tag{10.5.3}$$

and that due to a single spin a distance of h from the NV is

$$\left\langle \mathcal{B}_z^2 \right\rangle_i = \frac{21}{h^6} \left(\frac{\mu_0}{4\pi} \gamma_{\mathrm{nv}} g_G \mu_B \right)^2. \tag{10.5.4}$$

Hence, the effective number of spins detected by a single NV centre at a depth h below the nanocrystal surface is

$$\begin{aligned} N &= \left\langle \mathcal{B}_h^2 \right\rangle / \left\langle \mathcal{B}_z^2 \right\rangle_i \\ &= \frac{3\pi\sigma h^2}{8}. \end{aligned} \tag{10.5.5}$$

Gd dynamics

To determine the fluctuation rate of the effective Gd field, we proceed identically to the previous flow cell case. However, as we are detecting a two dimensional array of spins, we simply take $\theta = \pi/2$ in equation. 5.2.12, from which we find the autocorrelation function for the axial magnetisation

$$\left\langle M_z(t)M_z(0)\right\rangle = \frac{1}{2}\left[\cos\left(\frac{2}{3}S(S+1)\frac{bt}{r^3}\right) + \cos\left(2S(S+1)\frac{bt}{r^3}\right)\right], \tag{10.5.6}$$

where $b = \frac{\mu_0}{4\pi\hbar} g_G^2 \mu_B$. Given that we are now dealing with a two dimensional randomly distributed spin bath, the probability distribution for the separation distance between a given spin and its nearest neighbour, r, is now

$$\mathrm{P}(r) = 2\pi\sigma r \exp\left(-\pi\sigma r^2\right). \tag{10.5.7}$$

Integrating the autocorrelation function over this distribution yields

$$\begin{aligned} &\int_0^\infty 2\pi\sigma r \exp\left(-\pi\sigma r^2\right) \frac{1}{2}\left[\cos\left(\frac{2}{3}S(S+1)\frac{bt}{r^3}\right) + \cos\left(2S(S+1)\frac{bt}{r^3}\right)\right] dr \\ = \; &\frac{1}{4}\sqrt{\frac{3}{\pi}}\left[\mathfrak{G}_{0,5}^{4,0}\left(\frac{\tau}{432}\middle|\; 0, \tfrac{1}{3}, \tfrac{2}{3}, 1, \tfrac{1}{2}\;\right) + \mathfrak{G}_{0,5}^{4,0}\left(\frac{\tau}{48}\middle|\; 0, \tfrac{1}{3}, \tfrac{2}{3}, 1, \tfrac{1}{2}\;\right)\right], \end{aligned} \tag{10.5.8}$$

where $\mathfrak{G}$ is the Meijer-G function, and $\tau = S(S+1)\left(\pi\sigma\right)^{3/2} bt$, giving a correlation time of

$$T_c = 2\left[S(S+1)\left(\pi\sigma\right)^{3/2} b\right]^{-1}, \tag{10.5.9}$$

and a corresponding dipolar fluctuation rate of

$$\begin{aligned} f_{\text{dip}} &= \frac{1}{2} S(S+1)\,(\pi\sigma)^{3/2}\, b \\ &= 13.6\,\text{GHz}\,\text{nm}^3 \times \sigma^{3/2}. \end{aligned} \tag{10.5.10}$$

For %Wt concentrations of 1 %, 5 %, and 10 %, we have fluctuation frequencies of 58.0 MHz, 650 MHz and 1.83 GHz respectively.

As noted above, at very low Gd concentrations the lateral diffusion of lipid molecules may also play a role in causing the dipole field to fluctuate. During the experiment, the lateral diffusion rate was measured to be $D_l = 1\,\mu\text{m}^2\,\text{s}^{-1}$, giving a corresponding diffusion mediated fluctuation rate of

$$\begin{aligned} f_{\text{diff}} &= D_l \left(\frac{3}{4h}\right)^2 \\ &= 560 \times \text{MHz}\,\text{nm}^2 \times \frac{1}{h}. \end{aligned} \tag{10.5.11}$$

Gd III has a permanent magnetic dipole moment arising from the interaction between the seven unpaired electrons, giving a zero-field splitting of $D_{\text{Gd}} = 1.3$ GHz [BBC$^+$04]. In addition, low spin-orbit coupling suppresses intrinsic electronic spin relaxation due to, for example, collisions with water molecules. Overall, Gd III has significantly slower relaxation rates ($f_{\text{in}} \sim 1$ GHz) as compared with other lanthanides such as Yb III, which have relaxation times as short as 1-10 THz[BBL91].

The total autocorrelation function is the product of the functions associated with spin-spin interactions, self diffusion and intrinsic dynamics,

$$\left\langle B(t)B(t')\right\rangle = \left\langle B^2\right\rangle \exp\bigl(-f_e\,|t-t'|\bigr) \sum_k \cos\bigl(\omega_k\,(t-t')\bigr), \tag{10.5.12}$$

with a total fluctuation rate given by $f_e = f_{\text{diff}} + f_{\text{dip}} + f_{\text{in}}$. The effective Larmor precession frequencies, ω_k , are the transition frequencies between GD energy levels

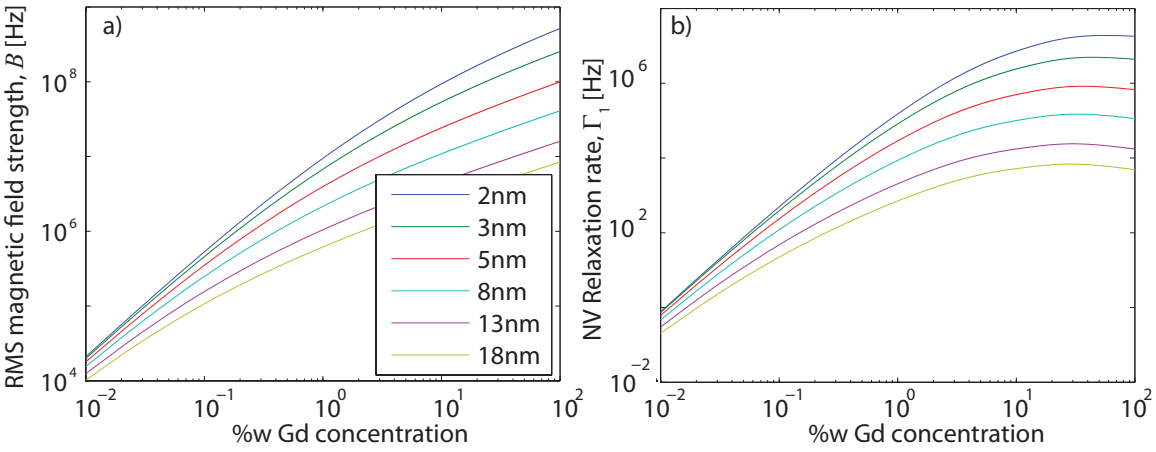

Figure 10.6: (a) Plot of the RMS strength of the effective GD magnetic field, B, vs % weight of Gd ions in the lipid membrane for different NV depths. At low concentrations, the average distance between two nearest neighbour Gd atoms is greater than the NV depth, hence the NV standoff is defined by the Gd density. At high concentrations, the standoff is simply determined by the NV depth below the nanodiamond surface. (b) Plot of the NV relaxation rate vs % weight of Gd ions in the lipid membrane for different NV depths.

as determined by the zero-field splitting, and thus may take values of $2D_{\mathrm{Gd}}$, $4D_{\mathrm{Gd}}$ and $6D_{\mathrm{Gd}}$. The corresponding normalised spectral density is then given by

$$S(\omega) = \sqrt{\frac{2}{\pi}} \sum_k \frac{f_{\mathrm{diff}} + f_{\mathrm{dip}} + f_{\mathrm{in}}}{(\omega - \omega_k)^2 + (f_{\mathrm{diff}} + f_{\mathrm{dip}} + f_{\mathrm{in}})^2}. \tag{10.5.13}$$

10.5.2 Results and Discussion

As there is no appreciable background magnetic field used in this experiment, we note that the $|\pm 1\rangle$ magnetic sublevels of the NV centre are degenerate, giving $\Gamma_+ = \Gamma_-$. Thus, using equation 10.2.18, the expressions for the $|0\rangle$ state population is

$$P_0 = \frac{1}{3}\left(1 + e^{-\Gamma_1^+ t} + e^{-2\Gamma_1^+ t}\right). \tag{10.5.14}$$

So the relaxation rate is given by

$$\begin{aligned} \langle \Gamma_1 \rangle &\approx \left\langle \left| \frac{dP_0}{dt} \right| \right\rangle \\ &= \langle \Gamma_1^+ \rangle. \end{aligned} \tag{10.5.15}$$

Since the effective width of Γ_+ is given by the inhomogeneous linewidth of the NV centre, $1/T_2^* \sim 10\,\text{MHz}$, which is significantly narrower than the width of $S(\omega) \sim 1$ to 10 GHz, Γ_+ behaves analogously to a delta function centred at 2.88 GHz. Rewriting the expressions for the decays rates of the $|0\rangle$ state of the NV centre into its $|\pm 1\rangle$ states in terms of Lorentzian distributions,

$$\Gamma_1^+ = 2\pi B^2 \left(\frac{1}{\pi} \frac{\Gamma_2}{\delta_+^2 + \Gamma_2^2} \right). \tag{10.5.16}$$

In the case where the centre experiences a field of 600 G, we have that $\omega_+ = 3.24\,\text{GHz}$ and $\omega_- = 2.28\,\text{GHz}$, ensuring that $\omega_+, \omega_-, \Gamma_2 \ll f_e$. As such, the Lorentzian distributions describing Γ_1^+ and Γ_1^- are effectively delta functions,

$$\Gamma_1^+ \approx 2\pi B^2 \delta(\omega - D). \tag{10.5.17}$$

Thus for the ensemble average we obtain

$$\langle \Gamma_1^+ \rangle \approx \int S(\omega) \Gamma_1^+ \, d\omega \approx 2\pi B^2 S(D) \tag{10.5.18}$$

$$= 2\pi B^2 \sqrt{\frac{2}{\pi}} \sum_k \frac{f_{\text{diff}} + f_{\text{dip}} + f_{\text{in}}}{(\omega - \omega_k)^2 + (f_{\text{diff}} + f_{\text{dip}} + f_{\text{in}})^2} \tag{10.5.19}$$

$$\approx 2\sqrt{2}\pi \frac{f_e B^2}{f_e^2 + (D - D_{\text{Gd}})^2}, \tag{10.5.20}$$

where the last line follows from the the fact that the other two Gd transition frequencies ($4D_{\text{Gd}}$ and $6D_{\text{Gd}}$) are too far detuned from D to have a significant effect on relaxation rate of the NV spin.

Using the definitions of B and fe in equations 10.5.1 and 10.5.13, we plot the NV decay rates in figure 10.6 as a function of the Gd concentration in the membrane. These curves are compared with experimental data obtained from 9 separate NV centres (NV1-NV9). As we do not know the NV depth, h, in each nanodiamond we plot a lower bound corresponding to the photostability limit of 2 nm[BGN$^+$10] and an upper bound from the AFM distribution of 18 nm. The data points all fall within the NV depth bounds, indicating that the observed relaxation rates are in agreement with those predicted by equation 10.5.20. The trend to shallower NV depths as we move from 10% to 1% Gd-lipid concentration is consistent with an etching step in the processing of the sample between the 10% and 1% measurements, resulting in the removal of several nanometres of material from the nanodiamond surfaces.

The effective number of spins detected, N, for a given Gd concentration, σ, is found from equation 10.5.5. Using the NV depth range in Figure 4 ($h \approx 8 \pm 5$ nm) we arrive at a lower bound estimate of the effective number of spins detected of $N = 4 \pm 2$ (at a Gd concentration of 1%), and $N = 28 \pm 24$ (at a Gd concentration of 10%).

10.6 Conclusions

In this chapter, we have discussed the advantages and limitations of performing decoherence microscopy using the relaxation rate of an NV spin, as compared with the dephasing methods discussed in previous chapters. Relaxation based sensing has been shown to be more sensitive to high frequency phenomena, and is therefore well suited to characterising electron spin systems. Furthermore, the comparatively long intrinsic T_1 times of NV centres (as compared with T_2) make this approach inherently more sensitive than methods based on measuring dephasing rates; and with the ability to

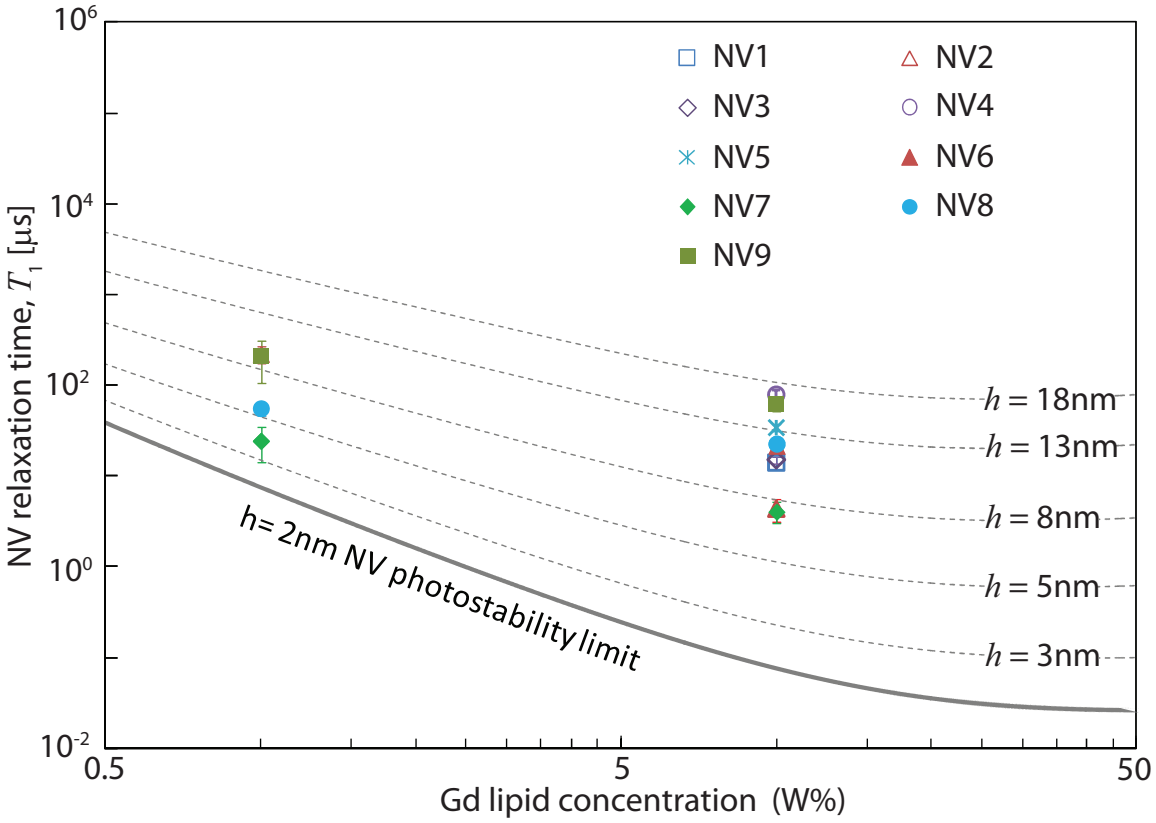

Figure 10.7: NV relaxation time due to the presence of Gd spin labeled lipids, T_1, as a function of Gd lipid concentration (%w/w) for all measured centres, NV1-NV9. Theoretical curves based on Gd-Gd spin interactions are given for a range of NV depths, h, corresponding to the photostability lower limit of $h = 2\,\text{nm}$ and an upper bound of h=18 nm determined from the measured AFM distribution.

tune the NV spin relaxation rates to different environmental frequencies, we have the additional advantage of being able to reconstruct arbitrary environmental spectra.

The practicality of relaxation based decoherence microscopy was demonstrated using two experiments. In the first, we measured and analysed the relaxation effects of an electron-spin rich aqueous solution on a widefield ensemble array of NV centres. The concentration dependence of the resulting relaxation rate was shown to be accurately explained by the theory developed in this chapter. The high temporal resolution of this widefield configuration is well suited to the sub-cellular visualization of label-free dynamic processes, such as the production of free radicals during cell death, the regulation of homeostasis through ion channels, and hemoglobin trafficking.

In the second experiment, we considered an arrangement of single gadolinium atoms in an artificial cell membrane, whose detection and characterisation is facilitated by a distribution of individually addressable nanodiamonds containing single NV centres. The comparatively high spatial resolution of this method, combined with the ability to control and measure NV centres at ambient temperatures, allowed us to detect and characterise the dynamics of individual clusters of 2-6 Gd spins in this biological environment. We have demonstrated excellent agreement between experimental results and the corresponding theoretical description developed here, highlighting the potential of the NV-nanodiamond system as a nanoscopic magnetic probe in biological systems.

Chapter 11

Decoherence and orientation tracking of nanodiamonds in living cells

To this point, all of the NV based sensing protocols we have considered have held the NV axis fixed with respect to some external axis, usually defined by a static background field or the orientation of the environment being measured. However, in some cases *in-situ* monitoring of the NV spin state may not allow us to maintain simultaneous control over the crystal orientation due to the lack of any mechanical contact. This is further complicated by the fact that the decoherence properties of the NV spin under pulsed-microwave control sequences depend on the relative orientations of the NV axis and the external magnetic field.

In this chapter, we discuss how the unique optical and spin properties of an NV centre in a diamond nanocrystal allow these potential problems to be resolved. In addition to obtaining information about the local magnetic environment, these properties allow for the determination of both the position and orientation of the crystal, yielding information about the mechanical forces and motion it may be subject to. These techniques are applied in analysing a set of experiments in which diamond

nanocrystals are taken up endosomally by human cervical cancer (HeLa) cells[1].

11.1 Introduction

As has been the focus of our discussion is the preceding chapters, the ability to optically monitor the quantum state of an NV probe has an enormous potential to monitor biological environments exhibiting electromagnetic properties (in particular, see chapters 8 and 9). In addition to their magnetic sensing capabilities, NV centres in nanocrystals have been employed as fluorescent bio markers in cellular systems as, despite a comparitively low fluorescence rate, nanodiamonds are completely non-cytoxic [YKC$^+$05, NZJ$^+$07, FLC$^+$07] and are perfectly photostable, exhibiting no blinking or photobleaching in nanocrystals as small as 5 nm in diameter [BGN$^+$10].

Despite the ability of the NV to act as a magnetometer *or* a fluorescent bio-marker, no previous *in-situ* measurements of the NV quantum spin state have been demonstrated before the work reported here [MYS$^+$11]. This simultaneous monitoring of both classical position and the quantum spin state is an important next step in order to facilitate simultaneous characterisation of nanomechanical intracellular forces and the dynamics of the intracellular electromagnetic environment. In order to achieve this, we must address how to non invasively perform a quantum measurement on an NV centre in a living cell, and conceive a measurement protocol that allows the NV to characterise relevant intra cellular processes, whilst remaining sufficiently robust during both rotational and translational motion of the nanocrystal.

In this chapter we discuss, with reference to experimental data, how these goals

[1]All experiments described in this chapter were performed by L.P. McGuinness, D.A. Simpson and Y. Yan at the University of Melbourne, and together with the theoretical analysis of this chapter, have been published in reference [MYS$^+$11].

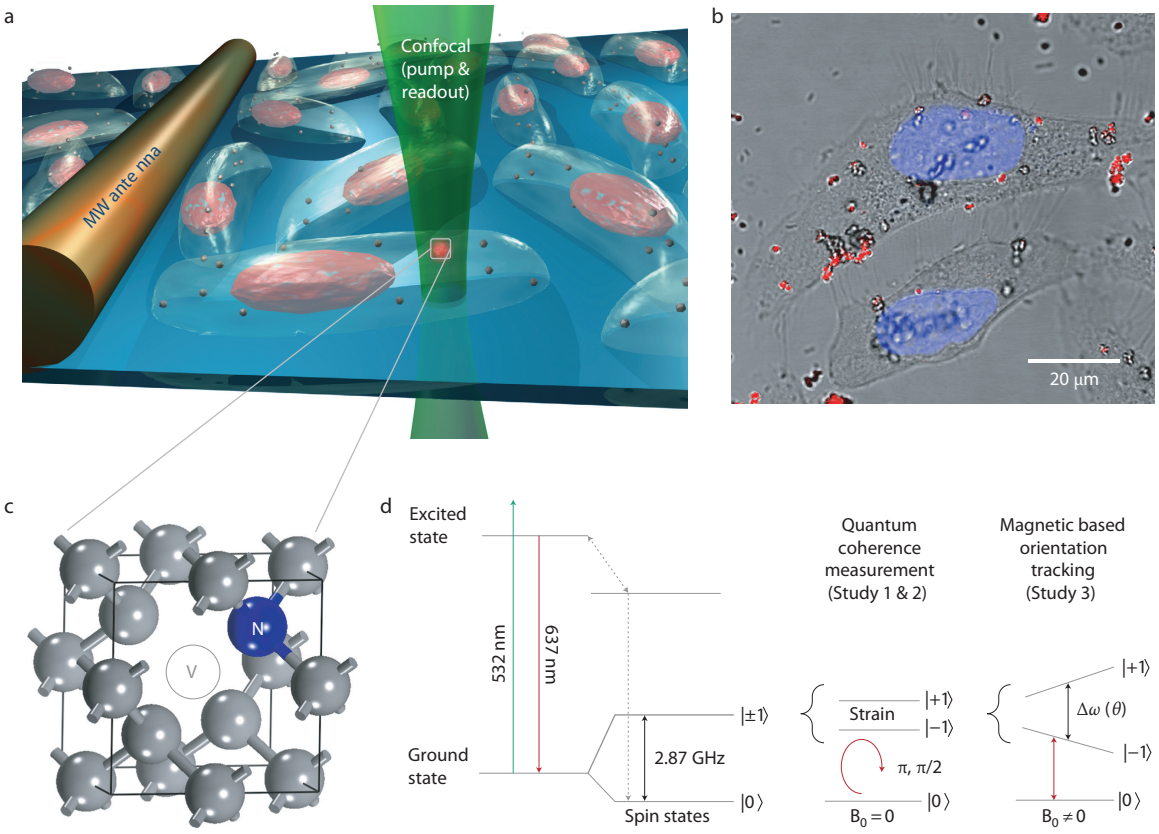

Figure 11.1: Quantum measurement of single spins in living cells, as taken from [MYS+11]. a) Experimental setup, including microwave control of the NV spin levels and confocal fluorescence readout. b) Overlay of bright-field and confocal fluorescence images of HeLa cells, showing uptake of nanodiamonds. NV fluorescence is shown in red and the nucleus is stained with Hoechst 33342 (blue). Images were obtained on a Leica TCS SP2 confocal microscope. c) Atomic lattice structure of the NV centre. d) Quantum measurement and control of the NV centre. Left: energy levels of the NV probe system and fluorescence dynamics. Middle: quantum control for study 1 (π and $\pi/2$ pulses for spin-echo). Right: orientation-dependent Zeeman splitting, $\Delta\omega(\theta)$, in an applied magnetic field B_0, measured in Study 2.

may be achieved using an investigation comprised of two separate studies. Firstly, we perform an analysis of the first intracellular coherence measurement of a single quantum system, in which both Rabi and spin-echo signals are monitored, providing a foundation for further nanobiomagnetometry studies. We then detail protocols for the robust and precise orientation tracking of nanodiamonds within living cells based on continuous ODMR monitoring. The experimental setup is comprised of a confocal microscope with a proximate wire used for control of the NV spin state (figure 11.1 (a)). A typical wide-field image of the uptake and internalisation of 45nm nanodiamonds in HeLa cells is shown in figure 11.1 (b).

11.2 Study 1: Demonstrating the quantum coherence of NV centres in living cells

In this section, we show how the decoherence imaging techniques discussed in previous chapters may be applied to the case of *in-situ* monitoring of mobile nanodiamonds in order to obtain information regarding the intracellular environment. By tuning the MW frequency to the $|0\rangle \leftrightarrow |+1\rangle$ transition, we coherently drove Rabi transitions between the quantum states of each NV system (figures 11.2 (a) & (b)), which were subsequently used to determine the duration of π and $\pi/2$ pulses for spin-echo measurements of the coherence time, T_2. The decoherence effects arise due to interactions of the NV spin with internal crystal spins, unpaired spins on the nanodiamond surface and magnetic fluctuations in the local intracellular environment. The initial spin echo envelopes of NV-1a and NV-1b are plotted in figure 11.2 (c), and subsequent measurements after a 13 hour period indicated that changes in the intra-cellular environment

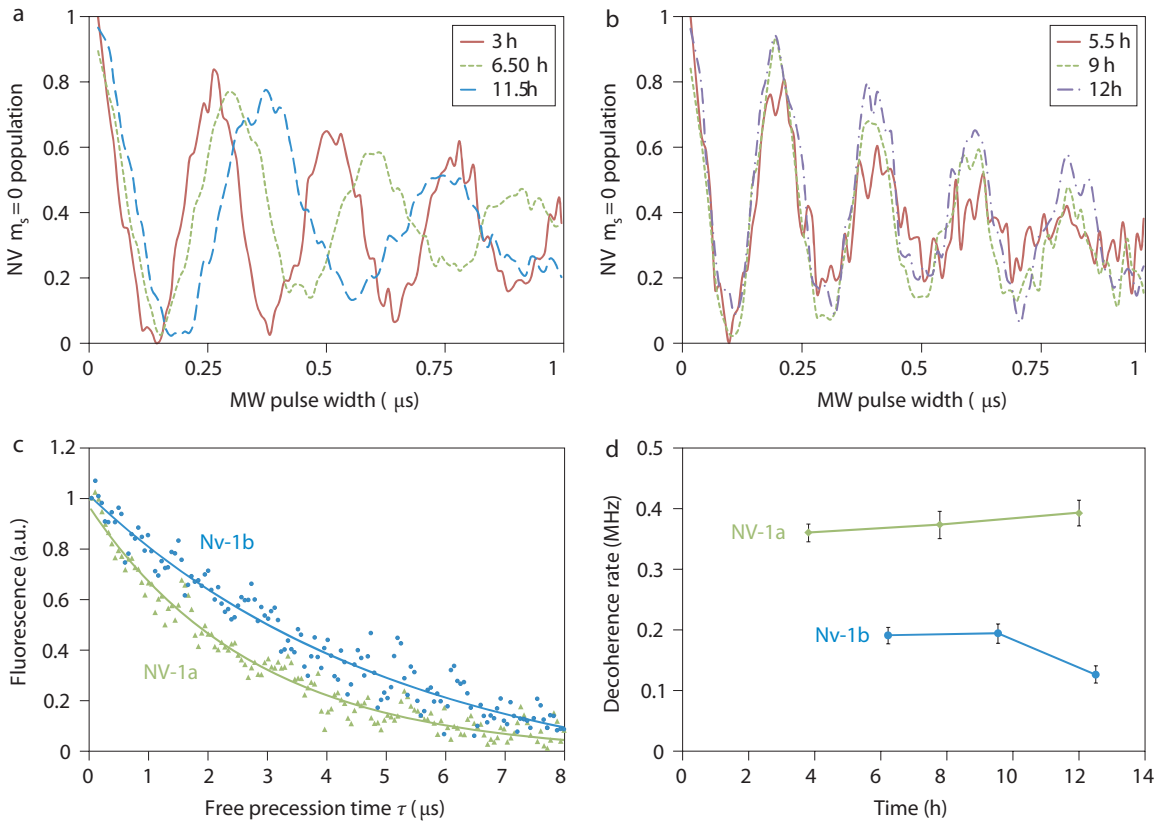

Figure 11.2: Quantum coherence properties of the probes NV-1a and NV-1b in HeLa-1, as taken from [MYS+11]. a) & b) Rabi oscillations of NV-1a and NV-1b measured at various times during the lifetime of the cell. c) Initial spin-echo measurements on both NV centres (statistical errors are at the 1% level). d) Time evolution of the decoherence rates extracted from the spin-echo profiles for both NV centres. The uncertainties in the extracted values, are determined from the fit to the data.

had resulted in a reduced decoherence rate for NV-1b (figure 11.2 (d)). This was observed simultaneously with increased cellular auto-fluorescence and a degradation in the integrity of the cell nucleus. These results are consistent with the production of unpaired electron species such as superoxide radicals at the nanocrystal surface, as would be generated during apoptosis[CJ98].

In chapter 3 we discussed the dependence of the Rabi frequency on the microwave power. In this experiment, the Rabi frequency was observed to differ not only between the two NV probes, but to also change over time, despite the delivered microwave power being held constant. This implies a change in the orientation of the nanocrystal, leading to a change in the projection of the microwave field along the axis perpendicular to that of the NV. In the case where the detuning is small compared to the microwave field strength, $\omega_x \gg \delta$, the Rabi frequency is given by

$$\Omega = \Omega_0 \sin(\theta), \tag{11.2.1}$$

where Ω_0 is the Rabi frequency for the case where the NV axis is perfectly aligned with the background field and θ is the angle between the background field and the NV axis.

From this, we note that the higher Rabi frequency of NV-1b is the result of better alignment of its NV axis with the background field than that of NV-1a. Whilst neither NV exhibits sufficient rotational motion to determine the extrema of the Rabi frequency, we may determine an upper bound for the extent of this motion by taking the maximum frequency of NV-1b to be the frequency at $\theta = 0$. The alignment of both NV-1a and NV-1b is plotted in figure 11.3 (b), showing that the two nanocrystals experienced very different nanoscale environments, with NV-1a rotating up to 20^o between time points, and NV-1b less than 10^o.

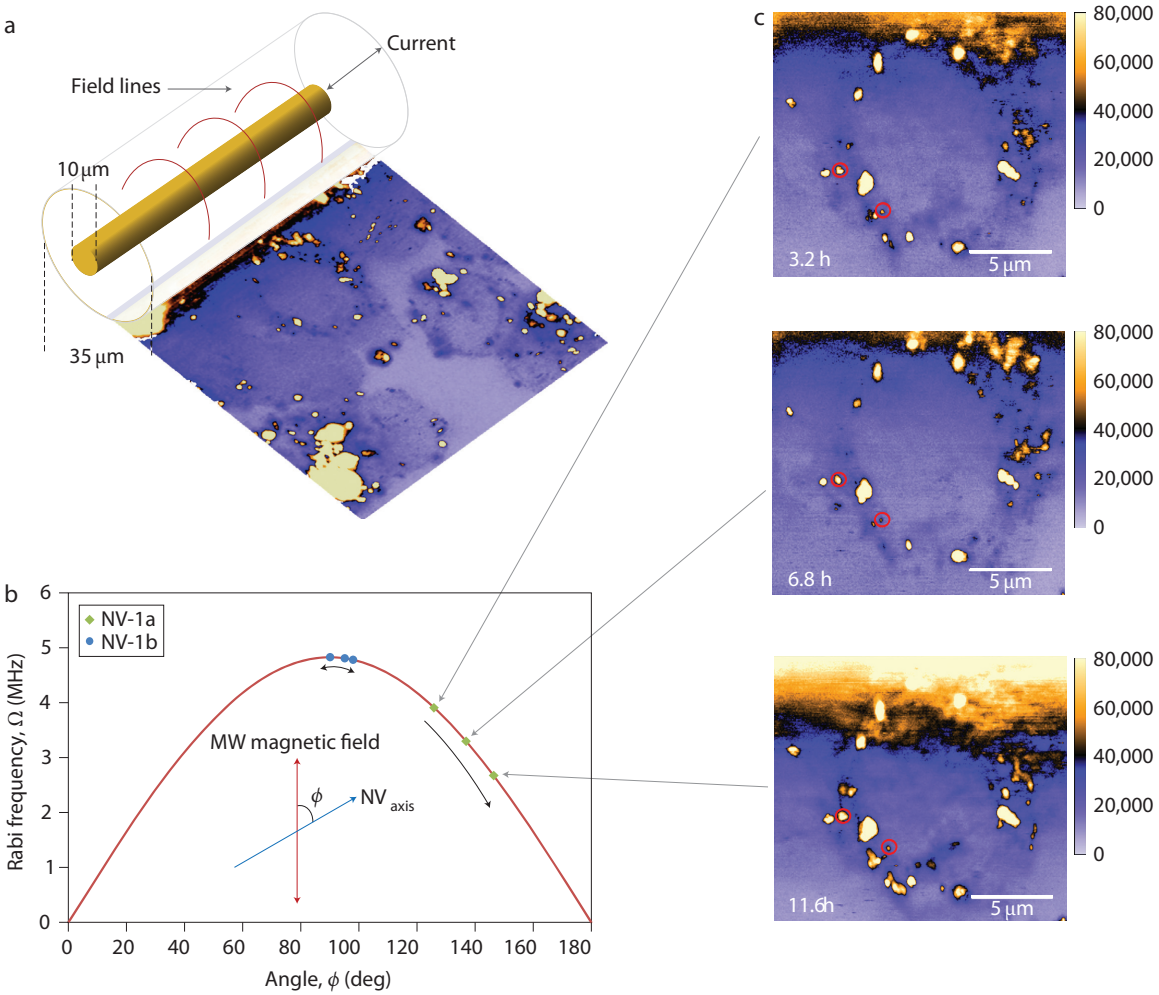

Figure 11.3: NV axis rotation owing to motion of the nanodiamonds in HeLa-1, as taken from [MYS+11]. a) With constant microwave power, the Rabi frequency is governed by the orientation of the NV axis with respect to the microwave driving field. b) Upper bounds on the change in orientation of the nanodiamonds based on a maximum initial perpendicular alignment of the higher Rabi frequency centre (NV-1b) with the microwave field. c) Confocal scan sequence showing the corresponding morphological changes in the cell during the same timeframe.

Although a changing Rabi period provides information on the orientation of internalized nanodiamonds, the long timescale (hours) of this measurement limits its use for particle tracking. In the following section, we demonstrate that continuous ODMR monitoring in the presence of an external magnetic field allows the rotational motion of an internalized nanodiamond to be measured over millisecond acquisition timescales.

11.3 Study 2: Orientation tracking of nanodiamonds in living cells

Whilst much of the focus of NV magnetometry has been in measuring electromagnetic properties of various environments, situations exist in which we may be interested in dynamic mechanical processes taking place in systems where electromagnetic couplings are negligible. Not only does the fluorescence of the NV make it well suited to optical position tracking, the ODMR spectrum facilitates simultaneous tracking of the NV's orientation. In this second study, we show how monitoring of the ODMR spectrum can provide an arbitrarily precise measurement of the rotational dynamics of the nanodiamond. In a spin-echo experiment, the linewidth is known to change dramatically with the orientation of the background field relative to the NV axis. This is not an issue here, as the linewidth due to the laser field is generally an order of magnitude larger than the static linewidth ($1/T_2^*$), and 2 orders of magnitude larger than the spin echo linewidth ($1/T_2$).

11.3.1 Determination of orientation angle using full ODMR spectrum

For a given external field, B_0, the maximal ODMR splittings occur at $\omega = D \pm \gamma B_0$ (figure 11.6 (a)). For an arbitrary orientation angle between the NV quantisation axis and the background field, θ, the frequency separation between the two peaks will be $\Delta\omega = 2B_0 \cos(\theta)$. The orientation of the quantisation axis with respect to the background field may then be determined via

$$\theta = \arccos\left(\frac{\Delta\omega}{2B_0}\right). \tag{11.3.1}$$

In what follows, we outline a protocol to determine this orientation from the continuous monitoring of ODMR spectra.

11.3.2 Optimised tracking, orientations sensitivity and temporal resolution

Because the $S_z = \pm 1$ splittings are symmetric about D, it is sufficient to consider only the region given by $D < \omega < D + \gamma B_0$. The peak position at any given instant will then be given by $\omega_1 = D + \gamma B_0 \cos(\theta_1)$, with the spectrum described by

$$S_1 = \frac{\Gamma^2}{(\omega - \omega_1)^2 + \Gamma^2}, \tag{11.3.2}$$

and described at some later time by

$$S_2 = \frac{\Gamma^2}{(\omega - \omega_2)^2 + \Gamma^2}. \tag{11.3.3}$$

Thus we are concerned with the number of measurements, N, required to find $\Delta\omega = \omega_2 - \omega_1$. It is clear that a limiting factor in the sensitivity of $\Delta\omega$ is the linewidth, Γ,

since if $\Gamma > \Delta\omega$, ΔS will be small. It would seem that this can be avoided by simply choosing a larger B_0, however, as the maximum sampling interval is of order Γ (see below), having a larger B_0 will require more sampling to locate ω_2.

In order to determine the orientation angle of the nanocrystal, (assuming S_1 has been characterised beforehand, or that Γ is at least known) we consider the following algorithm:

1. Beginning at ω_1, sweep outwards at alternating positive and negative intervals of Γ, ie at $\omega = \pm\Gamma,\ \pm 2\Gamma,$, etc.

2. Identify the half-maximum value of the *measured* spectrum, ω_n and sample either side of this point at $\omega_{\max} \pm \Gamma/2$.

3. Identify new half-maximum and sample either side of this point at $\omega_{\max} \pm 2^{-n}\Gamma$.

4. Repeat 3 until the desired level of accuracy is reached.

The number of measurements required by step 1 is bounded by

$$N_0 \quad = \quad \frac{\gamma B_0}{\Gamma}, \tag{11.3.4}$$

The maximal uncertainty in $\Delta\omega$ is given by $\delta\omega = 2^{-n}\Gamma$, where n is the level of iteration. To determine ω_{n+1}, we require

$$\frac{1}{2} - S_2(\omega_n) \quad > \quad \frac{1}{\sqrt{N}}, \tag{11.3.5}$$

Note that we have omitted the contrast parameter, C, employed in previous chapters, since the contrast will be intrinsically treated by via appropriate normalization of the ODMR spectrum, S, and definition of an effective photon count rate, R (see below).

The number of measurements required at the n^{th} level of iteration is bounded by

$$\begin{aligned} N_n &= \left[1 - 2\frac{\Gamma^2}{(\omega_n - \omega_2)^2 + \Gamma^2}\right]^{-2}, \\ &= 4\left[1 - \frac{2}{(1 + 2^{-n})^2 + 1}\right]^{-2} \\ &\sim 2^{2n+2} \end{aligned} \tag{11.3.6}$$

and the total number of measurements required is then

$$\begin{aligned} N = \sum_{n=0}^{n_{\max}} N_n &= \frac{\gamma B_0}{\Gamma} + 4\sum_{n=0}^{n_{\max}} 2^{2n} \\ &\sim \frac{\gamma B_0}{\Gamma} + 4\int_1^{n_{\max}} 2^{2x}\, dx \\ &\sim \frac{\gamma B_0}{\Gamma} + \frac{2^{2n_{\max}}}{\ln(2)}. \end{aligned} \tag{11.3.7}$$

The level of accuracy desired, $\delta\omega$, serves to define the number of measurements required at a given level of iteration, $n_{\max}$ That is, $n_{\max} = \log_2(\Gamma/\delta\omega)$, hence

$$\begin{aligned} N &= \frac{\gamma B_0}{\Gamma} + \frac{1}{\ln(2)}\left(2^{\log_2(\Gamma/\delta\omega)^2}\right) \\ &= \frac{\gamma B_0}{\Gamma} + \frac{1}{\ln(2)}\left(\frac{\Gamma}{\delta\omega}\right)^2. \end{aligned} \tag{11.3.8}$$

Recall that

$$\begin{aligned} \delta\omega &= B_0\big[\cos(\theta_2) - \cos(\theta)\big] \\ &= B_0 2\sin\left(\frac{\theta + \theta_2}{2}\right)\sin\left(\frac{\delta\theta}{2}\right) \\ &\sim B_0 \sin(\theta_2)\,\delta\theta, \end{aligned} \tag{11.3.9}$$

where the last approximation follows from the fact that the largest contribution to N comes as the tracking error approaches 0. Substituting this result back into equation 11.3.8

$$N \sim \frac{B_0}{\Gamma} + \left(\frac{\Gamma}{B_0}\right)^2 \frac{1}{\delta\theta^2}. \tag{11.3.10}$$

The minimum resolvable orientation angle is then

$$\delta\theta \sim \frac{\Gamma}{CB_0}\frac{1}{\sqrt{N}}. \tag{11.3.11}$$

Note that as $\theta \to 0, \pi$, we have $N \to \infty$, as a greater number of measurements are required in order to overcome the reduced peak splitting of the ODMR signal, thereby reducing the sensitivity of the system. This appears problematic, however the solid angle phase space density in polar coordinates is zero at both poles and maximal at the equator, hence we would never expect the NV centre to be perfectly aligned or anti-aligned with the external field.

We remark briefly here that this is a very conservative figure, and tracking times will be significantly reduced when the location of the peak to be measured is already know approximately, for example, if the nanocrystal has not moved appreciably since the last tracking experiment.

Noise analysis and temporal resolution

In order to obtain the temporal resolution from the sensitivity we must relate the number of measurements, N, to an effective measurement acquisition rate, R. To do this, we look at an experimentally obtained sample ODMR spectrum and analyse the dependence of the signal-to-noise ratio on the number of microwave sweeps across the spectrum.

Recall from chapter 3 that, at typical laser powers, the ODMR line width is dictated by optical processes and therefore exhibits a Lorentzian shape. ODMR data is shown in figure 11.4 for increasing numbers of sweeps, thus we fit each data set to

$$S_i = \frac{A_i}{(\omega - \omega_2)^2 + \Gamma^2} + B_i, \tag{11.3.12}$$

where ω_2 and Γ are determined from the curve obtained from 32 sweeps over the frequency range.

Since S_i represents the mean of the data, the normalised spread, or standard deviation, is obtained from

$$\Delta S_i = \frac{1}{A_i}\sqrt{\frac{1}{N}\sum_j (D_{ij} - S_{ij})^2}, \tag{11.3.13}$$

where D_{ij} is the j^{th} data point in the i^{th} data set comprising 2^{i-1} sweeps. The dependence of this spread on the number of microwave sweeps is shown in figure. 11.5(a), from which we find the variance in the data to be inversely proportional to the number of microwave sweeps, validating the assumption of shot-noise statistics.

Despite this validation, we do not accurately know the parameters associated with collection efficiencies and radiation geometries, hence we must determine an effective count rate from the collected data. Given that a 1000 point sweep takes 7 s, a single point acquisition takes 7 ms. Using equation 11.3.13, we find that after 32 sweeps, the normalised standard deviation is 0.0717. Since the assumption of shot noise statistics holds (again, see figure 11.5(a)), we know

$$\Delta S = \frac{1}{\sqrt{Rt}}, \tag{11.3.14}$$

where R is the effective acquisition rate, hence

$$\begin{aligned} R &= \frac{1}{0.0717^2 \times 32 \times 7 \times 10^{-3}\,\text{s}} \\ &= 868\,\text{Hz}. \end{aligned} \tag{11.3.15}$$

The temporal resolution is therefore given by

$$\begin{aligned} \delta t &= \frac{N}{R} \\ &= \frac{1}{R}\left[\frac{B_0}{\Gamma} + \left(\frac{\Gamma}{B_0}\right)^2 \frac{1}{\delta\theta^2}\right]. \end{aligned} \tag{11.3.16}$$

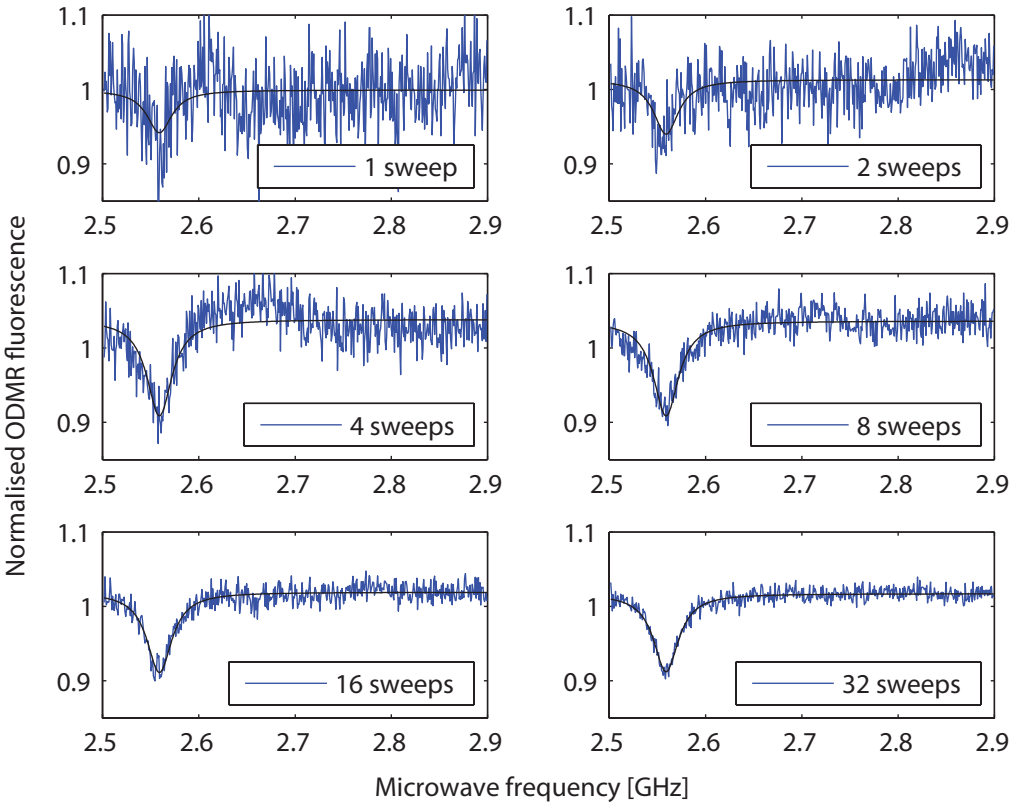

Figure 11.4: Fits to experimentally obtained ODMR data showing an increased signal to noise ratio with an increased number of sweeps.

For the operating conditions employed in this experiment, $B_0 = 350\,\mathrm{MHz}$ and $\Gamma = 16\,\mathrm{MHz}$ (see figure. 11.6(a)), we have

$$\delta t \approx 25\,\mathrm{ms} + \left(\frac{0.05}{\delta\theta}\right)^2 \mathrm{ms}. \tag{11.3.17}$$

For example, knowing the orientation angle to within one degree ($1^o \approx 0.017^c$) would take 8 ms, provided the initial 25 ms sweep across the entire spectrum was not required.

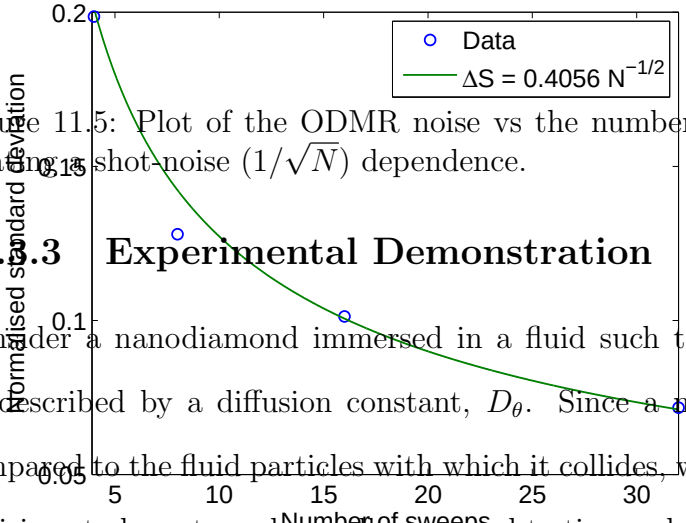

Figure 11.5: Plot of the ODMR noise vs the number of microwave sweeps demonstrating a shot-noise ($1/\sqrt{N}$) dependence.

11.3.3 Experimental Demonstration

Consider a nanodiamond immersed in a fluid such that its rotational motion may be described by a diffusion constant, D_θ. Since a nanodiamond is typically large compared to the fluid particles with which it collides, we expect the timestep between collisions to be extremely small compared to timescales associated with its rotational motion. Hence, on macroscopically relevant timescales, we expect the angle through which the nanodiamond has rotated during time Δt to be normally distributed with mean zero and variance $D_\theta t$.

To experimentally demonstrate this protocol, a uniform magnetic field of 3.6mT was used to produce an orientation-dependent Zeeman shift of the magnetic sublevels of the NV centre. The diamond nanocrystal was placed inside a living HeLa cell, and its ODMR spectrum was measured at 30 second intervals over a 16 hour period.

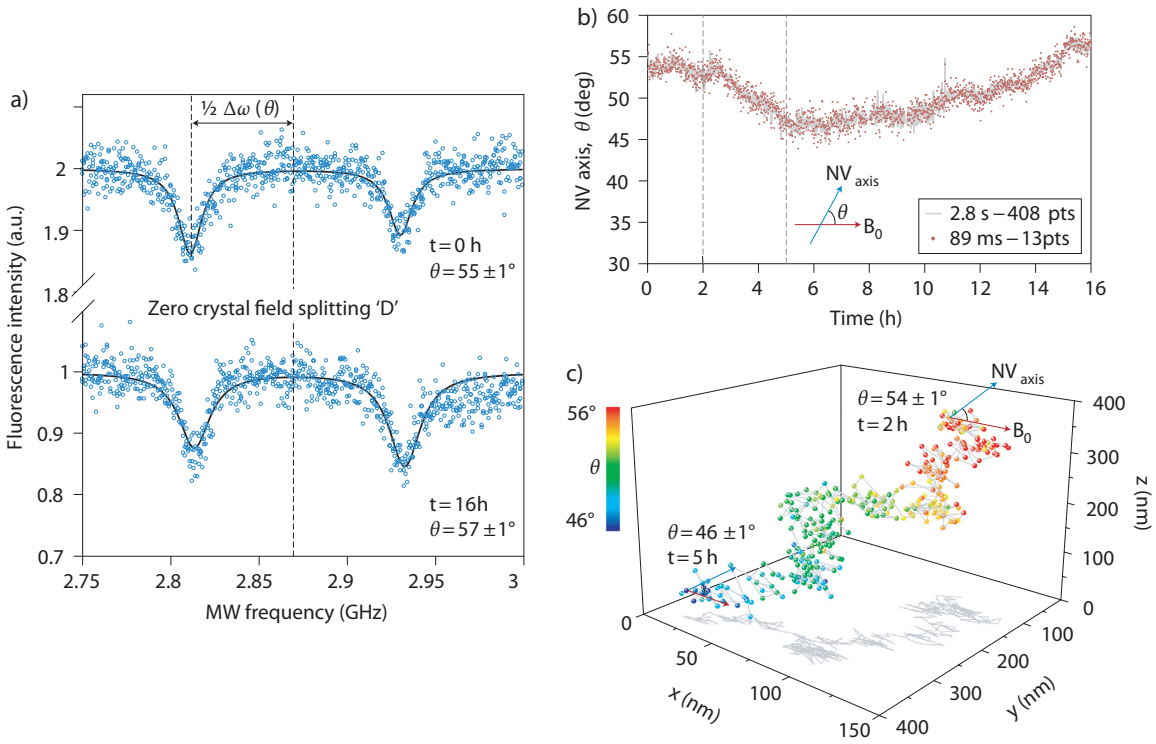

Figure 11.6: Orientation tracking of a single nanodiamond, as taken from [MYS+11]. a) Changes in the orientation of the NV quantisation axis (and hence the nanodiamond) to the external field are manifest in the ODMR spectrum and are measured at various times over the cell lifetime. b) Measured change in orientation of the nanodiamond as a function of time, taken at 30 seconds intervals. c) Four dimensional tracking of a single intracellular nanodiamond over a 3 hour period.

Figure 11.6 (a) shows representative spectra taken over the life of the cell demonstrating that the timescale for rotational monitoring is effectively only limited by the cell lifetime.

The translation and rotational motion of the nanocrystal over a 3 hour time period is plotted in figures 11.6 (b) & (c). The restricted motion exhibited by the nanocrystal is suggestive of immobilisation within a membrane-enclosed vesicle following endocytosis, as consistent with previous studies on internalization of similar

sized nanodiamonds in HeLa cells [NZJ+07].

11.4 Conclusion

Through the results and analysis performed here, we confirm that it is indeed possible to perform non-invasive quantum measurement on nanodiamonds moving within a living cell. We have shown that sophisticated NV spin-based magnetometry protocols discussed in earlier chapters may be applied to living systems, despite the diamond nanocrystals having no mechanical contact with the measurement apparatus. Furthermore, we have shown that, despite this lack of mechanical contact, the unique optical and spin properties of the NV centre permit the orientation tracking of the nanocrystal with millisecond temporal resolution. The combination of these imaging modes is expected to facilitate the simultaneous measurement of both the electromagnetic and micro/nano-mechanical properties of the surrounding environment, with sufficient temporal resolution to monitor events occurring on biologically relevant timescales.

Chapter 12

The central spin problem

Due to interest in both solid state based quantum computing architectures and the application of quantum mechanical systems to nanomagnetometry, there has been considerable recent attention focused on understanding the microscopic dynamics of solid state spin baths and their effects on the coherence of a controllable, coupled central electronic spin. Many analytic approaches are based on simplified phenomenological models in which it is difficult to capture much of the complex physics associated with this system. Conversely, numerical approaches reproduce this complex behaviour, but are limited in the amount of theoretical insight they can provide. Using a systematic approach based on the spatial statistics of the spin bath constituents, we develop a purely analytic theory for the NV central spin decoherence problem that reproduces the experimental and numerical results found in the literature, whilst correcting the limitations and inaccuracies associated with existing analytical approaches.

12.1 Introduction

As outlined in chapter 2, the central spin problem refers to a special class of open quantum systems, in which a central spin interacts with a large number of strongly

coupled spins in the environment (figure 12.1(a)). In the context of metrology, with particular regard to parameter estimation, the NV centre has emerged as a unique physical platform for nanoscale magnetometry, as has been the focus of chapters 2-11 of this work. In each case, the associated sensitivity is ultimately limited by the coherence properties of the NV spin that arise from the strong coupling to the surrounding bath of electron and/or nuclear spins. In all of these applications and platforms, a comprehensive understanding of the central spin problem is therefore necessary to make accurate predictions of the quantum properties and behaviour of the central spin arising from the material properties of the surrounding environment.

The first modern approach to this problem, in the context of phosphorus donors in silicon, involved treating the combined effect of the spin bath environment on the central spin as a semi-classical magnetic whose dynamic properties were intended to mimic the magnetic dipole flip-flop processes taking place amongst the environmental spins[dSD03a, dSD03b]. Despite not accounting for the effect of the central spin on the surrounding environment, this approach still finds considerable application today, particularly in the NV community[TCC$^+$08, HDF$^+$08, MTL08, DFHA09, LWR$^+$10, LRDH11, WdLR$^+$12]. In order to account for the full interaction between the central spin and its environment, quantum cluster expansion[WdSD05, WD06, SYS07], nuclear pair-wise[YS06, YLS07, LYS07], correlated cluster expansion[YL08, YL09], and disjoint cluster expansion[MTL08] models have been developed, in which the environment is systematically clustered into groups of strongly interacting spins, with each order of the cluster hierarchy corresponding to successively weaker, and hence less important, interactions. In addition, master equation approaches in which all hyperfine coupling constants are assumed to be identical have been developed [BCS11],

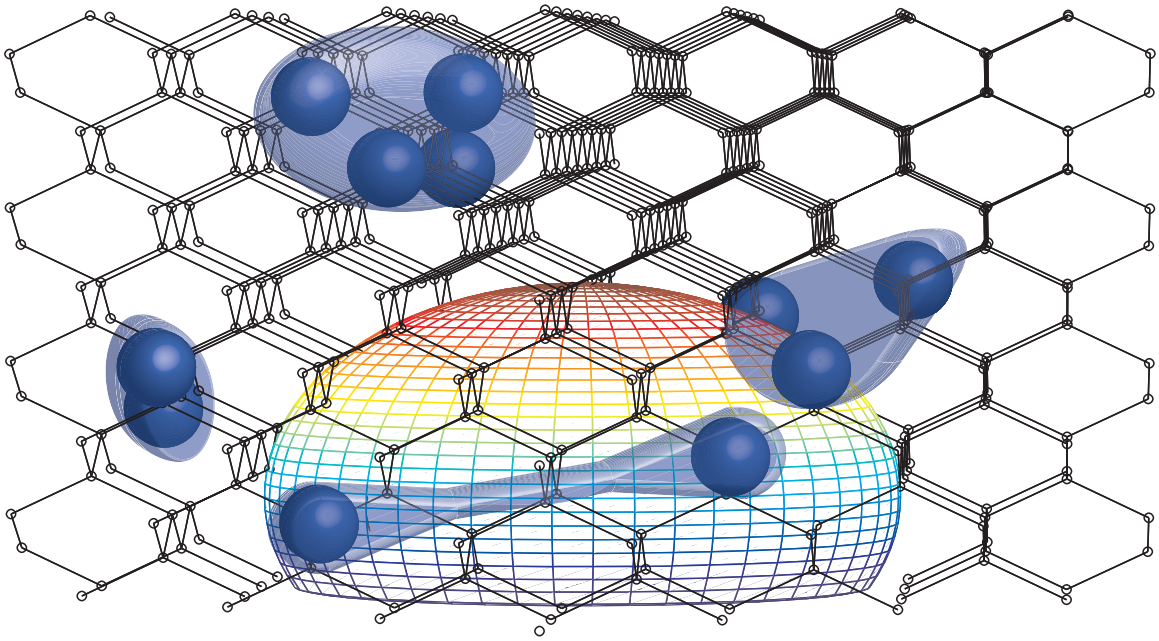

Figure 12.1: Schematic of the central spin problem showing a central spin coupled to clusters of randomly distributed environmental spins. The large central sphere represents the region concentric on the central spin inside which we expect to find, on average, less than one environmental spin.

with subsequent developments accounting for non-uniform couplings [BCS12].

Traditionally, the theoretical analysis of the central spin problem has been based on phenomenological assumptions regarding the self-interaction dynamics of the surrounding spin bath, namely by replacing the bath with a classical Ornstein-Uhlenbeck noise source [AW53, KA62]. This noise gives rise to fluctuations in the Larmor frequency of the central spin and leads to an eventual dephasing between its initially coherent basis states, a process referred to as spectral diffusion. Such approaches involve making an ad-hoc assumption of a decaying exponential form for the autocorrelation function of the effective magnetic dipole field, with the decay rate being deduced from the effective environmental flip-flop rates [dSD03a, dSD03b]. Despite the extensive application this theory has found throughout the literature [TCC+08,

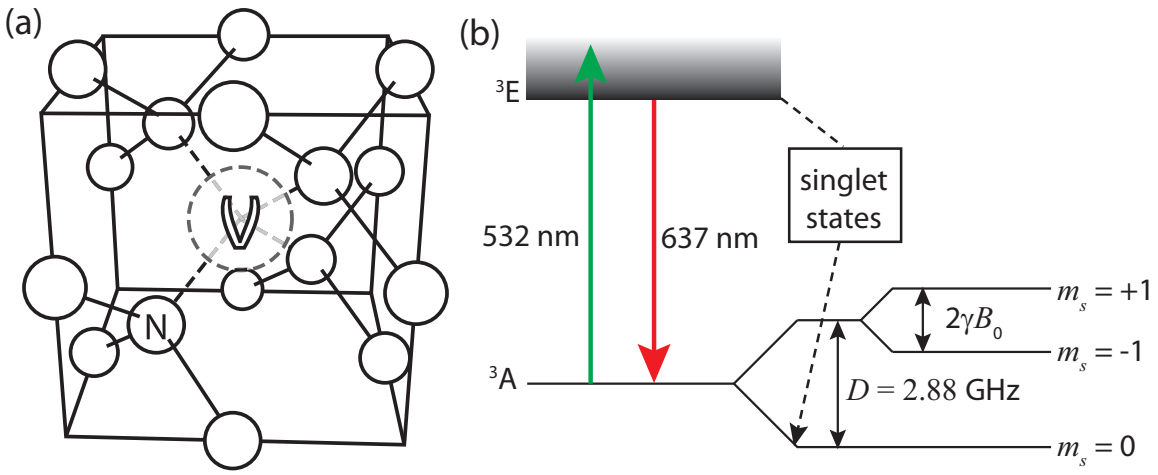

Figure 12.2: (a) The Nitrogen Vacancy (NV) centre point defect in a diamond lattice, comprised of a substitutional atomic nitrogen impurity (N) and an adjacent crystallographic vacancy (V). (b) The NV ground state spin sublevels are separated by $D = 2.87$ GHz. Upon optical excitation at 532 nm, the population of the $|0\rangle$ state may be readout by monitoring the intensity of the emitted red light.

MTL08, DFHA09, LWR$^+$10, LRDH11, WdLR$^+$12], three major problems persist: 1. There is no theroetical/experimental/numerical reason to suggest the phenomenological assumption of an exponential form for the autocorrelation function should be made; 2. Upon assuming a particular form for the autocorrelation function, the task of determining the correlation time (assuming the decay can, in fact, be described by a single time constant) still remains; and, 3. Inherent in this is the assumption that the central spin has no influence on the evolution of the environment constituents.

With regard to the first problem, the assumption of an exponential correlation function leads to a cubic exponential decay in the coherence of the central spin under a spin-echo pulse sequence for times shorter than the autocorrelation time (see reference [dS09] for a review). However, there have been a significant number of theoretical results in the literature suggesting that this decay may in fact show a

quartic exponential dependence[WdSD05, YS06, WD06, dS09, ZHL12]. Such behaviour can only arise from a Gaussian shaped autocorrelation function (or at least quadratic on relevant timescales), casting some doubt on the assumed exponential form. In addition, the numerical work in reference [WdSD05] shows that numerical computation of the combined effect of many randomly distributed clusters leads to an approximately Gaussian decay of coherence, the likes of which have been observed experimentally[BNT$^+$09]. These problems are addressed and clarified in this work, as our results show that the spatial distribution of spins around the central spin has a significant effect on the analytic form of the autocorrelation function. This is critical to the development of spin-based quantum technologies, as there have been many quantitative predictions of better performance with the use of pulse-based microwave control schemes [TCC$^+$08, LWD08, HHCH10], and the exact analytic form of the spectral cutoff was shown to directly affect the performance of such schemes [CLNS08, Uhr08].

Also outstanding is the determination of the environmental autocorrelation time. One of the earliest modern attempts at deriving this timescale from microscopic physical processes was given in reference [dSD03b], in which each magnetic dipole coupled nuclear spin pair (consisting of spins m and n) was treated as a bistable fluctuator, where the number of transitions between states in a given time interval t is treated as a Poissonian variable with parameter t/T_{mn}. The effective flip-flop rate of the pair, $1/T_{mn}$ could then be calculated using their mutual dipolar coupling strength via perturbation theory, resulting in a linear exponential decay of the autocorrelation function. However, this still requires certain phenomenological assumptions to be made about the associated density of states, and does not address the microscopic reasons behind how the T_{mn} quantities are distributed. Adopting this approach in the context

of quantum sensing applications would mean that, for a given T_2 measurement, one would be lead to infer that the associated correlation time of the environment is three orders of magnitude longer than its true value. As an example, using the treatment of the nuclear spin bath in reference [TCC+08], typical coherence times of $T_2^* = 1\,\mu$s and $T_2 = 300\,\mu$s would imply a correlation time of $T_c = T_2^3 / \left[6\,(T_2^*)^2\right] = 4.5\,$s. This is in stark contrast to what would be expected from an examination of the average nuclear-nuclear coupling strength of $1/nb \sim 40\,$ms, based on an average impurity density $n \approx 2\,\text{nm}^{-3}$, and indeed the correlation times of $T_c \approx 10\,$ms calculated in this work. In fact, as we will show here, a magnetisation conserving two spin flip-flop model must have an autocorrelation function with zero derivative at $t = 0$, and hence cannot produce the linear behaviour exhibited by a pure exponential decay.

In contrast to the ad-hoc fitting of data to phenomenological models which do not account for the influence of the central spin on its surrounding environment, fully quantum mechanical approaches to the problem have been developed over the last 5 years using cluster expansion [WdSD05, WD06, SYS07] and correlated cluster expansion [YL08, YL09] methods. Here the randomly distributed spins are aggregated into small, strongly interacting groups, with the latter showing better convergence in cases where the decoherence time of the central spin is comparable to, or longer than, the autocorrelation time of the environment, as is the case with a bath of electron spins. In the opposite regime, as would the case for an electron spin coupled to a nuclear spin bath, these two approaches agree, and to lowest non-trivial order they are in accordance with earlier nuclear pair-correlation approaches [YS06, YLS07, LYS07]. In this limit, at least for short times, all of these approaches are shown to be consistent with a quartic-exponential decay, the likes of which may also be deduced using a

generalised semi-classical argument [HCHH09].

In cases of relatively strong hyperfine interactions resulting from low magnetic field regimes, direct dipole-dipole couplings are either treated as a perturbation [CWS09b, SYS07], or ignored completely [CWS09a, CDS10, BCS11, BCS12]. Here, the dominant interaction between environmental constituents is due to hyperfine-mediated flip-flops, resulting from environmental spins becoming increasingly coupled to the lateral components of the central spin as the magnetic field strength decreases. Such effects are negligible in the case of NV centres in diamond, owing to its 2.88 GHz zero-field splitting. This approach is well suited to cases where the central spin always has a non-zero projection along its quantisation axis ($m_s = \pm\frac{1}{2}, \pm\frac{3}{2}, \ldots$), as is the case of the spin-$\frac{1}{2}$ Si:P and Ga:As systems, thus causing many of the bath spins to be off-resonance and hence unable to flip with each other, but is not valid in integer spin systems where the $m_s = 0$ state is appreciably populated, as is predominantly the case with the NV centre. Under these conditions, environmental spins are free to evolve exclusively under their mutual couplings, and information encoded onto them by the central is free to propagate throughout the environment. As such, these theories do not account for the irreversible leakage of quantum information from the central spin to distant environmental components. This approach is a reasonable approximation for times much shorter than the autocorrelation time of the environment, but not on timescales over which environmental interactions are appreciable. In the effective Hamiltonian models above [CWS09b, CDS10] or master equation approaches [BCS11] all hyperfine coupling constants are assumed to be identical, meaning the effects of the hyperfine distribution on the decoherence behaviour have not been addressed.

Non-uniform hyperfine couplings were treated in reference [BCS12], however the assumption of non-interacting nuclei renders this approach unsuitable for NV centres.

Finally, we remark that any short time expansion is only valid for times shorter than the reciprocal of the strongest dipolar coupling frequencies in the system, and of particular concern is that any two spins can be found arbitrarily close together (or effectively so on the length scales of the system), making an expansion in low orders of these couplings diverge. In this limit, it is the dipolar interaction between environmental spins that sets their quantisation axis, not the Zeeman interaction, invalidating the assumption of each cluster's magnetisation being conserved with respect to the global z axis. This is another instance where consideration of the spatial distribution of spin impurities becomes important, and despite being able to describe the decoherence in the compact forms given by the works described above, no discussion has been made regarding the statistical distributions of the spin-spin coupling strengths. Instead, one is forced to resort to Monte-Carlo based numerics at this point. The possible outcomes for various realisations of spatial distributions of spin impurities for the case of an NV centre coupled to a nuclear spin bath have been numerically investigated in refs. [MTL08, ZHL12, WCCD12], and that for electron donors and quantum dots in silicon in reference [WCCD12]. An extensive numerical study of the magnetic dependence of the coherence time of an NV centre on the strength of the applied background magnetic field was conducted in reference [ZHL12], taking both realistic hyperfine distributions and environmental spin-spin interactions into account. A fully analytic, quantum mechanical description of the effects of the entire range of magnetic field strengths on a central spin coupled to a completely randomly distributed spin bath is presented in this work. In what follows, we focus primarily

on the case of an NV centre interacting with its native 1.1% ^{13}C nuclear spin bath.

12.2 Theoretical background

The Hamiltonian describing this system is given by

$$\mathcal{H} = \mathcal{H}_{\rm S} + \mathcal{H}_{\rm SE} + \mathcal{H}_{\rm EZ} + \mathcal{H}_{\rm EE}, \tag{12.2.1}$$

where $\mathcal{H}_{\rm S}$ is the self-Hamiltonian of the central electron spin, which may include the coupling of the NV spin to its proximate nitrogen nuclear spin, as well as zero field and Zeeman splittings. The hyperfine interaction between the central spin (S) and the environment (E) is described by $\mathcal{H}_{\rm SE}$, which in the present context is a point-dipole interaction, but may also include Fermi-contact interactions in other systems. This is described by

$$\mathcal{H}_{\rm SE} \;=\; \sum_i \frac{a}{R_i^3}\left[\vec{\mathcal{S}}\cdot\vec{\mathcal{E}}_i - 3\frac{\left(\vec{\mathcal{S}}\cdot\mathbf{R}_i\right)\left(\mathbf{R}_i\cdot\vec{\mathcal{E}}_i\right)}{R_i^2}\right], \tag{12.2.2}$$

where $\vec{\mathcal{S}}$ and $\vec{\mathcal{E}}_i$ are the spin-vector operators for the NV spin and the $i^{\rm th}$ environmental spin, $\mathbf{R}_i$ is their mutual separation, and $a = \frac{\mu_0}{4\pi\hbar}\mu_{\rm S}\mu_{\rm E}$. The magnetic moments of the NV and environmental spins are denoted $\mu_{\rm S}$ and $\mu_{\rm E}$ respectively. The large zero-field splitting is some three orders of magnitude greater than any other coupling in this system, allowing us to ignore any coupling to the lateral components ($\mathcal{S}_x$ and $\mathcal{S}_y$) of the NV spin.

The Zeeman (Z) interaction of the environmental spins is described by $\mathcal{H}_{\rm EZ} = \sum_i \vec{\mathcal{E}}_i\cdot\vec{\omega}_i$, where $\vec{\omega}_i = \gamma_{\rm E}\mathbf{B}_0$ describes the Zeeman field felt by spin i, having gyromagnetic ratio $\gamma_{\rm E} = \mu_{\rm E}/\hbar$, due to a background field $\mathbf{B}_0$.

The nuclear spin-spin interactions (E) are described by

$$\mathcal{H}_{\mathrm{EE}} = \sum_{j<i} \frac{b}{r_{ij}^3} \left[\vec{\mathcal{E}}_i \cdot \vec{\mathcal{E}}_j - 3 \frac{\left(\vec{\mathcal{E}}_i \cdot \mathbf{r}_{ij}\right)\left(\mathbf{r}_{ij} \cdot \vec{\mathcal{E}}_j\right)}{r_{ij}^2} \right], \tag{12.2.3}$$

where $\mathbf{r}_{ij}$ is the mutual separation of spins i and j, and $b = \frac{\mu_0}{4\pi\hbar}\mu_{\mathrm{E}}^2$.

In the case of large Zeeman couplings, some transitions between environmental spin states due to the hyperfine and dipolar interactions will be disallowed due to energy conservation, ensuring that the total axial magnetisation of the spins involved in the interaction is conserved. However, at low fields, the energy cost for these transitions may be easily paid for by these interactions, meaning that axial magnetisation need not be conserved. In what follows, we refer to (non)axial magnetisation conserving transitions as being '(non)secular'.

For a given spin, $\mathcal{E}_i$, we may classify its parameter regime in terms of the relative strengths of the energy scales considered above: spin-environment coupling (S), environment self coupling (E), and Zeeman splitting (Z), as determined by the Hamiltonian components, $\mathcal{H}_{\mathrm{SE}}$, $\mathcal{H}_{\mathrm{ZE}}$, and $\mathcal{H}_{\mathrm{EE}}$ respectively. This gives rise to six distinct parameter regimes, as summarised below, and depicted schematically in figure 12.3, and parametrically in figures 12.5 and 12.6 for various examples of physical systems.

For the sake of brevity, we label these six regions according to the relative strengths of the environmental couplings. For example, a label of ZSE (read Z>S>E) would imply that both S-E and E-E couplings are secular (a consequence of their quantisation axis being set by the Zeeman field), and that the spins couple more strongly to the NV than to each other. Conversely, a label of ESZ would imply that both S-E and E-E couplings are non secular, and that the spins couple more strongly to each other than to the NV (see figure 12.4). The geometric boundaries on these regimes

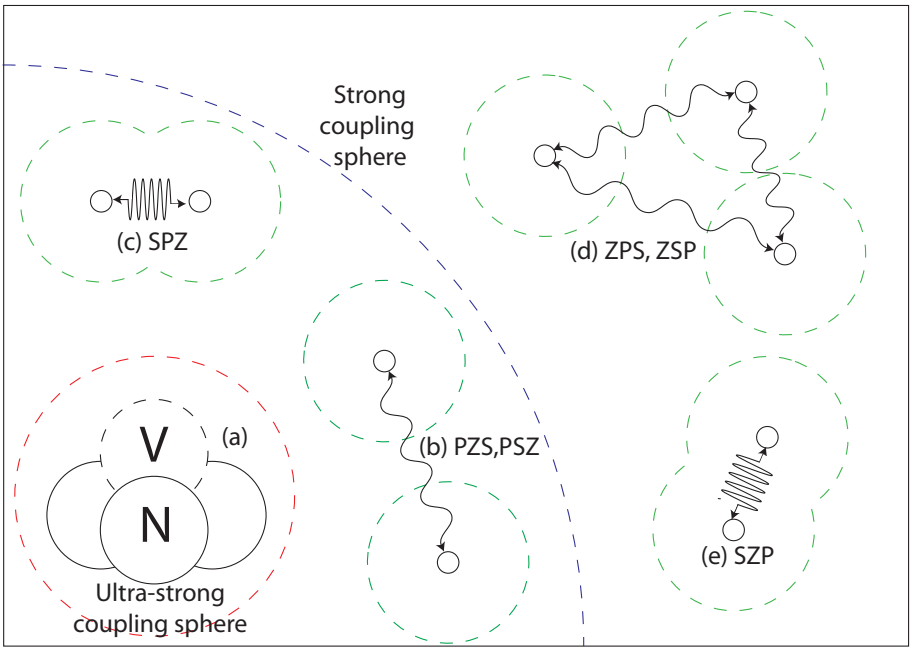

Figure 12.3: Schematic showing the parameter regimes relevant to the central spin problem. (a) Ultra strong coupling region, in which the interaction between the NV centre and an adjacent spin is stronger than its 2.88 GHz zero field splitting. This region is not considered in this work. (b) and (c) Strong coupling region, in which the coupling of the spins to the NV centre is stronger than their coupling to a background field. In (b), the spins are weekly coupled to each other and is representative of two possible regimes: SEZ and SZE. In (c), the spins are strongly coupled to each other and thus represent the ESZ regime. (d) and (e) Weak coupling region, in which the coupling of the spins to a background field is greater than their coupling to the NV. In (d), the spins are weakly coupled to each other and hence represent the ZSE and ZES regimes. In (e), the spins are strongly coupled to each other and represent the EZS regime.

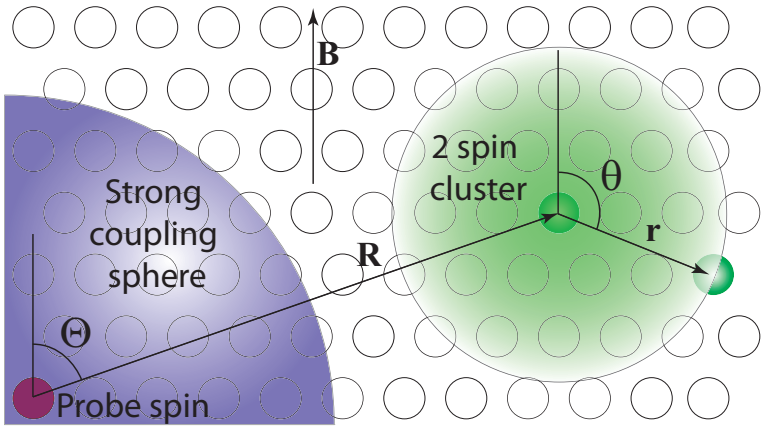

Figure 12.4: Schematic representation of a two spin cluster coupled to a central spin. The separation vector between the cluster and the central spin is defined by the location of the closest spin, **R**. The structure of the cluster is defined by the separation vector(s) of the cluster constituents, **r**. Evaluation of the ensemble averaged quantities requires integration over **R**, and averaging over **r**.

are summarised below.

In the **ZSE** regime, the nuclei are sufficiently far from both the NV and each other that the Zeeman interaction dominates over both the hyperfine and dipolar interactions, ensuring that both classes of interactions must conserve axial magnetisation. The $\langle \mathcal{H}_{\mathrm{ZE}}^2 \rangle \gg \langle \mathcal{H}_{\mathrm{SE}}^2 \rangle \gg \langle \mathcal{H}_{\mathrm{EE}}^2 \rangle$ condition yields the following constraints on the geometry of the cluster:

$$\begin{aligned} \left(\frac{a}{\omega}\right)^{1/3} \leq \quad R \quad &\leq r \left(\frac{a}{b}\right)^{1/3}, \\ R \left(\frac{b}{a}\right)^{1/3} \leq \quad r \quad &< \infty. \end{aligned}$$

Clusters in the **SZE** regime are sufficiently close to the NV to ensure that the hyperfine coupling dominates over the Zeeman interaction, however, the associated nuclei are still far enough apart to ensure that the Zeeman interaction is larger than their mutual

dipolar coupling. The $\langle \mathcal{H}_{\mathrm{SE}}^2 \rangle \gg \langle \mathcal{H}_{\mathrm{ZE}}^2 \rangle \gg \langle \mathcal{H}_{\mathrm{EE}}^2 \rangle$ condition ensures that

$$\begin{aligned} 0 \leq \quad R \quad &\leq \left(\frac{a}{\omega}\right)^{1/3}, \\ \left(\frac{b}{\omega}\right)^{1/3} \leq \quad r \quad &< \infty. \end{aligned}$$

Clusters in the **SEZ** regime are both sufficiently tightly bound and close to the NV to ensure that both hyperfine and dipolar couplings dominate over the Zeeman interaction, however, the associated nuclei are still far enough apart to ensure that the hyperfine interaction is larger than their mutual dipolar coupling. The $\langle \mathcal{H}_{\mathrm{SE}}^2 \rangle \gg \langle \mathcal{H}_{\mathrm{EE}}^2 \rangle \gg \langle \mathcal{H}_{\mathrm{ZE}}^2 \rangle$ condition ensures that

$$\begin{aligned} 0 \leq \quad R \quad &\leq r \left(\frac{a}{b}\right)^{1/3}, \\ R\left(\frac{b}{a}\right)^{1/3} \leq \quad r \quad &\leq \left(\frac{b}{\omega}\right)^{1/3}. \end{aligned}$$

The remaining three regimes, ZES, EZS and ESZ, may be quantified in an equivalent manner, however the physical constraints placed on R and r due to the diamond lattice render these regimes impossible for a naturally occurring 1.1% ^{13}C nuclear spin bath. This is illustrated in figure 12.5, where the possible physical locations an environmental spin may occupy are shown in the shaded region. The constraints on r arise from the fact that no two spins may be within a distance of less than one lattice site from each other; whereas having a large separation means that there is little chance of the two spins in question being part of the same cluster (this will be quantified in section 12.4). Similarly, the constraints on R arise from the lattice spacing, and the fact that the hyperfine field vanishes at large R. In particular, we see that, whilst changing the background field strength changes the relative number of spins in the ZSE, SZE and SEZ regimes, a 1.1% ^{13}C nuclear spin bath will never

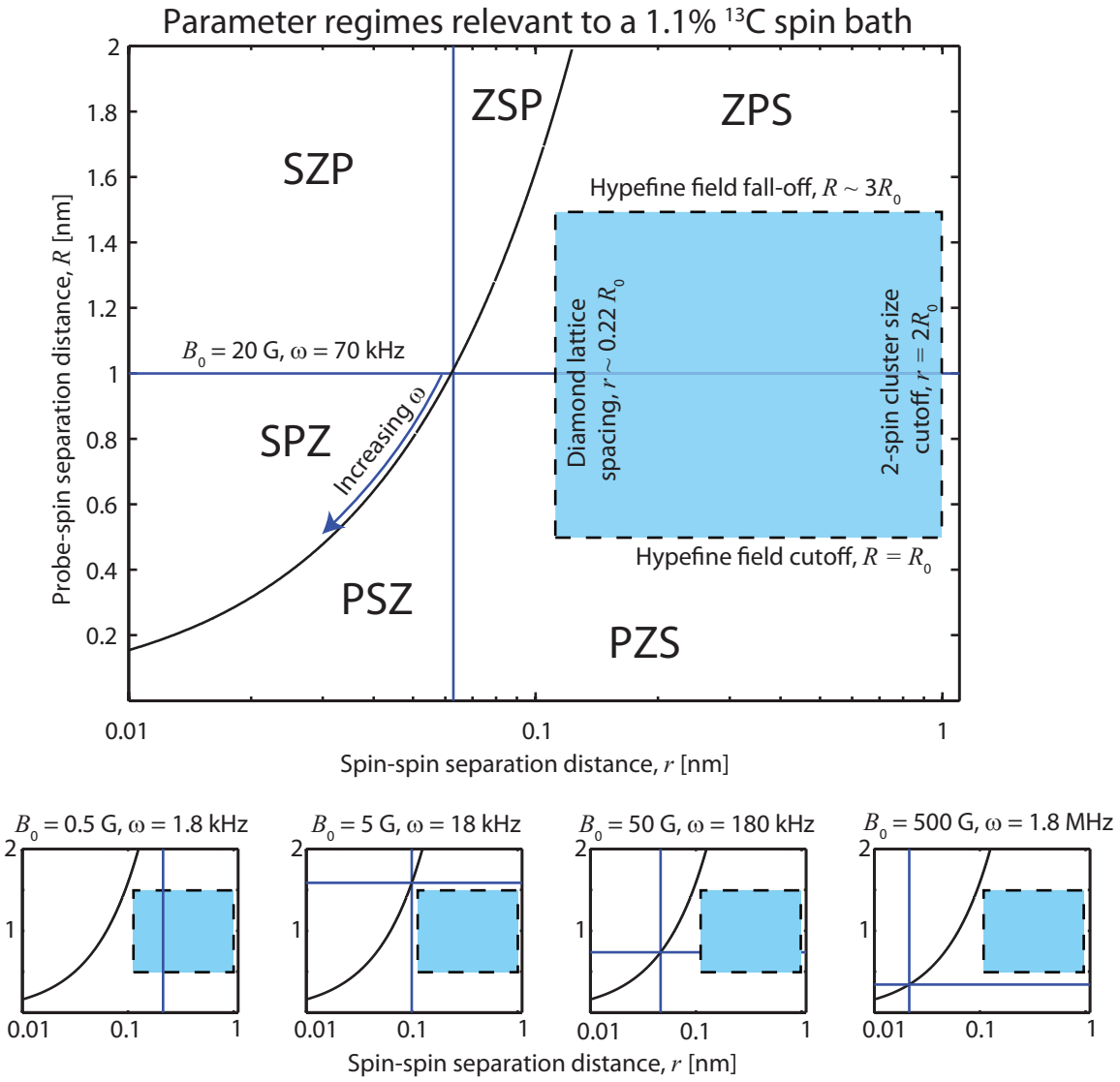

Figure 12.5: Plot showing the locations of the 6 parameter regimes in $R - r$ space for a naturally occurring 1.1% ^{13}C nuclear spin bath. The location of the intersection point (blue cross-hairs) changes along the S=E coupling line for different magnetic field strengths (the main plot depicts the case of 20 G, and the sequence below depicts the 0.5 G, 5 G, 50 G, and 500 G cases). For this spin bath, we see that only the regimes where $S \gg E$ (ie, SEZ, SZE and ZSE) are relevant.

occupy any regime for which E≫S. That is, in solving for this particular physical system, we need not consider any of the ZES, EZS or ESZ regimes.

This will not be true for all spin baths however, as shown by figure 12.6, in which 1.1%, 0.3% and 0.01%,^{13}C nuclear spin baths are considered, together with naturally occurring type-1b diamond containing an electron spin bath due to nitrogen donor impurities at parts-per-million (ppm) concentrations. The latter example presents a stark contrast to the 1.1%,^{13}C case, as the only appreciable regimes that need be considered here are ZES, EZS or ESZ, a consequence of the comparatively strong electron-electron coupling of the environmental spins, however electron spin baths are not the focus of this work.

In the present context, we define the decoherence of the NV as the loss of coherence between the $\left|0\right\rangle$ and $\left|+1\right\rangle$ states of the NV spin. This corresponds to the decay of the off diagonal terms in the corresponding density matrix, and may be computed directly from the lateral (in the $x-y$ plane) projection of the NV magnetisation vector, $S=\left\langle \mathcal{S}_x+i\mathcal{S}_y\right\rangle$. As the decoherence generally leads to a decay of this signal, we define a 'decoherence function', $\Lambda(t)$, such that we may write $L=e^{-\Lambda(t)}$, and we refer to the time taken to reach $\Lambda(t)=1$ as the 'coherence time.' Our task is then to determine the functional form of Λ in response to the separate parameter regimes discussed above.

In order to determine the full decoherence behaviour due to all spins in the environment, we may break up the environment into separate clusters consisting of strongly interacting spins and ignore the comparatively weak interactions between adjacent clusters. By virtue of the large zero-field splitting, and the maximum hyperfine coupling for an adjacent ^{13}C being of order 40 MHz, the NV spin exists in a 'pure

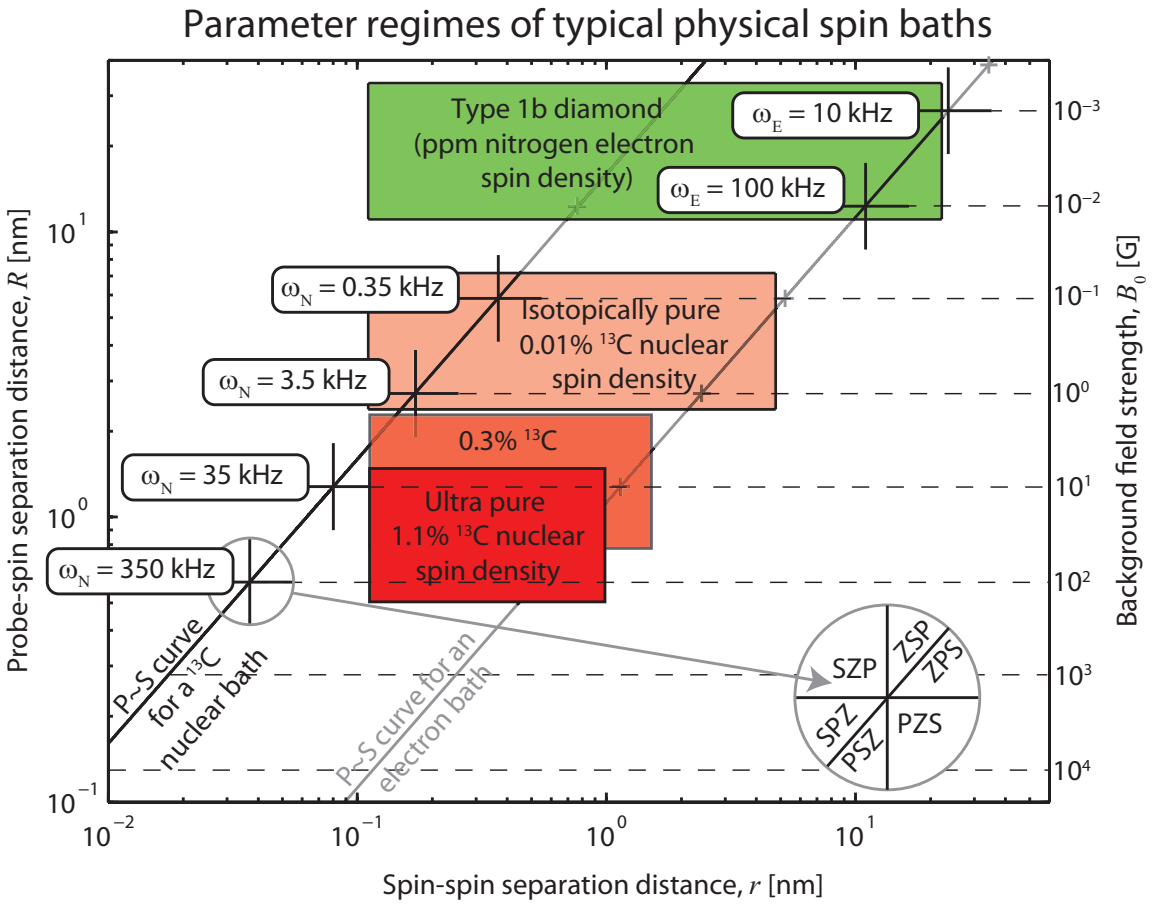

Figure 12.6: Plot showing the locations of the 6 parameter regimes in $R - r$ space for 1.1%, 0.3% and 0.01% ^{13}C nuclear spin baths and a naturally occurring electron spin bath arising from nitrogen donor spins at ppm concentrations. For the latter example, we see that only the regimes where $E \gg S$ (ie, ESZ, EZS and ZES) are relevant.

dephasing' regime in which only the relative phases of the spin states change and the respective populations do not. This will not be true for electron spin baths in the high density limit, however. We may then write the Hamiltonian as $\mathcal{H} = \sum_k \mathcal{H}_k$, where $\mathcal{H}_k$ acts only on the k^{th} cluster. Since all of the $\mathcal{H}_k$s commute, the time evolution operator may be factorised as $\mathcal{U}(t) = \prod_k \mathcal{U}_k(t)$. This implies that the full decoherence function is then simply a sum over all geometric configurations and locations of the environmental clusters. We note that this result will break down near the anti-crossing of the NV spin states at roughly 1024 Gauss, as the nuclear spins will be able to exchange energy with the NV spin. However, as the linewidth of the spin bath is of order kHz, this effect corresponds to a very narrow magnetic field interval of roughly 0.1 Gauss and is therefore ignored.

As we will show, incorporation of higher-order clustering has no effect on the leading order behaviour of the decoherence function, and is thus not important for the decoherence behaviour in the presence of low-order pulse sequences such as FID and spin-echo. In the following, we examine the decoherence functions associated with individual clusters of environmental spins, and then move on to discuss the statistics associated with how the environmental spins are distributed spatially. These distributions will then be used to compute the full decoherence behaviour due to all clusters in the environment.

12.3 Single cluster dynamics and decoherence

As mentioned above, in analysing the decoherence due to the native 1.1% ^{13}C spin bath, we need only consider the three 'strong coupling' regimes (ZSE, SZE and SEZ),

in which the interaction between the central spin and the environment, $\mathcal{H}_{\mathrm{SE}}$, dominates over the spin-spin interactions within the environment, $\mathcal{H}_{\mathrm{EE}}$. It is important to note that, due to the secular approximation imposed on the NV centre, this dominant S-E interaction is only apparent when the NV spin is in the $\left|+1\right\rangle$ state. In this case the large hyperfine interaction results in the nuclei having a large mismatch in their respective transition frequencies, meaning their comparatively weak mutual dipole interaction will be unable to cause a mutual flip-flop (this effect will we discussed in detail in section 12.3.1). This is somewhat advantageous, as the exponentiation of the full Hamiltonian, inclusive of all $\mathcal{H}_{\mathrm{SE}}$, $\mathcal{H}_{\mathrm{ZE}}$ and $\mathcal{H}_{\mathrm{EE}}$ terms, is not analytically possible in general. On the other hand, when the NV spin is in the $\left|0\right\rangle$ state, there will be no hyperfine coupling, and the environmental evolution will be self governed. This means that the environmental spins are free to evolve unperturbed according to $\mathcal{H}_{\mathrm{ZE}}$ and $\mathcal{H}_{\mathrm{EE}}$.

Since the evolution is so heavily dependent on the NV spin state, we can project this Hamiltonian along both basis states. Thus,

$$\mathcal{H} \equiv \left|1\right\rangle\!\left\langle 1\right|\mathcal{H}_1 + \left|0\right\rangle\!\left\langle 0\right|\mathcal{H}_0. \tag{12.3.1}$$

Because no hyperfine coupling exists when the NV is in the $\left|0\right\rangle$ state, projection onto the distinct NV states allows us to distinguish between the Hamiltonians associated with the $\left|0\right\rangle$ and $\left|+1\right\rangle$ states, namely $\mathcal{H}_0$ and $\mathcal{H}_1$ respectively.

An experiment in which the central spin is left to evolve under the action of the environment alone is referred to as a Free-Induction-Decay (FID), and the majority of the associated dephasing may be attributed to inhomogeneous broadening from quasi static components of the spin bath. In the case of an NV centre in either an electron or a nuclear spin bath, this broadening is typically of the order of a few

MHz, equating to an effective magnetic field of a few μT. As such, coherence times are typically of the order of $T_2^* \sim 1 - 10\,\mu$s, depending on the sample at hand. For such an experiment, the time evolution operator is given by,

$$\begin{aligned} \mathcal{U}_{\rm fid}(t) &= \big|1\big\rangle\big\langle 1\big| \otimes \exp\left(-i\mathcal{H}_1 t\right) + \big|0\big\rangle\big\langle 0\big| \otimes \exp\left(-i\mathcal{H}_0 t\right) \\ &\equiv \big|1\big\rangle\big\langle 1\big| \otimes \mathcal{U}_1(t) + \big|0\big\rangle\big\langle 0\big| \otimes \mathcal{U}_0(t), \end{aligned} \tag{12.3.2}$$

where $\mathcal{U}_1(t)$ and $\mathcal{U}_0(t)$ are the projections of the time-evolution operator onto the $\big|{+1}\big\rangle$ and $\big|0\big\rangle$ states of the NV spin respectively.

In general, we wish to consider the effect of different pulse sequences, which involve periods of free evolution followed by applied pulses at particular times. A general time evolution operator will contain exponents of the above Hamiltonians, however these exponents will appear as different components of the 2×2 matrix describing the central spin, depending on the pulse sequence considered. To keep things general, we write

$$\mathcal{U}(t) = \begin{pmatrix} \mathcal{K}_{11}(t) & \mathcal{K}_{10}(t) \\ \mathcal{K}_{01}(t) & \mathcal{K}_{00}(t) \end{pmatrix}, \tag{12.3.3}$$

however, just what the $\mathcal{K}_{mn}(t)$ are will depend on the pulse sequence employed. For the FID case just mentioned, we just simply have $\mathcal{K}_{11}(t) = \mathcal{U}_1(t)$, $\mathcal{K}_{00}(t) = \mathcal{U}_0(t)$, $\mathcal{K}_{10}(t) = \mathcal{K}_{01}(t) = 0$.

The relatively short coherence times of a FID experiment may be extended by 2-4 orders of magnitude by applying an appropriate sequence of π pulses (or 'bit-flips', denoted $\mathcal{F}$), under which the quantum amplitudes of the $|1\rangle$ and $|0\rangle$ states are swapped. In the simplest instance, we consider a Hahn-echo, or spin-echo pulse sequence, involving a single π pulse applied at time $t/2$. The effect of this sequence is

to refocus any static components of the bath, thereby extending coherence times by roughly 2 orders of magnitude, with typical times of 400 μs-1 ms. The time evolution operator for a spin echo experiment is

$$\mathcal{U}_{\rm se}(t) \;=\; \mathcal{U}_{\rm fid}(t/2)\,\mathcal{F}\,\mathcal{U}_{\rm fid}(t/2), \tag{12.3.4}$$

hence we make the identification

$$\begin{aligned}
\mathcal{K}_{10}(t) &= \mathcal{U}_1(t/2)\mathcal{U}_0(t/2),\\
\mathcal{K}_{01}(t) &= \mathcal{U}_0(t/2)\mathcal{U}_1(t/2),\\
\mathcal{K}_{11}(t) &= \mathcal{K}_{00}(t) = 0.
\end{aligned} \tag{12.3.5}$$

The density matrix, $\rho(t)$, at $t = 0$ is given by

$$\rho(0) \;=\; \Big[\,|1\rangle\langle 1| + |1\rangle\langle 0| + |0\rangle\langle 1| + |0\rangle\langle 0|\,\Big] \otimes \mathcal{M}_{\rm E},$$

where $\mathcal{M}_{\rm E}$ denotes a purely mixed environmental state. The in-plane magnetisation at time t is found from

$$L \;=\; {\rm Tr}\big\{(\mathcal{S}_x + i\mathcal{S}_y)\,\rho(t)\big\}. \tag{12.3.6}$$

From this, we see that the FID and spin echo signals are given by

$$\begin{aligned}
L_{\rm fid} &= \frac{1}{2^k}{\rm Tr}_{\rm E}\Big\{\mathcal{U}_0(t)\mathcal{U}_1^\dagger(t)\Big\},\\
L_{\rm se} &= \frac{1}{2^k}{\rm Tr}_{\rm E}\Big\{\mathcal{U}_0(t/2)\mathcal{U}_1(t/2)\mathcal{U}_0^\dagger(t/2)\mathcal{U}_1^\dagger(t/2)\Big\},
\end{aligned} \tag{12.3.7}$$

respectively, where k is the number of spins in the cluster. The exact forms of the propagators will be determined by the regime in question, allowing us to make asymptotic expansions in terms of the relative coupling scales, such as an/ω, bn/ω and a/b, where n is the density of the spins in the bath.

12.3.1 Environmental autocorrelation functions and frequency spectra

Before deriving the relevant decoherence functions, we take a brief detour to examine the dynamic behaviour of the nuclear spin bath environment as described by the effective semiclassical magnetic field felt at an arbitrary point in the lattice due to the interacting environmental spins. Whilst the existence of such a field is not sufficient to describe the induced decoherence behaviour of the central spin, due to the omission of the hyperfine couplings, it does give us an insight into the natural dynamic behaviour of the spin bath, and how it changes with the background magnetic field strength. In this section, we derive the autocorrelation functions of the effective magnetic field due to 2 and 3 spin clusters in the environment, for both secular (high-field) and non-secular (low-field) flip-flop regimes. We conclude this discussion of autocorrelation functions with an analysis of the effect of the hyperfine coupling on the nuclear dynamics. This analysis justifies why we may ignore the dipole-dipole coupling between nuclei when the NV spin is in either of the $\left|\pm 1\right\rangle$ states.

Secular nuclear dynamics

When a background field of sufficient strength to set the quantisation axis of the spins in the cluster is applied, some of the terms in the Hamiltonian describe spin transitions that are no longer energy conserving and are hence disallowed. In this case, we make the secular approximation in which all non-magnetisation conserving transitions are ignored, giving the following secular Hamiltonian,

$$\mathcal{H}_{\text{sec}} = B_{12}\vec{\mathcal{E}}_1 \cdot \vec{\mathcal{E}}_2 + \omega_1 \mathcal{E}_{1,z} + \omega_2 \mathcal{E}_{2,z}, \tag{12.3.8}$$

where $B_{12} = b/r_{12}^3[1 - 3\cos(\theta)]$. The effective magnetic field operator as felt by the central spin is due to the axial components of the hyperfine interaction,

$$\mathcal{B}_2 \;=\; \sum_{j=1}^{N_k} \left(A_{zx}^{(j)} \mathcal{E}_x^{(j)} + A_{zy}^{(j)} \mathcal{E}_y^{(j)} + A_{zz}^{(j)} \mathcal{E}_z^{(j)} \right), \tag{12.3.9}$$

where N_k is the number of spins in the k^{th} cluster. For $n_k = 2$, this leads to an autocorrelation function of

$$\begin{aligned} \left\langle \mathcal{B}_2(t)\mathcal{B}_2(0) \right\rangle_{\text{S}} \;=\; & A_{z,1}^2 + A_{z,2}^2 + \left(A_{x,1}^2 + A_{x,2}^2 + A_{y,1}^2 + A_{y,2}^2 \right) \cos(t\omega) \\ & - \left[\Delta_z^2 + \left(\Delta_x^2 + \Delta_y^2 \right) \cos(t\omega) \right] \sin^2 \left(\frac{B_{12} t}{2} \right), \end{aligned} \tag{12.3.10}$$

where $\Delta_{x,y,z} \equiv |A_{x,y,z,1} - A_{x,y,z,2}|$. Since we are only concerned with couplings to the axial (z) component of the NV spin, we have adopted the short hand notation of $A_{zx}^{(j)} \equiv A_{x,j}$, $A_{zy}^{(j)} \equiv A_{y,j}$ and $A_{zz}^{(j)} \equiv A_{z,j}$.

Equation 12.3.10 shows that there is always a static component of the secular autocorrelation function present regardless of the geometric arrangement of the spins in the cluster. The total axial magnetisation for a given cluster is constant, and hence the NV only sees a fluctuating field if the two spins have different hyperfine coupling strengths ($A_{z,1}$ & $A_{z,2}$). The larger this difference, the greater the strength of the effective fluctuating field, however the axial flipping rate, B_{12} decreases with their spatial separation. If the spins are sufficiently close together, such that their energy scale is dictated by their mutual interaction, transitions that do not conserve axial magnetisation become permissible and the secular condition is violated. This case is dealt with below in section 12.3.1.

These methods may be extended to obtain corrections for three spin interactions and higher. However, despite being interested in the short-time and relatively weak

coupling to the next-nearest-neighbour, we cannot use perturbation theory, as the couplings strengths still become infinite as the next-nearest-neighbour separation goes to zero. A short-time expansion of equation 12.3.10 would diverge as r approaches 0, hence to use perturbation theory at a given order for all possible geometric configurations (particularly when $B_{12}^2 \gg A_{z1}^2 + A_{z1}^2$, which defines the high frequency, and hence short-time behaviour of the dynamics), we require the leading order of the relevant probability density function to be at least $\mathcal{O}\{r^4\}$. As we will see in section 12.4, this corresponds to the third nearest neighbour and above. Hence, perturbation theory cannot be applied until cluster sizes of four or greater are considered.

In analysing the dynamics of a 3 spin cluster, we initially assume that a strongly coupled pair exists, and introduce a third impurity whose coupling to the initial two is comparatively weak. We assume the two couplings involving the third spin are of similar order and make small perturbations about this condition. This is justified by the rapid fall-off of the dipole-dipole coupling, which ensures that any large deviation from this condition will yield a 2 spin cluster and an effectively separate, uncoupled spin. From this, we find the autocorrelation function of a single 3 spin cluster to be

$$\left\langle \mathcal{B}_3(t)\mathcal{B}_3(0)\right\rangle_{\mathrm{S}} = \left\langle \mathcal{B}_2(t)\mathcal{B}_2(0)\right\rangle_z + A_{z3}^2 - \frac{4}{9}\left[\Delta_{13}\sin^2\left(\frac{3B_{13}t}{4}\right) + \Delta_{23}\sin^2\left(\frac{3B_{23}t}{4}\right)\right] + \text{Larmor terms.} \quad (12.3.11)$$

This result exhibits almost identical properties to the 2 spin cluster case, with a persistent static component, and fluctuating components whose amplitudes are again proportional to the respective hyperfine coupling differences.

Non-secular nuclear dynamics

In the opposite limit, where the quantisation axis of the nuclear spins is set by their mutual coupling, we cannot ignore the non-magnetisation conserving terms in the dipole tensor describing their interaction. The Hamiltonian describing the dipolar coupling between two spins when all possible terms are included is given by

$$\mathcal{H}_{\mathrm{N}} = \frac{b}{r^3}\left[\vec{\mathcal{E}}_1 \cdot \vec{\mathcal{E}}_2 - \frac{3}{r^2}\left(\mathbf{r}\cdot\vec{\mathcal{E}}_1\right)\left(\mathbf{r}\cdot\vec{\mathcal{E}}_2\right)\right], \tag{12.3.12}$$

which yields the following non-secular autocorrelation function of the axial magnetic field,

$$\begin{aligned}\left\langle \mathcal{B}_2(t)\mathcal{B}_2(0)\right\rangle_{\mathrm{N}} &= \left(A_{z1}^2 + A_{z2}^2\right)\left[1 - \frac{4}{3}\sin^2\left(\frac{3B_{12}t}{4}\right)\right] \\ &\quad -\frac{2}{3}\Delta_z^2\left[\sin^2\left(\frac{B_{12}t}{4}\right) + \frac{1}{2}\sin^2\left(\tfrac{B_{12}t}{2}\right) - \sin^2\left(\frac{3B_{12}t}{4}\right)\right]. \end{aligned} \tag{12.3.13}$$

Note that, where the secular autocorrelation function only had fluctuating components proportional to differences in prob-spin couple strengths (Δ_z) within a given cluster, the non-secular function also contains terms that are present regardless of the geometric arrangement of the cluster constituents. This is a consequence of the fact that, for a non-secular cluster, the background field does not set the quantisation axis of the spins, hence the magnetisation component along the background field direction is not constant. As we will see in section 12.5, when the contributions to the full autocorrelation functions are summed over all clusters in the environment, we see very large differences between the dynamic behaviour of spins in secular and non-secular flip-flop regimes.

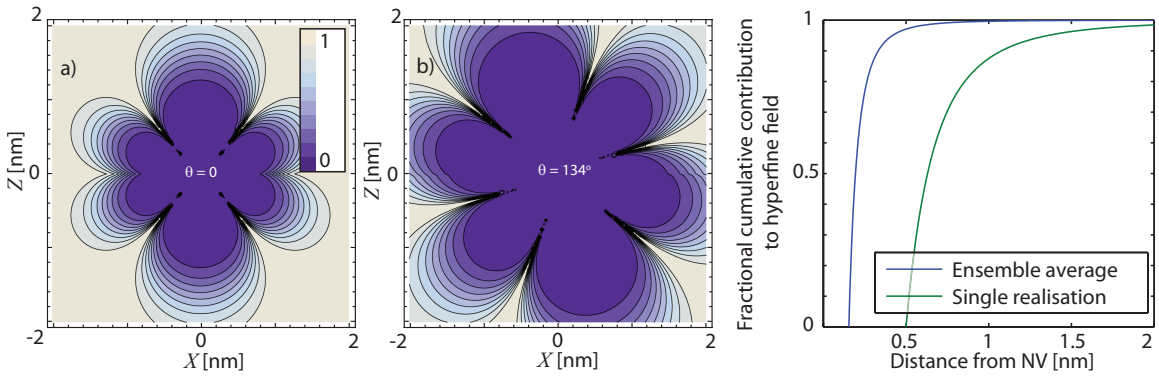

Figure 12.7: Plot showing the suppression of dipole mediated nuclear spin dynamics due to the hyperfine field of the NV centre. Values of the suppression constant, K (see equation 12.3.15) are plotted in a) and b) for cases where the two nuclei occupy adjacent lattice sites, with relative orientations of $\theta = 0$ and $\theta = 134^o$ respectively. The fractional cumulative contribution of all nuclei within a distance R to the total hyperfine field is shown in c) for both the ensemble case (blue) and that of a typical realisation of the environmental spin distribution (green). This plot show that effectively all nuclei making an appreciable contribution to the hyperfine field also reside in the suppression region.

Suppression of nuclear dynamics due to hyperfine fields

In cases where a strong magnetic field gradient exists, two nuclear spins will posses a mutual detuning between their respective Zeeman energies given by $\delta_z = |\omega_1 - \omega_2|$. Solving for the autocorrelation function in this case, we find

$$\left\langle \mathcal{B}_2(t)\mathcal{B}_2(0)\right\rangle_{\mathrm{S}} \;=\; A_{z,1}^2 + A_{z,2}^2 - \Delta_z^2 \frac{B_{12}^2}{B_{12}^2+\delta_z^2}\sin^2\left(\frac{t}{2}\sqrt{B_{12}^2+\delta_z^2}\right) + \text{Larmor terms}, \tag{12.3.14}$$

showing a modulation in the fluctuation amplitude by a factor of $B_{12}^2/\left(B_{12}^2+\delta_z^2\right)$, which becomes significantly damped as the magnitude of the detuning approaches that of the mutual dipolar coupling strength. We would not expect such a situation to arise as the result of inhomogeneities in an applied background as the associated detunings are simply not large enough over the distance of a few angstroms, which would require a magnetic field gradient of $\sim (b/l^3)/(l\gamma_{\mathrm{E}}) \approx 1\,\mathrm{mT\,nm^{-1}}$. Where significant detunings can arise however, are as the result of the hyperfine field generated by the central NV spin. For nuclear spins up to a few nanometres from the NV centre (which are responsible for the decoherence of the NV spin, as shown in figures 12.5 and 12.6), the difference in hyperfine couplings between two adjacent lattice sites is much greater than the associated dipolar coupling between them, leading to a complete suppression of the nuclear spin dynamics. We make this statement more precise as follows.

When the detuning between the Zeeman energies of two coupled nuclear spins is the result of the NV hyperfine field, we have that $\delta_z^2 = \Delta_z^2 = (A_{z,1} - A_{z,2})^2$. Equation 12.3.14 shows this leads to a suppression of the associated fluctuation amplitude by a factor of

$$K \;=\; \frac{B^2}{B^2+\Delta_z^2}. \tag{12.3.15}$$

Consider the cluster arrangement depicted in figure 12.4, where the separation vectors between the NV and two coupled nuclear spins is

$$\begin{aligned} \mathbf{R_1} &= R\Big(\cos(\Phi)\sin(\Theta), \sin(\Phi)\sin(\Theta), \cos(\Theta)\Big) \\ \mathbf{R_2} &= \mathbf{R_1} + \mathbf{r}, \end{aligned} \tag{12.3.16}$$

where $\mathbf{r}$ is the separation vector between the two spins, as given by

$$\mathbf{r} = r\Big(\cos(\phi)\sin(\theta), \sin(\phi)\sin(\theta), \cos(\theta)\Big). \tag{12.3.17}$$

As the largest coupling strength comes from nuclei that occupy adjacent lattice sites, we take $r = l$, where $l = 1.54\,\text{Å}$ is the lattice constant for diamond. From equation 12.2.2, the axial hyperfine coupling strengths are given by

$$A_{z,i} = \frac{a}{R_i^3}\left[1 - 3\cos^2(\Theta_i)\right], \tag{12.3.18}$$

and the nuclear dipolar coupling strength is

$$B = \frac{b}{l^3}\left[1 - 3\cos^2(\theta)\right]. \tag{12.3.19}$$

Using these quantities, we plot the magnitude of the suppression constant, K (equation 12.3.15), in figure 12.7. These results depict the worse case scenario (where the dipolar coupling is maximal and the hyperfine detuning is minimal) for the two possible cluster orientations of $\theta = 0$ (figure 12.7 a)) and $\theta = 134^o$ (figure 12.7 a)), and show that the nuclear dynamics are still strongly suppressed for NV-nuclear separations greater than 1 nm, and as great as 2 nm in the $\theta = 134^o$ case.

Naturally, as the NV-nuclear separation distance increases, both the hyperfine field and the corresponding hyperfine field detuning between adjacent lattice sites will decrease. For large enough NV-^{13}C separations, the dipolar coupling will eventually

dominate over the hyperfine detuning, however the reduced hyperfine coupling implies that spins in these regions will necessarily be too weakly coupled to the NV to have any effect on its evolution. To make this statement precise, consider the fractional contribution of the hyperfine field from a lower cutoff, R_0, to an arbitrary radial distance R as given by

$$\int_{R_0}^{R} nA_z^2 \, \mathrm{d}^3\mathbf{R} \Big/ \int_{R_0}^{\infty} nA_z^2 \, \mathrm{d}^3\mathbf{R} \;\; = \;\; 1 - \frac{R_0^3}{R^3}, \tag{12.3.20}$$

where n is the average density of ^{13}C spin in the lattice. The choice of R_0 will depend on the diamond sample at hand. In an ensemble average over many environmental distributions, all lattice sites will be equally populated, meaning that we must choose $R_0 = l$ as our lower cutoff. On the other hand, in a single realisation of the environmental distribution, we would not expect to find a nuclear spin within a distance of $R_0 = (3/4\pi n)^{1/3} = 5.0\,\mathrm{nm}$, which we take as our lower cutoff. We plot equation 12.3.20 for these two cases in figure 12.7 c), showing that there is effectively no contribution from spins residing more than a nanometre from the NV centre. It is for this reason that nuclear-nuclear dipolar couplings may be ignored for cases where the NV spin state is in either of its $\left|\pm 1\right\rangle$ basis states. Furthermore, as the NV spin must be in either of these states to feel the effect of the dipole field, this shows that a semi-classical mean-field approach cannot reproduce the decoherence behaviour of an NV centre coupled to a nuclear spin bath. This will be explored further in section 12.7.

12.3.2 Single spin clusters and free-induction decay

Having discussed the environmental dynamics of the nuclear spin flip-flops as unperturbed by the presence of the central spin, we now discuss the exclusive hyperfine

dynamics of environmental spins coupled to the NV without considering their mutual dipolar couplings. Again, this is not sufficient to explain the full decoherence behaviour under spin-echo and higher order pulse sequences, however it does gives us an insight into how the hyperfine dynamics transition from non-secular to secular behaviour with an increasing magnetic field strength. Furthermore, given that FID timescales are of the order of a few μs and thus too fast to see the effects of dipolar couplings between environmental spins, non interacting spins are sufficient to explain all FID effects.

Single spin clusters, by definition, do not include any interaction with adjacent spins. As we will show, such a simplified arrangement is not sufficient to describe any true decoherence in this system, however, it does serve as a useful exercise in demonstrating how some of the limiting parameter regimes emerge. The hyperfine and Zeeman coupling components of the Hamiltonian as projected onto the $\left|0\right\rangle$ and $\left|+1\right\rangle$ states of the NV spin are given by

$$\begin{aligned} \mathcal{H}_1 &= A_x\mathcal{E}_x + A_y\mathcal{E}_y + (A_z+\omega)\,\mathcal{E}_z, \\ \mathcal{H}_0 &= \omega\mathcal{E}_z, \end{aligned} \tag{12.3.21}$$

from which we determine the FID and spin-echo envelopes using equation 12.3.7,

$$\begin{aligned} L_{\text{fid}} &= \cos\left(\frac{t\lambda}{2}\right)\cos\left(\frac{t\omega}{2}\right) + \frac{\Omega}{\lambda}\sin\left(\frac{t\lambda}{2}\right)\sin\left(\frac{t\omega}{2}\right), \\ L_{\text{se}} &= 1 - 2\frac{A_x^2+A_y^2}{\lambda^2}\sin^2\left(\frac{t\lambda}{2}\right)\sin^2\left(\frac{t\omega}{2}\right), \end{aligned} \tag{12.3.22}$$

where $\Omega = A_z + \omega$ and $\lambda = \sqrt{A_x^2 + A_y^2 + \Omega^2}$. In this section, we will examine the behaviour of these expressions in cases of high and low magnetic fields, however one can immediately see that there is no spin-echo decoherence at both $\omega \to 0$ and

$\omega \to \infty$ limits. This is in direct contrast with experimental observations, where the decoherence rate is maximal at zero field, and decreases to a final, constant value at sufficiently high magnetic fields. This implies that we must introduce more complex spin-spin interactions to be able to explain this discrepancy. Higher order clusters are considered in the following sections, hence in this section we focus solely on FID behavior.

Expanding the above result for $\omega \gg A_z$, we find the contribution to the FID from a single spin to be

$$L_{\text{fid}}^{(1)}\Big|_{\omega \gg A} \sim \cos\left(\frac{A_z t}{2}\right) - \frac{A_x^2 + A_y^2}{2\omega^2} \sin\left(\frac{\omega t}{2}\right) \sin\left(\frac{1}{2}\left(A_z + \omega\right) t\right), \quad (12.3.23)$$

and in the low field limit ($\omega \ll A_z$) we find

$$L_{\text{fid}}\Big|_{\omega \ll A} \sim \left[\frac{A_z}{A} + \frac{\omega\left(A_x^2 + A_y^2\right)}{A^3} - \frac{3\omega^2\left(A_x^2 + A_y^2\right) A_z}{2A^5}\right] \sin\left(\frac{At}{2}\right) \sin\left(\frac{\omega t}{2}\right) + \cos\left(\frac{At}{2}\right) \cos\left(\frac{\omega t}{2}\right), \quad (12.3.24)$$

where $A = \sqrt{A_x^2 + A_y^2 + A_z^2}$.

There are a number of points worthy of discussion here, particularly with the regard to the effect of the magnetic field strength the effective hyperfine coupling strength. In the infinite magnetic field limit this coupling is completely determined by the axial hyperfine component, A_z, alone. This is because the Zeeman coupling is responsible for setting the quantisation axis of the nuclei, hence the NV spin is unable to drive transitions in the nuclear spins. On the other hand, in the zero field case, it is the hyperfine coupling thats sets the quantisation axis of the nuclei, meaning that their magnetisation need not be conserved with respect to the background magnetic field. This leads to a greater effective hyperfine coupling, owing to the inclusion of

A_x and A_y terms. This is an important effect that carries over into the analysis of higher order pulse sequences, as it distinguishes the ZSE regime from the SZE and SEZ regimes.

12.3.3 Two-spin clusters and spin-echo decay

In the previous sections, we discussed how treating the dipolar-dipole coupled nuclear spin bath as a fluctuating magnetic field does not explain the decoherence of the NV spin, as the NV can only sense the effect of the nuclei if its hyperfine field is simultaneously suppressing their activity. On the other hand, treatment of the hyperfine interaction exclusively, to the exclusion of the nuclear dipolar interaction, only shows periodic entanglement between the NV spin and the nuclei, with no permanent decay of NV spin coherence on long timescales. These results imply that the NV spin coherence is essentially two-part process (see figure 12.8), in which quantum information of the NV spin is first imparted to the independent nuclei via the hyperfine interaction when the NV spin is in the $\left|+1\right\rangle$ state. This information may then be propagated throughout the crystal via the nuclear dipole-dipole interaction whilst the NV spin is in the $\left|0\right\rangle$ state. As such, we must incorporate both interactions in order to be able to analyse the true decoherence behaviour of the NV spin.

We begin by discussing how the full Hamiltonian (equation 12.2.1) may be simplified according to the six parameter regimes in question to solve for the corresponding evolution.

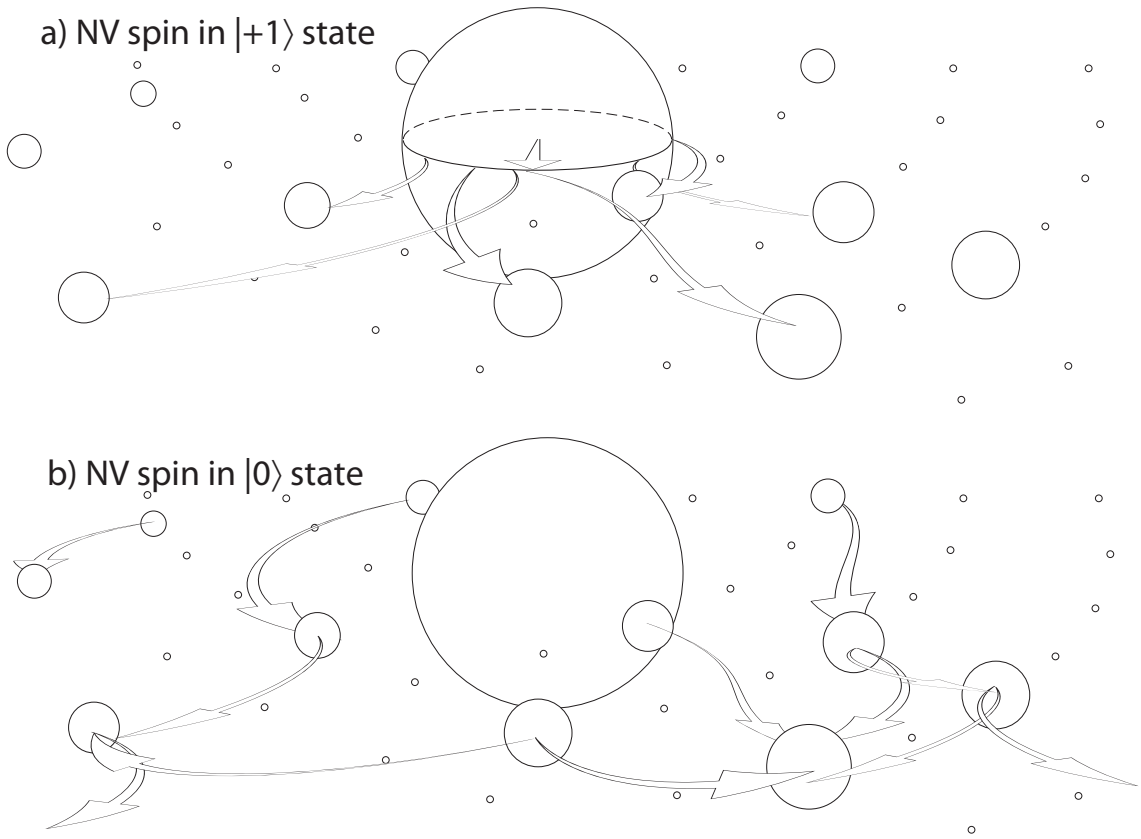

Figure 12.8: Schematic depicting the two step process of NV spin decoherence. In the first step (a), the NV spin is in its $\left|+1\right\rangle$ state, and quantum information regarding the NV spin state is imparted onto the environmental nuclear spins via the hyperfine interaction. This process is effectively reversible, as the nuclei cannot interact due to the strong hyperfine field of the NV. When the NV spin is flipped into its $\left|0\right\rangle$ state (b), the hyperfine coupling is turned off and this information is free to propagate throughout the lattice via the nuclear dipole-dipole interaction, rendering its loss irreversible.

Secular hyperfine coupling, secular dipole-dipole coupling (ZSE)

As discussed earlier, when the NV spin is in the $\left|+1\right\rangle$ state, the difference in the hyperfine couplings will yield sufficient detuning to suppress any dipolar flip-flops, hence we may ignore the dipolar term in the projection of the Hamiltonian on the $\left|+1\right\rangle$ spin state. Furthermore, the fact that the Zeeman terms are much greater than the dipolar terms allows us to ignore spin-spin interactions that do not conserve total magnetisation with respect to the background field, $\vec{\omega}$, and make the secular approximation for the dipole-dipole coupling. Thus the relevant Hamiltonians for the ZPS regime are given by

$$\begin{aligned}\mathcal{H}_1 &= \sum_{k=1}^{2}\left[A_{x,k}\mathcal{E}_{x,k} + A_{y,k}\mathcal{E}_{y,k} + (A_{z,k}+\omega)\,\mathcal{E}_{z,k}\right], \\ \mathcal{H}_0 &= B\vec{\mathcal{E}}_1\cdot\vec{\mathcal{E}}_2 + \omega\left(\mathcal{E}_{z1}+\mathcal{E}_{z2}\right). \end{aligned} \tag{12.3.25}$$

Using equation 12.3.7, and expanding to second order for small $A_{x,y,z}/\omega$ (the full expression is given in equation B.1.3), we obtain the contribution to the spin echo decoherence of the central spin due to a 2 spin cluster,

$$\begin{aligned} L_{\mathrm{ZSE}} &= 1-\sin^2\left(\frac{Bt}{4}\right)\sin^2\left(\frac{\Delta_z t}{4}\right) - \frac{\Delta_x^2+\Delta_y^2}{\omega^2}\sin^2\left(\frac{Bt}{4}\right)\sin^2\left[(A_{z,1}+\omega)\,\frac{t}{4}\right] \\ &\quad -4\frac{A_{x,1}^2+A_{y,1}^2}{\omega^2}\sin^2\left[(A_{z,1}+\omega)\,\frac{t}{4}\right]\sin^2\left(\frac{t\omega}{4}\right). \end{aligned} \tag{12.3.26}$$

We note that only the terms containing the dipole-dipole coupling, B, represent any actual decoherence, with the presence of a finite magnetic field increasing the effect by a factor of $1+\frac{\Delta_x^2+\Delta_y^2}{4\omega^2}$. The final term corresponds to the lateral dynamics (precession) of the nuclei, and hence does not contribute any decoherence, for reasons analogous to those discussed in section 12.3.2, however it does detail the emergence of the decay/revival behaviour seen in spin echo experiments on electron spins coupled to

nuclear spin baths. Specifically, we see that the amplitude of the revivals increase with decreasing magnetic field, as do their width.

Despite not contributing any true decoherence, the decays and revivals at the Larmor frequency are susceptible to inhomogeneous broadening from the axial couplings to all other spins in the bath, leading to an additional dephasing component in the evolution of the central spin. Such a distinction is important, as it explains the major difference between numerically calculated and experimentally observed behaviour of this system. This effect will be considered in detail later in section 12.6.2. Further corrections to the Larmor broadening due to larger cluster sizes may be calculated iteratively by employing the spectral distribution when performing the ensemble average, however these corrections will lead to terms with a dependence on t beyond that of leading order and are thus not important.

Non-secular hyperfine coupling, secular dipole-dipole coupling (SZE)

As with the ZSE regime, the $\left|+1\right\rangle$ state of the NV spin yields sufficient detuning to suppress any dipolar flip-flops, hence we may ignore the dipolar term in the projection of the Hamiltonian on the $\left|+1\right\rangle$ spin state. We are working in a regime where the Zeeman terms are still much greater than the dipolar terms, allowing us to ignore spin-spin interactions that do not conserve total magnetisation with respect to the background field. Thus the Hamiltonian, and hence the decoherence function, for the SZE regime are identical to that for the ZSE regime, however we instead expand

equation B.1.3 for small $\omega/A^{1,2}_{x,y,z}$, giving

$$\begin{aligned} L_{\mathrm{SZE}} &= 1-\sin^2\left(\frac{Bt}{4}\right)\sin^2\left(\frac{\Delta}{4}\,t\right) \\ &\quad -4\frac{A^2_{x,1}+A^2_{y,1}}{A^2_1}\left[1-\frac{2\omega A_{z,1}}{A^2_1}\right]\sin^2\left(\frac{t\lambda_1}{4}\right)\sin^2\left(\frac{t\omega}{4}\right) \\ &\quad +\frac{4\left(A^2_{x,1}+A^2_{y,1}\right)^2}{A^4_1}\left[1-\frac{4\omega A_{z,1}}{A^2_1}\right]\sin^4\left(\frac{t\lambda_1}{4}\right)\sin^4\left(\frac{t\omega}{4}\right), \end{aligned} \tag{12.3.27}$$

where $\Delta \equiv |A_1 - A_2|$. We note here that this expression is very similar to that of the ZSE regime, however the effective hyperfine coupling strength has increased from Δ_z to Δ. This is a consequence of the quantisation axis of the spins being set by their hyperfine coupling rather than their Zeeman coupling.

Non-secular hyperfine coupling, non-secular dipole-dipole coupling (SEZ)

In this regime, we still have that the hyperfine couplings dominate when the NV is in the $\left|+1\right\rangle$ state. When the NV is in the $\left|0\right\rangle$, the dipolar couplings between the environmental spins will dictate the evolution, as with the ZSE and SZE regimes, however in this regime, the dipolar couplings dominate over the Zeeman terms. This means that the quantisation axis of the spins are set by their mutual interaction, and the cluster is thus not required to conserve magnetisation with respect to the background field. Including all possible dipole interaction terms, we have

$$\begin{aligned} \mathcal{H}_1 &= \sum_{k=1}^{2}\left[A_{x,k}\mathcal{S}_{x,k}+A_{y,k}\mathcal{S}_{y,k}+\left(A_{z,k}+\omega\right)\mathcal{S}_{z,k}\right], \\ \mathcal{H}_0 &= B\left[\vec{\mathcal{S}}_1\cdot\vec{\mathcal{S}}_2-3\left(\mathbf{n}\cdot\vec{\mathcal{S}}_1\right)\left(\mathbf{n}\cdot\vec{\mathcal{S}}_2\right)\right], \end{aligned} \tag{12.3.28}$$

where $\mathbf{n}$ is the unit vector separating spins 1 and 2. The full spin echo envelope for the SEZ regime is too large to reproduce here, however we may simplify things

immensely by averaging over the angular components of the cluster geometry (θ, ϕ), giving

$$L_{\mathrm{SEZ}} = 1 - \frac{8}{15}\sin^2\left(\frac{3Bt}{4}\right)\left[\sin^2\left(\frac{At}{2}\right) + \sin^2\left(\frac{At}{4}\right)\right], \tag{12.3.29}$$

where $A = \sqrt{A_x^2 + A_y^2 + A_z^2}$. Notice that the hyperfine coupling now emerges as A instead of Δ, which is a consequence of the magnetisation no longer being conserved with respect to the background field. This results in a significantly larger fluctuation amplitude, as $\langle A^2\rangle = \left(\frac{4\pi na}{3}\right)^2$, whereas $\langle \Delta^2\rangle = (2na)^2$. The separation of hyperfine and dipolar processes also means that we need not distinguish between A_1 and A_2, as their relative locations are no longer important as far as the hyperfine component of the evolution is concerned. As the contributions of each spin will be summed over in an equivalent manner, we simply put $A_1 = A_2 = A$. This is in contrast to the ZSE and SZE cases, where the hyperfine couplings manifest as Δ_z and Δ respectively, as the treatment of spin 2 will depend on the location of spin 1.

In the following section we discuss the statistics associated with the random distribution of spin impurities in a spin bath environment. These statistics will be used to determine the combined effect on the coherence of the central spin from all clusters in the bath.

12.4 Spatial statistics of randomly distributed impurities

In this section, we derive the probability density functions associated with the distance between the nearest-neighbour (NN), next-nearest-neighbour (NNN), and so

forth, impurities in the environment. These distributions will be used to determine the collective dynamic behaviour of the environment and allow us to compare the contributions from the different orders of clustering. We firstly consider the case of a continuum distribution, in which spin impurities may adopt any position in the lattice according to their spatial density. We then consider the specific case of NV centres in diamond, in which carbon atoms are arranged in a tetrahedral diamond lattice.

For a given lattice site density (or carbon atom number density) of n_c, the volume V concentric on any one environmental spin impurity contains $N \approx n_c V - 1$ sites that may be occupied by a second impurity. The probability of finding X spins within V is then a binomial distribution with N independent trials, with each site having a probability $\chi = 0.011$ of being occupied by a nucleus of non-zero spin,

$$\mathrm{P}(X|N,\chi) \approx \frac{(V/V_0)!}{X!(V/V_0 - X)!}\chi^X(1-\chi)^{V/V_0 - X}, \tag{12.4.1}$$

which, in the limit of low spin concentrations, $\chi \ll 1$, approaches a Poisson distribution,

$$\mathrm{P}(X|V,\chi) \approx \frac{1}{X!}\left(\zeta r^3\right)^X \exp\left(-\zeta r^3\right), \tag{12.4.2}$$

where $\zeta \equiv \frac{4\pi\chi}{3V_0}$, implying an average spin impurity density of $n = \chi/V_0$. The probability that a sphere concentric on a given environment spin contains at least one other spin is given by $\mathrm{P}(X > 0, r) = 1 - \exp\left(-\frac{4\pi n r^3}{3}\right)$, which, by definition, is also the cumulative probability function. As such, the probability of encountering a spin *at* r (ie *on* the shell of V) is given by

$$\mathrm{P}(r) = \frac{d}{dr}\mathrm{P}(X > 0, r) = 4\pi n r^2 \exp\left(-\frac{4\pi n r^3}{3}\right). \tag{12.4.3}$$

In other words, $\mathrm{P}(r)$ is the probability density function for the distance between two nearest neighbour spins.

This analysis may be extended to compute the probability distribution of the distance to the k^{th} nearest neighbour. Consider the region bounded by concentric spheres of radii r_1 and r_0, the volume of which is $\frac{4}{3}\pi\left(r_1^3 - r_0^3\right)$. As above, the probability that at least one impurity exists in this region is $1 - \exp\left[-\zeta\left(r_1^3 - r_0^3\right)\right]$, which has the corresponding probability density function,

$$\mathrm{P}(r_1) \;=\; 3\zeta r_1^2 \exp\left[-\zeta\left(r_1^3 - r_0^3\right)\right].$$

Similarly, the probability density function for the distance to the k^{th} impurity is

$$\mathrm{P}(r_k) \;=\; 3\zeta r_k^2 \exp\left[-\zeta\left(r_k^3 - r_{k-1}^3\right)\right].$$

Taking $r_0 = 0$, the joint probability density function is

$$\mathrm{P}(r_1, \ldots, r_k) = \prod_{j=1}^{k} p_r\left(r_j\right) = (3\zeta)^k r_1^2 \ldots r_k^2 \exp\left[-\zeta r_k^3\right].$$

To obtain the distribution for each r_j, we successively integrate over all $r_1, \ldots, r_{j-1}$, $r_{j+1}, \ldots, r_k$ from 0 to r_{j+1}.

Thus, given the location of some environmental spin, the probability of finding its k^{th} nearest neighbour at a distance of r_k is given by

$$\mathrm{P}_k(r_k) \;=\; \frac{4\pi n r_k^2}{(k-1)!}\left(\frac{4\pi n r_k^3}{3}\right)^{k-1} \exp\left[-\frac{4\pi n r_k^3}{3}\right]. \tag{12.4.4}$$

Computing the first and second moments of this distribution, we find

$$\left\langle r_k \right\rangle \;=\; \left(\frac{4\pi n}{3}\right)^{-\frac{1}{3}} \frac{\Gamma\left(k + \frac{1}{3}\right)}{(k-1)!}, \tag{12.4.5}$$

$$\text{and} \quad \left\langle r_k^2 \right\rangle \;=\; \left(\frac{4\pi n}{3}\right)^{-\frac{2}{3}} \frac{\Gamma\left(k + \frac{2}{3}\right)}{(k-1)!}. \tag{12.4.6}$$

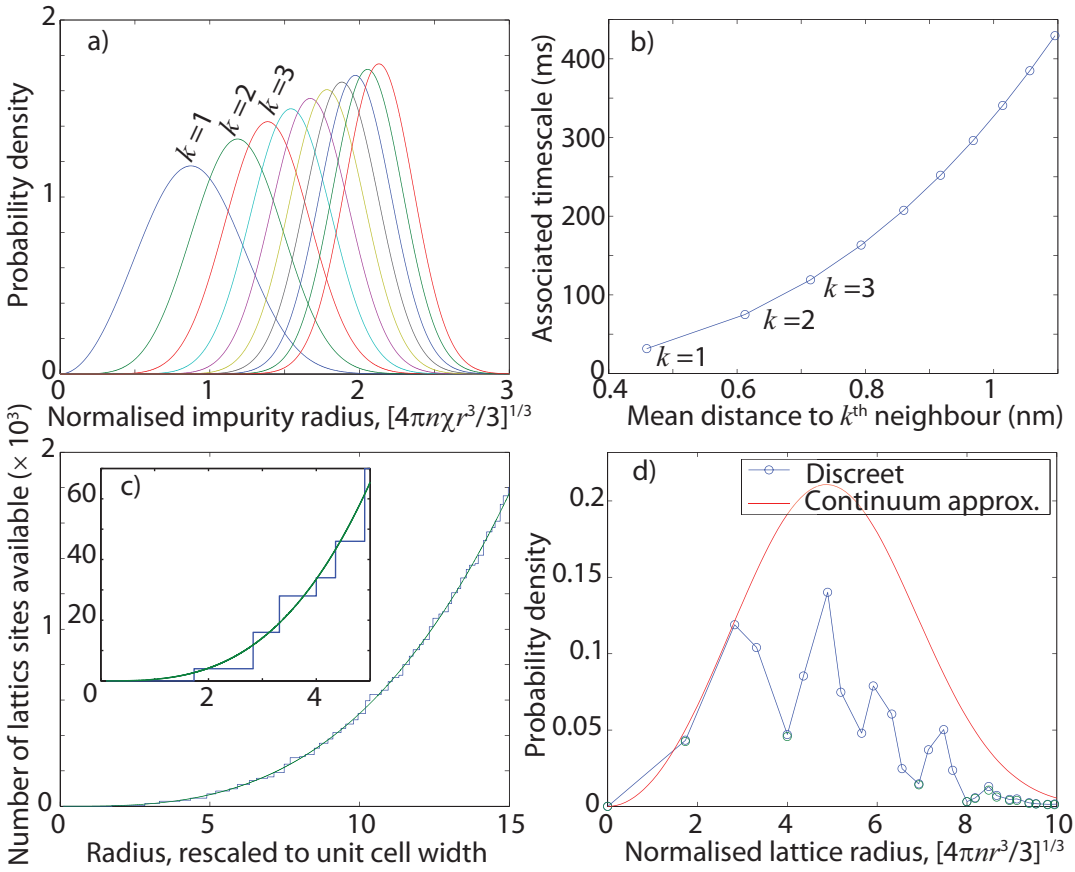

Figure 12.9: Probability distributions (a), and corresponding timescales and mean distance (b), associated with the first 10 nearest neighbours.

A plot of the mean distance to the first 10 nearest neighbours, $\langle r_k \rangle$ for $k = 1, \ldots, 10$, is shown in figure 12.9(b). This quantity gives us an indication of how large the considered region may be (and hence the timescale) before NNN interactions become important. As we can see, for the case of an NV centre coupled to a ^{13}C nuclear spin bath, where $T_2 < 1\,\text{ms}$, we need only consider 2-spin interactions.

In the above analysis, we have assumed that a given impurity may adopt any position within the environment, with the only constraint being the overall average density with which the impurities are distributed. However, as our primary focus

neighbour	1	2	3	4	5	6	...	odd n	even n
$(\times l^2/3)$ r_n^2	3	8	11	16	19	24	...	4n-1	4n
ν_n	4	12	12	6	12	24	...		

Table 12.1: Table of normalised squared-distances between crystal lattice sites, and the associated number of sites at that distance.

is on the NV centre in diamond, this is not strictly correct, as impurities may only occupy the atomic positions of a diamond cubic crystal structure.

Let $N(r)$ be the number of discreet lattice sites enclosed within a sphere of radius r, concentric on some impurity, and let $\nu_n \equiv \nu(r_n)$ denote the number of discreet lattice sites at radius r_n. Again invoking a binomial distribution, the probability of encountering the nearest neighbour impurity 1 spin at radius r_n, is the joint probability that 1 or more impurities reside at r_n and that there are no others within a sphere of this radius,

$$\mathrm{P}_n \;=\; [1-(1-\chi)^{\nu_n}]\,(1-\chi)^{N_{n-1}}. \tag{12.4.7}$$

The position vectors associated with the lattice sites in a cubic diamond unit cell of sidelength 4 are $\{\mathbf{u}_k\} = \{(0,0,0),(0,2,2)_{\circlearrowleft},(3,3,3),(3,1,1)_{\circlearrowleft}\}$, where $\circlearrowleft$ denotes a cyclic permutation of vectorial components. If we let $(l,m,n) \in \mathbb{N}^3$ index each individual cell, then the cartesian coordinates of a given site are $\mathbf{U}_k = 4(l,m,n) + \mathbf{u}_k$. From this we find that the squared distance to the n^{th} neighbour is $4n$ if n is even, and $4n-1$ if n is odd. Both r_n and ν_n are given in table 12.1. Note that values of r_n^2 have been normalised, however the distance between adjacent lattice sites is given by $l = 1.54\,\text{Å}$.

This derivation of the discreet probability distribution allows us to determine the extent to which the continuum approximation is valid when computing ensemble

averages of the various quantities that follow. We now use these spatial distributions to analyse the behavior of a central NV spin as coupled to a 1.1% ^{13}C nuclear spin bath in ultra pure, single crystal diamond.

12.5 Environmental autocorrelation functions and frequency spectra

In this section, we employ both the single cluster autocorrelation functions derived in section 12.3.1 corresponding to secular (equation 12.3.10) and non-secular (equation 12.3.13) evolution of an individual cluster, together with the spatial statistics developed in the previous section, to determine the respective autocorrelation functions due to the sum of all clusters in the environment.

A comparison of the autocorrelation functions associated with the secular and non-secular regimes is plotted in figure 12.10(a), using $\langle A_z^2 \rangle = \frac{4}{5}\left(\frac{4\pi}{3}an\right)^2$ and $\langle \Delta_z^2 \rangle \approx \frac{4}{5}(2an)^2$, from which we see that not only is the magnitude of the decay much greater in the non-secular case, but the non-secular decay is purely linear at $t = 0$, indicating a self-similar, Markovian regime at all timescales. On the other hand, the secular case has zero-derivative at $t = 0$, which is a consequence of the axial magnetisation of the cluster being conserved due to the dominant Zeeman coupling of the cluster constituents.

To obtain the correct short time scaling of the secular function, we note that it is only the small clusters ($r \ll R_0$) that contribute to short-time dynamics of the system. The constituents of larger clusters communicate on much longer timescales and hence manifest as an effectively DC signal. Another way to think of this is to view the

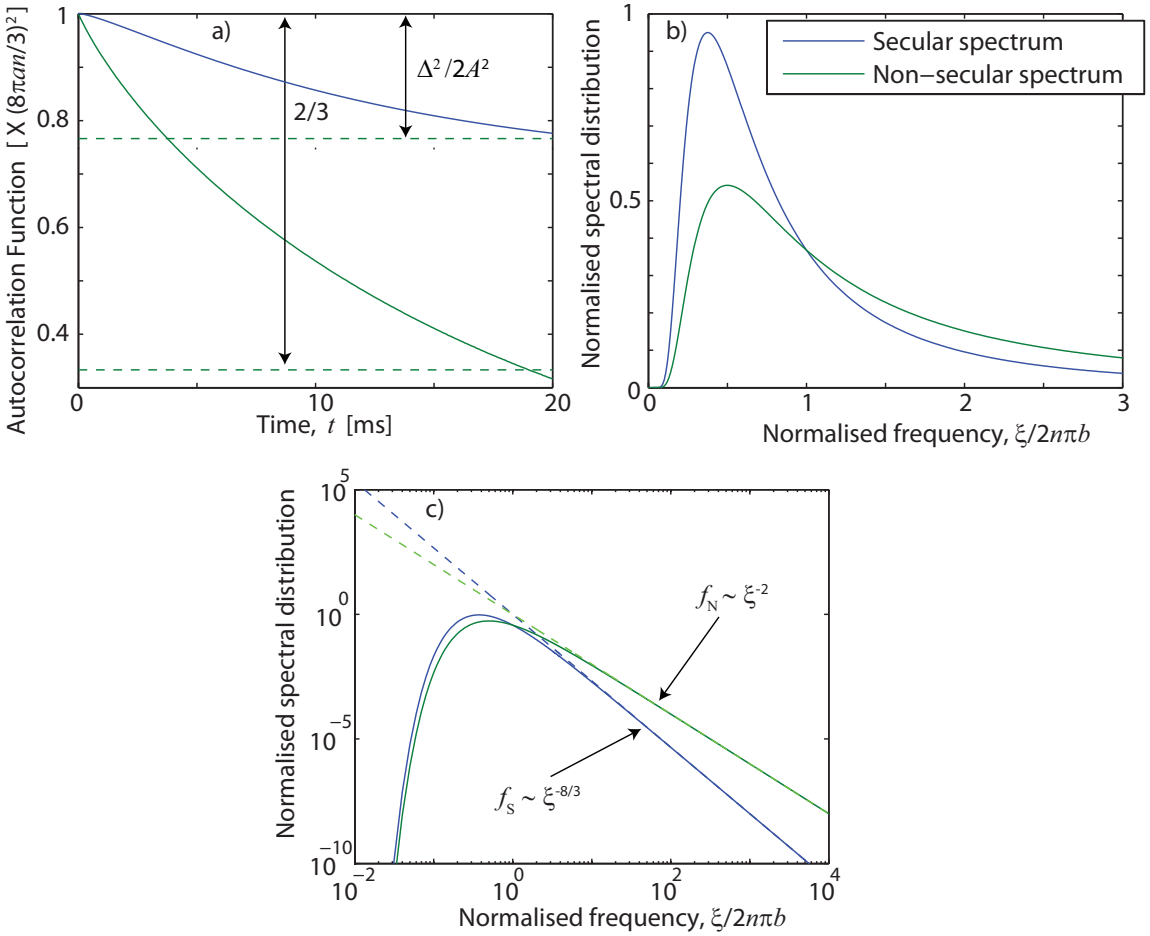

Figure 12.10: (a) Normalised secular (blue) and non-secular (green) autocorrelation functions. (b) Spectral distributions associated with the secular (blue) and non-secular (green) spin-spin dynamics. (c) As in (b), but plotted on a log-log scale to show the high-frequency scaling of the spectra.

ensemble averages taken over the spatial distributions (equation 12.4.3) as a Fourier transform, with the conjugate (frequency) variable given by $\xi \equiv 3br^{-3}/2$. The short time behaviour ($t \ll 1/bn$) of the autocorrelation function therefore corresponds to the high frequency behaviour ($\xi \gg bn$) of the spectral distribution. This is discussed further below. To obtain the short time behaviour, we expand $\Delta^2_{x,y,z}$ about $r = 0$, where, to lowest order, where $\Delta^2_{x,y,z} \sim \mathcal{O}\left(r^2/R^8\right)$ (See Appendix B.2 for a complete description). Substituting this result, we find the collective autocorrelation function for the secular environment to be

$$\left\langle \mathcal{B}_2(t)\mathcal{B}_2(0)\right\rangle_{\mathrm{S}} \;=\; \frac{2}{5}\left(\frac{4}{3}\pi an\right)^2\left[4+6\cos(\omega t)-\frac{1}{3}(7\cos(\omega t)+4)M(t)\right], \quad (12.5.1)$$

where $M(t)$ is related to the secular magnetisation, as detailed in Appendix B.2. This gives an autocorrelation time of

$$T_{\mathrm{S}} \;=\; \frac{9}{4\pi^2 bn} \;\approx\; 9.6\,\mathrm{ms}. \quad (12.5.2)$$

To leading order in t we have

$$M(t) \;\sim\; \frac{4\pi\sqrt[3]{6}}{\Gamma\left(\frac{8}{3}\right)}(\pi bnt)^{5/3}-\frac{8\pi}{\sqrt{3}\Gamma\left(\frac{4}{3}\right)}(\pi bnt)^2\,. \quad (12.5.3)$$

On the other hand, the collective autocorrelation function for the non-secular environment may be computed exactly,

$$\left\langle \mathcal{B}_2(t)\mathcal{B}_2(0)\right\rangle_{\mathrm{N}} \;=\; \frac{64}{9}\pi^2a^2n^2\left[1-N(t)\right], \quad (12.5.4)$$

where $N(t)$ is related to the non-secular magnetisation, as detailed in Appendix B.2, giving the same autocorrelation time of

$$T_{\mathrm{N}} \;=\; \frac{9}{4\pi^2 bn} \;\approx\; 9.6\,\mathrm{ms}. \quad (12.5.5)$$

To leading order, this results in a linear decay, given by

$$N(t) \sim \frac{4}{9}\pi^2 bnt. \tag{12.5.6}$$

Whilst these regimes show an almost identical correlation time, the non-secular regime shows a much greater fluctuation magnitude (see figure 12.10). This is a consequence of the fact that axial magnetisation must be conserved for a cluster in a secular regime, meaning that the central spin can only sense an effective field fluctuation if there is a difference in hyperfine couplings between the spins in that cluster. On the other hand, for the non-secular case, it is the cluster geometry that sets their quantisation axis, meaning that transitions that do not conserve axial magnetisation are now allowed.

It is important to note that whilst these results hold on timescales of order $T_{\mathrm{S,N}}$, they are not strictly correct for timescales associated with cluster sizes smaller than the diamond lattice spacing, ie $T_{\min} \sim l^3/b \approx 300\,\mu\mathrm{s}$. The $M(t) \sim t^{5/3}$ scaling at ultra-short timescales is the result of the $\mathrm{p}(r) \sim r^2$ scaling of the probability density function associated with the distance between neighbouring spins, which breaks down on length scales of $r \sim l$. By expanding equations 12.3.10 and 12.3.13 on timescales of order $T_{\min}$, it is trivial to show the initial quadratic scaling of both secular and non-secular autocorrelation functions.

Having obtained the autocorrelation functions of the effective magnetic field, we can compute their Fourier transforms to give their corresponding spectral distributions. We do this by noticing that the role of the conjugate frequency variable is played by $\xi \equiv B = 3br^{-3}/2$. By transforming variables from r to ξ, we identify the

secular and non-secular spectral distributions to be

$$\begin{aligned} f_{\mathrm{S}}(\xi) &= K_{\mathrm{S}} \left(\frac{3b}{2\xi}\right)^{2/3} \frac{b}{2\xi^2} \exp\left(-\frac{2n\pi b}{\xi}\right), \\ f_{\mathrm{N}}(\xi) &= K_{\mathrm{N}} \frac{b}{2\xi^2} \exp\left(-\frac{2n\pi b}{\xi}\right), \end{aligned} \tag{12.5.7}$$

respectively, where K_{S} and K_{N} are normalisation constants. The corresponding normalised spectra are plotted in figures 12.10 (b) & (c). The lack of any significant spectral component near $\xi = 0$ is symptomatic of the cutoff imposed by the statistics associated with the size distribution of 2-spin clusters. That is, since the exponential size cutoff associated with 2-spin clusters prohibits arbitrarily large cluster sizes, there is no corresponding low frequency region of the spectral density. Recall from the spatial statistics associated with higher order cluster sizes (equation 12.4.3), that each successive k^{th} neighbour introduces an associated probability distribution whose leading order behaviour scales as $r^{3k-1}/(k-1)!$. This, in turn, contributes an additional factor of $1/\xi$ to the spectral distribution for each successive order of clustering, with the modal frequencies occurring at

$$\begin{aligned} \overline{\xi_{\mathrm{S}}^{(k)}} &= \frac{2\pi nb}{k+\frac{5}{3}}, \\ \overline{\xi_{\mathrm{N}}^{(k)}} &= \frac{2\pi nb}{k+1}, \end{aligned} \tag{12.5.8}$$

for the secular and non-secular cases respectively. Incorporation of successively higher orders of clustering will resolve the true low frequency behaviour of the spectral distribution.

12.6 Decoherence in ultra-pure single crystal diamond

Having discussed the dynamic properties of the unperturbed spin bath environment, we move on to discussing the effect such an environment has on the coherence properties of a central NV spin. This analysis is performed by integrating the single cluster decoherence functions (see section 12.3) over the $\mathbf{r} - \mathbf{R}$ domains as defined by the background field for the case of the naturally occurring 1.1% ^{13}C nuclear spin bath in ultra-pure single single crystal diamond. We initially discuss the free-induction behaviour of the NV spin in response to the influence of the surrounding spin bath for the limiting cases of high and low magnetic fields. We also mention the differences that arise between the FID behaviour of an ensemble of NV centres and that of a typical realisation of the surrounding environment.

We then move on to the analysis of the NV spin coherence in the presence of a spin-echo pulse sequence, noting with reference to figures 12.5 and 12.6 that the only regimes necessary for consideration are, in order of decreasing magnetic field, ZSE, SZE and SEZ. We initially consider parameter regimes in which the decoherence is explained exclusively by each of the respective decoherence functions, and then consider the full dependence of the decoherence on the magnetic field strength. As with the FID case, we discuss the differences between the spin-echo decoherence of an NV ensemble and that of a single NV centre.

To determine the ensemble averaged decoherence behaviour, recall from that the full spin echo envelope is given by the product of all envelopes due to all clusters as

weighted by the relevant spatial distributions,

$$L = \prod_i L_i, \tag{12.6.1}$$

and taking the natural logarithm of both sides gives

$$\begin{aligned} \Lambda &= -\sum_i \ln(L_i) \\ &\mapsto -\langle \ln(L_i) \rangle, \end{aligned} \tag{12.6.2}$$

where the final line above denotes the ensemble average taken over all possible geometric cluster configurations. To compute these averages, we employ a formal expansion for the natural logarithm given by

$$\ln(1-x) = -\sum_{k=1}^{\infty} \frac{x^k}{k}, \tag{12.6.3}$$

which holds for $-1 \leq x < 1$. This condition is automatically satisfied, since $-1 \leq L_{\mathrm{ZS}}, L_{\mathrm{SZ}} \leq 1$ and $0 \leq L_{\mathrm{ZSE}}, L_{\mathrm{SZE}}, L_{\mathrm{SEZ}} \leq 1$. For example, in the ZSE case, we have

$$\Lambda_{\mathrm{ZSE}} = \sum_{k=1}^{\infty} \frac{1}{k} \left[\sin^2\left(\frac{Bt}{4}\right) \sin^2\left(\frac{\Delta_z}{4} t\right) \right]^k. \tag{12.6.4}$$

However, we are only interested in the leading order behaviour of the ensemble averaged decoherence function, to which all terms for $k \geq 2$ do not contribute.

12.6.1 Free-Induction Decay (FID)

In this section, we consider the FID behaviour of the NV spin due to the combined effect of all spin clusters in the environment. We firstly discuss the limiting regimes of both high and low magnetic fields as compared with the FID rate, and then move on to consider the full magnetic field dependence. We note that the timescales of the dipolar coupling in the environment are extremely slow (recall $T_{\mathrm{S}} = T_{\mathrm{N}} \sim 10\,\mathrm{ms}$)

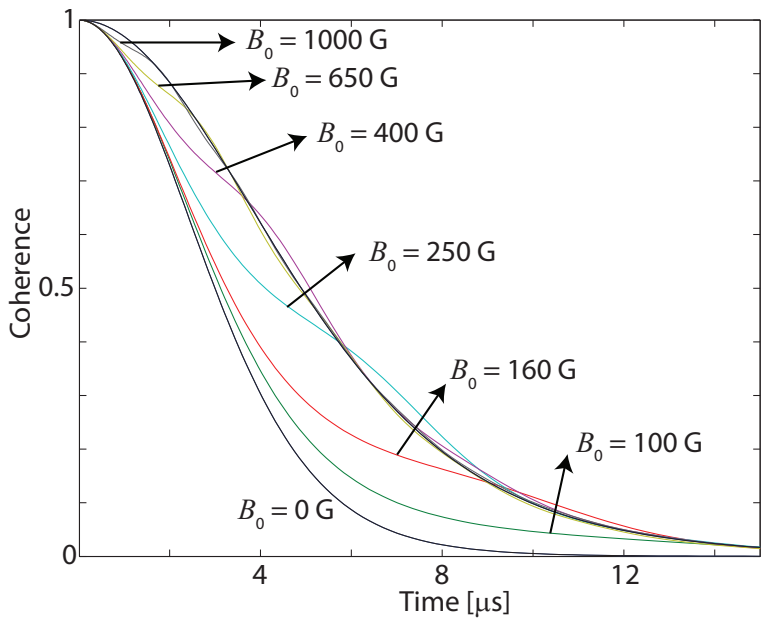

Figure 12.11: Plot showing the variation of the FID envelope with the strength of the background magnetic field. The transition from a SZ to a ZS regime occurs in the range of $100\,\mathrm{G} < B_0 < 1000\,\mathrm{G}$ at times associated with the Larmor period, $T_\omega \sim 2\pi/\gamma_\mathrm{E} B_0$.

compared to the $T_2^* = 1-10\,\mu$s FID times discussed here. This allows us to ignore the dipolar evolution, meaning that there are only two regimes important to the study of FID behavior, depending on the relative strengths of their Zeeman coupling (Z) to the background field, and their hyperfine coupling to the NV spin (S). Consequently, quantities derived in a regime where the Zeeman coupling dominates are labeled 'ZS' and similarly, quantities derived in a regime where the hyperfine coupling dominates are labeled 'SZ'. Whilst this is a somewhat simplistic situation compared with the six possible regimes discussed in section 12.2, these considerations detail the transition from secular to non-secular hyperfine couplings with decreasing magnetic field, leading to faster decoherence, and are thus an important precursor to the spin-echo behaviour to be discussed in section 12.6.2.

Figure 12.11 shows the variation of the FID envelope with the strength of the axial background magnetic field, B_0, determined numerically, using a typical realisation for the spin bath distribution. From this, we see a monotonic increase of the FID time, T_2^*, with increasing B_0, which results in the transition of the effective hyperfine coupling strength from A to A_z, as detailed in section 12.3.2. For magnetic fields of $100\,\mathrm{G} < B_0 < 1000\,\mathrm{G}$, we observe what is essentially a hybrid regime, in which the decoherence envelope looks like that of the pure ZS and SZ regimes for times above and below the Larmor period, $T_\omega \sim 2\pi/\gamma_\mathrm{E} B_0$ respectively. This can be understood by recalling that spins in the SZ regime are those closest to the NV centre ($R \lesssim a/\omega$), and are thus responsible for the short time evolution of the NV spin. This contribution saturates beyond the Larmor period however, from which point onward, where the remaining time evolution is governed by the weaker coupling to spins in the ZS regime.

Using equation 12.6.3, the leading order behaviour of the FID decoherence functions in the ZS and SZ regimes (equations 12.3.23 and 12.3.24) is given by

$$\begin{aligned} \langle \Lambda_\mathrm{ZS} \rangle &\sim \left\langle 2\sin^2\left(\frac{A_z t}{4}\right)\right\rangle, \\ \langle \Lambda_\mathrm{SZ} \rangle &\sim \left\langle 2\sin^2\left(\frac{A t}{4}\right)\right\rangle, \end{aligned} \tag{12.6.5}$$

respectively.

FID at high magnetic fields (ZS)

For magnetic fields greater than $\sim 1000\,\mathrm{G}$, every environmental spin will be in a regime where the Zeeman coupling is greater than the hyperfine coupling to the NV spin (SZ). To visualise the FID behaviour in this regime, we firstly employ a numerical cluster expansion method (to zeroth order, since nuclear-nuclear interactions are not

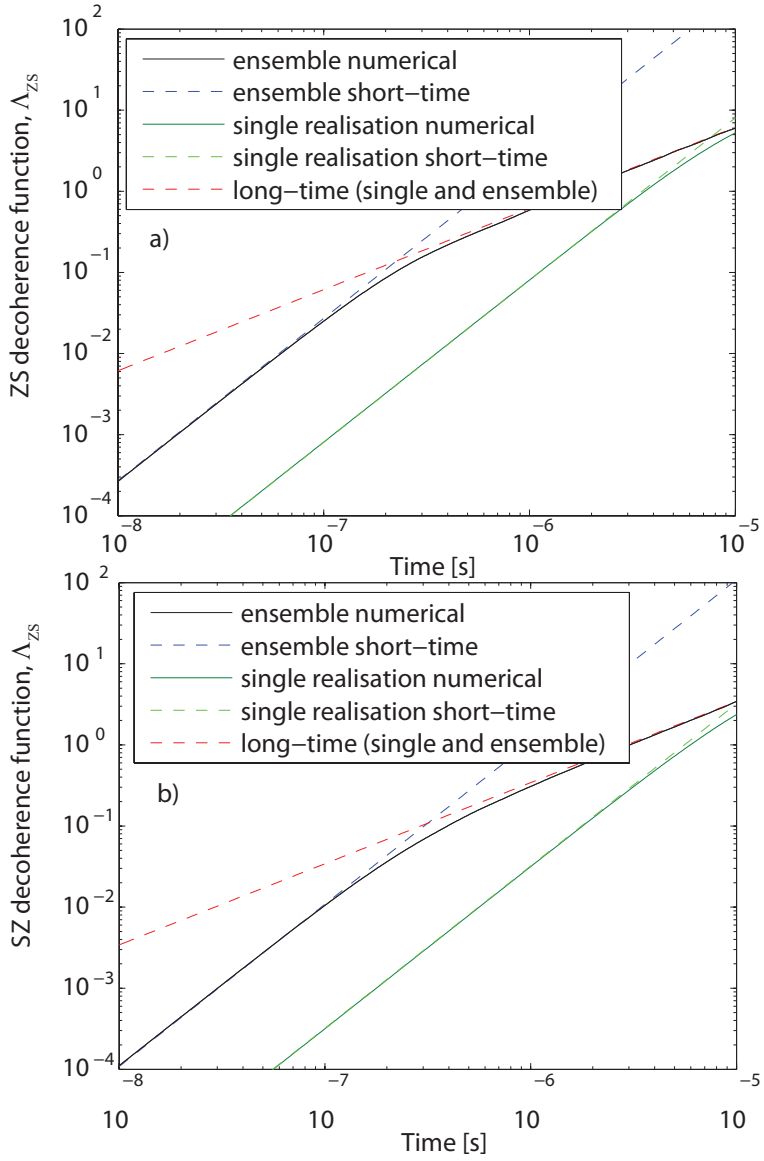

Figure 12.12: (a) Plot showing the behaviour of the FID decoherence function in the high field (ZS) regime, $\langle \Lambda_{ZS} \rangle$. The solid black curve shows the numerical calculation over 10^6 of the nuclear spin distribution, and the blue and red dashed curves depict the short/quadratic and long/linear analytic limits (see main text). The solid green curve shows the behaviour of a single realisation of the nuclear spin distribution, with the green dashed line showing the quadratic short time behaviour, that persists for times beyond T_2^*. The long-time limit of the single realisation behaviour is identical to that of the ensemble case. (b) As in (a), but for the low field (SZ) regime.

important), from which an ensemble average is performed over some 10^6 realisation of the environmental spin distribution. The resulting ensemble averaged decoherence function, $\langle \Lambda_{\mathrm{ZS}} \rangle$ is plotted in figure 12.12(a). From this, we can see a linear scaling of the decoherence function for times approaching the FID time, T_2^* (where $\langle \Lambda_{\mathrm{ZS}} \rangle \sim 1$) and beyond, however a quadratic scaling is shown for times much shorter than this. Furthermore, the quadratic scaling is shown to persist for much longer in the case of individual realisations than for the ensemble averaged function. The analytic origins of these features are discussed in what follows.

To obtain the ensemble-averaged behaviour we must integrate over all possible outcomes of the environmental impurity distribution, which means that all lattice sites will be populated with equal likelihood. The long time behaviour arises from the low-frequency ($\sim 1/T_2^*$) contributions to $\langle \Lambda_{\mathrm{ZS}} \rangle$, corresponding to spins more than a few lattice sites (roughly a nanometre) away from the NV, where the distribution effectively constitutes a continuum. The short-time behaviour, however, arises from spins that occupy the lattice sites surrounding the NV, where the bond-length of the diamond lattice, l, is important, ie on timescales of $T_{\mathrm{d}} = l^3/a \approx 50\,\mathrm{ns}$. These features may be reproduced by integrating Λ_{ZS} over R from the diamond bond length, l, to ∞, and over Θ from 0 to π (see Appendix B.3.1 for details). In the long time limit, where $t \gg t_d$, we find

$$\langle \Lambda_{\mathrm{ZS}} \rangle \Big|_{t \sim T_2^*} = \frac{4\pi^2}{9\sqrt{3}}\, ant, \tag{12.6.6}$$

showing a linear exponential free induction decay,

$$\langle L_{\mathrm{ZS}} \rangle = \exp\left(-\frac{t}{T_2^*}\right), \tag{12.6.7}$$

where the free induction decay time is $T_2^* = \frac{9\sqrt{3}}{4\pi^2 an} = 2.92\,\mu\mathrm{s}$. For times shorter than

T_{d}, we find a quadratic scaling in the decoherence function, given by

$$\begin{aligned} \langle \Lambda_{\mathrm{ZS}} \rangle \Big|_{0<t\ll T_2^*} &\sim \frac{2\pi a^2 n t^2}{15 l^3} \\ &= \left(\frac{t}{960\, ns} \right)^2 . \end{aligned} \tag{12.6.8}$$

Both the long and short-time analytic scalings are plotted together with the numerical results in figure, 12.12(a), showing excellent agreement.

Whilst this analysis accurately reproduces the experimental results for FID experiments conducted on NV ensembles (see, for example, reference [DFAH08]), experiments conducted on single NV centres exhibit a Gaussian shaped decay that typically persists as long as T_2^*. To reproduce this behaviour, we instead integrate $\langle \Lambda_{\mathrm{ZS}} \rangle$ from R_0 to ∞, as we would expect to find less than one impurity within a radius of R_0 from the NV centre. Following the same steps as in the ensemble case above, we find an initial quadratic scaling of

$$\begin{aligned} \langle \Lambda_{\mathrm{ZS}} \rangle \Big|_{t\sim T_2^*}^{(\mathrm{single})} &= \frac{8}{45} \pi^2 a^2 n^2 t^2 \\ &= \left(\frac{t}{5.58\, \mu \mathrm{s}} \right)^2 , \end{aligned} \tag{12.6.9}$$

followed by the same linear scaling as detailed in equation 12.6.6. The crossover point of these two regimes occurs at $t = 5/\left[2\sqrt{3} a n\right] \approx 11\, \mu$s, which is well past the point at which decoherence has occurred, showing that the FID behaviour of a single NV centre spin is dominated by a Gaussian decay.

FID at low magnetic fields (SZ)

Following on from the high-field limit of the previous section, we now move on to discussing the FID behaviour in the low field limit, the numerical result for which is

shown in figure 12.12(b). This analysis is performed in an identical manner, save for the replacement of $A_z \mapsto A$, as dictated by equation 12.6.5. This leads to a slight increase in the FID rate but qualitatively identical behaviour as the ZS regime. For the long-time limit, we obtain

$$\langle \Lambda_{\mathrm{SZ}} \rangle \Big|_{t \sim T_2^*} = \frac{\pi^2}{18} \left[6 + \sqrt{3} \operatorname{arcosh}(2) \right] ant, \tag{12.6.10}$$

again showing a linear exponential free induction decay, where the free induction decay time is now $T_2^* = 18/\left[\pi^2 an \left(6 + \sqrt{3}\cosh^{-1}(2)\right)\right] = 1.63\,\mu$s. For times shorter than t_d, we again see a quadratic scaling in the decoherence function, given by

$$\begin{aligned} \langle \Lambda_{\mathrm{SZ}} \rangle \Big|_{0 < t \ll T_2^*} &\sim \frac{\pi a^2 n t^2}{3 l^3} \\ &= \left(\frac{t}{607\, ns} \right)^2 . \end{aligned} \tag{12.6.11}$$

Finally, for the case of a typical single realisation of the SZ spin bath distribution, we find,

$$\begin{aligned} \langle \Lambda_{\mathrm{SZ}} \rangle \Big|^{(\mathrm{single})}_{t \sim T_2^*} &= \frac{4}{9} \pi^2 a^2 n^2 t^2 \\ &= \left(\frac{t}{3.53\,\mu\mathrm{s}} \right)^2 . \end{aligned} \tag{12.6.12}$$

Both the long and short-time analytic scalings are plotted together with the numerical results in figure, 12.12(b), showing excellent agreement.

It is interesting to note that in the single-realisation case, taking the ratio of the FID times for the high and low field cases gives

$$\frac{T^*_{2,\mathrm{ZS}}}{T^*_{2,\mathrm{SZ}}} = \sqrt{\frac{5}{2}} \approx 1.58, \tag{12.6.13}$$

in agreement with the results of reference [MDW$^+$12], whereas for the ensemble case we have

$$\frac{T^*_{2,\mathrm{ZS}}}{T^*_{2,\mathrm{SZ}}} = \frac{3}{8}\left[2\sqrt{3}+\cosh^{-1}(2)\right] \approx 1.80, \tag{12.6.14}$$

showing the ensemble FID times experience a greater enhancement from an increased magnetic field strength than those of a single realisation of the bath impurity distribution.

12.6.2 Spin-echo decoherence

We now move on to consideration of the spin-echo decoherence due to all spin clusters in the environment. Using equation 12.6.3, the leading order behaviour of the decoherence functions for the ZSE, SZE and SEZ regimes are given by

$$\begin{aligned}
\langle \Lambda_{\mathrm{ZSE}} \rangle &\sim \left\langle \sin^2\left(\frac{Bt}{4}\right)\sin^2\left(\frac{\Delta_z}{4}t\right)\right\rangle, \\
\langle \Lambda_{\mathrm{SZE}} \rangle &\sim \left\langle \sin^2\left(\frac{Bt}{4}\right)\sin^2\left(\frac{\Delta}{4}\,t\right)\right\rangle, \\
\langle \Lambda_{\mathrm{SEZ}} \rangle &\sim \left\langle \frac{8}{15}\sin^2\left(\frac{3Bt}{4}\right)\left[\sin^2\left(\frac{At}{2}\right)+\sin^2\left(\frac{At}{4}\right)\right]\right\rangle,
\end{aligned} \tag{12.6.15}$$

respectively.

Spin echo decay at high magnetic fields (ZSE)

At magnetic fields in excess of a few hundred Gauss, every ^{13}C nuclear spin exists in the ZSE regime. Thus, to compute the ensemble averaged decoherence function for the high field case, we integrate Λ_{ZSE} over the spatial distributions of the environmental spins. A numerical calculation using the cluster expansion method to 7^{th} order over

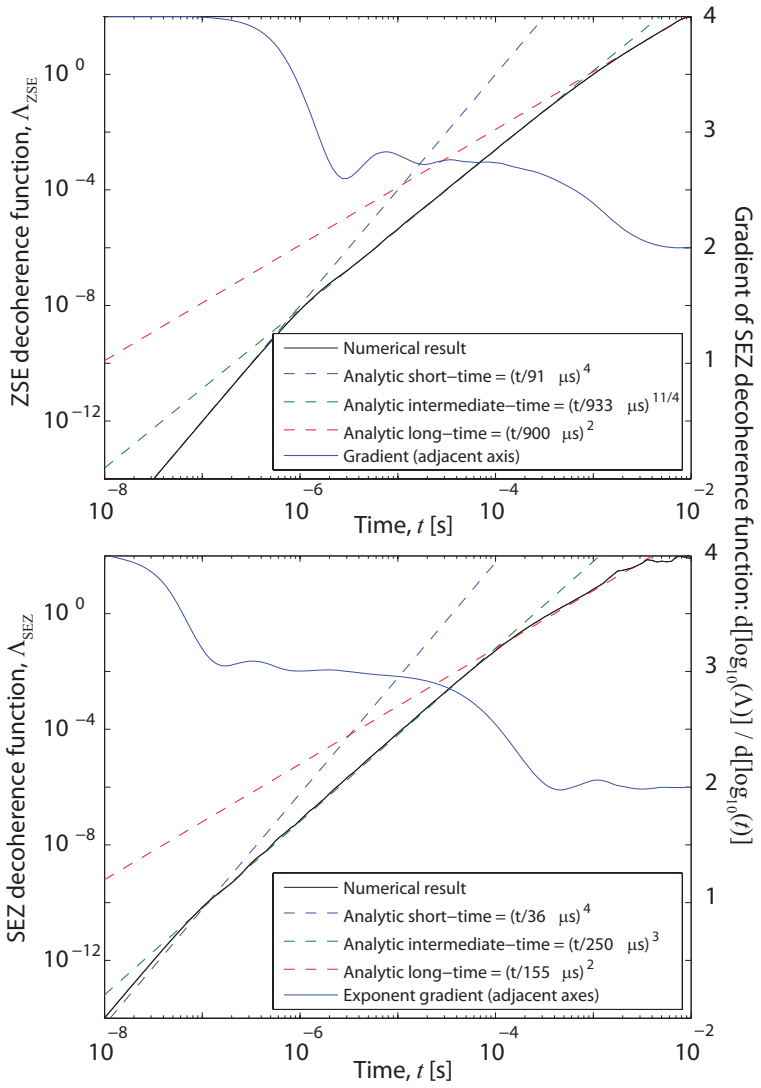

Figure 12.13: Plot showing the agreement between numerical and analytic results for the decoherence of an NV centre spin in a 1.1% ^{13}C nuclear spin bath. (a) Results for the ZSE regime. The black curve shows the numerical result for $\langle \Lambda_{\mathrm{ZSE}} \rangle$ computed using a 7$^{\mathrm{th}}$ order cluster expansion method averaged over 10^6 realisations of the surrounding impurity distribution. Analytic results for the short, intermediate and long-time scalings are given by the blue, green and red dashed curves respectively. The scaling exponent, found by numerically computing $k = \mathrm{d}\left[\ln\left(\langle \Lambda_{\mathrm{ZSE}} \rangle\right)\right] / \mathrm{d}\left[\ln\left(t\right)\right]$ is plotted as the blue solid curve (adjacent axis), and shows the transition from 4 to 2.75 to 2, as consistent with the analytic results. (b) As in (a) but for the SEZ regime.

10^6 realisations of the impurity distribution is shown in figure 12.13 (a), from which we see a number of complex features. In particular, the scaling of Λ_{ZSE} with t changes significantly between $t = 0.1$ and 1 ms from $\Lambda_{\mathrm{ZSE}} \sim \mathcal{O}\left(t^{2.75}\right)$ to $\Lambda_{\mathrm{ZSE}} \sim \mathcal{O}\left(t^2\right)$. At very short times, where $t \ll T_2^*$, we find $\Lambda_{\mathrm{ZSE}} \sim \mathcal{O}\left(t^4\right)$. The analytic origins of scaling are discussed in what follows.

We initially consider the long-time limit, where the decoherence function exhibits a quadratic scaling. Since dipolar interactions on these timescales correspond to impurity separations of 0.3 nm, enclosing some 28 lattice sites, the environmental distribution essentially resembles a continuum in which spin impurities may adopt any position within the lattice. Such timescales are still much shorter than the environmental correlation time however, meaning that we may expand Δ_z for small r, giving

$$\begin{aligned}\Delta_z &\sim \frac{3ar}{R^4}\Big[\sin(\theta)\sin(\Theta)\left(1-5\cos^2(\Theta)\right)\cos(\phi-\Phi) \\ &\qquad + \cos(\theta)\cos(\Theta)\left(3-5\cos^2(\Theta)\right)\Big] \\ &\equiv \frac{a_\alpha r}{R^4}. \end{aligned} \tag{12.6.16}$$

Integration of Λ_{ZSE} over $0 \leq r,\, R \leq \infty$ yields (see appendix B.3.2 for details)

$$\left\langle \Lambda_{\mathrm{ZSE}} \right\rangle \Big|_{t\sim T_2} \sim \pi\, (ant)^{3/4}\,(bnt)^{5/4}, \tag{12.6.17}$$

giving a spin-echo coherence time of

$$T_2^{\mathrm{ZSE}} = \left[\pi\, (an)^{3/4}\,(bn)^{5/4}\right]^{-1/2} = 900\,\mu\mathrm{s}, \tag{12.6.18}$$

in excellent agreement with the numerical results of [ZHL12].

Prior to this quadratic scaling, Λ_{ZSE} exhibits a scaling of $\sim \mathcal{O}\left(t^{11/4}\right)$, which, as we detail below, is the result of spin impurities only being able to adopt discreet

positions within the lattice. Such effects become important at short timescales, where the correspondingly small separation distances begin to approach the atomic spacing in the crystal. We can reproduce the effect of this spacing by choosing a lower cutoff for r of the diamond bond length, $l = 1.54\,\text{Å}$. We note that the integral of Λ_{ZSE} over r is intractable for arbitrary integration terminals, however we may integrate from 0 to ∞ as above, and subtract the contribution 0 to l by expanding the integrand for small r as follows (see appendix B.3.2 for details),

$$\begin{aligned} \langle \Lambda_{\text{ZSE}} \rangle \Big|_{T_2^* < t \ll T_2} &\sim \frac{a^{3/4} b^2 n^2 t^{11/4}}{l^{9/4}} \\ &= \left(\frac{t}{933\,\mu\text{s}} \right)^{11/4}. \end{aligned} \tag{12.6.19}$$

This expression shows perfect agreement with the numerical calculation in terms of both scaling and magnitude, as depicted in figure 12.13. At longer timescales, the magnitude of $\langle \Lambda_{\text{ZSE}} \rangle$ becomes much larger than the discreet correction term, and we simply recover the expression given in equation 12.6.18. This is to be expected: at long timescales, dipole-dipole interactions from spin impurities occupying adjacent sites essentially average out due to their high-frequency behaviour, whereas the more long range interactions become important. As the separation distance increases, the number of sites available for occupation essentially approaches that of a continuum.

Finally, to deduce the short-time quartic scaling, we again integrate over R and r from l to ∞, and and compute the formal short-time expansion, valid for $t : at/l^3 \ll 1$ and $bt/l^3 \ll 1$. As the smallest possible separation distance is l, we are only justified in making this expansion for $t < 50\,\text{ns}$ in the ensemble case. The resulting expression

is, to leading order (see appendix B.3.2 for details),

$$\begin{aligned}\langle\Lambda_{\mathrm{ZSE}}\rangle\Big|_{t\ll T_2^*} &= \frac{1}{80}\left(\frac{\pi nabt^2}{l^3}\right)^2\left[1-\frac{\sqrt[6]{3}\pi l\,(4\pi n)^{1/3}}{360\Gamma\left(\frac{4}{3}\right)}\right] \\ &= \left(\frac{t}{91\,\mu\mathrm{s}}\right)^4. \end{aligned} \tag{12.6.20}$$

We note that some variation will exist between individual realisations of the impurity distribution, as most NV centres will not have spin impurities on adjacent lattice sites, meaning that the quartic scaling may persist for longer than in the ensemble case. To show this, we instead perform the R integral from a lower cutoff, $R_0 = [3/(4\pi n)]^{(1/3)}$, defining the radius of a spherical volume in which we would expect to find less than one impurity on average for the ensemble case, meaning we would not expect impurities at distances closer than this in most individual cases. On the other hand, even the case of an individual distribution involves the NV coupling to many clusters, hence there is a large enough sampling of possible cluster configurations to justify an average over these configurations. Integrating $\langle\Lambda_{\mathrm{ZSE}}\rangle$ over R from R_0 to ∞, and over r from l to ∞, we find

$$\begin{aligned}\langle\Lambda_{\mathrm{ZSE}}\rangle\Big|^{(\mathrm{single})}_{t\ll T_2^*} &= \frac{1}{90}\pi^4a^2b^2n^4t^4\left(\frac{\sqrt[3]{6}}{l(\pi n)^{1/3}}-\frac{4\sqrt{3}\pi}{9\Gamma\left(\frac{4}{3}\right)}\right) \\ &= \left(\frac{t}{393\,\mu\mathrm{s}}\right)^4, \end{aligned} \tag{12.6.21}$$

again showing a quartic scaling of $\langle\Lambda_{\mathrm{ZSE}}\rangle$ with t, but one that persists for some 10-100 μs, as opposed to the 50 ns for the ensemble case.

Spin echo decay at moderate magnetic fields (SZE)

At magnetic fields between 0.01 G and 100 G, every ^{13}C nuclear spin exists in the SZE regime. The procedure to compute the ensemble averaged decoherence function

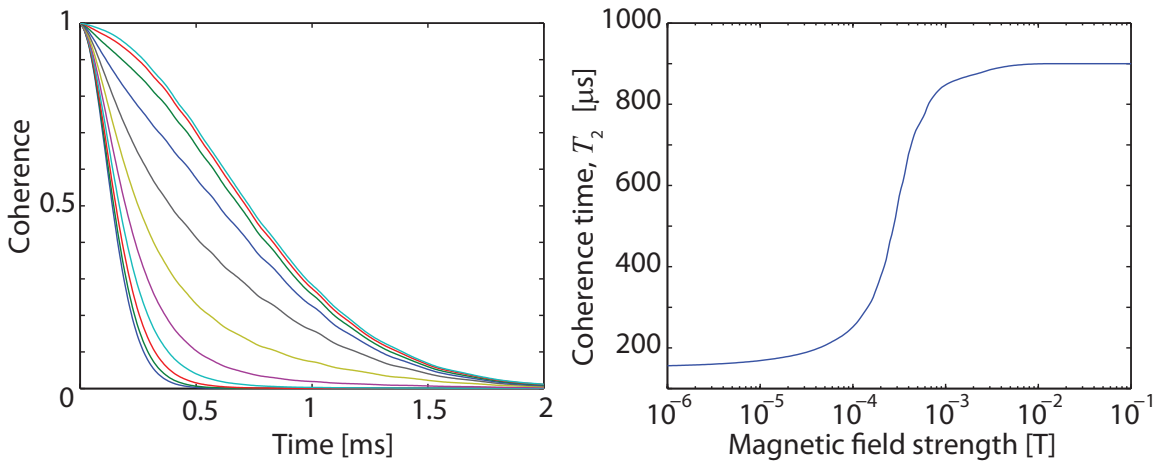

Figure 12.14: Magnetic field dependence of the NV spin coherence time. (a) Coherence envelopes of an NV centre coupled to a naturally occurring 1.1 % ^{13}C nuclear spin bath corresponding to external magnetic field strengths from 10 μT to 10 mT. (b) Plot showing the dependence of the coherence time on the strength of an external magnetic field.

is the same as for that above, however, we simply make the substitution $\Delta_z \mapsto \Delta$, leading to what is essentially a redefinition of a_α:

$$a_\alpha \mapsto \frac{1}{\sqrt{3\cos^2(\Theta)+1}}\Big(4\cos(\theta)\cos^3(\Theta) + \sin(\theta)\left[2\sin(\Theta)+\sin(3\Theta)\right]\cos(\phi-\Phi)\Big). \tag{12.6.22}$$

All subsequent results scale accordingly, the most important of which is $T_2^{\mathrm{SZE}} = 780\,\mu$s. Other notable properties that emerge in this regime are the electron spin-echo envelope modulation (ESEEM) peaks, which manifest as periodic decays and revivals at half the Larmor frequency of the NV. As these effects do not represent any true decoherence, we defer their discussion until section 12.6.2.

Spin echo decay at low magnetic fields (SEZ)

At magnetic fields below 0.01 G, every ^{13}C nuclear spin exists in the SEZ regime. The transition of the fluctuation amplitude from Δ to A effectively decouples the S-E from the E-E evolution in Λ_{SEZ}, drastically changing the nature of the resulting decoherence. This allows for a convenient separation of the contribution of the hyperfine and dipolar coupling to the overall decoherence. A calculation of the decoherence function using a numerical cluster expansion to 7^{th} order is shown in figure 12.13 (b) for 10^6 realisations of the impurity distribution, from which a number of features are evident. As with the ZSE and SZE regimes, we see quartic and quadratic scalings at short and long times respectively, but in contrast to the other regimes, we see a cubic scaling at intermediate times. Furthermore, the coherence times exhibited by the SEZ regime are effectively an order of magnitude shorter than the other two regimes. The analytic origins of these features are explained in what follows.

As with the ZSE and SZE cases, we begin with the consideration of the long time dynamics of the SEZ regime. As before we need not worry about the discretised lattice at these timescales, and we therefore integrate Λ_{SEZ} over both R and r from 0 to ∞ (see Appendix B.3.2 for details), giving

$$\begin{aligned} \left\langle \Lambda_{\mathrm{SEZ}} \right\rangle \Big|_{t\sim T_2} &\sim \frac{2}{15}\, ab \left(\pi^2 nt\right)^2 \\ &= \left(\frac{t}{155\,\mu\mathrm{s}}\right)^2 \end{aligned} \tag{12.6.23}$$

Again, we see an overall Gaussian behaviour at long timescales, but a very different dependence on the hyperfine and dipolar dynamics of the environment ($\Gamma_{\mathrm{ZSE,SZE}} \sim a^{3/4}b^{5/4}$ vs. $\Gamma_{\mathrm{SEZ}} \sim ab$). This is a consequence of the changes in behavior of the environmental autocorrelation function as the environment transitions from secular

to non secular dynamics. The corresponding coherence time of the SEZ regime is $T_2^{\mathrm{SEZ}} = 155\,\mu\mathrm{s}$.

To derive the intermediate cubic scaling of $\langle \Lambda_{\mathrm{SEZ}} \rangle$, we note that, as was the case with $\langle \Lambda_{\mathrm{ZSE}} \rangle$ and $\langle \Lambda_{\mathrm{SZE}} \rangle$, the integral of $\sin^2\left(\frac{3Bt}{4}\right)$ over the cluster size distribution (equation 12.4.3) from l to ∞ has no closed form. As such, we simply expand $\mathrm{P}(r)$ for small r, as detailed in Appendix B.3.2, giving

$$\begin{aligned} \langle \Lambda_{\mathrm{SEZ}} \rangle_{T_2^* < t \ll T_2} &\sim \frac{\pi^3 a b^2 n^2 t^3 \left[2(4\gamma - 5)\pi l^3 n + 3\right]}{15 l^3} \\ &= \left(\frac{t}{250\,\mu\mathrm{s}}\right)^3 . \end{aligned} \tag{12.6.24}$$

To determine the short time scaling, we again integrate Λ_{SEZ} over R and r from l to ∞, and use the same short-time expansion as employed in the ZSE case. As the smallest possible separation distance is l, we are only justified in making this expansion for $t < 50\,\mathrm{ns}$ in the ensemble case. The resulting expression is, to leading order (see appendix B.3.2 for details), yielding an initially quartic dependence on time, given by

$$\begin{aligned} \langle \Lambda_{\mathrm{SEZ}} \rangle \Big|_{t < T_2^*} &\sim \frac{5}{48} \left(\frac{\pi a b n t^2}{l^3}\right)^2 \left[2(4\gamma - 5)\pi l^3 n + 3\right] \\ &= \left(\frac{t}{36\,\mu\mathrm{s}}\right)^4 , \end{aligned} \tag{12.6.25}$$

where $\gamma \approx 0.577$ is the Euler-Mascheroni constant.

Full magnetic field dependence

We now consider the full magnetic field dependence of the coherence time of an NV centre exposed to a 1.1% ^{13}C nuclear spin bath. The full spin echo envelope is the product of contributions from the 6 parameter regimes, with the dominant contribution coming from the ZSE, SZE and SEZ regimes, $S_{\mathrm{C13}} \approx S_{\mathrm{ZSE}} S_{\mathrm{SZE}} S_{\mathrm{SEZ}}$, which

implies the full decoherence function is given by the sum of decoherence functions due to each region,

$$\left\langle \Lambda_{\mathrm{C13}} \right\rangle \;=\; \left\langle \Lambda_{\mathrm{ZSE}} \right\rangle_{r>r_{\mathrm{Z}}}^{R>R_{\mathrm{Z}}} + \left\langle \Lambda_{\mathrm{SZE}} \right\rangle_{r>r_{\mathrm{Z}}}^{R<R_{\mathrm{Z}}} + \left\langle \Lambda_{\mathrm{SEZ}} \right\rangle_{r<r_{\mathrm{Z}}}^{R<R_{\mathrm{Z}}},$$

where the R_z and r_z quantities denote the Zeeman dependent integration domains in $r - R$ space.

Figure 12.14(a) shows gradual transition of the decoherence envelopes from the SEZ regime through to the ZSE regime with increasing magnetic field. The full dependence of the corresponding coherence times, T_2, is shown in figure 12.14(b), where we see that coherence times of an NV spin coupled to the naturally occurring 1.1% ^{13}C nuclear spin bath can be almost 1 ms for magnetic fields in excess of 100 G. Our results show excellent agreement with the extensive numerical investigation conducted in reference [ZHL12]. The persistent Gaussian shape predicted by our theory is a radical departure from currently accepted theories in the literature claiming either a $\Lambda \sim (t/T_2)^3$ and $\Lambda \sim (t/T_2)^4$ dependence irrespective of the physical origin of the spin bath. We have shown here that the former is not valid for the case of an NV centre immersed in a ^{13}C nuclear spin bath, except where spin densities are well below those currently realised experimentally. The latter is only valid in the short time limit, and may be explained as follows.

Analysis of the electron spin echo envelope modulation (ESEEM)

One of the key features observed in experiments conducted on NV spins in ultra-pure diamond is the emergence of decays and revivals in the spin-echo envelope at half the Larmor frequency of the ^{13}C spins, an effect referred to as electron spin echo envelope modulation, or ESEEM. To this point we have only concerned ourselves with the

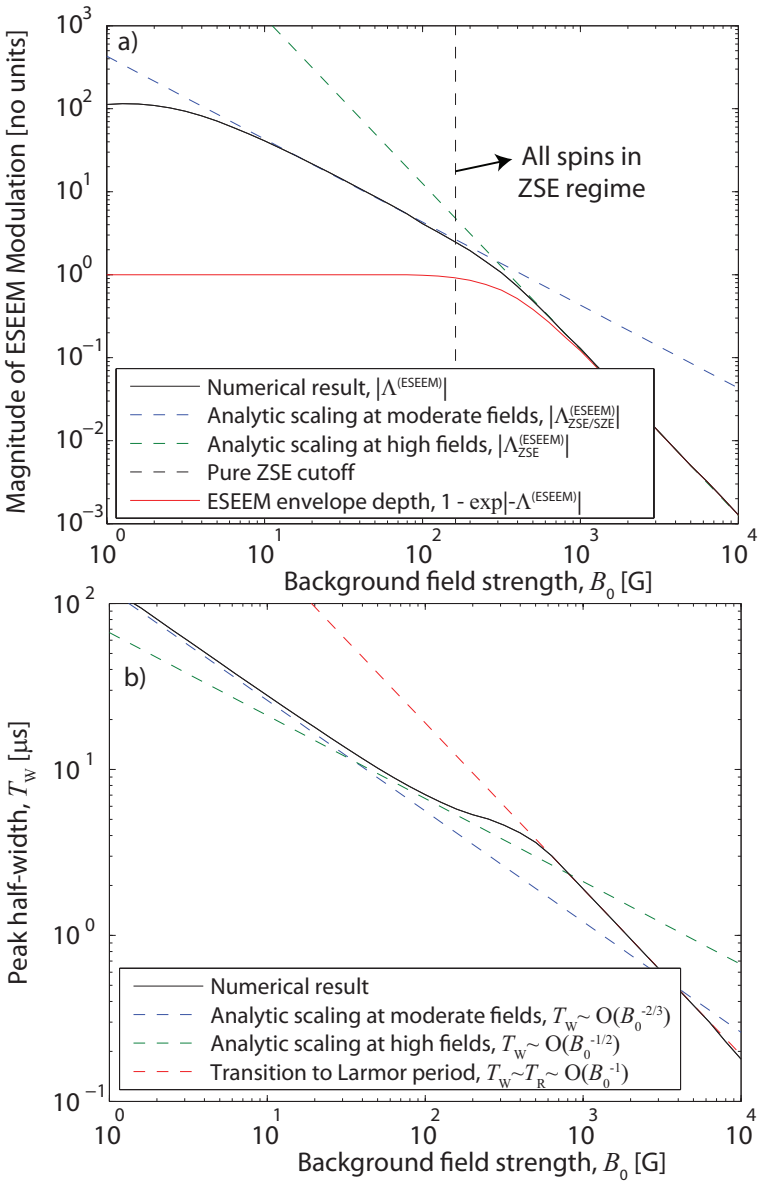

Figure 12.15: Magnetic field dependence of ESEEM features. (a) Plot detailing the magnitude of the modulation of the decoherence function. The numerical result is plotted in black, whereas the moderate and high field analytic limits are plotted in blue and green respectively. The saturation of the numerical result at low fields arises because the revival rate has decreased below the decoherence rate, which also saturates at low field. The red curve shows the magnitude of the corresponding spin-echo envelope contrast due to ESEEM, $1-L=1-\exp\left(-\Lambda^{(\mathrm{ESEEM})}\right)$, which saturates at unity when the decoherence function is greater than unity. (b) Plot detailing the dependence of the width of the ESEEM peaks on the magnetic field strength. The numerical result is plotted in black, and the low, moderate and high field analytic results are plotted in blue, green and red respectively. In the case of the high field result, the decay depth is less than unity, hence the width of the peaks is defined by the revival period instead of their decay time.

decoherence arising from flip-flop processes in the bath and have ignored the ESEEM contribution to the evolution. In this section, we analyse this effect and show how resulting properties such as the revival frequency, decay depth and revival peak width depend on the background magnetic field strength. For background field strengths below approximately $B_0 = 1\,G$, the revival frequency, $\omega_{\rm R} = \frac{1}{2}\gamma_c B_0 = 1.75\,{\rm kHz}$, is lower than the decoherence rate. As such, the notion of a decay depth no longer makes sense, as there will be no subsequent revival before decoherence has occurred. In the following, we derive the analytic origins of these scalings.

Where the oscillations in the FID envelope occured at the Larmor frequency, ω_0, the revival frequency during a spin-echo sequence is one half of the Larmor frequency, $\omega_{\rm R} = \frac{1}{2}\gamma_{\rm E} B_0 = 17.5\,{\rm MHz\,T^{-1}}\,B_0$. Some broadening of this effect will occur due to the distribution of axial dipolar couplings in the bath, leading to a perceived increase in the decoherence rate, however this effect will be addressed in the following section.

Next we detail the dependence of the depth of the decay valleys on the magnetic field strength. A numerical calculation of the maximum amplitude of the ESEEM component of the decoherence function, $\left|\Lambda^{(\rm ESSEM)}(t)\right|_{\rm max}$ is plotted in figure 12.15 (a). From this, we see that the decay depths scale with the inverse-square of the magnetic field strength at high fields, but only with the inverse at moderate field strengths.

Recall from equations 12.3.26 that in the ZSE limit, the ESEEM correction to $\Lambda_{\rm ZSE}$ due to a single nuclear spin is given by

$$\Lambda_{\rm ZSE}^{(\rm ESEEM)} \;=\; 4\frac{A_x^2 + A_y^2}{\omega^2}\sin^2\left[(A_z+\omega)\,\frac{t}{4}\right]\sin^2\left(\frac{t\omega}{4}\right). \qquad (12.6.26)$$

As this correction has been calculated in the $\omega \gg A$ limit, we must distinguish between cases where all spins are in the ZSE regime; and cases where distant spins from the NV are in the ZSE regime, but closer spins are in the SZE regime due to

their dominant hyperfine interaction. For the former case, we have that the Zeeman coupling is greater than the most strongly coupled nuclear spin (ie where $B_0 > 162\,\mathrm{G}$), giving

$$\begin{aligned}\left|\Lambda_{\mathrm{ZSE}}^{(\mathrm{ESEEM})}\right|_{\max} &= -4\left\langle\frac{A_x^2+A_y^2}{\omega^2}\right\rangle \\ &= -\frac{2}{15}\left(8\pi\frac{an}{\omega}\right)^2 \\ &= -\left(\frac{354\,\mathrm{G}}{B_0}\right)^2, \end{aligned} \tag{12.6.27}$$

thus reproducing the $\sim \mathcal{O}\left(B_0^{-2}\right)$ scaling of the numerical result, as plotted in figure 12.15 (a).

For the case where the field strength is low enough to have spins in both the ZSE and SZE regimes, we must determine the contribution from both. The ZSE contribution to the decay may be determined by integrating equation 12.6.26 over only the spins in this regime. To determine the SZE contribution, we expand the ESEEM terms for $\omega \ll A$ as given in equation 12.3.27,

$$\begin{aligned}\Lambda_{\mathrm{SZE}}^{(\mathrm{ESEEM})} &= 4\frac{A_{x,1}^2+A_{y,1}^2}{A_1^2}\left[1-\frac{2\omega A_{z,1}}{A_1^2}\right] \\ &\quad\times\sin^2\left(\frac{t\lambda_1}{4}\right)\sin^2\left(\frac{t\omega}{4}\right), \end{aligned} \tag{12.6.28}$$

and integrate over only the spins in the SZE regime. The sum of these two contributions gives

$$\begin{aligned}\left|\Lambda_{\mathrm{ZSE/SZE}}^{(\mathrm{ESEEM})}\right|_{\max} &= \frac{32\pi an}{5\omega}+\frac{448\pi\left(5\sqrt{3}\pi-27\right)an}{135\omega} \\ &= \frac{860\,\mathrm{G}}{B_0}, \end{aligned} \tag{12.6.29}$$

again in agreement with the numerical result (see figure 12.15 (a)).

Finally, we analyse the dependence of the decay widths, T_{w} on the magnetic field. The numerical results in plotted in figure 12.15 (b) show these width to scale as $T_{\mathrm{w}} \sim$

$B_0^{-0.67}$ at moderate fields, as consistent with the scaling of $B_0^{-0.63}$ in the numerical results of reference [ZHL12]. At high fields, our numerical results show a slight change in this scaling for a brief period, with $T_{\mathrm{w}} \sim B_0^{-1/2}$. If the magnetic field is increased further, the decay depths will be less than unity (see figure 12.15 (a)), meaning the widths will be effectively characterised by half the revival period, $T_{\mathrm{W}} \sim \frac{1}{2}T_{\mathrm{R}}$, showing an inverse linear dependence on the magnetic field strength, again consistent with the numerical results. We do not consider the low field regimes, as revivals are not visible prior to the onset of decoherence. The analytic origins of these results are discussed in the following.

In the high field (ZSE) limit, we expand equation 12.6.26 about any of the revival peaks, giving

$$\begin{aligned} \left\langle \Lambda_{\mathrm{ZSE}}^{(\mathrm{ESEEM})} \right\rangle &= \left\langle \frac{1}{64} t^4 \left({A_{x,1}}^2 + {A_{y,1}}^2 \right) (A_{z,1} + \omega)^2 \right\rangle \\ &\sim \frac{1}{30} \pi^2 a^2 n^2 t^4 \omega^2, \end{aligned} \tag{12.6.30}$$

giving a decay width of $T_{\mathrm{W}} = 61\,\mu\mathrm{s}\,\mathrm{G}^{1/2}/\sqrt{B_0}$

To find the decay widths at low fields, we integrate equation 12.6.28. This puts us in a regime where $\omega \ll an$, meaning we must integrate the resulting expression over $\mathbf{R}$, and then expand for $1/an \ll t \ll 1/\omega$, giving

$$\begin{aligned} \left\langle \Lambda_{\mathrm{SZE}}^{(\mathrm{ESEEM})} \right\rangle &= \left\langle \frac{\omega^2 t^2 \left({A_{x,1}}^2 + {A_{y,1}}^2 \right) \sin^2\left(\frac{1}{4} A_1 t\right)}{4 A_1^2} \right\rangle \\ &\sim \frac{1}{192} \pi^2 a n t^3 \omega^2 \left(18 - 5\sqrt{3} \cosh^{-1}(2) \right), \end{aligned}$$

showing the revival peaks to have a cubic shape. The resulting peak width is then

$$T_{\mathrm{W}}^{(\mathrm{SZE})} = \frac{121\,\mu\mathrm{s}\,\mathrm{G}^{2/3}}{B_0^{2/3}}. \tag{12.6.31}$$

Whilst this result is consistent with both the numerical work of our own, and that of reference [ZHL12], it differs from the analysis given in reference [CDT$^+$06], which claims a quartic shape for the peaks, leading to a $T_{\mathrm{W}}^{(\mathrm{SZE})} \sim \mathcal{O}\left(B_0^{-1/2}\right)$ dependence at moderate fields. This analysis was performed using a short-time expansion with respect to both Zeeman and hyperfine couplings, however such an expansion is not valid in the SZE regime where short-time with respect to $T_{\mathrm{R}} \sim 1/\omega$ is still long compared with $T_2^* \sim 1/an$.

Additional dephasing due to inhomogeneous broadening of the nuclear Larmor frequency

In addition to the NV spin decoherence resulting from its entanglement with ^{13}C spins, and their subsequent mutual interaction, there will be a dephasing effect due to the broadening of the ^{13}C Larmor frequencies due to both their Zeeman interaction, and the distribution of their axial couplings to all other spins in the bath. Whilst this is technically not representative of any true decoherence process, it does nevertheless give the illusion of additional decoherence due to an increase in the spin-echo envelope decay rate.

To treat the 'background' coupling of a given nuclear spin to other nuclei outside its associated cluster, we note that the total axial frequency shift will be a sum over that due to a large number of spins. As such, we expect the Larmor frequency, ω_i, of a given spin to be normally distributed with mean ω_0, due to the background magnetic field, and variance σ, due to the axial couplings to all other spins in the bath,

$$\mathrm{P}\left(\omega\right) \quad = \quad \frac{1}{\sigma\sqrt{2\pi}} \exp\left(-\frac{\left(\omega-\omega_0\right)^2}{2\sigma^2}\right). \tag{12.6.32}$$

Of course, a given realisation of this distribution only applies for a snapshot in time,

however, it will only change on timescales of the order of T_{S} (see section 12.5), meaning that we can regard realisations of this distribution as being static on timescales of T_2 and shorter. Higher order corrections to this approximation can be made by employing the associated autocorrelation function of the bath spins, however there will be no resulting correction to leading order.

To show the additional dephasing effect of this broadening, we return to the ESEEM contribution to the ZSE regime, as detailed in equation 12.6.26. Integrating this expression over equation 12.6.32 with $1/\omega^2 \sim 1/\omega_0^2$, and noting that we may ignore terms like $\sin^2\left(\frac{\omega_0 t}{4}\right)$ since they do not contribute to the dephasing, we find the broadened ESEEM contribution to the ZSE regime to be

$$\int_{-\infty}^{\infty} \mathrm{P}(\omega)\Lambda_{\mathrm{ZSE}}^{(\mathrm{ESEEM})}\,\mathrm{d}\omega \;=\; 4\frac{A_x^2+A_y^2}{\omega^2}\left(\frac{\sigma t}{4}\right)^2 \sin^2\left(\frac{A_z t}{4}\right). \tag{12.6.33}$$

Summing over the hyperfine contribution from all spins as before, we find

$$\left\langle \Lambda_{\mathrm{ZSE}}^{(\mathrm{ESEEM})} \right\rangle \;=\; \frac{4\pi^2 a^2 n^2 t^2 \sigma^2}{15\omega_0^2}. \tag{12.6.34}$$

To evaluate σ^2, we integrate over all axial nuclear-nuclear couplings, giving

$$\begin{aligned} \sigma^2 &\sim \frac{64}{45}\pi^2 b^2 n^2, \\ &= (89\,\mathrm{Hz})^2 \end{aligned} \tag{12.6.35}$$

This gives an additional Gaussian contribution to the decoherence envelope, with a corresponding decay rate of

$$\Gamma_{\mathrm{ZSE}}^{\mathrm{ESEEM}} \;=\; \frac{3.1\,\mathrm{kHz\,G}}{B_0}, \tag{12.6.36}$$

showing a negligible contribution to the overall dephasing in the ZSE regime.

We apply the same approach to the ESSEM correction of the SZE decoherence function, as given in equation 12.6.28.

$$\int_{-\infty}^{\infty} \mathrm{P}(\omega)\Lambda_{\mathrm{SZE}}^{(\mathrm{ESEEM})}\,\mathrm{d}\omega \;=\; 4\frac{A_x^2+A_y^2}{A^2}\left(\frac{\sigma t}{4}\right)^2 \sin^2\left(\frac{At}{4}\right) \tag{12.6.37}$$

Again, summing over the hyperfine contribution from all spins as before, we find the resulting contribution to the full SZE decoherence function to be

$$\left\langle \Lambda_{\mathrm{SZE}}^{(\mathrm{ESEEM})} \right\rangle \;=\; \frac{\pi^2}{3} ant \left(\frac{\sigma t}{16}\right)^2 \left[18 - 5\sqrt{3}\mathrm{arcosh}(2)\right], \tag{12.6.38}$$

which gives an additional cubic contribution to the decoherence envelope, with a corresponding decay rate of

$$\Gamma_{\mathrm{SZE}}^{\mathrm{ESEEM}} \;=\; 448\,\mathrm{Hz}. \tag{12.6.39}$$

This additional cubic component of the decoherence function, despite not representing any true decoherence, gives a perceived reduction in the coherence time, reducing it slightly from $T_2^{\mathrm{SZE}} = 780\,\mu\mathrm{s}$ to $T_2^{\mathrm{SZE}} = 724\,\mu\mathrm{s}$. As couplings between distant nuclei are not accounted for, this effect is generally not observed in numerical simulations.

12.7 On the question of whether the quantum spin bath may be modeled as a classical magnetic field

In treating the influence of the surrounding spin bath on a central spin, one commonly adopted approach[dSD03a, dSD03b, TCC+08, HDF+08, DFHA09, HHCH10,

LWR$^+$10] is to replace the collective hyperfine field felt by the NV spin with a semi-classical magnetic field whose internal dynamics are dictated by the autocorrelation functions discussed above. This field, the operator of which is denoted $\mathcal{B}(t)$, will produce a time dependent Zeeman shift given by $\mathcal{H}_z = \vec{\mathcal{B}} \cdot \vec{\mathcal{S}} \equiv \mathcal{S}_z B(t)$ and a corresponding free-time evolution operator of

$$\mathcal{U}_f(t', t'') = e^{-i\phi(t',t'')}\big|1\big\rangle\big\langle 1\big| + \big|0\big\rangle\big\langle 0\big| \tag{12.7.1}$$

where $\phi(t', t'') = \int_{t'}^{t''} B(t)\, dt$. Such an approach is potentially problematic, as it ignores the effect of the hyperfine couplings on the evolution of the nuclei, which as we have shown, are a critical component of this evolution.

The time evolution operator for a spin echo experiment is

$$\mathcal{U} = \mathcal{U}_f(t/2, t)\mathcal{F}\mathcal{U}_f(0, t/2), \tag{12.7.2}$$

and for an arbitrary pulse sequence with pulses applied at $t_k = \{t_1, t_2, \ldots, t_n\}$, we have

$$\begin{aligned} \mathcal{U}(t) &= \mathcal{U}(t_n, t)\mathcal{F} \ldots \mathcal{F}\mathcal{U}(t_1, t_2)\mathcal{F}\mathcal{U}(0, t_1) \\ &\equiv e^{-i\phi_1}\big|1\big\rangle\big\langle 1\big| + e^{-i\phi_0}\big|0\big\rangle\big\langle 0\big|, \end{aligned} \tag{12.7.3}$$

where

$$\begin{aligned} \phi_1 &= \phi(0, t_1) + \phi(t_2, t_3) + \ldots, \\ \phi_0 &= \phi(t_1, t_2) + \phi(t_3, t_4) + \ldots \end{aligned} \tag{12.7.4}$$

are the accumulated phases of the $\big|1\big\rangle$ and $\big|0\big\rangle$ states respectively.

Using this semi-classical approach for an initial probe spin state of $|\psi_0\rangle = \frac{1}{\sqrt{2}}\big(|0\rangle +$

$|1\rangle\big)$, we find the in-plane projection of the magnetisation to be

$$\begin{aligned} L &= \mathrm{Tr}\left\{(\mathcal{S}_x + i\mathcal{S}_y)\,\mathcal{U}(t)\rho_0\mathcal{U}^\dagger(t)\right\} \\ &= \frac{1}{2}\exp\big[i\left(\phi_1^*(t) - \phi_0(t)\right)\big] \end{aligned}$$

This quantity is an average over the quantum degrees of freedom in the system, but we have not yet addressed the statistics of the field B. Firstly, we note that the amplitude of $B(t)$ at any given t is a sum over a large number of sources and is therefore normally distributed. Furthermore, at room temperature, thermal energies are much larger than the coupling of environmental spins to static background fields, $k_BT \gg \omega\sqrt{S(S+1)}$, implying that $\langle B\rangle = 0$ and hence $\langle\varphi\rangle = 0$. To compute the ensemble average, $\big\langle S\big\rangle$, we make the substitution to the normally distributed variable $\varphi = \phi_1^*(t) - \phi_0(t)$, which, by definition, has standard deviation $\sqrt{\langle\varphi^2\rangle - \langle\varphi\rangle^2}$, giving $\big\langle S\big\rangle = \frac{1}{2}\exp\left(-\frac{1}{2}\langle\varphi^2\rangle\right)$ where

$$\varphi = \sum_{k=0}\left[\int_{t_{2k}}^{t_{2k+1}} - \int_{t_{2k+1}}^{t_{2k+2}}\right] B(t')\,dt' \tag{12.7.5}$$

and

$$\begin{aligned} \big\langle\varphi^2\big\rangle &= \sum_{k=0}\sum_{j=0}\left[\int_{t_{2k}}^{t_{2k+1}} dt' - \int_{t_{2k+1}}^{t_{2k+2}} dt'\right] \\ &\quad\times\left[\int_{t_{2j}}^{t_{2j+1}} dt'' - \int_{t_{2j+1}}^{t_{2j+2}} dt''\right]\big\langle B(t')B(t'')\big\rangle. \end{aligned} \tag{12.7.6}$$

We therefore define the semi-classical analogue of the decoherence function, Λ, via

$$\Lambda \equiv \frac{1}{2}\big\langle\varphi^2\big\rangle\,. \tag{12.7.7}$$

The problem of determining Λ then reduces to finding an expression for the autocorrelation function of the effective magnetic field, as was detailed in sections 12.3.1 and 12.5.

The phase shift of the central spin will always depend on the pulse sequence employed, but a certain degree of abstraction is achieved if we consider the second integral of the environmental autocorrelation function, G, defined by

$$\frac{d^2}{dt^2}G(t) \;=\; \big\langle B(t')B(t'')\big\rangle \tag{12.7.8}$$

It then becomes a simple exercise to show, using equation 12.7.6, the pulse sequence-specific decoherence functions are given by appropriate linear combinations of dilated G functions,

$$\begin{aligned}\Lambda_{\text{fid}} &= \frac{1}{2}\big\langle \phi^2_{\text{fid}}(t)\big\rangle = \big\langle G(t)\big\rangle,\\ \Lambda_{\text{se}} &= \frac{1}{2}\big\langle \phi^2_{\text{se}}(t)\big\rangle = 4\big\langle G(t/2)\big\rangle - \big\langle G(t)\big\rangle,\end{aligned} \tag{12.7.9}$$

and so on, showing that G essentially plays the role of a classical 'generalised decoherence function'.

Using the secular autocorrelation function (equation 12.5.1), we find the corresponding semiclassical spin-echo decoherence function for the ZSE regime to be

$$\begin{aligned}\Lambda \;&\sim\; \frac{128}{45}\frac{\sqrt[3]{2}\left(4-\sqrt[3]{2}\right)\pi^{14/3}(ant)^2(bnt)^{5/3}}{3^{2/3}\Gamma\left(\frac{14}{3}\right)}\\ &\quad -\frac{64\pi^5(ant)^2(bnt)^2}{135\sqrt{3}\Gamma\left(\frac{4}{3}\right)}\\ &= \left(\frac{t}{120\,\mu s}\right)^{11/3} - \left(\frac{t}{180\,\mu s}\right)^4,\end{aligned} \tag{12.7.10}$$

giving a coherence time of $127\,\mu$s. Notice that the effective magnetic field emanating from the lateral components of the nuclear spins have been suppressed to order $A^2_{x,y}/\omega^2$ by virtue of double integration with respect to t of terms involving $\cos(\omega t)$, leaving only $z-z$ components of the effective field in the Z > E limit. This is consistent with the suppression of lateral components seen in the transition from SZE to ZSE regimes in the quantum mechanical analysis of this work.

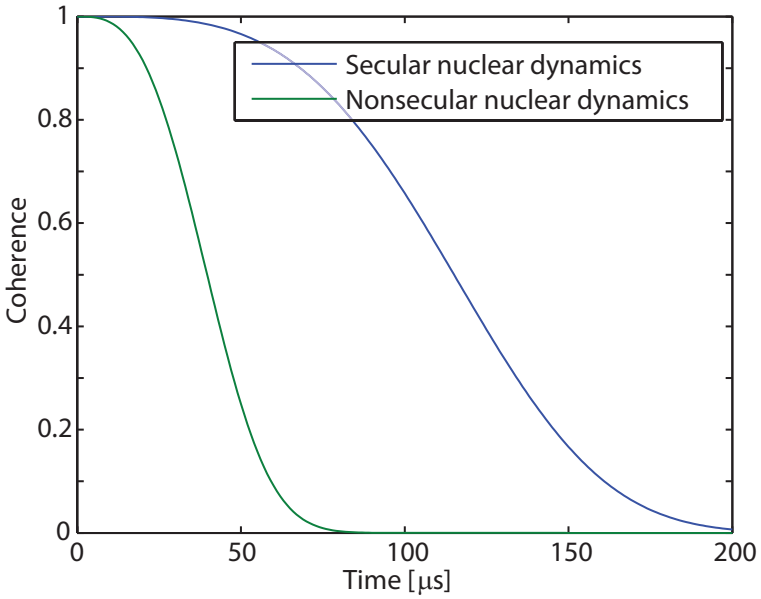

Figure 12.16: Plots showing the decoherence envelopes calculated using a semi-classical approach based on the determination of the autocorrelation function of the effective magnetic field from the hyperfine coupling of the environmental nuclei to the central spin. Qualitatively, this approach reproduces the effect of increasing the magnetic field, in that the decoherence rates are much faster for a non-secular environmental regime than those of a secular regime. However, the resulting coherence times are nearly an order of magnitude shorter than those computed with the quantum mechanical approach developed in this work, resulting from a mistreatment of the hyperfine couplings, ultimately showing that a semi-classical treatment of this problem is not adequate.

Similarly, using the non-secular autocorrelation function (equation 12.5.4), the semiclassical spin-echo decoherence function corresponding to the SEZ regime is

$$\Lambda = \frac{64}{243}\pi^4(ant)^2bnt, \tag{12.7.11}$$

which has an associated coherence time of $45\,\mu$s.

The resulting spin-echo envelopes from this semi-classical analysis are plotted in figure 12.16. From these results, we see that the associated coherence times are almost an order of magnitude shorter than those deduced using the quantum mechanical

approach developed in this work. We can attribute this discrepancy to the semi-classical approach not taking into account the back-action of the environment on the central spin, leading to a number of consequences.

Firstly, this allows for the environment to evolve freely under its own influence at all times, irrespective of the spin state (and hence the projected hyperfine field) of the NV, essentially doubling the effective fluctuation rate of the semi-classical spin bath field. In previous work[HCHH09], we have shown that this increases the spin-echo decoherence rate for systems that exist in a slowly fluctuating regime, as is the case for the nuclear spin bath considered here.

Secondly, the semi-classical approach over estimates the dependence of the scaling of the temporal scalings of the resulting decoherence functions, leading to scalings of $\Lambda \sim t^{11/3}$ and $\Lambda \sim t^3$ associated with the secular and non-secular nuclear dynamics. This is again in contrast to the quantum mechanical results, which show quadratic scalings for the three parameter regimes applicable to this problem.

The third consequence is more critical. Whereas in the quantum mechanical analysis, the hyperfine coupling entered into the decoherence function as $\sin^2(A_z t/4)$, in the semiclassical case the hyperfine coupling manifests as $(A_z t)^2$, showing the latter to correspond to the short-time limit of the former. This means the two approaches only agree on timescales that are shorter than the FID time, implying that the semiclassical approach is not valid in analysing the spin-echo decay of an NV centre coupled to a nuclear spin.

12.8 Conclusion

In this work we have developed a purely quantum mechanical methodology by which to treat the decoherence of an NV centre spin coupled to a nuclear spin environment. This approach, based on the spatial statistics of environmental impurities, affords a natural decomposition of the bath into 6 distinct parameter regimes as defined by the relative strengths of the hyperfine, Zeeman and mutual dipolar coupling of the environmental spins. Such a rigorous treatment of this problem negates the need for any unjustified ad-hoc assumptions regarding the environmental NV-nuclear or nuclear-nuclear dynamics, allowing us to definitively resolve the analytic scalings of the associated decoherence functions in each of the relevant regimes. This has, consequently, allowed us to analytically derive the dependence of quantities such as coherence times and characteristic ESEEM features on the strength of a background magnetic field. In doing so we have demonstrated excellent agreement with existing numerical and experimental work, whilst simultaneously falsifying many of the current and existing analytic results in the literature.

Chapter 13

Summary and Conclusions

The first part of this thesis was concerned with the application of few-state, spin-based quantum systems to measuring fluctuating biological, chemical and solid-state environments at the nanoscale. This was facilitated by exposing the system to the environment in a controlled manner, and using the resulting decoherence to obtain information about the dynamic processes taking place within the environment itself. In all practical contexts, this work was focused on the Nitrogen-Vacancy centre in diamond, owing to its narrow spectral features, bio-compatibility, and room temperature operation; although, the theoretical techniques developed here are applicable to many spin based open quantum systems.

In chapter 3, we began with a brief discussion on the physical origin of the NV centre, and then moved to a technical overview of the specific NV measurement protocols that were employed throughout this thesis. This included a complete mathematical description of the spin degrees of freedom of the NV centre optical groundstate, and the various means by which we can control and manipulate this spin using optical and microwave fields.

In chapter 4, we addressed the limitations of existing magnetometry techniques, based on Nitrogen-Vacancy (NV) defects, in measuring randomly fluctuating (FC) magnetic fields. We showed that not only does the presence of a fluctuating environment reduce the sensitivity of the NV spin to DC and AC magnetic fields, but that probing the dephasing rate of the NV spin in such an environment permits the characterisation of FC fields otherwise inaccessible to DC and AC based techniques. FC sensitivities were shown to be comparable to those of AC magnetometry, whilst requiring no additional experimental overheads or sample control.

Chapter 5 was focused on a detailed analysis of an experimental investigation into the techniques developed in chapter 4, using NV centres exposed to a manganese electronic spin-rich electrolyte. This combined experimental and theoretical study demonstrated the effectiveness of decoherence based sensing in studying the effects of external nanoscale magnetic environments on a central quantum system. These techniques allowed us to answer a number of critical questions surrounding such systems in the literature, revealing information regarding the physical origins of fluctuating magnetic phenomena on the nanodiamond surface, and the depths at which a given NV centre resides below this surface. Furthermore, the sub-10 nm spatial resolution reported in this study represents an improvement of more than 4 orders of magnitude over what is currently available with state of the art magnetic resonance based detection.

One major theme of chapters 4 and 5 was the limitations the intrinsic decoherence rate of the NV spin system put on the overall sensitivity of the measurement protocol. Existing approaches to improving this sensitivity had been to employ diamond crystals with a high NV density at the cost of spatial resolution, or extend T_2

via the manufacture of isotopically pure diamond crystal. In chapter 6, we adopted a complimentary approach in which optimal dynamic decoupling techniques are used to extend NV coherence times, allowing for a greater phase acquisition from the target system. Our results showed that dephasing times are ultimately limited by the self correlation time of the fluctuating environment, thus NV magnetometer interrogation times may be extended by nearly four orders of magnitude beyond the free-induction decay time. These results suggest that single spin, room temperature magnetometer sensitivities as low as $5\,\mathrm{pT\,Hz^{-1/2}}$ may be possible with current technology. The effectiveness of this approach was verified via an experimental investigation, the results of which were shown to be consistent with theoretical predictions. Such techniques have the potential to yield great improvements to nano-scale sensing, particularly nano-biological processes occurring at room temperature, and have thus been universally adopted in the NV magnetometry field following the publication of this work.

In continuing with the theme of trying to improve the sensitivity and fidelity of NV magnetometry techniques, chapter 7 was focused on investigating the artifacts present in the experimental results of chapter 5. To this point, our analysis had assumed that perfect, instantaneous pulses were possible, and that we may be completely detuned from the $|0\rangle \leftrightarrow |-1\rangle$ transition. This work, however, showed that the presence of the microwave field and the adjacent spin bath results in a broadening of both NV transitions, meaning that not only is it impossible to perfectly tune to the $|0\rangle \leftrightarrow |+1\rangle$ transition, we also achieve a non-resonant excitation of the $|0\rangle \leftrightarrow |-1\rangle$ transition, leading to a non-trivial population leakage into the $|-1\rangle$ state. These effects, and the resulting loss of measurement fidelity, were quantified in the context of an NV centre coupled to three different proximate spin baths: the

ppm nitrogen electron donor spin bath in type 1b diamond, the 1.1% ^{13}C nuclear spin bath in ultra-pure low nitrogen diamond, and the surface electron spin bath of diamond nanocrystals. These results were compared to the experimental data from chapter 5, demonstrating excellent agreement, and provide an accurate description of the previously unexplained experimental artifacts. Furthermore, this investigation has detailed the manner in which these artifacts, and the associated errors, may be suppressed.

In chapters 8 and 9, we analysed and discussed two important applications of decoherence sensing techniques to biological imaging, stemming from the bio-compatibility of diamond and the non-invasive NV measurement protocols discussed in previous chapters. The work of chapter 8 was undertaken following the recognition of a clear and urgent need for detection of cell membrane ion-channel operation with wide-field capability. We explored the quantum dynamics of a NV probe in proximity to the ion channel, lipid bilayer and surrounding aqueous environment, and showed that real-time detection of ion channel operation at millisecond resolution is possible by directly monitoring the quantum coherence of the NV spin. The results of this chapter demonstrate the potential for this platform to revolutionize the characterisation of ion channel action, and possibly other membrane proteins, with important implications for molecular biology and drug discovery.

The work of chapter 9 was focused on using the collective magnetic field sensing properties of NV-ensembles in diamond for widefield imaging of the dynamic activity of neuronal networks; a quantitative understanding of which is fundamental to gaining insight into information processing in the brain. We analysed the sensitivity of the system to the magnetic field generated by an axon transmembrane potential,

and confirmed these predictions experimentally using electronically-generated neuron signals. By numerical simulation of the time dependent transmembrane potential of a morphologically reconstructed hippocampal CA1 pyramidal neuron, we showed that the NV array is capable of imaging planar neuron activity non-invasively at millisecond temporal resolution and micron spatial resolution over wide-fields. The experimental results and theoretical work in this chapter have established the significant potential of this quantum based technique to visualise the key components of neuronal network activity to provide exciting new insight into biological neuronal network function.

Up to chapter 10, we had considered the detection of magnetic processes based exclusively on monitoring the dephasing of the NV electron spin. Such protocols were well suited to measuring processes with frequencies of less than a few MHz, however a method by which to sensitively detect rapidly fluctuating processes, without the need for complicated pulse sequences, was still lacking. In this chapter, our focus shifted from pure dephasing processes (in which we measure the dephasing time, T_2) to those allowing the central system to exchange energy with its surrounding environment (in which we measure the longitudinal relaxation time, T_1). The comparatively long intrinsic T_1 times of NV centres (as compared with T_2) make this approach inherently more sensitive than methods based on measuring dephasing rates. A detailed analysis of the response of the NV spin state to an arbitrary spectral density was performed, and used to develop a protocol by which this spectrum may be mapped. This framework was used to analyse two important milestone experiments, both of which demonstrate excellent agreement with the theoretical developments of this chapter.

One common theme amongst the NV based sensing protocols considered in chapters 3 to 10 was that the NV axis had been assumed to be fixed with respect to some external laboratory axis. Chapter 11 was based on the fact that, in some cases, *in-situ* monitoring of the NV spin state may not allow us to control the crystal orientation due to the lack of any mechanical contact. We discussed how the unique optical and spin properties of an NV centre in a diamond nanocrystal allow us to simultaneously obtain information regarding both the surrounding electromagnetic environment, and the mechanical forces and motion to which the diamond nanocrystal is subjected. We then demonstrated the use of these techniques by performing and analysing two experiments involving diamond nanocrystals being taken up endosomally by living human cervical cancer cells.

Finally, in chapter 12, we developed an analytic solution to the decades-old central spin problem in the context of an NV centre spin immersed in a 1.1% ^{13}C nuclear spin bath. Our approach was based on the spatial statistics of these spins, yielding a natural decomposition of the bath into 6 distinct parameter regimes, as defined by the relative strengths of the hyperfine, Zeeman and mutual dipolar coupling of the environmental spins. Such a rigorous treatment of this problem negates the need for any unjustified ad-hoc assumptions regarding the environmental NV-nuclear or nuclear-nuclear dynamics. This has allowed us to definitively resolve the analytic scalings of the associated decoherence functions for an arbitrary background magnetic field strength, and analytically derive the associated dependence of quantities such as coherence times and characteristic ESEEM features. Our results demonstrate excellent agreement with existing numerical and experimental work, and simultaneously falsify many of the current and existing analytic claims in the literature.

The results of future work in the field of spin-based magnetometry will undoubtedly prove exciting, as we improve our ability to probe systems at the nanoscale. As our knowledge of the world around us continues to deepen, new and often counter-intuitive ideas will surface, allowing us to probe deeper again. The application of sophisticated quantum based technology to the imaging of complex dynamical systems provide us with a perfect example of this, and will thus prove to be of great importance in the future of the physical and life sciences.

Bibliography

[AB07] P. Arhem and C. Blomberg, *Ion channel density and threshold dynamics of repetitive firing in a cortical neuron model*, Biosystems **89** (2007), 117–125.

[ABL+09] V. M. Acosta, E. Bauch, M. P. Ledbetter, C. Santori, K.-M. C. Fu, P. E. Barclay, R. G. Beausoleil, H. Linget, J. F. Roch, F. Treussart, S. Chemerisov, W. Gawlik, and D. Budker, *Diamonds with a high density of nitrogen-vacancy centers for magnetometry applications*, Phys. Rev. B **80** (2009), 115202.

[AW53] P.W. Anderson and P.R. Weiss, *Exchange narrowing in paramagnetic resonance*, Rev. Mod. Phys. **25** (1953), 269–276.

[BBC+04] I. Bertini, F. Bianchini, L. Calorini, S. Colagrande, M. Fragai, A. Franchi, O. Gallo, C. Gavazzi, and C. Luchinat, *Persistent contrast enhancement by sterically stabilized paramagnetic liposomes in murine melanoma*, Magnetic resonance in medicine **52** (2004), no. 3, 669–672.

[BBL91] L. Banci, I. Bertini, and C. Luchinat, *Nuclear and electron relaxation: The magnetic nucleus-unpaired electron coupling in solution*, 1 ed., Wiley-VCH, New York, 1991.

[BCK+08] G. Balasubramanian, I.Y. Chan, R. Kolesov, M. Al-Hmoud, J. Tisler, C. Shin, C. Kim, A. Wojcik, P.R. Hemmer, A. Krueger, T. Hanke, A. Leitenstorfer, R. Bratschitsch, F. Jelezko, and J. Wrachtrup, *Nanoscale imaging magnetometry with diamond spins under ambient conditions*, Nature **455** (2008), 648–651.

[BCS11] E. Barnes, L. Cywinski, and S. Das Sarma, *Master equation approach to the central spin decoherence problem: Uniform coupling model and role of projection operators*, Phys. Rev. B. **84** (2011), 155315.

[BCS12] ———, *Nonperturbative master equation solution of central spin dephasing dynamics*, Phys. Rev. Lett. **109** (2012), 140403.

[BGN+10] C. Bradac, T. Gaebel, N. Naidoo, M.J. Sellars, J. Twamley, L.J. Brown, A.S. Barnard, T. Plakhotnik, A.V. Zvyagin, and J.R. Rabeau, *Observation and control of blinking nitrogen-vacancy centres in discrete nanodiamonds*, Nature Nanotech. **5** (2010), 345–349.

[BKV+05] B.J. Baker, E.K. Kosmidis, D. Vucinic, C.X. Falk, L.B. Cohen, M. Djurisic, and D. Zecevic, *Imaging brain activity with voltage- and calcium-sensitive dyes*, Cell. Mol. Neurobiol. **25** (2005), no. 2, 245–282.

[BLS+06] H. Bannai, S. Levi, C. Schweizer, M. Dahan, and A. Triller, *Imaging the lateral diffusion of membrane molecules with quantum dots*, Nature Protocols **1** (2006), 2628–2634.

[BNT+09] G. Balasubramanian, P. Neumann, D. Twitchen, M. Markham, R. Kolesov, N. Mizuochi, J. Isoya, J. Achard, J. Beck, J. Tissler, V. Jacques, P.R. Hemmer, F. Jelezko, and J. Wrachtrup, *Ultralong spin coherence time in isotopically engineered diamond*, Nature Mat. **8** (2009), 383–387.

[BP06] H.P. Breuer and F. Pertuccione, *The theory of open quantum systems*, 1 ed., Oxford University Press, 2006.

[BSS+08] G Baaken, M. Sondermann, C. Schlemmer, J. Ruhe, and Jan C. Behrends, *Planar microelectrode-cavity array for high-resolution and parallel electrical recording of membrane ionic currents*, Lab Chip **8** (2008), 938–944.

[CB05] B. M. Chernobrod and G. P. Berman, *Spin microscope based on optically detected magnetic resonance*, J. Appl. Phys. **97** (2005), 014903.

[CDS10] L. Cywinski, V.V. Dobrovitski, and S.D. Sarma, *Spin echo decay at low magnetic fields in a nuclear spin bath*, Phys. Rev. B. **82** (2010), 035315.

[CDT+06] L. Childress, M. V. Gurudev Dutt, J. M. Taylor, A. S. Zibrov, F. Jelezko, J. Wrachtrup, P. R. Hemmer, and M. D. Lukin, *Coherent dynamics of coupled electron and nuclear spin qubits in diamond*, Science **314** (2006), 281–285.

[CGO+06] J.H. Cole, A.D. Greentree, D.K.L. Oi, S.G. Schirmer, C.J. Wellard, and L.C.L. Hollenberg, *Identifying a two-state hamiltonian in the presence of decoherence*, Phys. Rev. A. **73** (2006), 062333.

[CH09] J. H. Cole and L. C. L. Hollenberg, *Scanning quantum decoherence microscopy*, Nanotech. **20** (2009), 495401.

[CJ98] J. Cai and D. P. Jones, *Communication - superoxide in apoptosis - mitochondrial generation triggered by cytochrome c loss*, J. Biol. Chem. **273** (1998), 1140111404.

[CK01] F.T. Charnock and T.A. Kennedy, *Combined optical and microwave approach for performing quantum spin operations on the nitrogen-vacancy center in diamond*, Phy. Rev. B **64** (2001), 041201.

[CK11] M. R. Cohen and A. Kohn, *Measuring and interpreting neuronal correlations*, Nat. Neurosci. **14** (2011), no. 7, 811–819.

[CLNS08] L. Cywinski, R.M. Lutchyn, C.P. Nave, and S.D. Sarma, *How to enhance dephasing time in superconducting qubits*, Phys. Rev. B. **77** (2008), 174509.

[CPC+07] J. Chao, E. Perevedentseva, P. Chung, K. Liu, C. Cheng, C. Chang, and C. Cheng, *Nanometer-sized diamond particle as a probe for biolabeling*, Biophys. J. **93** (2007), 2199–2208.

[CSG+05] J.H. Cole, S.G. Schirmer, A.D. Greentree, C.J. Wellard, D.K.L. Oi, and L.C.L. Hollenberg, *Identifying an experimental two-state hamiltonian to arbitrary accuracy*, Phys. Rev. A. **71** (2005), 062312.

[CWS09a] L. Cywinski, W.M. Witzel, and S.D. Sarma, *Electron spin dephasing due to hyperfine interactions with a nuclear spin bath*, Phys. Rev. Lett. **102** (2009), 057601.

[CWS09b] ———, *Pure quantum dephasing of a solid-state electron spin qubit in a large nuclear spin bath coupled by long-range hyperfine-mediated interactions*, Phys. Rev. B. **79** (2009), 245314.

[Dam05] S. Damjanovich, *Biophysical aspects of transmembrane signalling*, 1 ed., Springer-Verlag, Berlin, Heidelberg, 2005.

[Deg08] C. L. Degen, *Scanning magnetic field microscope with a diamond single-spin sensor*, Appl. Phys. Lett. **92** (2008), 243111.

[DFAH08] V.V. Dobrovitski, A.E. Feiguin, D.D. Awschalom, and R. Hanson, *Decoherence dynamics of a single spin versus spin ensemble*, Phys. Rev. B. **77** (2008), 245212.

[DFD+11] F. Dolde, H. Fedder, M. W. Doherty, T. Nbauer, F. Rempp, G. Balasubramanian, T. Wolf, F. Reinhard, L. C. L. Hollenberg, F. Jelezko, and J. Wrachtrup, *Electric-field sensing using single diamond spins*, Nat. Phys. **7** (2011), 459463.

[DFHA09] V.V. Dobrovitski, A.E. Feiguin, R. Hanson, and D.D. Awschalom, *Decay of rabi oscillations by dipolar-coupled dynamical spin environments*, Phys. Rev. Lett. **102** (2009), 237601.

[DS00] M. H. Devoret and R. J. Schoelkopf, *Amplifying quantum signals with the single-electron transistor*, Nature **406** (2000), no. 6799, 1039–1046.

[dS09] R. de Sousa, *Electron spin as a spectrometer of nuclear-spin noise and other fluctuations*, Topics Appl. Physics **115** (2009), 183–220.

[dSD03a] R. de Sousa and S. DasSarma, *Electron spin coherence in semiconductors: Considerations for a spin-based solid-state quantum computer architecture*, Phys. Rev. B. **67** (2003), 033301.

[dSD03b] ———, *Theory of nuclear-induced spectral diffusion: Spin decoherence of phosphorus donors in si and gaas quantum dots*, Phys. Rev. B. **68** (2003), 115322.

[dSDS04] R. de Sousa, J.D. Delgado, and S. Das Sarma, *Silicon quantum computation based on magnetic dipolar coupling*, Phys. Rev. A **70** (2004), 052304.

[FDT+09] G.D. Fuchs, V.V. Dobrovitski, D.M. Toyli, F.J. Heremans, and D.D. Awschalom, *Gigahertz dynamics of a strongly driven single quantum spin*, Science **326** (2009), no. 5959, 1520–1522.

[FFL02] Y. Fang, A. Frutos, and J. Lahiri, *Membrane protein microarrays*, J. Am. Chem. Soc **124** (2002), no. 1, 2394–2395.

[FGJ+08] O. Faklaris, D. Garrot, V. Joshi, F. Druon, J. Boudou, T. Sauvage, P. Georges, P.A. Curmi, and F. Treussart, *Detection of single photoluminescent diamond nanoparticles in cells and study of the internalization pathway*, Small **4** (2008), no. 12, 2236–2239.

[FLC+07] C.C. Fu, H.Y. Lee, K. Chen, T.S. Lim, H.Y. Wu, P.K. Lin, P.K. Wei, P.H. Tsao, H.C. Chang, and W. Fann, *Characterization and application of single fluorescent nanodiamonds as cellular biomarkers*, Proc. Natl. Acad. Sci. U.S.A. **104** (2007), no. 3, 727–732.

[For00] J. A. Fornes, *Dielectric relaxation around a charged colloidal cylinder in an electrolyte*, J. Colloid Interface Sci. **222** (2000), 97–102.

[FYD11] L. Fenno, O. Yizhar, and K. Deisseroth, *The development and application of optogenetics*, Annu. Rev. Neurosci. **34** (2011), 389–412.

[GABS06] Y.M. Galperin, B.L. Altshuler, J. Bergli, and D.V. Shantsev, *Non-gaussian low-frequency noise as a source of qubit decoherence*, Phys. Rev. Lett. **96** (2006), 097009.

[GMDS+05] S. Grillner, H. Markram, E. De Schutter, G. Silberberg, and F.E.N. LeBeau, *Microcircuits in action - from cpgs to neocortex*, Trends Neurosci. **28** (2005), no. 10, 525–533.

[GR00] I. S. Gradshteyn and I. M. Ryzhik, *Tables of integrals, series, and products*, Academic Press, San Diego, CA, 2000.

[HBJ+09] R. Homma, B.J. Baker, L. Jin, O. Garaschuk, A. Konnerth, L.B. Cohen, and D. Zecevic, *Wide-field and two-photon imaging of brain activity with voltage- and calcium-sensitive dyes*, Philos. Trans. R. Soc. B-Biol. Sci. **364** (2009), no. 1529, 2453–2467.

[HBT+12] L.T. Hall, G.C.G. Beart, E.A. Thomas, D.A. Simpson, L.P. McGuinness, J.H. Cole, J.H. Manton, R.E. Scholten, F. Jelezko, J. Wrachtrup, S. Petrou, and L.C.L. Hollenberg, *High spatial and temporal resolution wide-field imaging of neuron activity using quantum nv-diamond*, Sci. Rep. **2** (2012).

[HCHH09] L.T. Hall, J.H. Cole, C.D. Hill, and L.C.L. Hollenberg, *Sensing of fluctuating nanoscale magnetic fields using nitrogen-vacancy centers in diamond*, Phys. Rev. Lett. **103** (2009), 220802.

[HDF+08] R. Hanson, V. V. Dobrovitski, A. E. Feiguin, O. Gywat, and D. D. Awschalom1, *Coherent dynamics of a single spin interacting with an adjustable spin bath*, Science **320** (2008), 352–355.

[HGAW06] L.C.L. Hollenberg, A.D. Greentree, Fowler A.G., and C.J. Wellard, *Two-dimensional architectures for donor-based quantum computing*, Phys. Rev. B **74** (2006), no. 4, 045311.

[HHC+10] L.T. Hall, C.D. Hill, J.H. Cole, B.Stadler, F.Caruso, P.Mulvaney, J.Wrachtrup, and L.C.L. Hollenberg, *Monitoring ion-channel function in real time through quantum decoherence*, Proc. Natl. Acad. Sci. U.S.A. **107** (2010), no. 44, 18777–18782.

[HHCH10] L.T. Hall, C. D. Hill, J. H. Cole, and L. C. L. Hollenberg, *Ultrasensitive diamond magnetometry using optimal dynamic decoupling*, Phys. Rev. B **82** (2010), no. 4, 045208.

[Hil05] B. Hillle, *Ionic channels of excitable membranes*, 3 ed., Sinauer Associates, Sunderland, MA, 2005.

[ITAY02] T. Ide, Y. Takeuchi, T. Aoki, and T. Yanagida, *Simultaneous optical and electrical recording of a single ion-channel*, Jpn. J. Physiol. **52** (2002), 429.

[JHM+09] L. Jiang, J. S. Hodges, J. R. Maze, P. Maurer, J. M. Taylor, D. G. Cory, P. R. Hemmer, R. L. Walsworth, A. Yacoby, A. S. Zibrov, and M. D. Lukin, *Repetitive readout of a single electronic spin via quantum logic with nuclear spin ancillae*, Science **326** (2009), 267–272.

[JPG+02] F. Jelezko, I. Popa, A. Gruber, C. Tietz, J. Wrachtrup, A. Nizovtsev, and S. Kilin, *Single spin states in a defect center resolved by optical spectroscopy*, Appl. Phys. Lett. **81** (2002), 2160–2162.

[JS09] R. Jelinek and L. Silbert, *Biomimetic approaches for studying membrane processes*, Mol. Biosyst. **5** (2009), 811–818.

[JW06] F. Jelezko and J. Wrachtrup, *Single defect centres in diamond: A review*, Phys. Stat. Sol. **203** (2006), 3207 – 3225.

[KA62] J.R. Klauder and P.W. Anderson, *Spectral diffusion decay in spin resonance experiments*, Phys. Rev. **125** (1962), 912–932.

[Kan98] B.E. Kane, *A silicon-based nuclear spin quantum computer*, Nature **393** (1998), 133–137.

[KF08] Y. C. Kim and M. E. Fisher, *Charge fluctuations and correlation lengths in finite electrolytes*, Phys. Rev. E **77** (2008), 051502.

[KKW04] D. Kruk, J. Kowalewski, and P.O. Westlund, *Nuclear and electron spin relaxation in paramagnetic complexes in solution: Effects of the quantum nature of molecular vibrations*, J. Chem. Phys. **121** (2004), 2215.

[KL07a] K. Khodjasteh and D. A. Lidar, *Fault-tolerant quantum dynamical decoupling*, Phys. Rev. Lett. **95** (2007), 180501.

[KL07b] ———, *Performance of deterministic dynamical decoupling schemes: Concatenated and periodic pulse sequences*, Phys. Rev. A **75** (2007), 062310.

[KSH+13] S. Kaufmanna, D.A. Simpson, L.T. Hall, V. Perunicic, P. Senn, S. Steinert, L.P. McGuinness, B.C. Johnson, T. Ohshima, F. Caruso, J. Wrachtrup, R. E. Scholten, P. Mulvaney, and L.C.L. Hollenberg, *Detection of atomic spin labels in a lipid bilayer using a single-spin nanodiamond probe*, Proc. Natl. Acad. Sci. U.S.A. **110** (2013), 10894.

[LBP+94] Kim Lefmann, Bronislaw Buras, E. Jonas Pedersen, Elizaveta S. Shabanova, Peter A. Thorsen, Finn Berg Rasmussen, and J. P. F. Sellschop, *Nmr spectra of pure* ^{13}C *diamond*, Phys. Rev. B **50** (1994), 15623–15627.

[LD98] D. Loss and D.P. DiVincenzo, *Quantum computation with quantum dots*, Phys. Rev. A **57** (1998), no. 1, 120–126.

[LMM07] H. Leontiadou, A.E. Mark, and S.J. Marrink, *Ion transport across transmembrane pores*, Biophys. J. **92** (2007), 4209–4215.

[LRDH11] G. De Lange, D. Riste, V.V. Dobrovitski, and R. Hanson, *Single-spin magnetometry with multipulse sensing sequences*, Phys. Rev. Lett. **106** (2011), 080802.

[Lun06] K. Lundstrom, *Structural genomics for membrane proteins*, Cell. Mol. Life Sci. **63** (2006), 2597–2607.

[LWD08] B. Lee, W. M. Witzel, and S. DasSarma, *Universal pulse sequence to minimize spin depahasing in the central spin decoherence problem*, Phys. Rev. Lett. **100** (2008), 160505.

[LWR+10] G. De Lange, Z.H. Wang, D. Riste, V.V. Dobrovitski, and R. Hanson, *Universal dynamical decoupling of a single solid-state spin from a spin bath*, Science **330** (2010), 60–63.

[LYS07] R. B. Liu, W. Yao, and L.J. Sham, *Control of electron spin decoherence caused by electron-nuclear spin dynamics in a quantum dot*, New J. Phys. **9** (2007), 226.

[LYS10] R.B. Liu, W. Yao, and L.J. Sham, *Quantum computing by optical control of electron spins*, Adv. Phys. **59** (2010), 703–802.

[MDH11] P. Delaney M.W. Doherty, N.B. Manson and L.C.L. Hollenberg, *The negatively charged nitrogen-vacancy centre in diamond: the electronic solution*, New J. Phys. **13** (2011), 025019.

[MDW+12] J. R. Maze, A. Drau, V. Waselowski, H. Duarte, J.F. Roch, and V. Jacques, *Free induction decay of single spins in diamond*, New J. Phys. **14** (2012), 103041.

[MG58] S. Meiboom and D. Gill, *Modified spin-echo method for measuring nuclear relaxation times*, Rev. Sci. Instrum. **29** (1958), 688691.

[MHS+13] L. P. McGuinness, L. T. Hall, A. Stacey, D. A. Simpson, C. D. Hill, J. H. Cole, K. Ganesan, B. C. Gibson, S. Prawer, P. Mulvaney, F. Jelezko, J. Wrachtrup, R. E. Scholten, and L. C. L. Hollenberg, *Ambient nanoscale sensing with single spins using quantum decoherence*, New J. Phys. **15** (2013), 073042.

[MKS+13] H. J. Mamin, M. Kim, M. H. Sherwood, C. T. Rettner, K. Ohno, D. D. Awschalom, and D. Rugar, *Nanoscale nuclear magnetic resonance with a nitrogen-vacancy spin sensor*, Science **339** (2013), 557–560.

[ML11] J. Morton and B. W. Lovett, *Hybrid solid-state qubits: The powerful role of electron spins*, Annu. Rev. Condens. Matter Phys. **2** (2011), 189.

[MNR+09] N. Mizuochi, P. Neumann, F. Rempp, J. Beck, V. Jacques, P. Siyushev, K. Nakamura, D. J. Twitchen, H. Watanabe, S. Yamasaki, F. Jelezko, and J. Wrachtrup, *Coherence of single spins coupled to a nuclear spin bath of varying density*, Phys. Rev. B **80** (2009), 041201(R).

[MRTW62] P. Mueller, D.O. Rudin, H. TiTien, and W.C. Wescott, *Reconstitution of cell membrane structure in vitro and its transformation into an excitable system*, Nature **194** (1962), 979 – 980.

[MSH+08] J. R. Maze, P. L. Stanwix, J. S. Hodges, J. M. Taylor S. Hong1, P. Cappellaro, L. Jiang, M. V. Gurudev Dutt, E. Togan, A. S. Zibrov, A. Yacoby, R. L. Walsworth, and M. D. Lukin, *Nanoscale magnetic sensing with an individual electronic spin in diamond*, Nature **455** (2008), 644 – 647.

[MTL08] J. R. Maze, J.M. Taylor, and M.D. Lukin, *Electron spin decoherence of single nitrogen-vacancy defects in diamond*, Phys. Rev. B **78** (2008), 094303.

[MWRT63] P. Mueller, W.C. Wescott, D.O. Rudin, and H. TiTien, *Methods for the formation of single bimolecular lipid membranes in aqueous solution*, J. Phys. Chem. **67** (1963), 534–535.

[MYS+11] L. P. McGuinness, Y. Yan, A. Stacey, D. A. Simpson, L. T. Hall, D. Maclaurin, S. Prawer, P. Mulvaney, J. Wrachtrup, F. Caruso, R. E. Scholten, and L. C. L. Hollenberg, *Quantum measurement and orientation tracking of fluorescent nanodiamonds inside living cells*, Nat. Nanotech. **6** (2011), 358363.

[NDH+11] B. Naydenov, F. Dolde, L.T. Hall, C. Shin, H. Fedder, L.C.L. Hollenberg, F. Jelezko, and J. Wrachtrup, *Dynamical decoupling of a single-electron spin at room temperature*, Phys. Rev. B **83** (2011), no. 8, 081201(R).

[NJD+13] P. Neumann, I. Jakobi, F. Dolde, C. Burk, R. Reuter, G. Waldherr, J. Honert, T. Wolf, A. Brunner, J. H. Shim, D. Suter, H. Sumiya, J. Isoya, and J. Wrachtrup, *High-precision nanoscale temperature sensing using single defects in diamond*, Nano Lett. **12** (2013), 27382742.

[NRB+10] B. Naydenov, V. Richter, J. Beck, M. Steiner, P. Neumann, G. Balasubramanian, J. Achard, F. Jelezko, J. Wrachtrup, and R. Kalish, *Enhanced generation of single optically active spins in diamond by ion implantation*, Appl. Phys. Lett. **96** (2010), no. 16, 163108.

[NZJ+07] F. Neugart, A. Zappe, F. Jelezko, C. Tietz, J.P. Boudou, A. Krueger, and J. Wrachtrup, *Dynamics of diamond nanoparticles in solution and cells*, Nano Lett. **7** (2007), 3588–3591.

[PFFF02] E. Paladino, L. Faoro, G. Falci, and R. Fazio, *Decoherence and 1/f noise in josephson qubits*, Phys. Rev. Lett. **88** (2002), 228304.

[PGD+04] I Popa, T Gaebel, M Domhan, C Wittmann, F Jelezko, and J. Wrachtrup, *Energy levels and decoherence properties of single electron and nuclear spins in a defect center in diamond*, Phys. Rev. B. **70** (2004), 201203.

[PHS+13] V.S. Perunicic, L.T. Hall, D.A. Simpson, C.D. Hill, and L.C.L. Hollenberg, *Single molecule nmr detection and spectroscopy using single spins in diamond*, arXiv:1307.8220 [quant-ph] (2013).

[PKH+03] M. Patra, M. Karttunen, M.T. Hyvonen, E. Falck, P. Lindqvist, and I. Vattulainen, *Molecular dynamics simulations of lipid bilayers: Major artifacts due to truncating electrostatic interactions*, Biophys. J. **84** (2003), 3636–3645.

[PMA+09] Amelie Perron, Hiroki Mutoh, Walther Akemann, Sunita Ghimire, Dimitar Dimitrov, Yuka Iwamoto, and Thomas Knopfel, *Second and third generation voltage-sensitive fluorescent proteins for monitoring membrane potential*, Frontiers in Molecular Neuroscience **2** (2009).

[PNJ+10] S. Pezzagna, B. Naydenov, F. Jelezko, J. Wrachtrup, and J. Meijer, *Creation efficiency of nitrogen-vacancy centres in diamond*, New J. Phys. **12** (2010), 065017.

[Pre98] J. Preskill, *Quantum computing: pro and con*, Proc. R. Soc. London, Ser. A **454** (1998), 385.

[PS11] A.M. Panich and A.I. Shames, *Nuclear spin-lattice relaxation in nanocarbon compounds caused by adsorbed oxygen*, Diamond Relat. Mater. **20** (2011), 201–204.

[QPT+10] Q. Qinga, S. K. Palb, B. Tiana, X. Duana, B. P. Timkoa, T. Cohen-Karnic, V.N. Murthy, and C.M. Liebera, *Nanowire transistor arrays for mapping neural circuits in acute brain slices*, Proc. Natl. Acad. Sci. U. S. A. **107** (2010), no. 5, 1882–1887.

[Qui02] M. Quick, *Transmembrane transporters*, 1 ed., Johnn Wiley & Sons, Inc, Hoboken, NJ, 2002.

[RHR+08] M. Royeck, M.T. Horstmann, S. Remy, M. Reitze1, Y. Yaari, and H. Beck, *Role of axonal na(v)1.6 sodium channels in action potential*

initiation of ca1 pyramidal neurons, J. Neurophysiol. **100** (2008), no. 4, 2361–2380.

[RS71] A. Rahman and F. H. Stillincera, *Molecular dynamics study of liquid water*, J. Chem. Phys. **55** (1971), 3336–3359.

[RTL+08] D. J. Reilly, J. M. Taylor, E. A. Laird, J. R. Petta, C. M. Marcus, M. P. Hanson, and A. C. Gossard, *Measurement of temporal correlations of the overhauser field in a double quantum dot*, Phys. Rev. Lett. **101** (2008), 236803.

[Sab11] Y. Sabharwal, *Digital camera technology for scientific bio-imaging*, Microscopy and Analysis **84** (2011), S5–S8.

[SDN+10] S. Steinert, F. Dolde, P. Neumann, A. Aird, B. Naydenov, G. Balasubramanian, F. Jelezko, and J. Wrachtrup, *High sensitivity magnetic imaging using an array of spins in diamond*, Review of Scientific Instruments **81** (2010), no. 4, 043705.

[SH11] R. S. Schoenfeld and W. Harneit, *Real time magnetic field sensing and imaging using a single spin in diamond*, Phys. Rev. Lett. **106** (2011), no. 3, 030802.

[SMS06] J. Schriefl, Y. Makhlin, and A. Shnirman, *Decoherence from ensembles of two-level fluctuators*, New J. Phys. **8** (2006), 1.

[SNB+10] M. Steiner, P. Neumann, J. Beck, F. Jelezko, and J. Wrachtrup, *Universal enhancement of the optical readout fidelity of single electron spins at nitrogen-vacancy centers in diamond*, Phys. Rev. B **81** (2010), 035205.

[SPM+10] P. L. Stanwix, L. M. Pham, J. R. Maze, D. Le Sage, T. K. Yeung, P. Cappellaro, P. R. Hemmer, A. Yacoby, M. D. Lukin, and R. L. Walsworth,

Coherence of nitrogen-vacancy electronic spin ensembles in diamond, Phys. Rev. B **82** (2010), no. 20, 201201R.

[SSMM05] A. Shnirman, G. Schon, I. Martin, and Y. Makhlin, *Low-and high-frequency noise from coherent two-level systems*, Phys. Rev. Lett. **94** (2005), 127002.

[SSP+13] T. Staudacher, F. Shi, S. Pezzagna, J. Meijer, J. Du, C. A. Meriles, F. Reinhard, and J. Wrachtrup, *Nuclear magnetic resonance spectroscopy on a (5-nanometer)^3 sample volume*, Science **339** (2013), 1231675.

[SWJS04] C. G. Specht, O. A. Williams, R. B. Jackman, and R. Schoepfer, *Ordered growth of neurons on diamond*, Biomaterials **25** (2004), no. 18, 4073–4078.

[SYS07] S.K. Saikin, W. Yao, and L.J. Sham, *Single-electron spin decoherence by nuclear spin bath: Linked-cluster expansion approach*, Phys. Rev. B **75** (2007), 125314.

[SZH+] S. Steinert, F. Ziem, L. T. Hall, A. Zappe, M. Schweikert, N. Gotz, A. Aird, G. Balasubramanian, L.C.L. Hollenberg, and J. Wrachtrup, *Magnetic spin imaging under ambient conditions with sub-cellular resolution*, Nature Communications **4**.

[TBN+] J. Tisler, G. Balasubramanian, B. Naydenov, R. Kolesov, B. Grotz, R. Reuter, J.P. Boudou, P.A. Curmi, M. Sennour, A. Thorel, M. Brsch, K. Aulenbacher, R. Erdmann, P.R. Hemmer, F. Jelezko, and J. Wrachtrup.

[TCC+08] J. M. Taylor, P. Cappellaro, L. Childress, L. Jiang, D. Budker, P. R. Hemmer, A. Yacoby, R. Walsworth, and M. D. Lukin, *High-sensitivity diamond magnetometer with nanoscale resolution*, Nature Phys. **4** (2008), 810–816.

[TV02] V.I. Tikhonov and A.A. Volkov, *Separation of water into its ortho and para isomers*, Science **296** (2002), 2363.

[Uhr07] G. S. Uhrig, *Keeping a quantum bit alive by optimized pi-pulse sequences*, Phys. Rev. Lett. **98** (2007), 100504.

[Uhr08] ———, *Exact results on dynamical decoupling by pi pulses in quantum information processes*, New J. Phys. **10** (2008), 083024.

[UL10] G. S. Uhrig and D. A. Lidar, *Rigorous bounds for optimal dynamical decoupling*, Phys. Rev. A **82** (2010), 012301.

[UP10] G. S. Uhrig and S. Pasini, *Efficient coherent control by sequences of pulses of finite duration*, New J. Phys. **12** (2010), 045001.

[vOG90] E. van Oort and M. Glasbeek, *Electric-field-induced modulation of spin echoes of n-v centers in diamond*, Chem. Phys. Lett. **168** (1990), no. 6, 529–532.

[WCCD12] W.M. Witzel, M.S. Carroll, L. Cywinski, and S. DasSarma, *Quantum decoherence of the central spin in a sparse system of dipolar coupled spins*, Phys. Rev. B. **86** (2012), 035452.

[WD06] W. M. Witzel and S. DasSarma, *Quantum theory for electron spin decoherence induced by nuclear spin dynamics in semiconductor quantum computer architectures: Spectral diffusion of localized electron spins in the nuclear solid-state environment*, Phys. Rev. B **74** (2006), 035322.

[WD07] ———, *Concatenated dynamical decoupling in a solid-state spin bath*, Phys. Rev. B **76** (2007), 241303(R).

[WdLR+12] Z. H. Wang, G. de Lange, D. Riste, R. Hanson, and V. V. Dobrovitski, *Comparison of dynamical decoupling protocols for a nitrogen-vacancy center in diamond*, Phys. Rev. B **85** (2012), 155204.

[WdSD05] W. M. Witzel, R. de Sousa, and S. DasSarma, *Quantum theory of spectral-diffusion-induced electron spin decoherence*, Phys. Rev. B **72** (2005), 161306(R).

[WG61] A. Watanabe and H. Grundfest, *Impulse propagation at the septal and commissural junctions of crayfish lateral axons*, J. Gen. Physiol. **45** (1961), 267–308.

[WJ06] J. Wrachtrup and F. Jelezko, *Processing quantum information in diamond*, J. Phys. Condens. Matter **18** (2006), S807.

[WRM+10] V.C. Wimmer, C.A. Reid, S. Mitchell, K.L. Richards, B.B. Scaf, B.T. Leaw, E.L. Hill, M.Royeck, M.T. Horstmann, B.A. Cromer, P.J. Davies, R. Xu, H. Lerche, S.F. Berkovic, H. Beck, and S. Petrou, *Axon initial segment dysfunction in a mouse model of genetic epilepsy with febrile seizures plus*, J. Clin. Invest. **120** (2010), no. 8, 2661–2671.

[WRS+10] V. C. Wimmer, C. A. Reid, E. Y. W. So, S. F. Berkovic, and S. Petrou, *Axon initial segment dysfunction in epilepsy*, J. Physiol.-London **588** (2010), no. 11, 1829–1840.

[YKC+05] S.J. Yu, M.W. Kang, H.C. Chang, K.M. Chen, and Y.C. Yu, *Bright fluorescent nanodiamonds: No photobleaching and low cytotoxicity*, J. Am. Chem. Soc. **127** (2005), no. 50, 17604–17605.

[YL08] W. Yang and R.B. Liu, *Quantum many-body theory of qubit decoherence in a finite-size spin bath*, Phys. Rev. B **78** (2008), 085315.

[YL09] ———, *Quantum many-body theory of qubit decoherence in a finite-size spin bath. ii. ensemble dynamics*, Phys. Rev. B **79** (2009), 115320.

[YLS07] W. Yao, R. B. Liu, and L.J. Sham, *Restoring coherence lost to a slow interacting mesoscopic spin bath*, Phys. Rev. Lett. **98** (2007), 077602.

[YS06] W. Yao and L.J. Sham, *Theory of electron spin decoherence by interacting nuclear spins in a quantum dot*, Phys. Rev. B **74** (2006), 195301.

[YSS+05] V. Yamazaki, O. Sirenko, R.J. Schafer, L. Nguyen, T. Gutsmann, L. Brade, and J.T. Groves, *Cell membrane array fabrication and assay technology*, BMC Biotechnol. **5** (2005), 18.

[ZHL12] N. Zhao, S.W. Ho, and R.B. Liu, *Decoherence and dynamical decoupling control of nitrogen vacancy center electron spins in nuclear spin baths*, Phys. Rev. B **85** (2012), no. 11, 115303.

Appendix A

The Interaction Picture

A.1 Definitions

Owing to its extensive employment throughout this thesis, we briefly review the basics of the interaction picture approach to quantum mechanics. In the cases considered in this work, we are interested in solving the evolution of a system under the influence of a Hamiltonian of the following form,

$$\mathcal{H} \;=\; \mathcal{H}_0 + \mathcal{V}, \tag{A.1.1}$$

where $\mathcal{H}_0$ is the static component (for example, the zero-field splitting of the NV centre, $D\mathcal{S}_z^2$), and $\mathcal{V}$ is a perturbation, which, in general, may be time-dependent (as in the case of a comparatively weak oscillating microwave field, $\omega_x \cos(\omega t)\mathcal{S}_x$).

For a general Schrodinger picture operator, $\mathcal{O}$, acting on an arbitrary system, we define the corresponding interaction picture operator via

$$\mathcal{O}_I \;=\; e^{i\mathcal{H}_0 t}\mathcal{O}e^{-i\mathcal{H}_0 t}. \tag{A.1.2}$$

This allows us to shift the time dependence of the system due to the static component of the Hamiltonian, $\mathcal{H}_0$, onto the operators, thereby leaving only $\mathcal{V}_I$ to dictate the time-evolution of the (interaction picture) density matrix.

Such an approach is particularly useful in the case of the NV centre spin, where

the static components are of the order of 1-10 GHz, whilst the interaction processes with which we are concerned in this work are typically in the kHz-MHz range.

A.1.1 The density matrix

The time evolution of the density matrix is described by the Liouville equation,

$$\frac{\mathrm{d}\rho}{\mathrm{d}t} = -i\big[\mathcal{H},\rho\big] + \mathcal{L}, \tag{A.1.3}$$

where $\mathcal{L}$ is the sum of all Lindbladian terms describing processes such as relaxation, dephasing, population transfer, etc, associated with the non-unitary dynamics of the open quantum system[BP06].

From equation A.1.2, the interaction picture density matrix is given by

$$\rho_I = e^{i\mathcal{H}_0 t}\rho e^{-i\mathcal{H}_0 t}. \tag{A.1.4}$$

Taking the derivative of this, we find

$$\begin{aligned}
\frac{\mathrm{d}}{\mathrm{d}t}\rho_I &= i\mathcal{H}_0 e^{i\mathcal{H}_0 t}\rho e^{-i\mathcal{H}_0 t} - ie^{i\mathcal{H}_0 t}\rho e^{-i\mathcal{H}_0 t}\mathcal{H}_0 + e^{i\mathcal{H}_0 t}\frac{\mathrm{d}\rho}{\mathrm{d}t}e^{-i\mathcal{H}_0 t} \\
&= i\big[\mathcal{H}_0,\rho_I\big] + e^{i\mathcal{H}_0 t}\Big(-i\big[\mathcal{H},\rho\big] + \mathcal{L}\Big)e^{-i\mathcal{H}_0 t} \\
&= i\big[\mathcal{H}_0,\rho_I\big] - i\big[\mathcal{H}_0,\rho_I\big] + e^{i\mathcal{H}_0 t}\Big(-i\big[\mathcal{V},\rho\big] + \mathcal{L}\Big)e^{-i\mathcal{H}_0 t} \\
&= -i\big[\mathcal{V}_I,\rho_I\big] + \mathcal{L}_I,
\end{aligned} \tag{A.1.5}$$

where the second line follows from equation A.1.3, and the third line follows from the decomposition of $\mathcal{H}$ (equation A.1.1. This expression shows that the equation of motion for the density matrix in the interaction picture is the same as that for the Schrodinger picture, but with the interaction picture operators substituted in place of the original Schrodinger picture operators.

Appendix B

Exact analytic forms relevant to the central spin problem

B.1 Exact form of single cluster decoherence envelopes

For completeness, we include the full spin-echo decoherence envelope of the NV spin due to a 2-spin cluster undergoing a secular flip-flop process. This expression is exact, and the ZSE and SZE analytic limits have been employed in the main text. This envelope will contain contributions from flip-flop (lateral and longitudinal), precession (lateral only) and simultaneous flip-flop and precession processes. For clarity, we outline these contributions separately, whence

$$L_{\rm sec} \;=\; 1 + L_{\rm FF} + L_{\rm P} + L_{\rm FF-P}. \tag{B.1.1}$$

The precession component is responsible for the decays and revivals at moderate magnetic fields, and is given by

$$\begin{aligned} L_{\rm P} \;=\; & -2\frac{A_{x,1}^2 + A_{y,1}^2}{\lambda_1^2}\sin^2\left(\frac{\lambda_1 t}{4}\right)\sin^2\left(\frac{\omega t}{4}\right) - 2\frac{A_{x,2}^2 + A_{y,2}^2}{\lambda_2^2}\sin^2\left(\frac{\lambda_2 t}{4}\right)\sin^2\left(\frac{\omega t}{4}\right) \\ & +4\frac{\left(A_{x,1}^2 + A_{y,1}^2\right)\left(A_{x,2}^2 + A_{y,2}^2\right)}{\lambda_1^2\lambda_2^2}\sin^2\left(\frac{\lambda_1 t}{4}\right)\sin^2\left(\frac{\lambda_2 t}{4}\right)\sin^4\left(\frac{\omega t}{4}\right), \end{aligned} \tag{B.1.2}$$

the flip-flop processes are responsible for the decoherence of the NV spin,

$$\begin{aligned} L_{\mathrm{FF}} &= \frac{A_{x,1}A_{x,2}+A_{y,1}A_{y,2}+\Omega_1\Omega_2}{2\lambda_1\lambda_2}\sin^2\left(\frac{Bt}{4}\right)\sin\left(\frac{t\lambda_1}{2}\right)\sin\left(\frac{t\lambda_2}{2}\right) \\ &\quad -\frac{1}{2}\sin^2\left(\frac{Bt}{4}\right)\left[1-\cos\left(\frac{t\lambda_1}{2}\right)\cos\left(\frac{t\lambda_2}{2}\right)\right] \\ &\quad -2\Bigg[\frac{\left(A_{x,2}A_{y,1}-A_{x,1}A_{y,2}\right)^2+\left(\Omega_1A_{x,2}-\Omega_2A_{x,1}\right)^2+\left(\Omega_1A_{y,2}-\Omega_2A_{y,1}\right)^2}{\lambda_1^2\lambda_2^2} \\ &\quad \times\sin^2\left(\frac{Bt}{4}\right)\sin^2\left(\frac{t\lambda_1}{4}\right)\sin^2\left(\frac{t\lambda_2}{4}\right)\Bigg], \end{aligned} \tag{B.1.3}$$

and the hybrid processes are described by

$$\begin{aligned} L_{\mathrm{FF-P}} &= 2\Bigg[\frac{\left(\Omega_1A_{x,2}-\Omega_2A_{x,1}\right)^2+\left(\Omega_1A_{y,2}-\Omega_2A_{y,1}\right)^2}{\lambda_1^2\lambda_2^2}\sin^2\left(\frac{t\lambda_1}{4}\right)\sin^2\left(\frac{t\lambda_2}{4}\right) \\ &\quad \times\sin^2\left(\frac{Bt}{4}\right)\sin^2\left(\frac{t\omega}{4}\right)\Bigg] \\ &\quad -\frac{A_{x,1}A_{x,2}+A_{y,1}A_{y,2}}{\lambda_1\lambda_2}\sin^2\left(\frac{Bt}{4}\right)\sin\left(\frac{t\lambda_1}{2}\right)\sin\left(\frac{t\lambda_2}{2}\right)\sin^2\left(\frac{t\omega}{4}\right) \\ &\quad +2\frac{A_{x,1}^2+A_{y,1}^2}{\lambda_1^2}\sin^2\left(\frac{Bt}{4}\right)\sin^2\left(\frac{t\lambda_1}{4}\right)\cos^2\left(\frac{t\lambda_2}{4}\right)\sin^2\left(\frac{t\omega}{4}\right) \\ &\quad +2\frac{A_{x,2}^2+A_{y,2}^2}{\lambda_2^2}\sin^2\left(\frac{Bt}{4}\right)\sin^2\left(\frac{t\lambda_2}{4}\right)\cos^2\left(\frac{t\lambda_1}{4}\right)\sin^2\left(\frac{t\omega}{4}\right). \end{aligned} \tag{B.1.4}$$

B.2 Exact forms of collective autocorrelation functions

The secular autocorrelation function for a two spin cluster is proportional to the difference in hyperfine couplings of the two nuclei. The leading order behaviour, corresponding to the high frequency limit associated with smaller cluster sizes comes from expanding these quantities for small r. In the ZSE regime, the magnitude of the fluctuating component only depends on the difference in the $z-z$ components of the

respective hyperfine couplings,

$$\begin{aligned}\Delta_z &= |A_{z,1} - A_{z,2}| \\ &\sim \frac{3ar}{4R^4}\Big(\sin(\theta)\big[\sin(\Theta) + 5\sin(3\Theta)\big]\cos(\phi - \Phi) + \cos(\theta)\big[3\cos(\Theta) + 5\cos(3\Theta)\big]\Big), \\ &\equiv a_\alpha, z \end{aligned} \tag{B.2.1}$$

whereas in the SZE limit, this magnitude depends on all couplings to the axial component of the NV spin,

$$\begin{aligned}\Delta &= \sqrt{A_{x,1}^2 + A_{y,1}^2 + A_{z,1}^2} - \sqrt{A_{x,2}^2 + A_{y,2}^2 + A_{z,2}^2} \\ &\sim \frac{6ar}{R^4}\frac{\sin(\theta)\big[2\sin(\Theta) + \sin(3\Theta)\big]\cos(\phi - \Phi) + 4\cos(\theta)\cos^3(\Theta)}{\sqrt{6\cos(2\Theta) + 10}}. \\ &\equiv a_\alpha \end{aligned} \tag{B.2.2}$$

Employing these expansions and averaging over the spatial degrees of freedom using equation 12.4.3, we find the collective secular autocorrelation function to be that given in equation 12.5.1, with the secular magnetisation function given by

$$\begin{aligned}M(t) &= \frac{1}{3}\Bigg(3\Gamma\left(\tfrac{2}{3}\right) + \sqrt[6]{6}\pi^{11/6}(bnt)^{5/6}\Bigg[\left(\sqrt{3} - 3\right)\mathrm{ber}_{\frac{5}{3}}\left(4\sqrt{\frac{\pi}{3}}\sqrt{bnt}\right) \\ &\quad - \left(3 + \sqrt{3}\right)\mathrm{bei}_{\frac{5}{3}}\left(4\sqrt{\frac{\pi}{3}}\sqrt{bnt}\right) + 2\sqrt{3}\mathrm{bei}_{-\frac{5}{3}}\left(4\sqrt{\frac{\pi}{3}}\sqrt{bnt}\right) \\ &\quad -2\sqrt{3}\mathrm{ber}_{-\frac{5}{3}}\left(4\sqrt{\frac{\pi}{3}}\sqrt{bnt}\right)\Bigg]\Bigg), \end{aligned} \tag{B.2.3}$$

where $\mathrm{ber}(x)$ and $\mathrm{bei}(x)$ are the Kelvin functions, defined by the real and imaginary parts of $J_\nu\left(xe^{3\pi i/4}\right)$ respectively, and $J_\nu(x)$ is the ν^{th} order Bessel function of the first kind.

Similarly, the collective non-secular autocorrelation function is given by equation 12.5.4, with the non-secular magnetisation function given by

$$N(t) = \frac{2}{9}\left[\pi bnt\,\mathfrak{G}_{0,4}^{3,0}\left(\frac{1}{9}b^2n^2\pi^2t^2\middle|\, -\tfrac{1}{2}, 0, \tfrac{1}{2}, 0\right) - 3\right], \tag{B.2.4}$$

where $\mathfrak{G}$ is the Meijer G-function[GR00].

B.3 Exact analytic forms of collective decoherence functions

B.3.1 Free induction decay

To obtain the FID decoherence functions for the ZS and SZ regimes, we start with the single-spin decoherence function as given by equation 12.6.5. Integration over R gives

$$\begin{aligned}\int_l^\infty 4\pi n R^2 \Lambda_{\mathrm{ZS}}\,\mathrm{d}R &= \frac{2}{3}\pi l^3 n\left[{}_1\mathfrak{F}_2\left(-\frac{1}{2};\frac{1}{2},\frac{1}{2};-\frac{a^2t^2(3\cos(2\Theta)+1)^2}{64l^6}\right)-1\right],\\ \int_l^\infty 4\pi n R^2 \Lambda_{\mathrm{SZ}}\,\mathrm{d}R &= \frac{2}{3}\pi l^3 n\left[{}_1\mathfrak{F}_2\left(-\frac{1}{2};\frac{1}{2},\frac{1}{2};-\frac{a^2t^2(3\cos(2\Theta)+5)}{32l^6}\right)-1\right],\end{aligned} \tag{B.3.1}$$

where $\mathfrak{F}$ is the generalised hypergeometric function. Expanding these expressions to leading order for short and long times, and integrating over the angular degrees of freedom gives the collective decoherence functions discussed in section 12.6.1 of the main text.

B.3.2 Spin-echo

Analytic limits of the decoherence function in the ZSE regime

To obtain the ZSE decoherence function in the long time limit, we integrate $\langle\Lambda_{\mathrm{ZSE}}\rangle$ (equation 12.6.15) over the spatial degrees of freedom, R and r, using equation 12.4.3,

$$\begin{aligned}\langle\Lambda_{\mathrm{ZSE}}\rangle &= \frac{(-1)^{15/16}\left(\sqrt[4]{-1}-1\right)\pi^{19/8}a_\alpha, z^{3/4}\sqrt[4]{b}nt\Gamma\left(-\frac{3}{4}\right)}{16\sqrt[8]{2}3^{3/8}}(bnt)^{3/8}\\ &\times\left[\left((-1)^{3/8}+i\right)\mathrm{ber}_{-\frac{5}{4}}\left(2\sqrt{\frac{2\pi}{3}}\sqrt{bnt}\right)+\left(\sqrt[8]{-1}+(-1)^{3/4}\right)\mathrm{ber}_{\frac{5}{4}}\left(2\sqrt{\frac{2\pi}{3}}\sqrt{bnt}\right)\right.\\ &\left.+\left(1+(-1)^{7/8}\right)\mathrm{bei}_{-\frac{5}{4}}\left(2\sqrt{\frac{2\pi}{3}}\sqrt{bnt}\right)+\left(\sqrt[4]{-1}+(-1)^{5/8}\right)\mathrm{bei}_{\frac{5}{4}}\left(2\sqrt{\frac{2\pi}{3}}\sqrt{bnt}\right)\right]\\ &+\left(\frac{2\pi}{3}\right)^{3/4}\sin\left(\frac{\pi}{8}\right)\Gamma\left(\frac{5}{4}\right)^2(a_\alpha, znt)^{3/4},\end{aligned} \tag{B.3.2}$$

where a_α is as defined in equation B.2.1 above. Expanding this expression for $t \gg 1/an$ and $t \ll 1/bn$, and integrating over the angular degrees of freedom gives the decoherence function for $t \sim T_2$ (equation 12.6.18).

To obtain the behaviour of the decoherence function at intermediate times, we must make a correction for the diamond bond length to the nuclear-nuclear component of the evolution, whilst integrating over the hyperfine dynamics as above. The associated integral is generally intractable for arbitrary limits of r, however, as $r \ll n^{-1/3}$ we may approximate the probability distribution, equation 12.4.3, by its leading order behavior, $\mathrm{P}(r) \sim 4\pi n r^2$, giving

$$\begin{aligned} \langle \Lambda_{\mathrm{ZSE}} \rangle &\sim \left(\int_0^\infty \mathrm{P}(r) - \int_0^l 4\pi r^2 \right) \frac{2\pi n}{3} \sin\left(\tfrac{\pi}{8}\right) \Gamma\left(\tfrac{1}{4}\right) \left(\frac{a_{\alpha,z} r t}{2} \right)^{3/4} \sin^2\left(\frac{3Bt}{4} \right) \mathrm{d}r \\ &= \frac{\pi^2}{20} \sqrt{2\left(\sqrt{2}-1\right)} l^{15/4} n^2 \Gamma\left(\frac{1}{4}\right) (a_{\alpha,z} t)^{3/4} \left[{}_1\mathfrak{F}_2\left(-\frac{5}{8}; \frac{3}{8}, \frac{1}{2}; -\frac{b^2 t^2}{16 l^6} \right) - 1 \right]. \end{aligned} \tag{B.3.3}$$

Expanding this expression for $t \gg 1/an$ and $t \ll 1/bn$, gives the expression for the ZSE decoherence function at intermediate times (equation 12.6.19).

To obtain the behaviour of the decoherence function at short times, we make a similar adjustment for the bond length in the hyperfine interaction, and then expand for $t \ll 1/an$ and $t \ll 1/bn$, as given by equations 12.6.20 and 12.6.21 of the main text.

Analytic limits of the decoherence function in the SZE regime

To obtain the SZE decoherence functions, we proceed in the same manner as the ZSE case above, instead using $\langle \Lambda_{\mathrm{SZE}} \rangle$ (equation 12.6.15) together with the definition of Δ (equation B.2.2).

Analytic limits of the decoherence function in the SEZ regime

To obtain the analytic limits of the SEZ decoherence function, we follow the same progression as in the ZSE limit above. The SEZ limit is somewhat simpler owing to the

fact that the hyperfine and dipole-dipole processes are decoupled from one another in the single-cluster SEZ decoherence function (equation 12.6.15). Integration over the hyperfine component from $l < R < \infty$ yields

$$\int_l^\infty \left[\sin^2\left(\frac{At}{2}\right) + \sin^2\left(\frac{At}{4}\right)\right] R^2 \mathrm{d}R = \frac{2}{3}n\left[l^3\left({}_1\mathfrak{F}_2\left(-\frac{1}{2};\frac{1}{2},\frac{1}{2};-\frac{a^2t^2}{16l^6}\right) + \cos\left(\frac{at}{l^3}\right) - 2\right) + at\mathrm{Si}\left(\frac{at}{l^3}\right)\right]. \tag{B.3.4}$$

Integration over r from l to ∞ in the dipolar interaction gives

$$\begin{aligned}\int_l^\infty \mathrm{P}(r)\sin^2\left(\frac{3Bt}{4}\right)\mathrm{d}r &= \frac{1}{4}\left[2 - \pi bnt\,\mathfrak{G}_{0,4}^{3,0}\left(\frac{b^2n^2\pi^2t^2}{4}\middle|\ -\tfrac{1}{2},0,\tfrac{1}{2},0\ \right)\right] \\ &\quad -\frac{1}{6}\pi n\left[-6bt\mathrm{Si}\left(\frac{3bt}{2l^3}\right) - 4l^3\cos\left(\frac{3bt}{2l^3}\right) + 3\pi bt + 4l^3\right],\end{aligned} \tag{B.3.5}$$

where Si is the Sine integral function, define by $\mathrm{Si}(x) = \int_0^x t^{-1}\sin(t)\,\mathrm{d}t$. Taking the relevant limits of the dipolar and hyperfine components, integrating over the angular degrees of freedom, and substituting into the definition of $\langle\Lambda_{\mathrm{SEZ}}\rangle$ (equation 12.6.15), we find the long, intermediate and short-time limits of the SEZ decoherence to be as given in equations 12.6.23, 12.6.24 and 12.6.25 respectively.